A NUMERICAL INVESTIGATION OF THE COMPRESSIBLE MIXING LAYER

A DISSERTATION

SUBMITTED TO THE DEPARTMENT OF MECHANICAL ENGINEERING

AND THE COMMITTEE ON GRADUATE STUDIES

OF STANFORD UNIVERSITY

IN PARTIAL FULFILLMENT OF THE REQUIREMENTS

FOR THE DEGREE OF

DOCTOR OF PHILOSOPHY

By

N. D. Sandham

September 1989

(Known errors corrected for pdf by NDS Nov. 2010)

I certify that I have read this thesis and in my opinion it is fully adequate, in scope and quality, as a dissertation for the degree of Doctor of Philosophy.

Prof. W. C. Reynolds (Principal Advisor)

I certify that I have read this thesis and in my opinion it is fully adequate, in scope and quality, as a dissertation for the degree of Doctor of Philosophy.

Prof. M. G. Mungal

I certify that I have read this thesis and in my opinion it is fully adequate, in scope and quality, as a dissertation for the degree of Doctor of Philosophy.

Prof. P. Moin

I certify that I have read this thesis and in my opinion it is fully adequate, in scope and quality, as a dissertation for the degree of Doctor of Philosophy.

Dr. N. N. Mansour

Approved for the University Committee on Graduate Studies:

Dean of Graduate Studies

Abstract

The effect of Mach number on the plane mixing layer has been investigated by means of linear stability theory and two- and three-dimensional direct numerical simulations of the compressible Navier-Stokes equations. The objective was to identify the effects of compressibility on a building-block fluid flow, with applications to supersonic mixing and combustion.

Results from linear stability theory show that the amplification rate is reduced as Mach number is increased. Above a convective Mach number of 0.6 it is found that three-dimensional waves are more amplified than two-dimensional waves and a simple relation is found to give the orientation of the most amplified waves. It is also shown that the linear stability theory can be used to predict the mixing layer growth rate as a function of velocity ratio, density ratio and Mach number.

Two-dimensional simulations show a strong reduction in growth rate of the two-dimensional motion as Mach number is increased, with more elongated structures forming at high Mach numbers. Shock waves are observed in two-dimensional simulations above a convective Mach number of 0.7. The supersonic modes of instability, which are the only two-dimensional unstable modes at high Mach numbers, are shown to be radiating and vortical, but have very low growth rates.

Three-dimensional simulations with random initial conditions confirm the linear stability result that oblique waves become the most amplified waves at high Mach numbers, with no evidence for any other modes of instability. Simulations beginning with a two-dimensional wave and a pair of equal and opposite oblique waves show a change in the evolved large-scale structure as Mach number is increased. Above a convective Mach number of 0.6 the oblique modes have most of the energy in the developed structure, and above a convective Mach number of 1 the two-dimensional instability wave has little effect on flow structure. Similar organized structure was found in a simulation with random initial conditions. No shock waves were found in the three-dimensional simulations, even at convective Mach numbers above 1.

Acknowledgements

This work was made possible by the financial assistance of the Air Force Office of Scientific Research as part of a Supersonic Combustion research initiative at Stanford University, and by the NASA-Ames Research Center which provided the computer facilities, most notably access to a Cray X-MP. This support is gratefully acknowledged, as is the receipt of a Fulbright-Hays Travel and Maintenance Award, administered by the United States-United Kingdom Educational Commission, which sustained me during my first year of study.

I wish to thank my advisor William C. Reynolds for his guidance and enthusiasm during this research project, and for giving me the freedom to pursue my own ideas. I am indebted to Professor Godfrey Mungal for helpful discussions throughout this work. I wish to thank my other readers, Professor Parviz Moin of Stanford and Dr. Nagi Mansour of NASA-Ames, for their careful reading of the manuscript and many helpful suggestions.

Many other people have provided help at various times during my thesis work. In particular, I wish to thank Dr. Patrick Lowery and Dr. Helen Yee for providing codes which got me started on numerical simulations. The final version of my codes made use of compact finite difference methods which were provided by Dr. Sangiva Lele of NASA-Ames, with whom I also had many profitable discussions.

Special thanks are due to my fellow students of compressible flow, Greg Blaisdell and Jackie Chen. Many problems were overcome through timely discussions with them. My office mates Gary Coleman and Hung Le were a constant source of humour during the long hours that this work demanded. Many other people made my stay in California more enjoyable, especially Bob Koch, Philippe Juvet, Ellen Longmire, Ann Anderson and Tony Dean.

Finally, I wish to thank my parents for their support and encouragement from afar.

Table of Contents

List of Tables

List of Figures

Nomenclature

Roman Symbols

a_c	Constant in Cain mapping, appendix A.
A	Constant in Taylor-Green problem, section 3.6.
A	Amplitude of a disturbance.
A_1, A_2	Amplitudes of disturbances.
A_s	Matrix for spatial stability problem, appendix A.
A_t	Matrix for temporal stability problem, appendix A.
a	Term in equation (3.48).
a_1, a_2	Constants.
a, b, c	Constants in the Padé schemes, section 3.3.2.
B	Jacobian $\partial G/\partial Q$, section 3.4.
B_s	Matrix for spatial stability problem, appendix A.
b	Constant in model equation (3.24).
b_y	Stretching parameter, equation (3.36).
c	Sound speed.
c_1	Sound speed of stream 1 (upper).
c_2	Sound speed of stream 2 (lower).
c_r	Phase speed of an instability wave, ω_r/α_r.
c_N	Phase speed of the neutral instability mode.
c_v	Specific heat at constant volume.
c_p	Specific heat at constant pressure.
CFL	Courant-Friedrichs-Lewy number, section 3.2.
d	Notation for $p\rho^{-\gamma}$, section 3.4.
D	Operator d/dy.
D_s	Diffusion coefficient.
D_c, D_μ	Terms in equation for time step, equation (3.26).
d_{lj}	Matrix elements, appendix A.

e_{lj}	Matrix elements, appendix A.
e	Internal energy per unit mass.
$E(k_x)$	Disturbance energy, defined in equation (3.53).
E_T	Total energy, defined by equation (3.4).
f	Mixture fraction.
$F(\eta)$	Dependent variable in equation (2.19).
g	Parameter in stability analysis, equation (2.41).
G	Column vector of terms in the Euler equations containing derivatives in the y direction, section 3.4.
$G(\xi)$	Alternate variable in solution for the mean flow, section 2.1.1.
h	Enthalpy per unit mass.
h', h''	Metrics in mapping, section 3.3.2.
H	Stagnation enthalpy, defined by equation (4.7).
H_2	Freestream stagnation enthalpy ratio.
i	Square root of -1.
k	Conductivity.
k	Integer wavenumber.
k_x	Integer wavenumber in the x direction.
k_z	Integer wavenumber in the z direction.
l	Length scale.
L_x	Computational box length in the x direction.
L_y	Computational box length in the y direction.
L_z	Computational box length in the z direction.
M	Local Mach number $= \sqrt{u^2+v^2}/c$.
M_1	Mach number of stream 1 (upper).
M_2	Mach number of stream 2 (lower).
M_c	Convective Mach number, $(U_1^* - U_2^*)/(c_1^* + c_2^*)$.
M_{c1}	Convective Mach number relative to stream 1, equation (1.1).
M_{c2}	Convective Mach number relative to stream 2, equation (1.1).

M_∞	General freestream Mach number.
N	Constant in exponential, section 2.3.2.
N	Number of points, appendix A.
N^*	Modified number of points, appendix A.
N_x	Number of points in x direction.
N_y	Number of points in y direction.
N_z	Number of points in z direction.
p	Pressure.
p_1	Pressure of stream 1 (upper).
p_{ref}	Refence pressure, Taylor-Green problem, section 3.6.
Pr	Prandtl number $c_p^*\mu^*/k^*$.
q	Exponent in asymptotic solution, equation (2.45).
q_i	Heat flux vector.
Q	Column vector of conservative variables, section 3.4.
Q_1, Q_2	Storage locations for time-advance, section 3.2.
r	Random number, uniformly distributed between -0.5 and 0.5.
R	Gas constant.
R	Jacobian $\partial Q/\partial U$, section 3.4.
Re	Reynolds number $U_1^*\rho_1^*\delta_{\omega_0}^*/\mu_1^*$.
Re_l	Reynolds number $U_1^*\rho_1^* l^*/\mu_1^*$.
S	Jacobian $\partial U/\partial V$, section 3.4.
S_{ij}	Strain rate tensor, defined in equation (4.10).
S_{ij}^a	Anisotropic strain rate tensor, equation (4.11).
s	Entropy, defined in equation (4.9).
Sc	Schmidt number $\mu^*/\rho^* D_s^*$.
t	Time.
T	Temperature.
T	Diagonalizing matrix, section 3.4.
T_2	Temperature of stream 2 (lower) or freestream temperature ratio.

U	Column vector of non-conservative variables, section 3.4.
U_c	Convective velocity in equation (1.1).
U_1	Velocity of stream 1 (upper).
U_2	Velocity of stream 2 (lower) or freestream velocity ratio.
u	Velocity component in the x direction.
u_i	Cartesian components of the velocity.
V	Column vector of alternate non-conservative variables, section 3.4.
v	Velocity component in the y direction.
w	Velocity component in the z direction.
x, X	Streamwise coordinate.
x_i	Cartesian coordinates.
y, Y	Cross-stream or normal coordinate.
Y_H	Howarth transformed y coordinate, equation (2.16).
z, Z	Spanwise coordinate.

Greek Symbols

α	Streamwise eigenvalue from linear stability.
α_i	Imaginary part of the spatial eigenvalue.
α_r	Real part of the spatial eigenvalue.
β	Spanwise eigenvalue from linear stability.
γ	Ratio of specific heats c_p^*/c_v^*.
γ_1	Ratio of specific heats in stream 1 (upper).
γ_2	Ratio of specific heats in stream 2 (lower).
δ	Mixing layer thickness.
δ_ρ	Mixing layer thickness based on mean density profile, see section 2.2.1.
δ_ω	Mixing layer vorticity thickness, defined in equation (2.21).
δ_{ω_0}	Initial mixing layer vorticity thickness.
$\delta_{\tilde{\omega}}$	Mixing layer vorticity thickness based on mass-weighted mean velocity profile, defined in equation (4.4).

δ'	Mixing layer growth rate $d\delta/dx$.
δ'_ρ	Mixing layer growth rate based on mean density profile.
δ'_ω	Mixing layer growth rate based on vorticity thickness.
δ_{ij}	Kronecker delta.
Δt	Time step.
Δx	Grid spacing in x direction
Δy	Grid spacing in y direction.
Δz	Grid spacing in z direction.
η	Mapped coordinate in y direction.
η	Independent variable in solution for mean flow, section 2.2.1.
η_j	Grip points in mapped space, appendix A.
θ	Angle of an instability wave, $\tan\theta = \beta/\alpha_r$.
λ	Velocity ratio parameter $(U_1^* - U_2^*)/(U_1^* + U_2^*)$
Λ	Diagonal eigenvalue matrix, section 3.4.
μ	Viscosity.
μ_1	Viscosity of stream 1 (upper).
ξ	Alternate independent variable in solution for mean flow, section 2.2.1.
ρ	Density.
ρ_1	Density of stream 1 (upper).
ρ_2	Density of stream 2 (lower) or freestream density ratio.
τ_{ij}	Shear stress tensor.
ϕ	Relative phase of instability waves.
ϕ	A general variable, section 3.2.
ϕ_j	A general variable at grid point j, section 3.3.
χ	Independent variable in shooting method, defined by equation (2.42).
ω_z	Spanwise vorticity, defined in equation (2.55).
ω	Temporal eigenvalue from linear stability.
ω_i	Imaginary part of the temporal eigenvalue.
ω_r	Real part of the temporal eigenvalue.

ω_F	Frequency of the fundamental mode of instability.
ψ	Stream function, defined by equation (2.14).

Other Symbols

$()^*$	Dimensional quantity.
$\hat{()}$	Eigenfunction depending on y only.
$\widetilde{()}$	Fourier coefficient.
$()^T$	Transpose of a vector or matrix.
$()^{-1}$	Inverse of a matrix.
$\overline{()}$	Mean quantity.
$()'$	Disturbance quantity, except where explicitly labeled as a derivative.
$\|()\|$	Magnitude.

Note on non-dimensionalization

Non-dimensionalization has followed the practice of existing literature for linear stability and numerical simulation. The scheme for linear stability theory is defined in equation (2.5) and the scheme for the numerical simulations in equation (3.8). A slight difference between the two methods has resulted in the pressure being non-dimensionalized differently between Chapter 2, where the non-dimensional p is p^*/p_1^*, and the remaining chapters where p is $p^*/\rho_1^* U_1^{2*}$. Other variables such as T, ρ, u_i are unaffected.

CHAPTER 1

Introduction

1.1 Motivation

Free shear layers are of fundamental importance in the study of turbulence. They are found in many situations in nature (*e.g.* atmospheric flows, volcanic eruptions, stellar jets) and in industrial applications (*e.g.* gas turbine combustor, airfoil wake, rocket exhaust). Detailed understanding of the physics of free shear layers is essential for the development of new turbulence and mixing models. Improved models of mixing in free shear layers will lead to a better capability for the prediction of chemical reactions and control of pollutant emissions, for example from oil and gas burners in power generation plant.

Progress in space research is dependent on developing more efficient propulsion systems, and vehicles capable of carrying a higher payload into orbit. Future fully re-usable space vehicles have been proposed, which would be capable of taking off from conventional runways and attaining earth orbit. Such vehicles would use air breathing engines, and in the range of flight Mach numbers from 5 to 20 it appears (Swithenbank *et al.* [1989]) that the best efficiency is obtained in a supersonic combustion ram jet (scramjet). In such an engine the heat addition takes place at supersonic speeds and the air velocity throughout the engine is approximately equal to the flight velocity. The limiting process in these engines is the time taken to mix the fuel and oxidizer, which must occur within the combustion chamber for the heat release to be of value in generating thrust. Mixing occurs in supersonic free shear layers within the combustor. A general understanding of the physics of compressible mixing may suggest methods of reducing the mixing time and making scramjets more efficient.

The plane mixing layer is a simple prototype of a free shear layer, consisting of two streams of fluid with unequal velocities, and in the compressible case often unequal densities. The low speed version has been extensively studied in the laboratory, and compressible experiments are now being performed. The flow is amenable to solution by direct numerical simulation, and has been selected as the basic flow for this study.

1.2 Survey of Previous Work

Much previous research has been directed towards the incompressible mixing layer, but the effect of compressibility has received relatively little attention. For completeness, the literature for both high and low speed mixing layers is reviewed here.

1.2.1 Experiments

Early mixing layer research mapped out the time-averaged character of the flow (Liepmann and Laufer [1947]), and identified the strong dependence of the downstream development of the flow on upstream effects (Bradshaw [1966]). A major change in thinking about the mixing layer occurred when Brown and Roshko [1974] observed that large-scale nearly two-dimensional structures, which had previously been associated with a transition phenomena, persisted in the flow at high Reynolds numbers, when the mixing layer was statistically self-similar. The large scale structure has been found by many succeeding researchers, including Dimotakis and Brown [1976] at even higher Reynolds numbers. Oster and Wygnansky [1982] found that two-dimensional disturbances applied at the splitter plate were able to control the appearance of the large-scale structures downstream in the mixing layer. They identified regions where growth was enhanced or retarded by the effects of the forcing.

Three-dimensional structure was observed in the original work of Brown and Roshko [1974], showing up as streamwise streaks in the braid region between successive rollers. This secondary structure was investigated in detail by Bernal and Roshko [1986], who showed that it consisted of counter-rotating streamwise vortices in the braids, the ends of which became wrapped around the neighboring large rollers. The counter-rotating vortices move fluid between them up or down which shows up as a mushroom shaped structure in the scalar field, shown clearly in Bernal's pictures. The streamwise vortices were initially fixed in space, developing from small rig-dependent disturbances in the upstream flow field. Later in the mixing layer development they appear to move around in space, since long time-exposure pictures did not show their presence.

Identification of dominant structures in the incompressible mixing layer has led to the development of new models capable of predicting the behavior of the flow.

Dimotakis [1986] proposed a model for entrainment, based on the geometry of the primary two-dimensional motion, which successfully predicts the experimentally-observed phenomenon of asymmetric entrainment of fluid, with more fluid from the high-speed side than the low-speed side being entrained into the mixing layer. An important new model for mixing and chemical reactions has been developed by Broadwell and Breidenthal [1982], and for reactions with finite-rate chemistry by Broadwell and Mungal [1988]. The model uses observations from experiment to identify various fluid states in the mixing layer: (i) unmixed fluid, (ii) fluid in the structures, mixed at the entrainment ratio, and (iii) fluid in strained laminar diffusion layers between the two free streams (*e.g.* in the braid region). Mixing in each region has its own characteristic behavior as a function of Reynolds and Schmidt numbers. The Broadwell-Breidenthal-Mungal model correctly predicts many trends in experiments with chemical reactions (Mungal and Dimotakis [1984], Breidenthal [1981], Koochesfahani and Dimotakis [1986], Mungal and Frieler [1988]), and has been used to predict the effects of forcing on mixing (Sandham *et al.* [1988]).

The effect of compressibility on the plane mixing layer was first investigated in the 1960's, for the mixing layer between one high-speed stream, and another stream at rest. The data, compiled by Birch & Eggers [1973], showed a reduction in the growth rate of the mixing layer as the Mach number was increased. Brown & Roshko [1974] found that the density ratio alone could not account for the reduction in growth rate, implying that a true compressibility effect was being observed.

Renewed interest in compressible mixing in the 1980's led to experiments by Bogdanoff [1983], and by Papamoschou & Roshko [1986, 1988], in which high-speed mixing layers with various velocity and density ratios were investigated. Both sets of researchers proposed a parameter, called the convective Mach number by Papamoschou & Roshko, which seemed to collapse all the available growth rate data onto one curve, showing reduced growth rate as the convective Mach number was increased. The reasoning behind the convective Mach number concept can be found in Papamoschou and Roshko [1988]. It is based on the existance of organized large-scale structure in the compressible mixing layer. If one looks at the flow in a reference frame convecting with the large structures, then the Mach number of the free-streams is an intrinsic Mach number for the flow. Respectively for each stream, we have:

$$M_{c1} = \frac{U_1^* - U_c^*}{c_1^*} \qquad M_{c2} = \frac{U_c^* - U_2^*}{c_2^*} \tag{1.1}$$

where U_c^* is the convective velocity of the structures, U_1^* and U_2^* are the free-stream velocities, and c_1^* and c_2^* the sound speeds. The superscript * denotes a dimensional quantity. In the incompressible mixing layer in a reference frame moving at U_c^* there is a stable stagnation point in the braid region. If the existence of a similar point is assumed for the compressible layer, and that this point is reached by an isentropic process from the free-streams, then an expression for U_c^* can be derived (Papamoschou and Roshko [1988]). For gases with $\gamma_1 = \gamma_2$ it is found that $M_{c1} = M_{c2}$ and:

$$U_c^* = \frac{U_1^* c_2^* + U_2^* c_1^*}{c_1^* + c_2^*} \tag{1.2}$$

We can also eliminate U_c^* from equation (1.1), and define the Mach number M_c as:

$$M_c = \frac{U_1^* - U_2^*}{c_1^* + c_2^*} \tag{1.3}$$

More recently, Papamoschou [1989] has attempted to measure the convective velocities of the large scale structures directly from experimental Schlieren images. He finds disagreement between experiment and theory, and has proposed an alternative two-dimensional large-scale structure, in which shock waves are allowed on one side of the mixing layer, breaking the assumption of isentropic flow in the above derivation.

Recent experiments by Samimy *et al.* [1989] show a reduction in turbulence levels as Mach number is increased. Ongoing flow-visualization work at Stanford (Clemens *et al.* [1989]) shows little evidence for organized two-dimensional motion at a convective Mach number of 0.6.

1.2.2 Linear Stability Theory

Numerical solutions of the linearized equations first began to appear in the early 1960's. Applications to the incompressible mixing layer were presented by Michalke [1965a,b,c], and to the compressible mixing layer by Lessen *et al.* [1965,1966], and by Gropengiesser [1970]. Earlier analytical work had revealed the instability of a

velocity profile with an inflection point (Rayleigh [1880]) and the preference for amplification of two-dimensional waves in incompressible flows (Squire [1933]).

The valuable contributions of Gropengiesser [1970] were largely overlooked at the time. He found the second mode of instability, previously observed by Lessen *et al.* [1966], which keeps the mixing layer unstable in two dimensions at high Mach number. This instability was subsequently rediscovered by Blumen, Drazin *et al.* [1970, 1975, 1977]. Gropengiesser used spatial stability theory and used a solution of the compressible laminar boundary-layer equations as the base flow, instead of a simple hyperbolic tangent profile. He noted the high amplification rate of three-dimensional waves at high Mach number, as found for the compressible wall boundary-layer by Mack (see *e.g.* Mack [1984]).

When there are walls present in the flow, or in wakes with an embedded subsonic region relative to the free-stream, there can be additional modes of instability present. These 'acoustic' modes were found by Mack [1989] in wall boundary layers and in near wakes. Additional modes were found for the confined mixing layer by Greenough *et al.* [1989], referred to by them as 'wall modes', which may be the same kind of instability.

The important effects of the mean velocity profile were investigated by Monkewitz and Huerre [1982]. They found that only the amplification rate computed by spatial theory for the Blasius mixing layer velocity profile showed growth rate proportional to $\lambda = (U_1^* - U_2^*)/(U_1^* + U_2^*)$, as found in experiments. Morkovin [1988] makes the point that only the results from spatial stability analysis based on a mean profile satisfying the boundary-layer equations can be compared with experiments. Earlier attempts to transform results from the temporal theory gave poor agreement with the measurements.

Huerre and Monkewitz [1985] introduced the notion of convective and absolute instabilities for free shear layers, which affects the choice of temporal versus spatial theory. If the flow is convectively unstable the linear theory for spatially growing disturbances is applicable, whereas the temporal theory should be used for absolutely unstable flows. They found that the transition from absolute to convective instability for the mixing layer, unfortunately based on a hyperbolic tangent velocity profile, occurred at $\lambda = 1.315$, *i.e.* for flows with a significant backflow on one side.

Recent work by Ragab and Wu [1988] shows that, as with incompressible free shear layers, the compressible mixing layer has a basically inviscid, inflectional instability and the effect of viscosity is only to damp the disturbances. They also found that non-parallel effects are negligible in compressible mixing layers.

1.2.3 Secondary Stability Theory

Secondary stability theory was developed to allow a further step into transition, beyond the primary instability, to be studied. The theory assumes that the primary instability has developed, modifying the basic flow field. A new eigenvalue stability problem is set up, in which the base flow and eigenfunction are dependent upon both the streamwise and the normal location. This approach has proven very successful for wall boundary-layer and channel flows, predicting the appearance of both K (Klebanoff) and H (Herbert) type breakdown towards turbulence (Herbert [1983], Herbert and Bodonyi [1989]), which have been observed in experiment and in direct numerical simulation (Singer *et al.* [1987]).

The major work in this field for the mixing layer was performed by Pierrehumbert and Widnall [1982]. They assumed a base flow consisting of the hyperbolic tangent mixing layer mean flow, with superposed Stuart [1967] vortices, which are steady solutions to the incompressible Navier-Stokes equations. Two classes of instability modes were found: fundamental and subharmonic. The fundamental modes have the same wavelength in the streamwise direction as the vortex spacing, and the subharmonic modes have twice the wavelength. Two fundamental modes were found, corresponding to vortex core deformations – a core 'bulging' mode (spanwise symmetric), and a core 'translative' mode (spanwise antisymmetric). The translative mode was the more unstable, and the wavelength of the most (rapidly) amplified instability was roughly equal to the spanwise spacing of streamwise vortices found in the experiments of Bernal and Roshko [1986]. The most amplified subharmonic wave was the two-dimensional subharmonic, corresponding to the 2D pairing process most commonly observed in experiments. Pierrehumbert and Widnall did find another, three-dimensional, subharmonic mode. This produced a helical pairing, and may possibly have been observed in the flow visualizations of Chandrsuda *et al.* [1978].

The only work in secondary stability for the compressible mixing layer was carried out by Ragab and Wu [1989]. They used a base mixing layer profile, and

superimposed the neutral mode of the two-dimensional instability. They studied the subharmonic instability, and found that, above a convective Mach number of 0.4, the helical pairing mode was more amplified than the 2D pairing mode. This is a further indication that the dominant instability modes at high Mach number are three-dimensional modes.

1.2.4 Numerical Simulations

Techniques for time-accurate numerical simulation of free shear layers can be divided into three categories (i) vortex dynamics calculations, (ii) large-eddy simulations and (iii) direct numerical simulations. The first (*e.g.* Ashurst and Meiberg [1988]) assumes inviscid, incompressible flow. The Biot-Savart rule for vortex induction assumes an instantaneous transfer of information in the flowfield, which does not happen in compressible flow, where the speed of sound is finite. The method of large-eddy simulation (LES) requires a model for the smallest scales of turbulence. The method of direct numerical simulation (DNS) can produce spatially and temporally accurate solutions of the full Navier-Stokes equations with no modeling, when care is taken to choose the flow parameters (*e.g.* Reynolds number, Schmidt number) in order to fully resolve *all* the scales of motion. Usually the requirement for spatial resolution of a wide range of scales necessitates the use of spectral or very high order finite-difference numerical methods.

Two types of mixing layer problem can be tackled numerically. The spatially-developing mixing layer computations (figure 1.1) use the same reference frame as the experiments, with inflow at one end of the computational box and outflow at the other end. These inflow/outflow boundaries require special treatment – given the convective nature of the instability, the computed mixing layer will be dominated by the upstream forcing, as specified by the inflow boundary condition. The outflow boundary must allow all structures to smoothly leave the computational domain, without reflection of waves back into the simulation. The alternative computations are for the time-developing mixing layer (figure 1.2). Here the computational domain is fixed in a reference frame moving with the structures, and the flow then develops in time, rather than in space. Periodic boundary conditions are enforced in the streamwise direction and the flow develops from a specified initial condition. Time-developing simulations permit a more efficient use of computational resources,

and the periodic boundary conditions in the streamwise and spanwise direction are tailor-made for highly accurate Fourier methods.

The earliest mixing layer computations were performed with LES for the time-developing mixing layer (Mansour *et al.* [1978], Cain *et al.* [1981]). The first direct numerical simulations were presented by Riley and Metcalfe [1980] for a time-developing layer developing from random initial conditions, using methods developed by Orszag and Pao [1974]. Recent work (Metcalfe *et al.* [1987], Rogers and Moser [1989]) has shown that the experimentally observed phenomena of primary roll-up and secondary streamwise vortices leading to mushroom shaped structures in the braids can be fully realized in numerical simulations.

The spatially-developing mixing layer was simulated by Lowery and Reynolds [1986]. Lowery used inflow boundary conditions consisting of the mean flow, with eigenfunctions of the fundamental and two subharmonic frequencies (from linear stability analysis) superimposed. This resulted in the generation of a forced mixing layer and he was able to show that the asymmetry of entrainment, observed in experiments, could be captured in a spatially-developing computation. Lowery also performed three-dimensional computations in which streamwise vortices were present in the inflow field. These developed the characteristic mushroom structure in the braid region. Follow-up work by Sandham and Reynolds [1989], using Lowery's 2D code, showed that the large asymmetry of entrainment, observed in the initial development of the mixing layer (Koochesfahani and Dimotakis [1986]) could be traced to the effect of the wake of the splitter plate, upstream of the development of the mixing layer. It was also shown that a random-walk, applied to the phase of the forcing eigenfunctions, could be used at the inflow to simulate a more natural mixing layer, with linear growth rates and more nearly self-similar statistics.

The approach of Corcos *et al.* (Corcos and Sherman [1984], Corcos and Lin [1984] and Lin and Corcos [1984]), has been to directly simulate simple deterministic model flows of the mixing layer, and extract physical information from these. Part I of their study deals with the two-dimensional roll-up, Part II with the development of the secondary instability, and Part III with the effect of the staining field from the primary roll-up on the development of streamwise vorticity. They found that the plane strain field, produced in the braid region by the roll-up of the primary instability, acted to 'collapse' the streamwise vorticity associated with the secondary

instability of the flow, into circular streamwise vortices, which then generated the mushroom structures in the scalar field in the braid.

Direct numerical simulations of the compressible mixing layer have only recently appeared. Both the two-dimensional simulations in the current work, and those of Lele [1988, 1989] show the reduction in growth rate of the mixing layer as the convective Mach number is increased, and the appearance of weak embedded shock waves in the flow for convective Mach numbers above 0.7. Lele also shows that simulations started from low level random perturbations evolve first into the usual primary roll-up, with wavelength getting longer as the Mach number is increased, as predicted by the linear stability analysis. Other work is limited, but Soestrisno *et al.* [1988] presented two-dimensional simulations of the time-developing mixing layer, and Eberhardt *et al.* [1988] have presented simulations of the 'wall mode' of instability for the confined mixing layer. The simulations show that this mode tends to kink the mixing interface, but does not lead to a roll-up, and probably would not contribute to enhanced mixing at high Mach number.

1.3 Objectives and Overview

The objective of this work is to secure a fundamental understanding of the effect of compressibility on the development of the plane mixing layer. Several important questions emerge from the previous work in this area. (1) Why does the mixing layer grow more slowly at higher Mach numbers? (2) Is the convective Mach number a good parameter to describe the complete behavior of the flow? (3) What is the structure of the largest scales in the mixing layer at high Mach number, and what implications, if any, does this have for mixing at supersonic speeds?

The approach of this work is numerical. First, in Chapter 2, the linear stability problem is formulated and solved for a wide variety of mixing layers. Spatial stability analysis is used to compare with experiments and temporal stability to obtain eigenfunctions for use in the direct numerical simulations in later chapters. Interesting features emerge in their own right from the stability computations. First, it is shown that the amplification rate of the most unstable mode from the linear stability analysis can be used to correctly predict the growth rate of the developed

mixing layer. This suggests that linear processes may be very important, even in the developed mixing layer.

Secondly, it is found that three-dimensional waves are far more amplified at high Mach numbers than two-dimensional waves, implying that the developed structure at high Mach number is highly three-dimensional.

Results from linear theory are used to provide eigenfunctions for initial conditions for the numerical simulations. Linear theory is also used to indicate the key Mach numbers at which the instability characteristics of the flow change, where changes in physics may be observed, and to suggest Reynolds numbers to use in the simulations, low enough to resolve the flow, but high enough to capture the inviscid nature of the instabilities.

The numerical methods, used for the direct numerical simulations, are presented in Chapter 3. The three-dimensional code is spectral (Fourier) in the periodic directions, and high-order compact finite difference in the normal direction.

In Chapter 4 two-dimensional simulations are presented, which illustrate the reduction in growth rate as the Mach number is increased. Consideration of the compressible vorticity equation shows how dilatational and baroclinic effects can explain the stabilization of the two-dimensional instability, as compressibility becomes marked. At higher Mach numbers the two-dimensional simulations show the appearance of weak shock waves, embedded around the vortices.

The key three-dimensional effects are presented in Chapter 5. At low Mach number the modes found by Pierrehumbert and Widnall [1982] are simulated, by carefully choosing the phasing of a pair of oblique instability waves relative to the fundamental 2D wave. The effect of increasing Mach number on the structure of the mixing layer is investigated by running three simulations at Mach numbers where (i) the 2D mode is dominant, (ii) both 2D and 3D waves are approximately equally amplified, and (iii) high Mach number where the 3D waves are dominant. The latter two simulations identify new structures in the mixing layer, which are highly three-dimensional. A model structure for high Mach number flow ($M_c > 1$) is developed, based on the non-linear development of two equal and opposite oblique waves.

The main contributions of this work are:

- mixing layer growth rate can be predicted by linear stability analysis. The mixing layer growth rate is found to be directly proportional to the linear amplification rate of the most amplified spatial instability wave, using a solution to the boundary-layer equations for the base velocity and temperature profiles.
- the most amplified instability wave becomes an oblique wave above a convective Mach number of 0.6. At higher Mach numbers the most amplified wave becomes more oblique, and the relation $M_c \cos\theta = 0.6$ was found to predict the orientation of the most amplified waves at high convective Mach numbers.
- the non-linear growth rate of the two-dimensional instability wave, which dominates the incompressible mixing layer, is reduced as Mach number is increased.
- if the flow is forced to be two-dimensional then shock waves develop for convective Mach numbers above 0.7.
- three-dimensional instability waves at high Mach number grow strongly in the non-linear region of roll-up, as well as in the linear regime. The developed structure is found to change as Mach number is increased, with less spanwise coherence and strong streamwise vorticity at higher convective Mach numbers.
- the structure that develops at high Mach number from a pair of equal and opposite oblique instability waves consists of a pair of hairpin-like vortical structures which are split in a peak-valley manner in the streamwise direction.

CHAPTER 2

Linear Stability Theory

In this chapter the linearized theory describing the growth of small disturbances in the compressible mixing layer is considered. The linearized equations are solved to find the most amplified wave for given profiles of velocity and density. It will be shown how linear stability theory can be used to predict the growth rates of mixing layers, giving good agreement with experiments for the effects of velocity ratio, density ratio and Mach number. Three-dimensional waves are found to be important in the compressible mixing layer at high Mach number. The structure of the eigensolutions gives important information about the structure and growth of the vortices which develop out of the linear instability.

In the following sections the inviscid equations are used and parallel flow is assumed. Spatial theory is used when comparisons with experiments are desired. Temporal theory is used when eigenfunctions are desired as inputs to direct numerical simulations of the time-developing mixing layer.

2.1 Numerical Solution Schemes

The compressible boundary-layer equations are solved using a shooting technique to obtain the mean flow. The linear disturbance equations are then solved using a shooting procedure. The methods are basically from Gropengiesser [1970], but have been extended to allow computation of both temporal and spatial instability characteristics of a variety of planar free shear layers.

2.1.1 Solution for the Mean Flow

The boundary-layer equations for steady two-dimensional flow of a compressible perfect gas with zero streamwise pressure gradient are (White [1974]):

$$\frac{\partial(\rho^* u^*)}{\partial x^*} + \frac{\partial(\rho^* v^*)}{\partial y^*} = 0 \tag{2.1}$$

$$\rho^* u^* \frac{\partial u^*}{\partial x^*} + \rho^* v^* \frac{\partial u^*}{\partial y^*} = \frac{\partial}{\partial y^*}\left(\mu^* \frac{\partial u^*}{\partial y^*}\right) \tag{2.2}$$

$$\rho^* u^* \frac{\partial h^*}{\partial x^*} + \rho^* v^* \frac{\partial h^*}{\partial y^*} = \frac{\partial}{\partial y^*}\left(\frac{\mu^*}{Pr}\frac{\partial h^*}{\partial y^*}\right) + \mu^*\left(\frac{\partial u^*}{\partial y^*}\right)^2 \tag{2.3}$$

The streamwise direction is x^* and the normal direction y^*. Velocity components in these directions are u^* and v^* respectively. The density is denoted by ρ^*, the viscosity by μ^* and the enthalpy per unit mass by h^*. The superscript * represents a dimensional quantity and the Prandtl number is defined by $Pr = c_p^* \mu^* / k^*$, where k^* is the conductivity.

The perfect gas law is

$$p^* = \rho^* R^* T^* \tag{2.4}$$

where R^* is the gas constant and p^* is the pressure. Constant specific heats are assumed, and we write $dh^* = c_p^* dT^*$, where c_p^* is the specific heat at constant pressure.

Non-dimensionalization of the above equations is obtained by dividing the dimensional quantity by the corresponding dimensional quantity on the high-speed ($y > 0$) side of the mixing layer (subscript 1). The new dimensionless variable has no superscript. For example:

$$u = \frac{u^*}{U_1^*} \qquad \rho = \frac{\rho^*}{\rho_1^*} \qquad T = \frac{T^*}{T_1^*} \qquad p = \frac{p^*}{p_1^*} \qquad \mu = \frac{\mu^*}{\mu_1^*} \tag{2.5}$$

The reference length-scale is for the time being an arbitrary constant l^*, and the reference time-scale is l^*/U_1^*. Non-dimensional parameters are the Reynolds number $Re_l = \rho_1^* U_1^* l^* / \mu_1^*$, the Mach number of the high-speed side of the mixing layer $M_1 = U_1^*/c_1^*$, where the sound speed is denoted by c^*, and the ratio of specific heats $\gamma = c_p^*/c_v^*$.

The boundary-layer equations in dimensionless form become:

$$\frac{\partial(\rho u)}{\partial x} + \frac{\partial(\rho v)}{\partial y} = 0 \tag{2.6}$$

$$\rho u \frac{\partial u}{\partial x} + \rho v \frac{\partial u}{\partial y} = \frac{1}{Re_l}\frac{\partial}{\partial y}\left(\mu \frac{\partial u}{\partial y}\right) \tag{2.7}$$

$$\rho u\frac{\partial T}{\partial x}+\rho v\frac{\partial T}{\partial y}=\frac{1}{Re_l Pr}\frac{\partial}{\partial y}\mu\frac{\partial T}{\partial y}+\frac{M_1^2(\gamma-1)}{Re_l}\mu\Big(\frac{\partial u}{\partial y}\Big)^2 \tag{2.8}$$

and

$$\rho T=1 \tag{2.9}$$

since pressure has been assumed uniform.

The first step is to derive a relation between temperature and velocity. The procedure, described in White [1974], is to search for a solution $T=T(u)$. Substituting into the energy equation (2.8), and using for example

$$\frac{\partial T}{\partial y}=\frac{dT}{du}\frac{\partial u}{\partial y} \tag{2.10}$$

we have

$$\frac{dT}{du}\Big(\rho u\frac{\partial u}{\partial x}+\rho v\frac{\partial u}{\partial y}-\frac{1}{Re_l Pr}\frac{\partial}{\partial y}\mu\frac{\partial u}{\partial y}\Big)=\Big(M_1^2(\gamma-1)+\frac{d^2T}{du^2}\Big)\mu\Big(\frac{\partial u}{\partial y}\Big)^2 \tag{2.11}$$

If the Prandtl number is assumed unity then the left hand side must be zero by the momentum equation (2.7), and we have the equation

$$\frac{d^2T}{du^2}=-M_1^2(\gamma-1) \tag{2.12}$$

This can be integrated twice, subject to the boundary conditions that $T=1$ when $u=1$ and $T=T_2$ when $u=U_2$, giving:

$$T=M_1^2\frac{(\gamma-1)}{2}\Big(u(1+U_2)-u^2-U_2\Big)+\frac{T_2(1-u)}{(1-U_2)}+\frac{(u-U_2)}{(1-U_2)} \tag{2.13}$$

This is the general $T-u$ relation, referred to as a Crocco-Busemann relation after the original developers.

The next step is to find a solution to the continuity and momentum equations. A stream function ψ, which automatically satisfies continuity, is defined by:

$$\rho u=\frac{\partial \psi}{\partial y}\qquad \rho v=-\frac{\partial \psi}{\partial x} \tag{2.14}$$

The momentum equation now becomes:

$$\frac{\partial\psi}{\partial y}\frac{\partial u}{\partial x} - \frac{\partial\psi}{\partial x}\frac{\partial u}{\partial y} = \frac{1}{Re_l}\frac{\partial}{\partial y}\mu\frac{\partial u}{\partial y} \tag{2.15}$$

We now introduce Howarth's transform (also known as the Illingworth-Stewartson transform, see Schlichting [1979]):

$$Y_H = \int_0^y \frac{dy}{T} \qquad \frac{dy}{dY_H} = T \tag{2.16}$$

Using this, together with equation (2.9), we can rewrite (2.15) as:

$$\frac{\partial\psi}{\partial Y_H}\frac{\partial^2\psi}{\partial x \partial Y_H} - \frac{\partial\psi}{\partial x}\frac{\partial^2\psi}{\partial Y_H^2} = \frac{1}{Re_l}\frac{\partial}{\partial Y_H}\frac{\mu}{T}\frac{\partial^2\psi}{\partial Y_H^2} \tag{2.17}$$

This can be reduced to an ordinary differential equation by making the transformation:

$$\psi = F(\eta)\sqrt{\frac{x}{Re_l}} \qquad \eta = Y_H\sqrt{\frac{Re_l}{x}} \tag{2.18}$$

If we also assume that viscosity varies linearly with temperature we obtain

$$2F''' + FF'' = 0 \tag{2.19}$$

where the prime here denotes differentiation with respect to η. Boundary conditions are that $F(0) = 0$, the dividing streamline, and the free stream velocities $F'(\infty) = 1$ and $F'(-\infty) = U_2$. Equation (2.19) can then be solved by shooting.

The shooting procedure is simplified by using the invariance of the equation to the transform $G(\xi = a\eta) = F(\eta)/a$, reducing the shooting parameters from 2 to 1. The method is as follows.

(a) Guess $F'(0)$ and $F''(0)$ and shoot to $+\infty$.

(b) Evaluate the constant a and transform the equation so that G satisfies the upper boundary condition exactly.

(c) Shoot to $-\infty$ and compare $G'(-\infty)$ with U_2.

(d) Choose new $F''(0)$ and iterate.

A fourth order Runge-Kutta scheme was used for the integrations and secant iteration was used to vary $F''(0)$ until $G'(-\infty)$ converged to U_2. Once the mean velocity profile $G'(Y_H)$ is known the temperature can be found using (2.13). The shooting cannot proceed to infinity, so a cutoff at $Y_H = 20$ was used, after checking that this had negligible effect on the results. The last step in the procedure is to reverse Howarth's transform and convert back to the physical y coordinate by integrating:

$$\frac{dy}{dY_H} = T \qquad y(0) = 0 \tag{2.20}$$

and normalizing the y coordinate by the vorticity thickness, defined by

$$\delta_\omega = \frac{1 - U_2}{|du/dy|_{\max}} \tag{2.21}$$

Papamoschou [1986] noted that the results presented by Gropengiesser [1970] showed a larger than expected sensitivity to density ratio. Both the current calculations, and those of Ragab & Wu [1988] show that the work of Gropengiesser was not in error. The reason for the discrepancy lies in the normalization of the mean profiles. Gropengiesser normalized the thickness by the momentum thickness in the Y_H domain. Thus his plots for different density ratios are normalized differently, according to the effect of density on the transform $Y_H \rightarrow y$. To properly assess the effect of density ratio on amplification rate one has to normalize by a consistent thickness parameter. The vorticity thickness was chosen since Monkewitz and Huerre [1982] found that vorticity thickness rather that momentum thickness gave direct proportionality between spatial amplification rate and mixing layer growth rate.

Rather than fit the profiles to a generalized hyperbolic tangent, as done by Gropengiesser [1970], it was decided to use the computed profiles directly. A cubic spline was fitted through the integration points and this was used as the base profile for stability calculations.

2.1.2 Linearized Disturbance Equations and Shooting Method

The inflectional instability of the mixing layer provides an inviscid instability mechanism, and the only effect of viscosity is to damp the growing disturbances (Betchov and Szewczyk [1963]). It was therefore decided to solve the simpler inviscid stability problem. The starting equations are the Euler equations, obtained by dropping the viscous and heat conduction terms from the Navier-Stokes equations. In dimensional form these equations for continuity, momentum and energy are as follows (White [1974]):

$$\frac{\partial \rho^*}{\partial t^*} + u_i^* \frac{\partial \rho^*}{\partial x_i^*} + \rho^* \frac{\partial u_i^*}{\partial x_i^*} = 0 \tag{2.22}$$

$$\rho^* \Big(\frac{\partial u_i^*}{\partial t^*} + u_j^* \frac{\partial u_i^*}{\partial x_j^*} \Big) = - \frac{\partial p^*}{\partial x_i^*} \tag{2.23}$$

$$\rho^* \Big(\frac{\partial h^*}{\partial t^*} + u_i^* \frac{\partial h^*}{\partial x_i^*} \Big) = \frac{\partial p^*}{\partial t^*} + u_i^* \frac{\partial p^*}{\partial x_i^*} \tag{2.24}$$

Using the continuity equation, the perfect gas equation (2.4), and the definitions of h^* and γ from the previous subsection, the energy equation can be rewritten as:

$$\rho^* \Big(\frac{\partial T^*}{\partial t^*} + u_i^* \frac{\partial T^*}{\partial x_i^*} \Big) = - p^* (\gamma - 1) \frac{\partial u_i^*}{\partial x_i^*} \tag{2.25}$$

Non-dimensionalization is obtained by the same method as in the previous section, equation (2.5). The non-dimensional equations for continuity, momentum and energy are:

$$\frac{\partial \rho}{\partial t} + u_i \frac{\partial \rho}{\partial x_i} + \rho \frac{\partial u_i}{\partial x_i} = 0 \tag{2.26}$$

$$\rho \Big(\frac{\partial u_i}{\partial t} + u_j \frac{\partial u_i}{\partial x_j} \Big) = - \frac{1}{\gamma M_1^2} \frac{\partial p}{\partial x_i} \tag{2.27}$$

$$\rho \Big(\frac{\partial T}{\partial t} + u_i \frac{\partial T}{\partial x_i} \Big) = - p (\gamma - 1) \frac{\partial u_i}{\partial x_i} \tag{2.28}$$

and the non-dimensional perfect gas equation is

$$p = \rho T \tag{2.29}$$

We introduce the following decomposition:

$$u = \overline{u} + u', v = v', w = w', T = \overline{T} + T', \rho = \overline{\rho} + \rho', p = 1 + p' \tag{2.30}$$

where an overbar denotes a mean quantity and a prime a small disturbance. It is assumed that the stability analysis may be conducted neglecting the slow streamwise variation of the mean flow, *i.e.* $\overline{u} = \overline{u}(y)$, $\overline{T} = \overline{T}(y)$ etc. The mean velocity, density and temperature profiles need to be specified. The mean pressure is constant and non-dimensionally unity.

Under the parallel-mean-flow assumption, the linearized disturbance equations have coefficients which are independent of x, z and t. Hence the solutions are exponentials in these independent variables and disturbances have the form of travelling waves

$$(u', v', w', T', \rho', p') = (\hat{u}, \hat{v}, \hat{w}, \hat{T}, \hat{\rho}, \hat{p}) e^{i(\alpha x + \beta z - \omega t)} \tag{2.31}$$

where $\hat{u}, \hat{v}, \hat{w}, \hat{T}, \hat{\rho}, \hat{p}$ are complex eigenfunctions depending only on the y coordinate. In equation (2.31) ω is the frequency and α and β are wavenumbers in the streamwise (x) and spanwise (z) directions respectively. The angle θ of a disturbance is given by

$$\tan\theta = \beta/\alpha_r \tag{2.32}$$

where α_r is the real part of α. The wavenumber β has to be real, since we require disturbances not to amplify for $z \to \pm\infty$. The form of α and ω depends on the particular problem. For the temporal stability problem disturbances grow in time and not in space, so α has to be real and ω complex. In the spatial problem ω is real and α complex so that disturbances grow in space, but not in time. The amplification rate of a disturbance is given by ω_i in the temporal case and $-\alpha_i$ in the spatial case.

The pressure perturbation can be easily found from the density and temperature using the linearized form of the perfect gas law (2.29):

$$p' = \overline{\rho} T' + \rho' \overline{T} \tag{2.33}$$

After substituting equations (2.30) and (2.31) into the governing equations (2.26)-(2.29) and linearizing, we obtain the following linearized equations for continuity, three components of momentum, energy and the perfect gas law:

$$\hat{\rho}i(\alpha\overline{u}-\omega)+\hat{v}D\overline{\rho}+\overline{\rho}[i(\alpha\hat{u}+\beta\hat{w})+D\hat{v}]=0 \tag{2.34}$$

$$\overline{\rho}[i(\alpha\overline{u}-\omega)\hat{u}+\hat{v}D\overline{u}]=\frac{-i\alpha\hat{p}}{\gamma M_1^2} \tag{2.35}$$

$$\overline{\rho}i(\alpha\overline{u}-\omega)\hat{v}=\frac{-D\hat{p}}{\gamma M_1^2} \tag{2.36}$$

$$\overline{\rho}i(\alpha\overline{u}-\omega)\hat{w}=\frac{-i\beta\hat{p}}{\gamma M_1^2} \tag{2.37}$$

$$\overline{\rho}[i(\alpha\overline{u}-\omega)\hat{T}+\hat{v}D\overline{T}]=-(\gamma-1)[i(\alpha\hat{u}+\beta\hat{w})+D\hat{v}] \tag{2.38}$$

and

$$\hat{p}=\overline{\rho}\hat{T}+\hat{\rho}\overline{T} \tag{2.39}$$

where D represents the operator d/dy.

These equations can be reduced to a set of two equations as follows. First we multiply equation (2.34) by $\overline{T}$ and then add it to (2.38), using the fact that differentiating (2.29) with respect to y gives $\overline{T}D\overline{\rho}+\overline{\rho}D\overline{T}=0$. This gives

$$i(\alpha\overline{u}-\omega)\hat{p}=-\gamma[i(\alpha\hat{u}+\beta\hat{w})+D\hat{v}] \tag{2.40}$$

Now $\hat{u}$ and $\hat{w}$ can be eliminated using equations (2.35) and (2.37), giving

$$(\alpha\overline{u}-\omega)D\hat{v}-\alpha\hat{v}D\overline{u}=\frac{i\hat{p}\alpha^2 g}{\gamma M_1^2} \tag{2.41a}$$

where

$$g=\frac{\alpha^2+\beta^2}{\overline{\rho}\alpha^2}-\frac{M_1^2(\alpha\overline{u}-\omega)^2}{\alpha^2} \tag{2.41b}$$

Equations (2.36) and (2.41) form a set of two equations for $\hat{v}$ and $\hat{p}$. These can be further reduced by following the method of Gropengiesser [1970], who defined a new variable χ:

$$\chi = \frac{i\alpha\hat{p}}{\gamma M_1^2 \hat{v}} \tag{2.42}$$

The equation to be integrated for χ then becomes:

$$\frac{d\chi}{dy} = \frac{\alpha^2(\overline{u} - \omega/\alpha)}{\overline{T}} - \frac{\chi(\chi g + D\overline{u})}{(\overline{u} - \omega/\alpha)} \tag{2.43}$$

The boundary conditions are obtained by considering the asymptotic behavior of disturbances in the freestreams. In the freestream $D\overline{u}$ is zero and equations (2.36) and (2.41) can be written as

$$D^2\hat{p} = \overline{\rho}\alpha^2 g\hat{p} \tag{2.44a}$$

$$D^2\hat{v} = \overline{\rho}\alpha^2 g\hat{v} \tag{2.44b}$$

The general solutions to these equations, vanishing for $y \to \pm\infty$ are

$$\hat{p} = a_1 e^{\mp qy} \tag{2.45a}$$

$$\hat{v} = a_2 e^{\mp qy} \tag{2.45b}$$

where a_1 and a_2 are constants and q is $\overline{\rho}\alpha^2 g$. Note that $\hat{p}$ and $\hat{v}$ decay with the same complex exponential in the freestream. Therefore, the new variable χ, formed as a ratio of these solutions, must go to a constant as $y \to \pm\infty$. Setting $d\chi/dy = 0$ and $D\overline{u} = 0$ in equation (2.43) leaves

$$\chi(y = \pm\infty) = \frac{\alpha(\overline{u} - \omega/\alpha)}{\sqrt{g\overline{T}}} \tag{2.46}$$

The numerical solution procedure is iterative. First, a guess is made of the eigenvalue. For spatial analysis ω is specified and α guessed, whereas for temporal analysis α is specified and ω guessed. Knowing the eigenvalue, we can evaluate χ in the freestreams using equation (2.46). Then we integrate equation (2.43) from each

of the freestreams to the centerline of the mixing layer at $y = 0$. At the centerline the value of χ computed by integrating from the upper freestream, $\chi^+(0)$, is compared with the value computed by integrating from the lower freestream, $\chi^-(0)$. Then a new eigenvalue is chosen, and iterated upon until the eigenvalue has converged to a specified tolerance. The shooting method was implemented using subroutines from Press *et al.* [1986]. The integrations were carried out using a variable step fifth order Runge-Kutta scheme, and the iteration was achieved by a Newton-Raphson method. An error control of 10^{-6} was used for the integrations, and the iteration continued until the eigenvalue converged to 10^{-7}. Single precision arithmetic was sufficient for most computations. However, double precision was required for some of the weakly amplified supersonic modes of instability (section 2.2.4).

Generally the integrations were performed with y as the independent variable, starting the integrations 10 vorticity thicknesses away from the centerline. Instead of solving the problem on the domain $[-\infty, \infty]$ it is possible (Gropengiesser [1970]) to reduce the domain of integration to $[U_2, 1]$ by transforming the independent variable in equation (2.43) from y to u. This method was also implemented and was found to be slightly quicker than the method integrating in y, and gave exactly the same results. However, there were problems with this method for wake flows and for mixing layer profiles where the base flow was not an analytic function. Results from compressible wake calculations using the above methods can be found in Chen *et al.* [1989]. The procedure for the wake calculations was similar. However, for the symmetric wake mode $\hat{v}$ at the centerline is zero, so χ defined by equation (2.42) goes to infinity. This was remedied by working with a new variable $1/\chi$.

Once the eigenvalues have been found the eigenfunctions are calculated by integrating equations (2.36) and (2.41) out from the centerline into the freestream. Initial conditions are calculated from the solution for $\chi(0)$, choosing the phase of the eigenfunctions so that $\hat{v}(0) = 1 + i0$. From (2.42) this means that $\hat{p}(0)$ is given by:

$$\hat{p}_r(0) = \gamma M_1^2 \chi_i(0) \tag{2.47a}$$

$$\hat{p}_i(0) = -\gamma M_1^2 \chi_r(0) \tag{2.47b}$$

After computation the eigenfunctions are renormalized without phase change so that the magnitude of $\hat{u}$ is 1. In all cases this renders the other components of the eigenfunction less than 1.

2.1.3 Validation

The first method of validation was to compare results obtained with the shooting method described in the previous section with results from a code for direct solution of the linearized equations, developed in collaboration with J. H. Chen and described in Appendix A. This is an ideal situation for checking numerical methods. When two completely different methods give the same results one is confident that the solution is correct. The superior performance of the shooting method for weakly amplified disturbances led to its being used for all the stability calculations presented here.

In addition, results were checked against published data including the graphs of Gropengiesser [1970], and at low Mach number against results for incompressible flow by Michalke [1965a,b], Monkewitz and Huerre [1982] and Lowery and Reynolds [1986]. Comparisons are presented below in tables 2.1 and 2.2.

Table 2.1 Comparison of temporal results at $M_1 = 0.01$ with Michalke [1965]

α_r	ω_i Michalke	ω_i current
0.2	0.06975	0.06974
0.4	0.09410	0.09409
0.6	0.08650	0.08649
0.8	0.05388	0.05386

Table 2.2 Comparison of spatial results at $M_1 = 0.02$ with Lowery and Reynolds [1986]

ω_r	α Lowery	α current
2/3	$0.88869, -0.12850i$	$0.88891, -0.12850i$
1/3	$0.43110, -0.09913i$	$0.43110, -0.09913i$
1/6	$0.20908, -0.05860i$	$0.20908, -0.05860i$

2.2 Results

Results are presented for a variety of mixing layers. In non-dimensional terms (equation (2.5)) these flows are characterized by U_2, the velocity ratio and ρ_2, the density ratio. Since pressure is assumed uniform we can also write $\rho_2 = 1/T_2$.

2.2.1 Low Mach Number Results

It was shown by Monkewitz and Huerre [1982] that, when spatial theory and the Blasius mixing layer profile are used, the maximum amplification rate $|\alpha_i|_{\max}$ is proportional to $\lambda = (U_1^* - U_2^*)/(U_1^* + U_2^*)$. Also, the best fit through the experimental data for the incompressible mixing layer with uniform density, compiled by Brown and Roshko [1974], is a straight line $d\delta/dx$ proportional to λ. Thus, for the incompressible mixing layer with constant density it appears that $|\alpha_i|_{\max}$ from the linear theory is proportional to $d\delta/dx$ from experiments (Morkovin [1988]).

In this section we test the postulate that the relation $|\alpha_i|_{\max} \sim d\delta/dx$ applies to all mixing layers, with any velocity ratio, density ratio and Mach number, with the following provisos:

(a) use spatial stability theory since this is a convectively unstable flow (Huerre and Monkewitz [1985])

(b) use a solution of the laminar boundary-layer equations as the base flow

(c) normalize the profiles by the vorticity thickness.

The effect of the mean velocity profile can be important. A comparison between hyperbolic tangent velocity profiles and the boundary-layer solution is shown for two different velocity ratios in figure 2.1. In each case the densities of the free-streams are equal ($\rho_2 = 1$). The profiles are all normalized with their vorticity thickness and shifted so that $u = (1 + U_2)/2$ at $y = 0$. The most amplified spatial instability wave was computed from these profiles. The percentage difference in amplification rate of the case with a hyperbolic tangent profile relative to the case with a boundary-layer profile is shown on table 2.3.

Table 2.3 Percentage difference in $|\alpha_i|_{\max}$ between tanh and laminar velocity profiles at $M_1 = 0.1$ and $\rho_2 = 1$

U_2	% difference
0.00	+16.0
0.25	+4.0
0.50	+0.5

The largest effect was at $U_2 = 0$ where the wave with the highest amplification rate was 16% more rapidly amplified on the hyperbolic tangent mean flow than on the boundary-layer mean flow. At higher values of U_2 the effect was much smaller.

To investigate the effect of profile shape some calculations were made with a profile constructed from a hyperbolic tangent on the low speed side and the boundary-layer solution on the high speed side. Such profiles are smooth to the eye but derivatives are discontinuous at the centerline. No numerical problems were encountrered but results have to be treated with caution. It was found that a 'fuller' velocity profile on the high speed side was stabilizing, and from the reverse calculation that a longer tail on the low speed side was also stabilizing. The latter effect was larger by a factor of about 3. This kind of argument may explain why tripping the high speed boundary-layer, making it turbulent and hence having a much 'fuller' mean velocity profile reduces the growth rate of the developed mixing layer by approximately 30% (Browand and Latigo [1979], Mungal *et al.* [1985]).

The differences in the velocity profile are generally small when the two free-streams have equal densities, but can become very large when there is a large density ratio. The effect of density ratio on the mean velocity and density profiles at $U_2 = 0.5$ and $\rho_2 = 1/7, 1, 7$ is shown in figure 2.2. The profiles for $\rho_2 = 1/7$ and $\rho_2 = 7$ are very different from a hyperbolic tangent. Clearly in this situation a hyperbolic tangent would be a poor choice for the mean velocity profile. The most unstable case corresponds to $\rho_2 = 7$, which is the least 'full' profile on the high speed side and the shortest tail on the low speed side, in agreement with the above arguments.

The effect of density and velocity ratios on the amplification rate of the most amplified spatial instability wave ($|\alpha_i|_{\max}$) is shown in figure 2.3*a* for the boundary-layer mean velocity profile and on figure 2.3*b* for the hyperbolic tangent mean velocity profile The growth rate is plotted against λ for three different density ratios, as done by Bogdanoff [1984] and Dimotakis [1986]. Experimental points from Brown and Roshko [1974] are also plotted, both the original vorticity thicknesses as well as density thicknesses. The density thicknesses were evaluated by Bogdanoff [1984] by joining the 20% and 80% points on the density profile and measuring the distance between the points where this line intercepts the free-stream density. The agreement between the linear amplification rate and the experimental growth rate is remarkable, especially when mixing layer thicknesses based on the experimental

mean density profile are used. For these and other experiments the ratio $\delta'/|\alpha_i|_{\max}$, where $\delta' = d\delta/dx$, is shown on table 2.4 below.

Table 2.4 Relationship between δ' from experiments and $|\alpha_i|_{\max}$ from linear theory

Experiment	U_2	ρ_2	$\delta'_\rho/\|\alpha_i\|_{\max}$	$\delta'_\omega/\|\alpha_i\|_{\max}$
Brown & Roshko [1974]	$1/\sqrt{7}$	7	0.591	0.491
Brown & Roshko [1974]	$1/\sqrt{7}$	1/7	0.623	0.537
Brown & Roshko [1974]	1/7	7	0.604	0.344
Fiedler [1974]	0.0	1.09	0.594	—
Bogdanoff [1984]	0.0	0.2	0.557	—
Dimotakis & Brown [1976]	0.19	1.0	—	0.432

From these results, we conclude the following relations between linear amplification and experimental growth rate ($\pm 20\%$):

$$\frac{d\delta_\rho}{dx} = 0.6|\alpha_i|_{\max} \tag{2.48a}$$

$$\frac{d\delta_\omega}{dx} = 0.45|\alpha_i|_{\max} \tag{2.48b}$$

Comparison between figures 2.3*a* and 2.3*b* shows that the linear results based on a hyperbolic tangent mean velocity profile do not show the correct trends. At $\lambda = 0.3$, for example, the effect of increasing density ratio with the hyperbolic tangent mean velocity profile is that first the amplification rate rises and then it falls. This can be compared with the results for the boundary-layer mean flow, which show a continuous rise in amplification rate with increasing density ratio.

The variation in $|\alpha_i|_{\max}$ over two orders of magnitude change in temperature ratio T_2 (recall $T_2 = 1/\rho_2$) is shown in figure 2.4 for velocity ratios $U_2 = 0$ and 0.5. The case $U_2 = 0$ was computed by Maslowe and Kelly [1971] for a hyperbolic tangent mean velocity and a specified, non Crocco-Busemann, mean temperature profile. They found a peak amplification rate, at a density ratio of $\rho_2 = 33$, that was 64% higher than the amplification rate for equal densities. The current results for that velocity ratio show a much stronger effect of density ratio on amplification rate, in better agreement with the experiments of Davey and Roshko [1972]. At a

density ratio $\rho_2 = 5$, the amplification rate is three times that of the equal-density case. When $U_2 = 0$ the amplification rate appears to become very large when the low speed stream has a large density compared to the high speed stream. However, it should be noted that for the case $U_2 = 0$ the v component of velocity on the low speed side of the layer will be large relative to the u component and the boundary-layer assumption is no longer strictly valid.

We have seen that there is a good agreement between the linear theory and the existing experimental data for the effect of density and velocity ratio on the mixing layer growth rate at low Mach numbers. It therefore appears reasonable to use the linear theory over the full range of possible conditions (not just at experimental points) to compare with some of the models that have been proposed for the growth rate of the mixing layer as a function of density and velocity ratios. In particular, two models are compared. The first is a form originally proposed by Brown [1974], and used by Papamoschou [1986] to compute the growth rates of incompressible mixing layers with the same velocity and density ratio as his compressible mixing layer experiments:

$$\frac{d\delta}{dx} \sim \frac{(1-U_2)(1+\sqrt{\rho_2})}{(1+U_2\sqrt{\rho_2})} \tag{2.49}$$

The second model is a modified form of the above, and was proposed from geometrical arguments by Dimotakis [1986]

$$\frac{d\delta}{dx} \sim \frac{(1-U_2)}{(1+U_2\sqrt{\rho_2})}\left\{1+\sqrt{\rho_2}-\frac{1-\sqrt{\rho_2}}{1+2.9/\lambda}\right\} \tag{2.50}$$

These models will be referred to as model 1 and model 2. For comparison purposes the constant of proportionality is set so that both models coincide with the linear growth rate prediction (equation (2.48)) for the equal-density case. The comparison between the models and the linear theory is shown in figure 2.4 for velocity ratios 0 and 0.5. Agreement is generally not good. We can also check the models by comparing the growth rate plotted against the right hand sides of equations (2.49) and (2.50) above. A straight line would indicate agreement between the model for growth rate and the linear theory prediction. Figures 2.5*a* and 2.5*b* show this plot for each model. Model 2 is closer to a straight line.

Both model 1 and model 2, and the linear theory prediction of equation (2.48) agree well with the available, but limited, experimental data. However the different predictions of these three models for other velocity and density ratios suggests that this is not a cut-and-dried issue. In particular, the method of normalization used by Papamoschou and Roshko [1988] (dividing the compressible mixing layer growth by the (model 1) prediction of growth rate of an incompressible mixing layer with the same velocity and density ratio) has the built-in assumption that model 1 is correct.

2.2.2 Oblique Waves at High Mach Number

The basic effect of compressibility is first considered for the temporal stability of the time-developing mixing layer with equal free-stream densities and temperatures, and with a simple velocity profile:

$$\overline{u} = \tanh(2y) \tag{2.51}$$

Equation (1.3) for the convective Mach number can be non-dimensionalized as follows:

$$M_c = \frac{1 - U_2}{c_1 + c_2} = \frac{M_1\sqrt{\rho_2}(1 - U_2)}{1 + \sqrt{\rho_2}} \tag{2.52}$$

In the time-developing reference frame $U_2 = -1$ and for $\rho_2 = 1$ we have $M_1 = M_c$, so the convective Mach number is the same as the Mach number of each of the free-streams.

Figure 2.6*a* shows the effect of increasing Mach number on the amplification rate of two-dimensional waves. The observed trend is the same as found by Gropengiesser [1970] for the spatial theory, including the appearance of a second (supersonic) mode of instability. This mode is characterized by a different phase speed $c_r = \omega_r/\alpha_r$, as evident from the plot of ω_r shown in figure 2.6*b*. The effect of increasing Mach number is to reduce the amplification rate and ultimately stabilize the subsonic two-dimensional mode. Only the emergence of the second mode keeps the mixing layer unstable to two-dimensional disturbances at high Mach numbers. The subsonic (first) mode is stationary in the time-developing mixing layer reference frame, while the second mode travels to the left or right (see section 2.2.4).

The amplification rates of oblique waves at angles of 0°, 30°, and 60° are shown in figures 2.7 through 2.9 for Mach numbers 0.01, 0.8, and 1.2 respectively. At $M_1 = 0.01$ the most amplified wave is the two-dimensional wave ($\theta = 0°$), as expected from Squires theorem, which applies only to incompressible flow (Squire [1933]). At $M_1 = 0.8$ it is found that waves of 0°, 30° and 60° are all about equally amplified, and by $M_1 = 1.2$ the wave at 60° is substantially more amplified than the less oblique waves.

The increasing obliquity of the most amplified waves is better illustrated in figures 2.10 and 2.11. In these figures the amplification rate is plotted against θ for various Mach numbers, where for each Mach number the wavelength is fixed at the most amplified wavelength (including oblique waves). Figure 2.10 is the plot for the time-developing mixing layer from above, whereas figure 2.11 is for a spatially developing mixing layer with $T_2 = 1.0$ and $U_2 = 0.5$, and with a compressible laminar boundary-layer solution as the base flow. The plots are very similar for the two cases, indicating that for mixing layers *with equal densities* the hyperbolic tangent velocity profile can be reliably used to compute the fundamental effects of compressibility. In each case the curves split into two regimes. For $M_c < 0.6$ the two-dimensional wave is always the most amplified wave. Above $M_c = 0.6$ a three-dimensional wave of increasing obliquity is most amplified. The second mode is amplified at high Mach number, but never more than the oblique first mode. The cusp in the plots corresponds to the transition as one mode becomes more amplified than the other.

The angle of the most amplified disturbance was determined empirically to satisfy

$$M_c \cos\theta \approx 0.6 \tag{2.53}$$

This means that the Mach number perpendicular to the wave crest is approximately 0.6. This might be considered similar to the case of swept-back airfoils, where the key Mach number is $M_\infty \cos\theta$. In the mixing layer, waves at $\theta = 90°$ are not amplified and two-dimensional waves ($\theta = 0°$) have growth rates that are strongly reduced by compressibility effects (see section 2.2.4 and Chapter 4). The most amplified wave has to be somewhere in between.

Table 2.5 shows values of $M_c \cos\theta$ for spatially-developing mixing layers constructed in three different ways:

(a) Equal temperatures and fixed velocity ratio: $T_2 = 1$ and $U_2 = 0.5$

(b) Equal stagnation enthalpies (dimensionally we have $H^* = c_p^* T^* + u^{*2}/2$, non-dimensionally $H = T/((\gamma-1)M_1^2) + u^2/2$) and zero velocity on the low-speed side: $H_2 = 1$ and $U_2 = 0$. This case corresponds to the earliest experiments on the compressible mixing layer.

(c) Fixed Mach numbers $M_1 = 2.0$ and $M_2 = 1.0$. In this case the convective Mach number is varied by changing the ratio of stagnation enthalpies and the velocity ratio.

In each case a boundary-layer mean flow was used, for comparison with experiments. The value of $M_c \cos\theta$ is consistently between 0.58 and 0.59 for case (a) but shows some deviation at high Mach number for the cases (b) and (c).

Table 2.5 Variation of $M_c \cos\theta$ for oblique waves

$T_2 = 1, U_2 = 0.5$		$H_2 = 1, U_2 = 0$		$M_1 = 2, M_2 = 1$	
M_c	$M_c \cos\theta$	M_c	$M_c \cos\theta$	M_c	$M_c \cos\theta$
0.6	0.587	0.854	0.571	0.610	0.599
0.8	0.585	1.122	0.623	0.773	0.601
1.0	0.588	1.311	0.734	0.888	0.628
1.2	0.582			0.973	0.651
1.4	0.581			1.045	0.699
1.6	0.586			1.107	0.769

2.2.3 Convective Mach Number

The variation of the amplification rate of the most unstable mode with Mach number is shown in figure 2.12*a* for the temporal stability of the time-developing mixing layer. The curve of the most amplified two-dimensional wave is found by varying the wavenumber α_r until a maximum is found, keeping θ fixed at 0°. The curve for oblique waves is found by varying both wavenumber and angle until a maximum is obtained. Above $M_1 = 0.6$ the three-dimensional waves are the most rapidly amplified and the curve of the most amplified oblique disturbance is a much better fit to the existing experimental data (Papamoschou and Roshko [1988], see also figure 2.14) than the two-dimensional curve. Figure 2.12*b* shows the extension of the curve for oblique waves to very high Mach numbers. It can be observed that,

at least for the case of equal densities, the growth rate continues to decrease as Mach number is increased.

To check the convective Mach number concept, and to provide data for comparison with experiment, curves of the maximum spatial amplification rate, $|\alpha_i|_{\max}$, against convective Mach number were compiled. In each case the compressible boundary-layer equations were solved for the mean flow, and the most amplified disturbances (as a function of both frequency and angle) were determined. These were normalized with the amplification rate of the most amplified disturbance at $M_1 = 0.1$, with the same velocity and density ratio. Figure 2.13 shows the graphs of peak amplification rate against Mach number, using the three different methods of varying the convective Mach number described in the previous section. A good collapse of the data with M_c is obtained for $M_c < 0.8$, but there is some divergence at high convective Mach numbers.

It appears from recent work by Papamoschou [1989] that the fundamental idea behind the convective Mach number concept, of a large-scale structure convecting in the flow and 'seeing' the relative Mach number of the free-streams, may be flawed, since actual measured convective velocities do not agree with the theory. An alternative viewpoint is that M_c, as defined by equation (1.3), (*i.e.* the velocity difference divided by twice the average sound speed) is just a dimensionless parameter that can include only the first-order effects of compressibility. With this latter viewpoint we do not expect perfect collapse of growth rates at high Mach numbers.

It was mentioned in section 2.2.1 that a source of error in the normalization used by Papamoschou and Roshko [1988] is the model for incompressible growth rate, equation (2.49). An alternative method it to normalize experimental data by the growth rate of the most amplified spatial instability wave, $|\alpha_i|_{\max}$, at low Mach number. This is shown on figure 2.14 for the available pitot thickness data from Papamoschou [1986], together with a typical curve for the linear theory with $T_2 = 1.0$. The linear theory curve has been anchored to be 0.6 at $M_1 = 0$, using equation (2.48*a*) and assuming that density thickness and pitot thickness are equal. Unfortunately the large spread in the experimental data prevents a definitive conclusion on the performance of this method of normalization.

2.2.4 Supersonic Instability Modes

We have seen that the two-dimensional instability mode that is most amplified at low Mach number becomes stable at high Mach number. Previous researchers (Lessen *et al.* [1965,1966], Gropengiesser [1970]) have found other modes of instability at high Mach number which keep the mixing layer unstable in two-dimensions at any Mach number. These modes have been described as 'radiating vorticity modes' by Mack [1989], and are distinct from the 'Mack modes' found in supersonic wall boundary layers, confined shear layers, and compressible wakes, which require the presence of a region of trapped subsonic flow relative to the free-stream. The radiating vorticity modes are supersonic with respect to one of the free-streams and radiate energy into that stream. Two such modes exist in the mixing layer, one mode supersonic relative to the low-speed stream, and the other mode supersonic relative to the high-speed stream.

Jackson and Grosch [1988] investigated the supersonic modes for the mixing layer described by a hyperbolic tangent profile in Howarth-transformed space (see equation (2.16)). In the present work a similar case to Jackson and Grosch is studied, but using a solution to the boundary-layer equations as the base flow. The flow chosen has $U_2 = 0$ and $T_2 = 1$ and spatial stability theory is used. Figure 2.15 shows the variation in growth rate of the most amplified two-dimensional modes with Mach number, in the interesting region around a free-stream Mach number $M_1 = 2$ (*i.e.* around $M_c = 1$ since for $T_2 = 1$ and $U_2 = 0$ the convective Mach number is always one half the Mach number of the high speed stream). Figure 2.16 shows the phase speeds of these modes, which led Jackson and Grosch to classify them as a fast supersonic mode, supersonic relative to the low speed stream, and a slow supersonic mode, supersonic relative to the high speed stream. The various modes are plotted as a function of frequency in figures 2.17 and 2.18 at $M_1 = 2.2$. Figure 2.17 shows the growth rate and figure 2.18 the phase speed. From these plots we see that the most amplified mode is the fast mode. The second peak at the left of the curve for the fast mode is the remnant of the subsonic mode, which was the dominant mode at low Mach number. As Mach number is increased this mode becomes less and less amplified, and the peak moves to longer and longer wavelengths. From vortex sheet instability theory (Blumen *et al.* [1975]) we expect this mode to finally become stable at $M_1 = 2\sqrt{2}$.

The radiative nature of these instability waves becomes apparent when the eigenfunctions for pressure are plotted. The same case as above is chosen, with $M_1 = 2.2$. Figure 2.19*a* shows the pressure eigenfunction for the fast supersonic mode, radiating into the low speed side, and figure 2.19*b* shows the slow supersonic mode, which radiates into the high-speed side. Figure 2.19*c* shows the subsonic non-radiating mode. The eigenfunctions shown in figure 2.19 have the form of damped waves, since we are considering amplified waves, and the disturbances away from the centerline were created at an earlier time and then propagated into the free-stream. Jackson and Grosch [1988] only showed eigenfunctions for the neutral instability modes, which do not decay in the free-stream.

Which mode is most amplified depends upon the temperature ratio. At a temperature ratio of 2 the fast mode is the dominant mode, while at a temperature ratio of 0.5 the slow mode is dominant. Unlike the subsonic mode, increasing the angle of the supersonic mode disturbance does not increase its amplification rate, and for highly oblique disturbances these modes are stable.

The supersonic modes are very interesting from a physical perspective. However, it should be remembered that the most amplified waves in the flow are the oblique modes of the subsonic instability, and since these are amplified more rapidly by a factor of 3 or 4 we expect the resulting flow to be dominated by the oblique waves. The supersonic modes will come into play only if there is very strong two-dimensional forcing of the mixing layer.

2.2.5 Eigensolution Structure

Eigenfunctions from the linear theory are used in following chapters as inputs to direct numerical simulations. However they are interesting in their own right, providing important clues to the structure and physics of the large scale motions which develop from the linear instability. In this section eigenfunctions from two-dimensional stability calculations for the time-developing mixing layer are presented to illustrate the effects on compressibility on the linear eigenfunctions.

Figures 2.20 and 2.21 show the eigenfunctions $\hat{u}, \hat{v}, \hat{\rho}, \hat{T}$ as functions of the y coordinate for $M_1 = 0.01$ and $M_1 = 0.6$ respectively. The main effect is the rise in importance of the density and temperature eigenfunctions. These keep the same

basic shape at $M_1 = 0.6$ but are increased by four orders of magnitude relative to the case $M_1 = 0.01$.

Additional information can be found by generating contour plots of the eigenfunctions. For example the real part of the u velocity

$$u = \overline{u} + A \text{ Real}[\hat{u}e^{i\alpha x}] \tag{2.54}$$

can be found over one wavelength in the x direction, and similarly derivatives of the flow variable can be easily found. Results are shown on figures 2.22a–g for various flow quantities at $M_1 = 0.6$. Note that the y axis has been stretched to better illustrate the structure. The amplitude of the disturbance A is chosen to be 0.5 for the spanwise vorticity ω_z, as well as for ω_z/ρ and ρ, to better illustrate the structure, which would otherwise be dominated by the mean flow. The remaining plots use a disturbance amplitude of 0.01.

Even at $M_1 = 0.6$ the plots of ω_z and ω_z/ρ are little different from the vorticity structure for the incompressible case, found by Michalke [1965a]. The two 'elementary vortices' in the eigensolution will subsequently rotate around each other in the non-linear region of growth and merge to form the fundamental vortex in the mixing layer. What is interesting is that the density and pressure disturbance fields (figures 2.22c,d) show striking similarities with the fields to be presented in Chapter 4 from the non-linear roll-ups in the mixing layer. Low density and pressure perturbations are found in the vortex core and high density and pressure are found in the region between vortices where the braid will eventually form.

Some insight into mechanisms can be obtained by examining terms in the compressible vorticity equations for the linear eigensolutions. The equations for ω_z and for ω_z/ρ are as follows.

$$\omega_z = \frac{\partial u}{\partial y} - \frac{\partial v}{\partial x} \tag{2.55}$$

$$\frac{D\omega_z}{Dt} = -\omega_z\left(\frac{\partial u}{\partial x} + \frac{\partial v}{\partial y}\right) + \frac{1}{\rho^2}\left(\frac{\partial p}{\partial x}\frac{\partial \rho}{\partial y} - \frac{\partial p}{\partial y}\frac{\partial \rho}{\partial x}\right) \tag{2.55}$$

$$\frac{D(\omega_z/\rho)}{Dt} = \frac{1}{\rho^3}\left(\frac{\partial p}{\partial x}\frac{\partial \rho}{\partial y} - \frac{\partial p}{\partial y}\frac{\partial \rho}{\partial x}\right) \tag{2.56}$$

The terms on the right hand side are plotted on figures 2.22*f* and 2.22*g*. Both the baroclinic and dilatational terms are negative (dashed contours) in precisely those regions where the elementary vortices develop, and act to reduce the vorticity in the region where vortex roll-up is trying to occur, Thus both these terms act to reduce the growth rate of the two-dimensional instability as Mach number is increased. Recent work by Lele and Shariff (private communication [1989]) suggests that the advection term is more important than either of these terms and is the main reason for the stabilizing effect of Mach number.

The appearance of the same physical processes in the linear eigensolutions as are observed in the later non-linear development, as found by direct numerical simulation, may help to explain the surprising finding that the linear amplification rate is directly proportional to mixing layer growth rate.

2.3 Linear Instability Model for the Mixing Layer

Results from sections 2.2.1 and 2.2.5 suggest that linear processes may be important, even in the fully developed mixing layer. It is therefore worthwhile to consider a simple linear instability model of the mixing layer flow. Some of the arguments were presented by Monkewitz and Huerre [1982] to explain their successful prediction of shear layer growth rate, and are extended here.

2.3.1 Model

Consider first the incompressible uniform density mixing layer. Experiments show that the flow is dominated by the primary two-dimensional instability, and the developed structures show strong coherence in the spanwise direction. The spatial development of the flow can be described by the successive growth of linear instability modes, with longer and longer wavelengths. The phases in the development are as follows:

(1) Growth of the fundamental, most unstable, linear instability mode of the initial profile. This mode, frequency ω_F^*, grows until the layer has grown by a factor of two in width, and then saturates out, neither growing nor diminishing.

(2) Growth of the first subharmonic wave, frequency $\omega_F^*/2$. This mode grows and eventually results in pairing of two of the fundamental mode structures.

After the pairing the layer has again grown by a factor of two and this mode saturates.

(3) Growth of the next subharmonic wave, frequency $\omega_F^*/4$, again resulting in pairing, doubling of width, and saturation.

The essential behavior of the model is shown on figure 2.23. The exponential growth in a measure of energy, say E, of each mode is shown schematically. First the fundamental mode (F) grows and saturates, and we associate the developed structure with the neutral instability mode (see figure 2.24). The (non-dimensional) frequency of the neutral mode ω_N is approximately twice the frequency of the most amplified mode, ω, where ω is non-dimensionalized by $\omega = \omega^*\delta^*/U_1^*$. Since it is the same wave which has grown and saturated, the dimensional frequency, ω^* is the same for the two cases, and the layer must have grown by a factor of 2. Now that the layer has doubled in width the frequency of the new 'most amplified wave' is $\omega_F^*/2$, the first subharmonic wave ($S1$). This grows exponentially, following linear theory, until it saturates, resulting in pairing of two of the neutral modes of the original instability. The resulting structure can again be associated with a neutral mode, since by the pairing the layer has grown by a factor of 2. The same process of successive subharmonic growth, pairing, and saturation at the neutral mode, continues ad infinitum in the streamwise direction, and is not Reynolds number dependent.

The essential assumption of the linear instability model is that the time taken during the exponential growth of an unstable wave is long compared to the time taken for the ultimate non-linear process of pairing and saturation.

$$t_{\text{exponential growth}} >> t_{\text{non-linear}} \tag{2.58}$$

However, in reality both linear and non-linear processes may be governed by similar physical processes, and it may be that the time taken in the two stages are linked. So, even if equation (2.58) is not satisfied exactly, the linear model may still give good predictions.

Before discussing model predictions, we note that in reality the growth of subharmonic waves in the mixing layer is dependent upon the phase of the growing wave relative to the large-scale structure. The model considers only linear waves, for which phasing is not important. In the real case there will be a random phasing

of growing waves, which has the effect of moving the pairing locations around in space, resulting in the time average of linear growth rather than as a series of steps. (see also Sandham and Reynolds [1989]). Modes with certain phases will be more amplified by the presence of large-scale structure, and modes with other phases will have their growth rates diminished by the large-scale structure. The model relies on these effects cancelling out in the long time average.

2.3.2 Prediction of Growth Rate

The first implication of the model is on growth rate. Spatial instability waves grow exponentially like $e^{-\alpha_i x}$. The x distance for the n'th most amplified wave to grow by a factor of e^N is $N/|\alpha_i|_{\max}$. In this time the mixing layer has doubled in width, so $\Delta\delta = \delta^{n+1} - \delta^n = \delta^n$ or $\Delta(\delta/\delta^n) = 1$, so the growth rate is given by:

$$\frac{\Delta(\delta/\delta^n)}{\Delta(x/\delta^n)} = \frac{1}{N/|\alpha_i|_{\max}} \tag{2.59}$$

In the long time average this gives

$$\frac{d\delta}{dx} \sim |\alpha_i|_{\max} \tag{2.60}$$

thus providing a theoretical basis for the relation found in section 2.2.1. (equation (2.48)).

It should be noted that this derivation is dependent on the factor N being a constant. This means that the ratio of the amplitude of a wave at saturation to the amplitude when the wave was the most amplified wave from the previous saturated state is assumed constant for all x locations.

2.3.3 Prediction of Convective Velocities

A second corollary of the model is that the large-scale structures found in the mixing layer are linked to the neutral instability modes. The model picture, figure 2.23, is that what are observed in the mixing layer at any time are not the growing instability waves, but the neutral mode from saturation of the previous instability. The neutral modes are steady solutions of the parallel flow equations and, since they

are neither growing nor decaying, would persist for a long time once generated in the flow. For the hyperbolic tangent velocity profile the neutral instability modes are a subset of the family of mixing layer vortices found by Stuart [1967]. The Stuart vortices were compared to experimental mixing layer structures by Browand and Weidman [1982]. The comparison was qualitatively good, though some differences were found. Thus it may be that the neutral instability modes are a way to understand features of the organized structures in free shear flows. In particular, it is postulated here that the convective velocity of the large-scale structures in the flow is close to the phase speed of the neutral mode.

It was found that the phase speeds of the neutral modes were dependent on profile shapes. When a hyperbolic tangent was used for the mean velocity profile it was found that results matched the convective velocity formula (1.2) almost exactly. However, when the solution of the boundary-layer equations was used for the mean velocity profile it was found that the phase speed of the neutral mode c_N was different to the U_c formula (1.2). In fact it was always biassed towards the speed of the free-stream with the highest density, as shown on table 2.6 for the Brown and Roshko [1974] velocity and density ratios (recall $T_2 = 1/\rho_2$), at $M_1 = 0.1$.

Table 2.6 Phase speeds of neutral modes (low Mach number)

M_1	U_2	T_2	c_N	U_c
0.1	0.378	1.0	0.712	0.689
0.1	0.378	0.143	0.444	0.549
0.1	0.378	7.0	0.943	0.829
0.1	0.143	1.0	0.628	0.572
0.1	0.143	0.143	0.243	0.378
0.1	0.143	7.0	0.924	0.765

It is not surprising that the c_N results for a hyperbolic tangent mean profile match the U_c formula (1.2). The hyperbolic tangent velocity profile has an antisymmetry about the centerline. The same antisymmetry is in the structure model from which the convective velocity formula (1.2) is derived. This effect may explain some results of Lele [1989], who performed direct two-dimensional simulations of spatially-developing compressible mixing layers beginning with a hyperbolic tangent mean velocity profile, and found good agreement with the U_c formula. It may be that this observation was not a confirmation of the U_c formula, but rather that an

antisymmetry was built into the whole simulation by the choice of inflow velocity profile.

Convective speeds for the compressible mixing layer have been measured experimentally by Papamoschou [1989]. Table 2.7 shows a comparison between the measured convective velocity, the prediction of the U_c formula (1.2) (matching c_N results from a hyperbolic tangent profile), and the phase speed of the neutral mode c_N using the boundary-layer mean flow. All except the last of the experimental results show phase speed skewed towards the velocity of the more dense stream, as in the c_N yielded by stability theory with the boundary-layer mean flow. A plot of M_{c1} versus M_{c2} is shown on figure 2.25. This kind of plot was used by Papamoschou to demonstrate how different the actual measured convective velocities were from the U_c prediction. The figure shows the straight line $M_{c1} = M_{c2}$ (which is the U_c prediction), Papamoschou's data points, and the phase speeds of the neutral modes, c_N. The linear model seems on the whole to do a better job of predicting the experimental data than the U_c formula (1.2).

Table 2.7 Phase speeds of neutral modes compared with Papamoschou [1989]

M_1	U_2	T_2	c_N	U_c	expt
3.2	0.94	4.167	0.991	0.980	0.978
3.1	0.75	1.852	0.925	0.894	0.906
2.8	0.75	0.556	0.832	0.857	0.829
1.7	0.50	0.109	—	0.624	0.512
3.2	0.13	4.348	0.903	0.718	0.878
2.7	0.13	1.493	0.771	0.608	0.844
2.6	0.42	0.182	0.478	0.593	0.435
3.1	0.30	0.400	0.439	0.571	0.355
3.2	0.08	1.205	0.757	0.561	0.959
3.0	0.06	0.535	0.382	0.457	0.853

These results led Papamoschou [1989] to propose an alternative large-scale structure with shock waves, to account for the biassing of the convective velocity towards one or other of the free-streams. The contention here is that this biassing is due to the experimental mean profiles not having any built-in antisymmetry. When this effect is put into the stability analysis (by using the boundary-layer mean flow) the biassing is captured in the linear theory, without resort to such non-linear effects as shock waves.

Other experimental measurements of convective velocities are limited. Brown and Roshko [1974] measured one case, with $U_2 = 1/\sqrt{7}$ and $\rho_2 = 7$, and found a structure velocity of $U_c = 0.53$, compared to the linear estimate of 0.444 and the U_c formula estimate of 0.55 (table 2.6). For this case it was found that the mean profiles of velocity and density plotted by Brown and Roshko did not match well with the solution to the boundary-layer equations. We note that the solution for mean profiles from the boundary-layer equations is the same as solving the self-similar mixing layer problem for the mean flow, assuming an eddy-viscosity turbulence model. The linear theory is thus limited by the accuracy of the mean flow upon which it is performed.

2.3.4 Prediction of Pairing Locations

Another use for the model is in generalizing the findings of Bradshaw [1966] that approximately 1000 initial momentum thicknesses are required in the streamwise direction before self-similarity occurs, and of Ho and Huerre [1984] who modeled the downstream location of pairings in terms of the initial instability.

Using equation 2.48*b* above and the linear model of the growth process (figure 2.23), we can write

$$\text{x to n}^{\text{th}}\text{ pairing} = \frac{2^{n+1}-1}{0.45|\alpha_i|_{\max}} \tag{2.61}$$

where x is normalized as $x^*/\delta^*_{\omega_0}$ (δ_ω is 4 momentum thicknesses for the tanh profile). The $n = 0$ event is the roll-up of the first structure.

As an example, consider the mixing layer simulated numerically by Lowery and Reynolds [1986]. This was an incompressible simulation, with equal free-stream densities and a velocity ratio $U_2 = 0.5$. From table 2.2 we have that $|\alpha_i|_{\max}$ is 0.12850. Using equation (2.61) we find that the first roll-up is predicted to occur at $x = 17.3$, with the first pairing at $x = 51.9$ and the second pairing at $x = 121.1$, all in good agreement with the simulations. The Bradshaw [1966] criterion for self-similarity would occur for this case around the third pairing event $x = 260.0$, or 1040 in intial boundary-layer momentum thickness units. In view of the work of Ho *et al.* [1988], who found phase decorrelation in mixing layers to be associated with the pairing events, it may be that self-similarity is only achieved after enough

pairings have happened, and the flow has forgotten the initial conditions. Three or four levels of pairing would seem to be necessary to satisfy Bradshaw's criterion.

For incompressible mixing layers it is found that the ratio $\omega_{\text{neutral}}/\omega_{\text{most amplified}}$ is always near 2. However for compressible mixing layers, using the boundary layer velocity profile, this was not found to be always true. In this case multiple interactions (*e.g.* triplings) may be more common, and equation (2.61) can be rewritten as:

$$\text{x to n}^{\text{th}} \text{ agglomeration} = \frac{(\omega_{\text{neutral}}/\omega_{\text{most amplified}})^{n+1} - 1}{0.45|\alpha_i|_{\max}} \tag{2.62}$$

It is hoped that this discussion of a linear instability model for the mixing layer prompts more experimental measurements of growth rate, mean profiles, and the details of the large scale structure in the flow, including convective velocities, average pairing locations, number of structures involved in agglomerations etc. In this way the limitations of the model can be explored and improvements made.

2.4 Chapter Summary

In this chapter it has been shown that the linear theory can be a very useful tool for investigating the compressible mixing layer. In particular :

(1) The maximum amplification rate found from spatial theory, using the solution of the compressible boundary-layer equations as the mean flow, appears to be directly proportional to the growth rate of the developed mixing layer (equation (2.48)). This was demonstrated for the effect of density and velocity ratios on mixing layer growth rate at low Mach number.

(2) Oblique waves are dominant in the mixing layer above a convective Mach number of 0.6. The obliquity of the most amplified wave selected by the linear theory is such that the convective Mach number perpendicular to the wave crest is approximately 0.6 (equation (2.53)).

(3) The experimental observation of Papamoschou [1989], that actual convective velocities did not agree with the U_c theory (equation (1.2)), was confirmed in the linear regime by calculating the phase speeds of the neutral modes of instability.

CHAPTER 3

Numerical Formulation for Direct Simulations

In a direct simulation the time-dependent Navier-Stokes equations are solved in full, with no turbulence model. This chapter describes the numerical methods used to simulate the compressible time-developing mixing layer, which is assumed to be periodic in the streamwise and spanwise directions (x and z). The code was written in the VECTORAL language (Wray [1988]), and implemented on a Cray X-MP 4/8 at NASA-Ames.

3.1 Governing Equations

The conservation laws for mass, momentum and energy can be written in the following form (Anderson, Tannehill and Pletcher [1984]), using the conservative variables $(\rho^*, \rho^* u_i^*, E_T^*)$, cartesian tensor notation, and the superscript * for a dimensional quantity:

$$\frac{\partial \rho^*}{\partial t^*} + \frac{\partial (\rho^* u_i^*)}{\partial x_i^*} = 0 \tag{3.1}$$

$$\frac{\partial (\rho^* u_i^*)}{\partial t^*} + \frac{\partial (\rho^* u_i^* u_j^* + p^* \delta_{ij})}{\partial x_j^*} = \frac{\partial \tau_{ij}^*}{\partial x_j^*} \tag{3.2}$$

$$\frac{\partial E_T^*}{\partial t^*} + \frac{\partial [(E_T^* + p^*) u_i^*]}{\partial x_i^*} = -\frac{\partial q_i^*}{\partial x_i^*} + \frac{\partial (u_j^* \tau_{ij}^*)}{\partial x_i^*} \tag{3.3}$$

where ρ^* is the density, u_i^* are the velocity components, p^* is the pressure, τ_{ij}^* is the shear stress tensor and q_i^* is the heat flux vector. E_T^* is the total energy, defined by:

$$E_T^* = \rho^* (e^* + \frac{u_i^* u_i^*}{2}) \tag{3.4}$$

where e^* is the internal energy per unit mass. The perfect gas law is

$$p^* = \rho^* R^* T^* \tag{3.5}$$

where R^* is the gas constant and T^* the temperature. We assume a Newtonian fluid and Fourier heat conduction, so the constitutive equations for τ_{ij}^* and q_i^* are:

$$\tau_{ij}^* = \mu^* \left(\frac{\partial u_i^*}{\partial x_j^*} + \frac{\partial u_j^*}{\partial x_i^*} - \frac{2}{3} \frac{\partial u_k^*}{\partial x_k^*} \delta_{ij} \right) \tag{3.6}$$

$$q_i^* = -k^* \frac{\partial T^*}{\partial x_i^*} \tag{3.7}$$

where μ^* is the viscosity and k^* is the thermal conductivity.

Non-dimensionalization of these equations is obtained by:

$$u_i = \frac{u_i^*}{U_1^*} \qquad \rho = \frac{\rho^*}{\rho_1^*} \qquad p = \frac{p^*}{\rho_1^* U_1^{*2}} \qquad T = \frac{T^*}{T_1^*} \tag{3.8a}$$

$$\mu = \frac{\mu^*}{\mu_1^*} \qquad e = \frac{e^*}{U_1^{*2}} \qquad t = \frac{t^* U_1^*}{\delta_{\omega_0}^*} \qquad x_i = \frac{x_i^*}{\delta_{\omega_0}^*} \tag{3.8b}$$

where the subscript 1 represents the upper ($y > 0$) free-stream value. The reference length scale is $\delta_{\omega_0}^*$, the vorticity thickness of the initial velocity profile:

$$\delta_\omega^* = \frac{U_1^* - U_2^*}{|d\bar{u}^*/dy^*|_{\max}} \tag{3.9}$$

The non-dimensional equations for continuity, momentum and energy are:

$$\frac{\partial \rho}{\partial t} = -\frac{\partial (\rho u_i)}{\partial x_i} \tag{3.10}$$

$$\frac{\partial (\rho u_i)}{\partial t} = -\frac{\partial (\rho u_i u_j + p\delta_{ij})}{\partial x_j} + \frac{\partial \tau_{ij}}{\partial x_j} \tag{3.11}$$

$$\frac{\partial E_T}{\partial t} = -\frac{\partial [(E_T + p) u_i]}{\partial x_i} - \frac{\partial q_i}{\partial x_i} + \frac{\partial (u_j \tau_{ij})}{\partial x_i} \tag{3.12}$$

with constitutive relations

$$\tau_{ij} = \frac{\mu}{Re}\left(\frac{\partial u_i}{\partial x_j} + \frac{\partial u_j}{\partial x_i} - \frac{2}{3}\frac{\partial u_k}{\partial x_k}\delta_{ij}\right) \tag{3.13}$$

$$q_i = \frac{-\mu}{(\gamma-1)M_1^2 Pr Re}\frac{\partial T}{\partial x_i} \tag{3.14}$$

The Reynolds number of the flow is defined by $Re = \rho_1^* U_1^* \delta_{\omega_0}^* / \mu_1^*$, and the Prandtl number by $Pr = c_p^* \mu^* / k^*$. The Prandtl number is assumed constant with value 1. The viscosity is assumed to follow a power law, so non-dimensionally

$$\mu = T^{0.67} \tag{3.15}$$

The constant 0.67 is the value for nitrogen (White [1974]).

Constant specific heats are assumed, and if we set $e^* = 0$ at $T^* = 0$, we can write $e^* = c_v^* T^*$. The non-dimensional form of the perfect gas law can then be written as either:

$$p = \rho(\gamma - 1)e \tag{3.16}$$

or

$$\gamma p = \rho c^2 \tag{3.17}$$

where c is the sound speed (normalized as c^*/U_1^*) and we have used the result for the sound speed of a perfect gas with constant specific heats:

$$c^{*2} = \gamma R^* T^* \tag{3.18}$$

In all the simulations a passive scalar field is computed. The dimensional equation for the scalar f (see *e.g.* Kays and Crawford [1980]) is

$$\frac{\partial(\rho^* f)}{\partial t^*} + \frac{\partial(\rho^* f u_i^*)}{\partial x_i^*} = \frac{\partial}{\partial x_i^*}\left(\rho^* D_s^* \frac{\partial f}{\partial x_i^*}\right) \tag{3.19}$$

where D_s^* is the diffusion coefficient for the scalar. One can think of $\rho^* f$ as the concentration per unit volume of a trace species. We define a Schmidt number by $Sc = \mu^*/\rho^* D_s^*$ and using the non-dimensionalization method of equation (3.8) we have:

$$\frac{\partial(\rho f)}{\partial t} + \frac{\partial(\rho f u_i)}{\partial x_i} = \frac{1}{ReSc}\frac{\partial}{\partial x_i}\left(\mu \frac{\partial f}{\partial x_i}\right) \tag{3.20}$$

3.2 Time Advance

The time advance method is fully explicit. The variables $(\rho, \rho u, \rho v, \rho w, E_T)$ are advanced using a three-step compact-storage third order Runge-Kutta scheme of the family derived by Wray [1986]. Two storage locations are employed for each time-dependent variable and at each substep these locations, say Q_1 and Q_2, are updated simultaneously (using a feature of VECTORAL) as follows:

$$Q_1^{\text{new}} = a_1 \Delta t Q_1^{\text{old}} + Q_2^{\text{old}} \qquad Q_2^{\text{new}} = a_2 \Delta t Q_1^{\text{old}} + Q_2^{\text{old}} \tag{3.21}$$

The constants (a_1, a_2) are chosen to be $(2/3, 1/4)$ for substep 1, $(5/12, 3/20)$ for substep 2 and $(3/5, 3/5)$ for substep 3. At the beginning of each full time step Q_1 and Q_2 are equal. The data in Q_1 is used to compute the right hand side of equations (3.10) through (3.12). The computed right hand side is stored in Q_1 (overwriting the old Q_1). Equation (3.21) is then used to update Q_1 and Q_2.

An estimate of the time step limitation can be made by considering a model convection-diffusion equation (Blaisdell [1988], private communication):

$$\frac{\partial \phi}{\partial t} + u\frac{\partial \phi}{\partial x} + v\frac{\partial \phi}{\partial y} + w\frac{\partial \phi}{\partial z} = a\frac{\partial^2 \phi}{\partial x_i \partial x_i} \tag{3.22}$$

Assuming periodic boundary condition in all directions we can Fourier transform and rearrange this equation to give:

$$\frac{\partial \tilde{\phi}}{\partial t} = -\Big[i2\pi\Big(\frac{k_x u}{L_x} + \frac{k_y v}{L_y} + \frac{k_z w}{L_z}\Big) + a4\pi^2\Big(\frac{k_x^2}{L_x^2} + \frac{k_y^2}{L_y^2} + \frac{k_z^2}{L_z^2}\Big)\Big]\tilde{\phi} \tag{3.23}$$

This equation can be compared with a simple ordinary differential equation:

$$\frac{d\tilde{\phi}}{dt} = b\tilde{\phi} \tag{3.24}$$

for which the time step limitation for stability is

$$\Delta t = \frac{(CFL)_{\max}}{|b|_{\max}} \tag{3.25}$$

where CFL is the Courant-Friedrichs-Lewy number. The maximum CFL number for stability is fixed by the time-advance method. For linear equations the limit is $\sqrt{3}$ for the third order Runge-Kutta method described above.

The magnitude of a complex number $a+ib$ is less than $|a|+|b|$, so we can substitute absolute values for the terms on the right hand side of equation (3.23). We choose the worst case for the terms in brackets in (3.23), *i.e.* $k_x = N_x/2$, $u = c + |u|$, etc. The value for a in (3.22) is obtained from (3.14) as $\mu/(\gamma-1)M_1^2RePr$, which is a more stringent limitation than the momentum equation for $M_1 < 1.6$ (for $Pr = 1$ and $\gamma = 1.4$). Letting $\Delta x = L_x/N_z$ and similarly for Δy and Δz we get:

$$\Delta t = \frac{CFL}{D_c + D_\mu} \tag{3.26a}$$

where

$$D_c = \pi c\Big(\frac{1}{\Delta x} + \frac{1}{\Delta y} + \frac{1}{\Delta z}\Big) + \pi\Big(\frac{|u|}{\Delta x} + \frac{|v|}{\Delta y} + \frac{|w|}{\Delta z}\Big) \tag{3.26b}$$

$$D_\mu = \frac{\pi^2\mu/\rho}{(\gamma-1)M_1^2RePr}\Big(\frac{1}{\Delta x^2} + \frac{1}{\Delta y^2} + \frac{1}{\Delta z^2}\Big) \tag{3.26c}$$

The worst-case cell is used to fix the time step.

Simulations with various time steps were made for a time-developing mixing layer problem at $M_1 = 0.4$ and $Re = 400$, initialized with the fundamental mode from linear stability analysis. The simulations were run up to the non-linear saturation of the instability. It was found that there was no numerical instability or degradation of accuracy until the CFL number was raised above 4, indicating that the above criteria is very conservative. In all the simulations a CFL number of 2 was used.

3.3 Evaluation of Derivatives

3.3.1 Periodic Directions

In the periodic directions x and z the Fourier method is used to calculate derivatives. The quantity to be differentiated is transformed using the Fast Fourier Transform, multiplied by ik, and inverse transformed. No attempt was made to dealias

the non-linear products, since no complete method is known for the compressible equations which have many terms involving divisions.

When an even-length Fourier transform is used there is one wavenumber $k_x = N_x/2$ which has no complex part. This wavenumber is commonly referred to as the 'oddball' wavenumber. The Fourier component at the oddball wavenumber is always zeroed out when taking derivatives. In an implicit scheme this Fourier component is forced to remain zero. However in an explicit scheme, such as that used here, roundoff error will accumulate at this wavenumber as one goes back and forth between Fourier space and physical space. In the present code this is compounded by conversions back and forth between 64 bit arithmetic representation and 32 bit storage representation (Blaisdell [1988], private communication). It is thus necessary to explicitly zero out the oddball component of the flow during any computation. Blaisdell's procedure for doing this (for one direction) is to define a filtered flowfield ϕ_j^f, subtracting the oddball as follows:

$$\phi_j^f = \phi_j - \widetilde{\phi}(N_x/2) e^{i2\pi \frac{N_x}{2} \frac{(j-1)}{N_x}} \tag{3.27}$$

From the definition of a transform pair, we have

$$\phi_j = \sum_{k_x=-\frac{N_x}{2}+1}^{N_x/2} \widetilde{\phi}(k_x) e^{i2\pi k_x \frac{(j-1)}{N_x}} \tag{3.28}$$

$$\widetilde{\phi}(k_x) = \sum_{j=1}^{N_x} \phi_j e^{-i2\pi k_x \frac{(j-1)}{N_x}} \tag{3.29}$$

Substituting for $\widetilde{\phi}_{N_x/2}$ into equation 3.27 gives

$$\phi_j^f = \phi_j - \frac{(-1)^j}{N_x} \sum_{j'=1}^{N_x} (-1)^{j'} \phi_{j'} \tag{3.30}$$

This method of removing the oddball in real space vectorizes efficiently and was found to be substantially cheaper than the alternative method of Fourier transforming, zeroing the oddball, and inverse transforming. The method was applied at each substep of the integration.

In the three-dimensional code the oddball needs to be removed in each spectral direction, x and z. Following the same procedure as above, the filter function is derived as:

$$\phi^f_{j,k} = \phi_{j,k} - \frac{(-1)^k}{N_z}\sum_{k'=1}^{N_z}(-1)^{k'}\phi_{j,k'} - \frac{(-1)^j}{N_x}\sum_{j'=1}^{N_x}(-1)^{j'}\phi_{j',k} + \frac{(-1)^j(-1)^k}{N_xN_z}\sum_{j'=1}^{N_x}\sum_{k'=1}^{N_z}(-1)^{j'}(-1)^{k'}\phi_{j',k'} \tag{3.31}$$

3.3.2 Normal Direction

In the normal direction (y) there are several alternative differentiation methods which can be used. Firstly, one can subtract the mean flow from the quantity to be differentiated, and use regular Fourier differentiation. This would only be appropriate for a periodic array of mixing layers, which is not the case we wish to consider here. Secondly, one can use a mapping (*e.g.* Cain *et al.* [1984]), to transform an infinite physical domain onto a finite computational one. This method was implemented, but was found to produce point-to-point oscillations in the free-stream. This effect is probably due to a lack of resolution of sound waves in the free-stream, where the grid spacing becomes very large. The method finally adopted was to use high-order finite difference methods on a grid of finite extent in the normal direction, and then to apply characteristic boundary conditions to simulate an infinite flow domain.

A family of high order modified Padé schemes has been derived by Lele [1989]. These schemes can be written in the following form for the first derivative:

$$\phi'_{j+1} + a\phi'_j + \phi'_{j-1} = b\frac{\phi_{j+1} - \phi_{j-1}}{2\Delta y} + c\frac{\phi_{j+2} - \phi_{j-2}}{4\Delta y} \tag{3.32a}$$

Solution for ϕ'_j is obtained by solving the tridiagonal system of equations. A family of fourth order schemes are obtained if we choose:

$$b = \frac{2+4a}{3} \qquad c = \frac{4-a}{3} \tag{3.32b}$$

For $a = 4$, the conventional Padé scheme is recovered, whilst with $a = 3$ we have a sixth order scheme, used in all the current work. A similar scheme can be derived for the second derivative:

$$\phi''_{j+1} + a\phi''_j + \phi''_{j-1} = b\frac{\phi_{j+1} - 2\phi_j + \phi_{j-1}}{\Delta y^2} + c\frac{\phi_{j+2} - 2\phi_j + \phi_{j-2}}{4\Delta y^2} \tag{3.33a}$$

$$b = \frac{4a-4}{3} \qquad c = \frac{10-a}{3} \tag{3.33b}$$

This time $a = 10$ gives the usual Padé scheme, and $a = 5.5$ is a sixth order scheme, used in this work.

The viscous terms in the governing equations require evaluation of successive derivatives, for example the term

$$\frac{\partial}{\partial y}\left(\mu\frac{\partial u}{\partial y}\right) \tag{3.34}$$

When a spectral method is used there is no loss of accuracy if these are computed by two applications of a first derivative. However, with finite difference methods we find that two applications of a first derivative gives a much worse representation of the high wavenumbers than a single second derivative computation. This is because the modified wavenumber (Lele [1989]) goes to zero for the first derivative at high wavenumbers. The remedy for this is to expand all terms in the y direction like (3.34) into two terms (non-conservative formulation):

$$\mu\frac{\partial^2 u}{\partial y^2} + \frac{\partial \mu}{\partial y}\frac{\partial u}{\partial y} \tag{3.35}$$

A mapped grid is used in the normal direction to resolve the shear layer more efficiently. The mapping function is a sinh function, which concentrates points around $y = 0$ (Anderson, Tannehill and Pletcher [1984]):

$$y = \frac{L_y}{2}\frac{\sinh(b_y\eta)}{\sinh b_y} \tag{3.36}$$

where L_y is the box length in the normal direction. The mapped coordinate is η, and b_y is the stretching parameter in the y direction, chosen to be 1.7 in the current work. If we define the metrics

$$h' = \frac{dy}{d\eta} = \frac{L_y}{2}\frac{b_y \cosh(b_y \eta)}{\sinh b_y} \tag{3.37}$$

$$h'' = \frac{d^2 y}{d\eta^2} = \frac{L_y}{2}\frac{b_y^2 \sinh(b_y \eta)}{\sinh b_y} \tag{3.38}$$

then the first and second derivatives of a function ϕ are evaluated as:

$$\frac{\partial \phi}{\partial y} = \frac{1}{h'}\frac{\partial \phi}{\partial \eta} \tag{3.39}$$

$$\frac{\partial^2 \phi}{\partial y^2} = \frac{1}{h'^2}\frac{\partial^2 \phi}{\partial \eta^2} - \frac{h''}{h'^2}\frac{\partial \phi}{\partial y} \tag{3.40}$$

3.4 Free-Stream Boundary Condition

In these simulations we are considering the problem of an unbounded compressible mixing layer. The infinite extent could be obtained by using a mapping function, but this would lead to poor resolution of the flow far away from the mixing layer. In particular, sound waves would propagate into regions of the computation where they would be poorly resolved, and might be reflected back and contaminate the main flow. Thus, we require boundary conditions which simulate an infinite domain, even though the computational domain is finite. Such schemes were investigated by Thompson [1987], and his method is followed here. The basic idea is to consider the characteristic form of the Euler equations at the boundary. Outgoing characteristics use information within the computational domain, and can be computed with no problem. Incoming characteristics are handled by setting the time derivative of their amplitude equal to zero, thus ensuring that no waves enter the domain during the simulation, giving the boundary conditions a non-reflecting character.

We begin by writing the Euler equations in terms of the conservative variables $Q = (\rho, \rho u, \rho v, \rho w, E_T, \rho f)^T$

$$\frac{\partial Q}{\partial t} + \frac{\partial G}{\partial y} = (\text{r.h.s}) \tag{3.41}$$

$$G = (\rho v, \rho uv, \rho v^2 + p, \rho vw, (E_T + p)v, \rho vf)^T \tag{3.42}$$

We are concerned here only with the Euler derivatives in the y direction. Derivatives in x and z, including viscous terms, are evaluated at the boundary using information from the previous substep, and are included in the right hand side (r.h.s). The flux Jacobian of G is more easily derived if we work with the non-conservative flow variables $U = (\rho, u, v, w, d, f)^T$, where $d = p\rho^{-\gamma}$. Setting $B = \partial G/\partial Q$ (*i.e.* $B(\text{row } i, \text{col } j) = \partial G(i)/\partial Q(j)$) and $R = \partial Q/\partial U$, we have

$$\frac{\partial U}{\partial t} + B\frac{\partial U}{\partial y} = R^{-1}(\text{r.h.s}) \tag{3.43}$$

and

$$\frac{\partial G}{\partial y} = RB\frac{\partial U}{\partial y} \tag{3.44}$$

Now B can be diagonalized, $B = T^{-1}\Lambda T$, where the elements of the diagonal matrix Λ are $(v - c, v, v, v, v + c, v)$. Pressure is more easily found computationally than the quantity d, so we use a new non-conservative vector $V = (\rho, u, v, w, p, f)^T$ and define $S = \partial U/\partial V$. Equation (3.44) can now be written

$$\frac{\partial G}{\partial y} = RT^{-1}\left(\Lambda TS\frac{\partial V}{\partial y}\right) \tag{3.45}$$

This is the relation that is used to calculate $\partial G/\partial y$ in equation (3.41) at the boundary.

The quantity in brackets in equation (3.45) is a vector. The sign of each of the eigenvalues in Λ is used to determine the course of action for each element in the vector. If the characteristic velocity is directed out of the computational domain

(positive at the top boundary or negative at the bottom boundary), then the quantity is calculated as is. On the other hand, if the characteristic is directed inwards then the vector element is zeroed out. This gives the non-reflecting character of the boundary condition. The final step is to premultiply the vector by the matrices T^{-1} and R. The various vectors and matrices required in the computation are:

$$\Lambda T S \frac{\partial V}{\partial y} = \begin{pmatrix} (v-c)[\frac{\partial p}{\partial y} - \rho c \frac{\partial v}{\partial y}] \\ v \frac{\partial u}{\partial y} \\ v[\frac{\partial p}{\partial y} - c^2 \frac{\partial \rho}{\partial y}] \\ v \frac{\partial w}{\partial y} \\ (v+c)[\frac{\partial p}{\partial y} + \rho c \frac{\partial v}{\partial y}] \\ v \frac{\partial f}{\partial y} \end{pmatrix} \tag{3.46}$$

$$T^{-1} = \begin{pmatrix} \frac{1}{2c^2} & 0 & -\frac{1}{c^2} & 0 & \frac{1}{2c^2} & 0 \\ 0 & 1 & 0 & 0 & 0 & 0 \\ -\frac{1}{2\rho c} & 0 & 0 & 0 & \frac{1}{2\rho c} & 0 \\ 0 & 0 & 0 & 1 & 0 & 0 \\ 0 & 0 & \frac{1}{\rho^\gamma} & 0 & 0 & 0 \\ 0 & 0 & 0 & 0 & 0 & 1 \end{pmatrix} \tag{3.47}$$

$$R = \begin{pmatrix} 1 & 0 & 0 & 0 & 0 & 0 \\ u & \rho & 0 & 0 & 0 & 0 \\ v & 0 & \rho & 0 & 0 & 0 \\ w & 0 & 0 & \rho & 0 & 0 \\ a & \rho u & \rho v & \rho w & \frac{\rho^\gamma}{(\gamma-1)} & 0 \\ f & 0 & 0 & 0 & 0 & \rho \end{pmatrix} \tag{3.48}$$

$$\text{where} \qquad a = \frac{c^2}{\gamma - 1} + \frac{u^2 + v^2 + w^2}{2}$$

The boundary condition for the two-dimensional code is a simple extract from the above, removing the fourth row and column from each vector and matrix.

3.5 Initial Conditions

To start the calculation we need to specify the values of all computational variables. The specifications are described in subsequent chapters.

3.6 Validation

The objective is to subject the code to as many checks as possible. We rely on three methods: (a) validation in the incompressible limit using Taylor-Green flow, (b) checking the Euler terms in the compressible equations by comparison of linear growth rates with inviscid linear stability theory, and (c) checks of resolution by monitoring energy spectra during simulations, to ensure that enough modes are being used to fully resolve the flow. The only terms that cannot be verified using these methods are the viscous terms involving $\partial u_k/\partial x_k$ (equation (3.13)). Here we must rely on thorough sight-checking of the code.

The Taylor-Green flow (Taylor [1923]) consists of a decaying array of vortices in the $x-z$ plane, specified non-dimensionally by:

$$u = -\sqrt{A}\cos(2\pi kx)\sin(2\pi kz)e^{-8\pi^2k^2t/Re} \tag{3.49}$$

$$w = \sqrt{A}\sin(2\pi kx)\cos(2\pi kz)e^{-8\pi^2k^2t/Re} \tag{3.50}$$

$$p = p_{\text{ref}} - \frac{A}{4}[\cos(4\pi kx) + \cos(4\pi kz)]e^{-8\pi^2k^2t/Re} \tag{3.51}$$

We choose $k = 1$, $Re = 1$, a box size $L_x = L_z = 1$, and uniform conditions in y with $L_y = 2$. The reference pressure is $p_{\text{ref}} = 1/(\gamma M_1^2)$. The reference Mach number M_1 was set to 0.2 and the constant A was taken as 0.0016, so that we begin with a peak local Mach number of approximately 0.01, *i.e.* near the incompressible limit. The Taylor-Green problem needs only a few Fourier modes. The test case was run for the three-dimensional code with $N_x \times N_y \times N_z = 8 \times 11 \times 8$ corresponding to 4 complex Fourier modes in each of the x and z directions. The solution for u at $x = 0.5$ and $z = 0.25$ is shown on figure 3.1 as a function of time. The error at time $t = 1/(8\pi^2)$, when the solution should have decayed by a factor e, is less than 0.03%. This remaining error is attributed to the slight difference in Mach number.

The growth of linear disturbances in the three-dimensional code was checked against the inviscid linear stability theory. The code was initialized with the eigenfunctions, and run at high Reynolds number through the linear regime. The linear growth rate was extracted from the Fourier coefficients from the relation

$$\omega(k_x) = \frac{d}{dt} \ln\{\text{Real}[\tilde{\phi}(k_x)]\} \tag{3.52}$$

For the fundamental mode we have $k_x = 1$. Plots of $\ln(\text{Real}[\tilde{\phi}(1)])$ are shown on figure 3.2 for the functions $\phi = (u, v, w, \rho, T, p)$. The simulation was for a 45° oblique wave growing in a mixing layer at $M_1 = 0.8$, $Re = 10^6$. All functions show the correct linear growth. In addition, the eigenfunctions at the end of the simulation were renormalized and compared with the initial eigenfunctions. An example is shown on figure 3.3 for temperature. All the eigenfunctions were found to collapse on top of each other. The worst error in the growth rate compared to the inviscid theory was approximately 2%, attributed to the finite Reynolds number, and changes in the mean flow (setting up a small $\overline{v}$ velocity profile) during the simulation. The latter effect could be removed by running for just one time step, when the mean flow had no time to change; in that case the error dropped to 0.01%.

The effect of the positioning of the boundaries in the y direction was investigated by running three simulations at $M_1 = 0.4$, $Re = 400$. The length of the domain in the streamwise direction was $L_x = 8.0554$ and the length in the y direction was varied, with L_y set to 6, 10 or 20. $L_y = 10$ means that the domain extends to $y = \pm 5$ initial vorticity thicknesses on either side. The number of grid points in y was chosen to be 61, 81 and 99 respectively. The growth of the vorticity thickness is plotted on figure 3.4 for each case, and the developed structure at the same time in the simulation is shown on figure 3.5 for $L_y = 10$ and figure 3.6 for $L_y = 6$. The physics of such simulations are discussed in more detail in the following chapter. Here we note that with $L_y \geq 10$ we get a converged solution for the growth history of the flow. However, even the case with $L_y = 6$ captures most of the interesting roll-up of large-scale structure. The detailed feature which arises when the boundaries are too close is the development of low-level vorticity at the boundary, shown in figure 3.6*b*. All calculations reported herein were run with $L_y \geq 10$.

One of the most important checks on the code is that of resolution. In general if the same result is obtained with two grids, one with twice as many points in each direction as the other, then we have some confidence in the result. With a spectral method there is an inbuilt check on resolution, namely the fall-off in the energy spectrum at high wavenumbers. A large drop-off in energy at high wavenumbers means that the flow is fully resolved, and adding modes would not improve the solution. Any lack of resolution will show up as an upturning in the spectrum at high k_x. During the simulations the energy spectrum is monitored. The energy is defined by:

$$E(k_x) = \int_{-L_y/2}^{L_y/2} \tilde{u}_i(k_x)\tilde{u}_i^{\dagger}(k_x)dy \tag{3.53}$$

where † indicates a complex conjugate. A typical well-resolved spectrum for the $L_y = 10$ case above is plotted on figure 3.7, showing 9 orders of magnitude roll-off in energy. Monitoring of the spectrum is also used to improve the efficiency of the code. When linear modes are used for initial conditions the code needs few modes to resolve the flow. As the harmonics develop, and the flow becomes non-linear, we need more and more modes to resolve the flow, until the flow is fully-developed and the small diffusion scales get no smaller. The simulations were usually started with few modes, *e.g.* $16 \times 99 \times 16$ and then as the spectrum filled out the spectral directions x and z were extended, ending up, for example, at $96 \times 99 \times 96$. In the y direction we need the full number of points right from the start in order to resolve the mean flow. Factors of 2 were typically saved in run-time using this method.

As a last point on verification it is noted that the two-dimensional simulations from the current work have been compared with results from an earlier code (Sandham and Yee [1989]), which used TVD and MacCormack methods, and with the simulations of Lele [1989]. All such comparisons show qualitatively similar behavior.

CHAPTER 4

Two-Dimensional Simulations

In this chapter results are presented from direct simulations of the compressible Navier-Stokes equations in two dimensions. The simulations show the effect of compressibility on the development of the primary two-dimensional instability, which has been observed to be the dominant mode in incompressible experiments.

4.1 Initial Conditions and Parameters

The simulations have been performed for the temporal development of the two-dimensional time-developing mixing layer. Mean profiles of velocity and temperature need to be specified at the initial time. The mean velocity in the streamwise direction is given by an error-function:

$$u = \mathrm{erf}(y\sqrt{\pi}) \tag{4.1}$$

The mean temperature is obtained from the mean velocity profile via the Crocco-Busemann relation (equation (2.13)), which assumes parallel flow and unity Prandtl number. Pressure is assumed uniform, and then density is obtained simply as the inverse of temperature, since both density and temperature are normalized by the value on the upper side of the mixing layer (equation (3.8)).

Perturbations are added to the mean profiles in the form of eigenfunctions of unstable modes from the inviscid linear stability analysis (Chapter 2). For example:

$$u = \overline{u} + A\ \mathrm{Real}\{\hat{u}(y)e^{i\alpha x}\} \tag{4.2}$$

and similarly for the v velocity, density and temperature. The amplitude A of the disturbances was usually specified to be 0.05. The length of the box in the streamwise direction (L_x) was chosen to match the most unstable wavelength of inviscid linear stability theory *i.e.* $L_x = 2\pi/|\omega_i|_{\max}$.

Non-dimensional parameters for the flow also have to be specified. For most of the simulations in this chapter an initial Reynolds number $Re = 400$ was chosen based on the following considerations. The Reynolds number has to be chosen

small enough so that the flow can be fully resolved, yet high enough to capture the inviscid nature of the instability. The effect of Reynolds number on the linear growth rate of the most amplified inviscid eigenfunction was investigated by running the viscous code, initialized with an inviscid eigenfunction, for one time step. The linear growth rate can be found directly from the change in the Fourier coefficient for the relevant mode using equation (3.52). Results are shown in figure 4.1. The asymptotic growth rate at high Reynolds numbers matches the inviscid theory to within 0.1 percent. The drop in amplification as viscosity is increased can be clearly observed. It should be noted that only the growth rate of the inviscid eigenfunction is plotted. There will be a viscous eigenfunction, with a longer wavelength, that is more amplified. Thus the curves at low Reynolds numbers for the most amplified viscous wave will not drop so rapidly as these. However, these plots do give a good idea of the range of Reynolds numbers where we expect to capture the basic inviscid processes, as might be found in high Reynolds number experiments. In choosing Reynolds numbers for the simulations, we would like at least to be in the region where the inviscid eigenfunction is linearly amplified, and not damped. It can be seen from the plot that as the Mach number is increased we have to move to higher and higher Reynolds numbers to get near the asymptotic high-Re region.

The effect of Reynolds number on the non-linear development of a single structure at $M_1 = 0.4$ was computed. The growth of vorticity thickness is plotted on figure 4.2, and the scalar and vorticity fields for the $Re = 100$ and $Re = 800$ cases are shown on figures 4.3 and 4.4. At even lower Reynolds numbers, with the same low amplitude forcing, the layer is laminar and grows with thickness proportional to the square root of time. As the Reynolds number is increased, it can be seen that the width of the strained diffusion layer in the stagnation region ($x = 3L_x/4$, $y = 0$) is reduced. Broadwell and Breidenthal [1982] predict that the width of this layer varies in inverse proportion to the square root of the Reynolds number. This is the small scale that makes flows at higher Reynolds number more difficult to resolve numerically.

The Prandtl number and Schmidt number for the flow were chosen to be unity (see section 3.1). The ratio of specific heats was set to $\gamma = 1.4$, and the mixture fraction, f, was initialized with a hyperbolic tangent profile:

$$f = \frac{1}{2}(1 + \tanh(2y)) \tag{4.3}$$

4.2 Mach Number Effects

In the time developing mixing layer U_2 can be chosen as $U_2 = -1/\rho_2$, so that the Mach number of each free-stream is the same as the convective Mach number (equation (2.52)). Thus, in the simulations we can use free-stream Mach number and convective Mach number interchangeably. Figure 4.5 shows the effect of Mach number on the growth of the most amplified disturbance. The most amplified wavelength was $L_x = 2\pi/\alpha = (7.48, 8.06, 9.52, 13.37)$ for each of the cases $M_1 = (0.2, 0.4, 0.6, 0.8)$. The figure shows the growth in the vorticity thickness of the layer, defined by equation (2.21). For each case a 64×81 grid was used, with $Re = 400$, $L_y = 10.0$ and disturbance amplitude 0.05. Each wave grows until it fills the computational box and saturates. If the computation is allowed to proceed further in time, the behavior shown on figure 4.6, for $M_1 = 0.4$, is obtained. The layer thickness exhibits a damped oscillation in time. Lele [1989] showed that this behavior is associated with a 'nutation' (shape change) of the developed vortex, which also produces sound waves that radiate away from the mixing layer. The final structure is shown in figure 4.7. The vorticity field is reminiscent of the Stuart vortices (Stuart [1967]), and the neutrally stable mode of linear analysis (Michalke [1965a]). The scalar is diffuse, since no new fluid is wrapped around the structure in the nutation phase, only rotation of old fluid.

Another measure of thickness was tested, based on the mass-weighted mean velocity profile:

$$\delta_{\tilde{\omega}} = \frac{1 - U_2}{\left| d(\overline{\rho u}/\overline{\rho})/dy \right|_{\max}} \tag{4.4}$$

Figure 4.8 shows this measure compared with the conventional vorticity thickness, defined by equation 4.4. Two Mach numbers are considered. At $M_1 = 0.2$ there is no difference between the two measures, while at $M_1 = 0.8$ the mass-weighted vorticity thickness has a higher value than the usual vorticity thickness. It is not clear what the significance of this difference is. In all the following simulations the usual vorticity thickness is used.

The growth in energy $E(k_x = 1)$ of the disturbances, computed by equation (3.53), is plotted on figure 4.9. There is initially an exponential growth of the

disturbance energy, a straight line on this semilog plot. This is followed by slower growth with eventual saturation and decay in mode energy.

The effect of Mach number on the developed structure is shown in a series of contour plots of mixture fraction, pressure, vorticity and vorticity divided by density. These are plotted for Mach numbers $M_1 = 0.2$, 0.4, 0.6 and 0.8 on figures 4.10 through 4.13. All such contour plots show equally spaced contours between the maximum and minimum values shown. Dashed contour lines are used wherever a function is negative. Plots of mixture fraction are for $f - 0.5$ and show how fluid from each of the free streams is wrapped into the large-scale structure. The pressure fields show reduced pressure in the vortex cores (at $x = L_x/4$, $y = 0$), and increased pressure (near the isentropic stagnation pressure) at the saddle point ($x = 3L_x/4$, $y = 0$). At $M_1 = 0.2$ the pressure is reduced by 5.9% in the core, relative to the free-stream, and raised by 2.5% at the saddle point. At $M_1 = 0.8$ the reduction in the core is 37.5%, and the rise at the saddle point is 48.7%.

A comparison is made in table 4.1 of the rise in fluid properties at the saddle point, compared to the rise assuming an isentropic stagnation process (Liepmann and Roshko [1957]) from the free-stream to the stagnation point:

$$\frac{T_0}{T_1} = 1 + \frac{\gamma - 1}{2} M_1^2 \tag{4.5a}$$

$$\frac{p_0}{p_1} = (1 + \frac{\gamma - 1}{2} M_1^2)^{\gamma/(\gamma-1)} \tag{4.5b}$$

$$\frac{\rho_0}{\rho_1} = (1 + \frac{\gamma - 1}{2} M_1^2)^{1/(\gamma-1)} \tag{4.5c}$$

where the subscript 0 represents stagnation conditions. The comparison gets better later in the simulation, as the remaining vorticity is moved away from the saddle point by the local strain field. It can be seen that, at least for the cases of equal density considered here, the assumption of an isentropic process to predict fluid conditions at the saddle point is quite good.

Table 4.1 Comparison of computed rise in fluid properties at the saddle point with rise assuming an isentropic process.

M_1	time	$\Delta p/\Delta p_{\text{is}}$	$\Delta \rho/\Delta \rho_{\text{is}}$	$\Delta T/\Delta T_{\text{is}}$
0.2	15.0	0.875	0.791	1.085
0.4	17.6	0.872	0.803	1.049
0.6	24.0	0.882	0.833	1.016
0.8	37.2	0.936	0.844	1.170

The plots of vorticity and vorticity divided by density show a clear change in structure as the Mach number is raised. The vortices become very elongated in the streamwise direction at high Mach numbers. The effect is much more noticeable in the plots of vorticity ω_z, but is still evident in the plots of ω_z/ρ. To understand this change in structure we turn to the compressible vorticity equations (2.29)-(2.31). Terms from these equations are plotted on figure 4.14 for $M_1 = 0.6$. The equation for ω_z has both a dilatational term and a baroclinic term on the right hand side. It was found that for mixing layers with equal free-stream densities the dilatation term was larger by a factor of 3 or 4. This term is plotted on figure 4.14*c*, and shows a quadrupole structure.

A physical explanation of the shape change will now be suggested. A fluid element approaching the structure from the upper left hand side experiences an expanding flow ($\partial u_i/\partial x_i > 0$), and a reduction in vorticity, until it is alongside the vortex. Then the element is subject to a compression ($\partial u_i/\partial x_i < 0$), with an associated increase in vorticity as it approaches the trailing edge of the vortex, and the stagnation region behind. A similar process affects fluid elements approaching from the lower right hand side. The overall effect is to reduce vorticity above and below the vortex, and to increase vorticity in front and behind the vortex, leading to a structure elongated in the streamwise direction.

The same basic structure is found for the baroclinic term, figure 4.14*d*, on the right hand side of the equation for ω_z/ρ. Hence this term leads to elongation of the ω_z/ρ structure in x. For this equation the term on the right hand side, though large enough to cause the elongation effect, is small enough to make ω_z/ρ nearly a conserved quantity. Fluid particles follow more closely the ω_z/ρ contours than the ω_z contours. This is demonstrated by observing that the contours of the mixture

fraction, figure 4.12*a*, which tracks fluid elements during the simulation, show that fluid has been transported around paths resembling the ω_z/ρ contours.

The change in structure can be related to growth rate by considering the efficiency of the various structures at entraining new fluid. Consider the limiting cases of a circular vortex, and a fully elongated vortex. The fully elongated vortex (*i.e.* parallel flow) does not wrap any new fluid around the structure, and it cannot then be engulfed and mixed, and there is only growth by viscous diffusion. The circular vortex wraps fluid from the free-streams around itself, and grows strongly. If we assume a monotonic trend between these two limiting cases then we see that the effect of an elongated vortex structure is to reduce the growth rate of the mixing layer.

4.3 Effect of Mach Number on Pairing

At low Mach numbers the non-linear mechanism by which the mixing layer changes its lateral scale is observed in experiments to be the vortex pairing process (Winant and Browand [1974]). Two simulations were run, at $M_1 = 0.2$ and $M_1 = 0.6$, with an initial Reynolds number of 200, to investigate the effect of Mach number on pairing. The fundamental (F) and first subharmonic ($S1$) wavelengths were included in the initial conditions, with a relative amplitude of 2:1

$$u = \overline{u} + A\ \text{Real}\{\hat{u}_F(y)e^{i(\alpha_F x+\phi)}\} + \frac{A}{2}\ \text{Real}\{\hat{u}_{S1}(y)e^{i\alpha_{S1}x}\} \qquad (4.6)$$

where ϕ is the phase difference between the two modes. Figure 4.15 shows the various options for phase. The case $\phi = \pi/2$ was chosen, since this is the optimum to enhance pairing. The opposite case is when $\phi = 3\pi/2$, which corresponds to a slow tearing process, where one vortex is trapped in the strain field of the subharmonic and is pulled apart. All other phases result in pairing or tearing in various degrees.

The time histories of the vorticity thickness are shown on figure 4.16 and the growth in energy on figure 4.17, for Mach numbers 0.2 and 0.6. The energy plot shows how the fundamental mode grows first and saturates, and then the subharmonic wave takes over. The vorticity thickness is very sensitive to the structure of the flow. Other measures, such as integrated momentum thickness, or visual

thickness, do not show all the detail of the vorticity thickness. Events in the vorticity thickness time history can be related to specific events in the flow. This is illustrated in the following sequence for the $M_1 = 0.2$ simulation.

(1) The fundamental mode grows and saturates. Figure 4.18 shows the mixture fraction, pressure and vorticity at time $t = 9$ during roll-up of the fundamental instability.

(2) After saturation of the fundamental mode, the subharmonic mode grows and two of the primary structures begin to rotate around each other. When the structures have rotated such that when viewed in the x direction they are two separate vortices, there is an event in the vorticity thickness time history. At $M_1 = 0.2$ this occurs at $t = 20$, and is illustrated in figure 4.19.

(3) Rotation continues and the peak in vorticity thickness is reached when the structures lie one above the other. The structure shortly following this, time $t = 24$ is shown on figure 4.20. Now the structure on top is beginning to move downwards, and the two vortices are rotating around each other.

(4) The next event in the vorticity thickness occurs when the vortices once again lie above each other, having rotated by 180°. This occurs at time $t = 27$, and is shown on figure 4.21.

(5) The last point shown here is at time $t = 32$, figure 4.22, where the vortices have rotated all the way around. If the simulation is carried further, the core of the structure continues to rotate and the vorticity thickness continues a damped oscillatory behavior, similar to that found for a single structure (figure 4.5). In practice the next subharmonic would now grow and the process would repeat, beginning with step 2 above.

The same sequence was observed at $M_1 = 0.6$, though the pairing process was slowed both linearly and non-linearly. Figures 4.23 through 4.26 show the structure of the flow at times 16, 29, 37 and 47, corresponding approximately to items 1 to 4 in the above pairing process. If we associate the process between items 1 and 2 as the linear growth of the subharmonic, and the remaining processes as non-linear, then it can be seen from figure 4.16 that both linear and non-linear aspects of pairing are slowed by compressibility. Some delay is expected due to the increase in wavelength of the most amplified disturbances as Mach number is increased. A simulation was therefore performed at $M_1 = 0.2$ with the same wavelengths as the

$M_1 = 0.6$ case. Figure 4.27 shows the growth rate comparison with wavelength effects removed, showing that both linear and non-linear growth is indeed slowed by compressibility.

The slowing of the growth of the initial stage of pairing is accounted for by the effect of Mach number in reducing the linear amplification rate of the subharmonic disturbance. There are several possible reasons for the reduction in growth rate in the non-linear region: (i) the shape of the pairing vortices has changed, and the more elongated structures may be less inclined to pair, (ii) the delay in the Biot-Savart type of vortex induction process, due to the finite sound speed, may make the pairing process less efficient, and (iii) continued compressibility effects due to dilatational and baroclinic torques may be slowing the rotation of the vortices around each other. It is not clear from the current study which of these effects is dominant, or whether they are all important.

The pairing involves a displacement of the vortices into the free-stream, which distorts the streamlines outside the vortical region, and creates regions of locally high velocity. During the pairing at $M_1 = 0.6$ it was found that for a short period of time, around the peak in the vorticity thickness curve, there was a region of supersonic flow above and below the structures, although this did not persist long enough to generate shock waves. At any higher Mach number shock waves would certainly form during the two-dimensional pairing. It is interesting to note the evidence that the flow would prefer not to have shock waves. Lele (private communication [1988]) has shown that tearings may be more common at higher Mach numbers, and Ragab and Wu [1989] have shown that a helical pairing may be preferred even as low as $M_1 = 0.4$. This, and the tendency toward three-dimensional structures at high Mach numbers (see Chapter 5), seems to indicate that the flow will try to avoid generating shock waves if at all possible. However, there is no general theory to predict why this is so.

4.4 Two-Dimensional Structure

In this section the two-dimensional structure, under the influence of compressibility, is explored. The evolution of the vorticity and scalar fields at this Mach number have already been described in section 4.2. Here we consider the behavior of other fluid properties, such as stagnation enthalpy, entropy, and strain rate.

Contours of temperature at $M_1 = 0.6$ are shown on figure 4.28*a*. They show high temperature at the stagnation point in the braid, and lower temperature in the vortex core. The stagnation enthalpy for a perfect gas with constant specific heats is given by:

$$H^* = c_p^* T^* + \frac{u^{*^2} + v^{*^2}}{2} \tag{4.7a}$$

and non-dimensionally:

$$H = \frac{c^2}{(\gamma - 1)} + \frac{u^2 + v^2}{2} \tag{4.7b}$$

A contour plot of H is shown on figure 4.28*b*. The stagnation enthalpy is lowest in the vortex core, and remains approximately constant in the rest of the flow. This effect can be understood by considering an inviscid, non-conducting form of the energy equation (Liepmann and Roshko [1957]).

$$\frac{DH}{Dt} = \frac{1}{\rho}\frac{\partial p}{\partial t} \tag{4.8}$$

In the cores of the structures during roll-up the pressure is reducing with time, so a fluid particle being wrapped around the developing structure experiences decreasing pressure, and by equation (4.8) the stagnation enthalpy drops. In situations where the two free streams have different stagnation enthalpies the reduced H in the core is overshadowed by the mean H profile.

The entropy of the flow (non-dimensionalized as $s = s^* T_1^* / U_1^{*^2}$ since e is normalized by $U_1^{*^2}$), relative to the free-stream 1, is defined by

$$s = \frac{\ln T}{\gamma(\gamma - 1)M_1^2} - \frac{\ln \rho}{\gamma M_1^2} \tag{4.9}$$

A contour plot is shown on figure 4.28*c*. The entropy structure is similar to the vorticity, with high entropy found in the center of the vortex. The assumption of an isentropic process from the free streams to the saddle point can be seen to be valid for free-streams with equal entropy.

Strain rate in the flow is of interest from two perspectives. Firstly, because it strongly affects the development of streamwise vorticity in the flow, and strain rate near the saddle point can lead to the 'collapse' of streamwise vorticity into streamwise vortices (Lin and Corcos [1984]). This produces mushroom structures in the scalar field, observed experimentally by Bernal and Roshko [1986]. Secondly, strain rate is of interest when applications to combustion are considered. If the strain rate is too high in any region of the flow then any flame that forms may be quenched, and reactions generating heat release may be prevented. Unlike incompressible flow, the strain rate tensor is not trace-free and there are alternative ways to document the strain rate magnitude. The usual definition of strain rate tensor is

$$S_{ij} = \frac{1}{2}(u_{i,j} + u_{j,i}) \tag{4.10}$$

An anisotropic strain rate tensor can also be defined (Reynolds [1988]):

$$S^a_{ij} = S_{ij} - \frac{S_{kk}\delta_{ij}}{3} \tag{4.11}$$

The magnitudes of the strain rates for each case are defined by:

$$|S| = \sqrt{S_{ij}S_{ij}} \tag{4.12}$$

$$|S^a| = \sqrt{S^a_{ij}S^a_{ij}} \tag{4.13}$$

For the simulations presented here it was found that the high strain rate regions in the flow were not associated with regions of high dilatation, so the values for peak strain rate magnitude were not affected by choice of equation (4.12) or (4.13). At different times in the simulation for $M_1 = 0.6$ contour plots of the strain rate field are shown on figures 4.29 and 4.30, and slices through the flow at various x locations are shown on figure 4.31. It can be seen that the usual picture of strain rate, high in the braid regions and low in the cores, is observed at time $t = 18.2$ during the early stage of roll-up. However at later times, *e.g.* at $t = 24.0$, figure 4.31*b*, the strain rate peak in the braid is not dominant, and regions of high strain rate are also found within the vortex core.

For combustion application, it would be useful to be able to model the magnitude of the peak strain rate in the flow. The time history of the peak strain rate is shown

on figure 4.32. When normalized by the initial vorticity thickness and free-stream velocity, the strain rate is seen to decrease during the simulation. When the strain rate is renormalized by the local vorticity thickness and velocity difference, shown on curve 2 of figure 4.32, we find that the strain rate increases slightly during roll-up, and then declines. In the latter case the non-dimensional peak strain rate is always of order unity, so that peak strain rate in the mixing layer can be modeled by the ratio of the free-stream velocity difference to the local vorticity thickness.

4.5 Effect of Density Ratio

Most compressible mixing layer experiments are performed for free-streams with unequal densities. Additional baroclinic torques can appear in the flow, especially in the braid region where the two free-streams are brought close together and steep density gradients are formed. To investigate these effects, two simulations are compared; one has free-streams of equal density, and the other has a density ratio $\rho_2 = 0.5$ ($T_2 = 2$).

The simulations are run at $M_c = 0.6$, with a Reynolds number of 400. To check the convective velocity formula, we arrange U_2 so that the predicted convective velocity is zero. For the density ratio of 0.5, this means setting $U_2 = -\sqrt{2}$. The velocity profile is then obtained from the error function as:

$$\overline{u} = \frac{1}{2}\Big[1 + U_2 + (1 - U_2)\mathrm{erf}(y\sqrt{\pi})\Big] \tag{4.14}$$

The temperature profile is obtained from the velocity profile in the usual way (equation (2.13)).

The growth in vorticity thickness for each simulation is shown on figure 4.33, and the growth in integrated energy $E(1)$ (the fundamental mode), on figure 4.34. The plots of $E(1)$ show that the simulations start from a different origin. This is simply a reflection of differences in the shape of the eigenfunctions, since the normalization is done by amplitude of the u eigenfunction, and not by integrated energy. The developed structure is shown on figure 4.35, and can be compared with the simulation for uniform density shown on figure 4.12. It can be seen that there is generation of vorticity with the opposite sign to that of the dominant roll-up, which

can be explained by considerations of the baroclinic torque acting in the saddle-point region of the mixing layer. A sketch of the saddle region is shown on figure 4.36. In region 1 the gradients of pressure and density are nearly perpendicular to each other and application of a right hand rule shows that clockwise vorticity (positive in the current definition) is produced. This is then convected away from the saddle point by the local strain rate field, and becomes wrapped around the structure to the left. In region 2 the pressure and density gradients act to produce vorticity with the opposite sign to the main roll-up (anti-clockwise), which becomes wrapped around the structure to the right. The counter-clockwise vorticity does not produce *vortices* of the opposite sign, it merely modifies the path of fluid particles rotating around the main structure, and results in a more asymmetric scalar field.

A simulation was run with a density ratio of 0.2 to investigate the U_c formula (1.2), compared with the predictions of the linear instability theory. For this case ($T_2 = 5$, $U_2 = -\sqrt{5}$) the convective velocity formula predicts zero convective velocity, whilst from the linear theory the phase speed of the growing wave is 0.05 and the phase speed of the neutral mode is 0.16, which are both very definitely non-zero. The developed structure is shown in figures 4.37. The scalar field is highly asymmetric due to the baroclinic terms. Figure 4.38 shows the initial and final pressure contours. Initially the pressure minima is at $x = L_x/4$ and the pressure maxima is at $x = 3L_x/4$. At the later time the pressure minima has moved to $x = L_x/2$ and the pressure maxima is at $x = L_x/6$. The structure has moved to the right. The approximate convective velocity, based on the movement of the stagnation point (a peak in pressure) is 0.15. It is 0.12 based on the movement of the minima of pressure in the vortex core. The reason for the difference is that the structure is evolving and the convective velocity changes depending on which feature of the flow we look at. These rough estimates agree better with the phase speed of the neutral mode than with the U_c formula (1.2), which would predict no convection.

4.6 Embedded Shock Waves

In two-dimensional simulations above a convective Mach number of 0.7 it was found that shock waves developed in the flow. Pressure contours for a simulation at $M_1 = 0.8$ at a Reynolds number of 400 are shown on figure 4.39*a*, and show the location of the shock waves. Local Mach contours are shown on figure 4.39*b*.

Flow around the top of the vortex is accelerated to supersonic speeds, and then has to stagnate at the saddle point in the braid. It does this by compression through a weak ($M_{\max} \approx 1.2$) near-normal shock wave. The process is similar to the flow around a transonic airfoil. The same process occurs for the lower stream moving from right to left below the vortex. Profiles of pressure, density and temperature through the shock wave are shown on figure 4.40. They show that for this flow condition the shock wave is adequately captured by the numerical method, using a grid with 192 points in the streamwise direction.

The computational problem is that at lower Reynolds numbers (*e.g.* 200) the roll-up of the vortex is not strong enough to generate a shock wave (*i.e.* we are in a viscous regime), while at higher Reynolds numbers the shock is stronger, and thinner, so that a prohibitively large number of modes are required to resolve it properly. During an earlier phase of this project, TVD (Total Variation Diminishing) numerical methods were tested for mixing layer flows. These numerical methods are of the shock-capturing genre (Yee [1989]), and were found to do a good job of capturing the shock waves, no matter how strong, without encountering numerical difficulties. However, this shock capturing capability is obtained by introducing extra dissipation in regions of the flow where oscillations develop. This extra dissipation also tends to damp out the growth of the large-scale structure in the flow. It was found that with the TVD schemes a large number of grid points were required in order to capture the instability correctly (Sandham and Yee [1989]). Neither spectral methods (relying on shock resolution), nor TVD methods (shock capturing) were found to be efficient for flows involving both shock waves and growth of instabilities.

A model two-dimensional large-scale structure with shock waves has been proposed by Papamoschou [1989], and separately by Dimotakis [1989], to explain some of Papamoschou's experimental results concerning convective velocities. (An alternative explanation of the results using linear stability theory was presented in section 2.4.) The shock waves proposed by Papamoschou are strong and are inclined to the streamwise direction, so that there is a large entropy rise through the shock wave. This breaks the symmetry in the convective velocity formula, and was offered as an explanation of the experimental finding that convective speeds are biassed towards one free-stream speed or the other (Papamoschou [1989]). The model structure made no prediction of the angle or strength of the shock waves. However, the shocks observed in the current work were always weak, nearly normal

to the streamwise direction, and were found on both sides of the vortices. Thus, they are not reminiscent of the model shock structure proposed by Papamoschou and by Dimotakis.

4.7 Simulation of Supersonic Mode Instability

The 'radiating vorticity' modes of instability, supersonic with respect to one of the free-streams, are the most amplified modes in two dimensions above a convective Mach number of approximately 1 (see section 2.2.4). Although we expect three-dimensional modes to be dominant at these Mach numbers, it is interesting to simulate the non-linear development of these modes, which might be excited in experiments by strong two-dimensional forcing of the mixing layer.

The time-developing mixing layer with equal densities at a Mach number of 1.05 was chosen for simulation. The Reynolds number was fixed at 800, which is just high enough so that the inviscid eigenfunction is amplified. The high Reynolds number necessary for simulation of this weak instability means that shock waves cannot resolved, since these will be very thin. The computations have to be stopped as soon as shock waves form.

The mode that is supersonic with respect to the lower stream was simulated. The other mode, supersonic relative to the upper stream, will have the same behavior. From the linear stability theory the amplification rate of this mode is 29% of the amplification rate of the most amplified three-dimensional wave (angle 56°).

The growth in vorticity thickness and energy $E(1)$ for this supersonic mode are shown in figures 4.41 and 4.42 respectively. Contours of relevant features are shown on figure 4.43 at time $t = 82$. We see that roll-up does occur, so that this is indeed a 'vortical' instability mode, which can act to mix fluid from the two streams. However, the roll-up is very weak and takes a long time to develop. The structure, shown for example in the contours of density on figure 4.43*b*, seems to reside on the upper side of the mixing layer, and the contours of mixture fraction show that the cores of the structures are mostly fluid from the upper stream, *i.e.* the stream that is subsonic relative to the structure. The pressure contours, figure 4.43*c*, show clearly the radiating nature of the instability. On the upper side we have the usual picture of pressure: high at the stagnation point and low in the vortical structure. However

on the lower side, where the free-stream is supersonic relative to the structure, we find an arrangement of expansion and compression waves. The compression waves develop into shock waves during the simulation. At a later time $t = 92.5$ the structure, shown on figure 4.44, has developed shock waves which can no longer be resolved on the computational grid; oscillations can be observed in the pressure contours in the lower left corner of the plot.

The presence of walls in experiments would cause the waves to reflect back into the shear layer. Such a mechanism lies at the heart of the wall-modes and Mack modes proposed by other authors (Greenough *et al.*[1989], Mack [1989]), though is is not clear that those modes are vortical modes that could act to mix fluid. In any case, as long as the walls aren't too close, the three-dimensional instability is more amplified, and this is the subject of the next chapter.

4.8 Chapter Summary

The main effect of compressibility in two-dimensional simulations is to damp the growth of the instability, both linearly and non-linearly. As Mach number is increased the developed vortical structure becomes elongated in the streamwise direction and less efficient at wrapping new fluid into the mixing layer. The pairing process is also slowed by compressibility. For convective Mach numbers above 0.7 we find weak shock waves developing in the flow.

Above a convective Mach number of 1 the only unstable two-dimensional modes in the mixing layer are the weakly amplified supersonic modes. Simulation of these modes showed that the structures developing from these instabilities are weakly vortical, and are able to mix fluid. The structures are supersonic relative the one of the free-streams, and on that side a pattern of shocks and expansion fans forms.

CHAPTER 5

Three-Dimensional Simulations

In this chapter simulations are presented of the three-dimensional instabilities, which are expected to dominate the mixing layer at high Mach number. The large-scale structures which develop from the non-linear growth of these instabilities are analyzed.

5.1 Initial Conditions and Parameters

The time-developing mixing layer is again chosen for simulation. The initial mean flow is the same as for the two-dimensional simulations of Chapter 4, with the mean velocity given by equation (4.1) and the mean temperature by equation (2.13).

Three Mach numbers were selected for detailed study. A free-stream Mach number $M_1 = 0.4$ was chosen as a low Mach number where we expect to find near-incompressible behavior. An intermediate Mach number was chosen to be $M_1 = 0.8$. At this Mach number an oblique wave is slightly more amplified than the two-dimensional wave, and a broad range of waves in between are about equally amplified. Mach number $M_1 = 1.05$ was selected as the high Mach number case for study.

The instability characteristics of the flow change around a convective Mach number of 1. Just below $M_c = 1$ the two-dimensional wave, though no longer the most amplified wave, is still only a factor of about 2 less amplified than the most amplified wave, and may still be expected to have an effect on the development of the flow. Above $M_c = 1$ the two-dimensional wave is much more weakly amplified than the oblique waves, and the flow is expected to be dominated by a narrow band of oblique waves. This change is illustrated on figure 5.1, where the linear amplification rate is plotted as a function of angle at Mach numbers $M_1 = 0.95$ and 1.05 for the time-developing mixing layer with equal free-stream densities. The simulation at $M_1 = 1.05$ is expected to be typical of higher Mach number mixing layers, since

the only further change in the stability characteristics of the flow is the increasing obliquity of the most amplified disturbances.

The Reynolds numbers for the simulations were chosen by considering the effect of viscosity on the growth rate of an eigenfunction from inviscid linear stability analysis. Figure 5.2 shows the effect of Reynolds number on the amplification rate for three different oblique waves: a 45° wave at $M_1 = 0.4$, a 45° wave at $M_1 = 0.8$, and a 60° wave at $M_1 = 1.05$. The latter two are expected to be the most amplified waves at their respective Mach numbers. Ideally, we would like to be at the high Reynolds number end of these curves in order to capture the inviscid nature of the instabilities. The Reynolds number was selected to be 400, 600 or 800 for the Mach numbers 0.4, 0.8 and 1.05 respectively. The problem with simulating high Mach number flows is the higher Reynolds numbers that are required to capture the instability. The higher the Reynolds number the more modes are required later in the simulation in order to resolve the flow. For this reason the highest Mach number simulated was 1.05.

The three-dimensional simulations presented in this chapter were all run for a Prandtl number of 1 and a Schmidt number of 1. Initial perturbations were usually specified as eigenfunctions from the linear stability analysis. However, some simulations (sections 5.4 and 5.6) were performed with random initial conditions, to check that the most amplified waves were indeed those predicted by linear stability analysis. The simulations were usually started on a $16 \times 99 \times 16$ grid, with boundary conditions applied at $y = \pm 5$ initial vorticity thicknesses away from the mixing layer centerline. As the high wavenumbers gained energy the number of points used in x and z was extended, ending at typically $96 \times 99 \times 96$.

5.2 Simulations at Low Mach Number

At $M_1 = 0.4$ we expect to get nearly incompressible behavior. This case therefore partially serves as a check on the code, comparing against previous incompressible mixing layer simulations and against incompressible secondary stability theory. However, some compressibility effects may be evident even at this low Mach number since Ragab and Wu [1989] found some changes from incompressible secondary stability behavior at $M_1 = 0.4$.

The major work in secondary stability analysis for the incompressible mixing layer is that of Pierrehumbert and Widnall [1982]. They used Stuart [1967] vortices as the base flow and solved the resulting Floquet problem for both fundamental and subharmonic instabilities. The fundamental instabilities were of the core 'bulging' or core 'translative' kinds, while the subharmonic instabilities were either regular pairing or a 'helical pairing'. Simulations of all these instabilities can be made by choosing an initial disturbance field of a two-dimensional wave, and two equal and opposite oblique waves.

The fundamental mode instabilities have the same streamwise wavelength as the initial roll-up. The initial disturbance field is specified by:

$$u' = A_1 \mathrm{Real}\{\hat{u}(\alpha,0)e^{i(\alpha x+\phi)}\} + A_2 \mathrm{Real}\{\hat{u}(\alpha,\beta)e^{i(\alpha x+\beta z)} + \hat{u}(\alpha,-\beta)e^{i(\alpha x-\beta z)}\} \tag{5.1}$$

where $\hat{u}(\alpha,\beta)$ is an eigenfunction of the linear instability wave with streamwise wavelength $L_x = 2\pi/\alpha$ and spanwise wavelength $L_z = 2\pi/\beta$. Similar disturbances are added for ρ', v', w' and T'. The phase of the oblique waves relative to each other is not important, since this does not change the basic pattern of the addition of two oblique waves, only translating it in space. However the phase, ϕ, of the two-dimensional wave relative to the pair of oblique waves is important.

With the phase $\phi = 0$ we get the 'bulging' mode of Pierrehumbert and Widnall [1982]. The structure of the initial field for this case can be shown by a cut through the x–z plane at $y = 0$, figure 5.3. Pressure contours are shown on figure 5.3*a* and contours of ω_x, ω_y and ω_z on figures 5.3*b*-*d* respectively. The pressure minima, which shows where the core of the vortical structure will form, is at $x = L_x/4$, and is fairly uniform across the span. The contours of ω_x and ω_y show a pattern of counter-rotating vortices, resulting from the addition of the two equal and opposite oblique waves. For these plots the sign of vorticity has been chosen so that clockwise motion is shown with solid contours and counter clockwise motion with dashed contours. It can be seen that the effect of these vortices is to distort the core of the two-dimensional instability and give it a varying cross-sectional area in the spanwise direction.

With the phase ϕ changed to $\pi/2$ we get the 'translative' mode of Pierrehumbert and Widnall [1982]. The initial condition is shown on figure 5.4. Now the primary roller is at $x = 0$, which coincides with a peak in both streamwise and vertical

components of vorticity. The effect is to make the pressure minima oscillate in the spanwise direction, alternately forcing it forwards or backwards.

Direct simulations were made for both the bulging and translative modes at $M_1 = 0.4$. The Reynolds number was set to 400 and the disturbance amplitudes were $A_1 = 0.05$ and $A_2 = 0.025$ (equation (5.1)). The angle for the most amplified disturbance from Pierrehumbert and Widnall was 56.3°, but the variation with angle was weak. It was found that at this angle and Reynolds number the initial instability wave was damped. A smaller angle is needed in order to get a disturbance that grows on the mean flow and 45° was selected. Plots of the vorticity thickness growth for the two simulations are shown on figure 5.5, and the time history of the energy E (equation (3.53)) is shown on figure 5.6 for the bulging mode and on figure 5.7 for the translative mode. Modes are defined by (k_x, k_z) where k_x and k_z are integer wavenumbers in the x and z directions. Mode $(1,0)$ is the two-dimensional wave, and $(1,1)$ and $(1,-1)$ are the two oblique waves. For these simulations the oblique waves are equal and opposite, and grow in exactly the same way. There is a line of symmetry in the simulations at $z = L_z/2$, the preservation of which serves as another check on the code. Comparison of figures 5.6 and 5.7 shows that the $(1,0)$ mode is unaffected by its phasing relative to the oblique waves. However the growth of the three-dimensional waves is much stronger for the phase $\phi = \pi/2$ than for $\phi = 0$, which agrees with Pierrehumbert and Widnall's finding that the translative mode of instability is more amplified than the bulging mode.

The best method that was found for identification of rotational regions in the flow was to search for a local minima in pressure. Perspective views of a surface of constant pressure, enclosing a region of low pressure, are shown on figures 5.8 and 5.9 for the bulging and translative modes respectively. The bulging mode appears to be only weakly unstable, and the developed structure is very two-dimensional. The translative mode results in a vortex core that oscillates in the spanwise direction.

The fate of the streamwise and vertical vorticity initially in the saddle point region of high strain between two large spanwise rollers is of much interest, since Lin and Corcos [1984] showed that straining of vorticity in this region can lead to the formation of streamwise vortices. These vortices produce mushroom-like structures in a scalar field, as observed in experiments by Bernal and Roshko [1986]. For the initial condition of the bulging mode (figure 5.3) the saddle point lies between two of the regions of streamwise vorticity. Development of the primary roller creates

a straining in this region, which pulls the streamwise and vertical vorticity away from the saddle point. A perspective view of the developed streamwise vorticity is shown on figure 5.10, corresponding to the pressure field of figure 5.8. There is no streamwise vorticity in the saddle region, and the streamwise vorticity from the initial condition has been pulled away from the saddle point towards the vortex core.

In the initial condition for the translative mode (figure 5.4) there is streamwise and vertical vorticity centered on the saddle point (located by the pressure peak at $x = L_x/2$). Now the straining field acts to pull this vorticity into long thin regions of vorticity (the braids). If the initial vorticity is strong enough Lin and Corcos [1984] predict a 'collapse' of the streamwise and vertical vorticity into vortices aligned with the principal axis of strain. This effect has been confirmed in the incompressible numerical simulations of Rogers and Moser [1989]. Figure 5.11 shows the streamwise vorticity for the structure that develops from the translative instability at $M_1 = 0.4$. The vorticity has indeed become elongated in the saddle region, but for this initial condition there has been no collapse into the near-circular vortices of Lin and Corcos. A higher amplitude of initial disturbances would be required in order to get these structures.

The subharmonic instabilities of Pierrehumbert and Widnall [1982] are those with wavelength twice that of the primary roll-up. The two-dimensional subharmonic instability is the two-dimensional pairing process, described in section 4.3 of this work. The other subharmonic instability was labeled a 'helical pairing' by Pierrehumbert and Widnall, and has not been simulated numerically before. This mode can be obtained by the following combination of instability waves:

$$u' = A_1 \text{Real}\{\hat{u}(2\alpha, 0) e^{i(2\alpha x + \phi)}\} + A_2 \text{Real}\{\hat{u}(\alpha, \beta) e^{i(\alpha x + \beta z)} + \hat{u}(\alpha, -\beta) e^{i(\alpha x - \beta z)}\} \tag{5.2}$$

The computational box length is $L_x = 2\pi/\alpha$ and the box width is $L_z = 2\pi/\beta$. The initial field with phase $\phi = \pi/2$ is shown on figure 5.12. The spanwise vortices are located by the pressure minima at $x = 0, L_x/2$. The 'helical' instability occurs when the streamwise and vertical vorticity from the oblique waves is superimposed on the centers of these structures. At $z = L_z/2$ the left structure is lifted and moved to the right, while the right structure is pushed down and moved to the left. At $z = 0$ the situation is reversed.

A 'helical' pairing simulation was run with an initial Reynolds number of 200, a box size of $L_x = L_z = 15.7$ (*i.e.* the 45° oblique subharmonic wave was excited), and boundaries at $y = \pm 10$. The growth in vorticity thickness is shown on figure 5.13 and the growth in mode energies on figure 5.14. Mode $(2,0)$ is the two-dimensional fundamental wave, and modes $(1,1)$ and $(1,-1)$ are the oblique subharmonic waves. The structure after roll-up of the primary instability is shown as a perspective view of pressure on figure 5.15. The two vortices have been perturbed by the action of the oblique waves. At a later time the structure is shown on figure 5.16. The perturbation shape has developed into strong oscillation of the vortices in the spanwise direction. However, contrary to Pierrehumbert and Widnall's interpretation, we find no evidence for rotation of the two vortices around each other, in other words no *merging* by pairing. Instead the flow has *evolved* into a subharmonic structure, with wavelength twice that of the original roll-up. The final structure resembles the hairpin structures found in wall boundary layer transition, though here there is an antisymmetry between the upper and lower parts of the vortex tubes, and there are 4 heads and 4 legs per periodic structure. Near the head of the hairpins there is an induced motion due to the legs, which will tend to pull the structure into a more upright orientation, and will oppose any tendency to rotate around neighboring structures. This prevents the 'helical' instability becoming a 'helical pairing'. The presence of any two-dimensional wave would eventually lead to pairing, but if the time to reach this pairing is long compared to the time taken for the next stage of instability to develop we may see structures similar to those on figure 5.16.

Cuts through the mixture fraction and pressure fields at the plane $y = 0$ are shown on figure 5.17. The final structure found here is very similar to that which will be presented for high Mach number flows in section 5.5. The difference is that here the oblique waves grow on a base flow of developed spanwise rollers, whereas in section 5.5 the oblique waves grow on the unperturbed mean flow.

Evidence for the existence of these structures in experiments is slim, but a 'helical' structure was claimed to have been observed by Chandrsuda *et al.* [1978], which may have been due to an underlying structure like the one in figure 5.16. For incompressible flows this instability is less amplified than the classical two-dimensional pairing, so it may only be found in experiments with high levels of background noise, where local disturbances might excite its development. However, the secondary stability analysis of Ragab and Wu [1989] shows that this mode can

become important when compressibility is included, and may be important down to $M_1 = 0.4$.

5.3 Effect of Mach Number

Most of the three-dimensional effects observed in experiments were captured in the simulations of the translative mode of instability in the previous section. It was therefore decided to use this combination of instability waves to investigate the effect of Mach number. Three simulations were made, at Mach numbers $M_1 = 0.4$, 0.8 and 1.05, with Reynolds numbers 400, 600, 800 and box lengths corresponding to the most amplified wavelengths of $L_x = 7.85$, 13.37, 18.48 and $L_z = 7.85$, 13.37, 12.465 respectively. The angles of the oblique instability waves were 45° for the $M_1 = 0.4$ and 0.8 cases, and 60° for the case $M_1 = 1.05$. The wave combination was the fundamental two-dimensional wave and two equal and opposite oblique waves with the same wavelength. The amplitudes were chosen to be $A_1 = A_2 = 0.025$ (equation (5.1)), with $\phi = \pi/2$.

The effect of Mach number on the growth of the mixing layer is shown on figure 5.18. The growth in the energy for the amplified waves is shown on figures 5.19 through 5.21. At $M_1 = 0.4$ it can be seen that the $(1,0)$ wave is the most amplified initially and is always more energetic than the oblique waves. At $M_1 = 0.8$ the oblique waves $(1,1)$ and $(1,-1)$ are slightly more amplified than the two-dimensional wave and, although they start with slightly less energy, they soon overtake the $(1,0)$ wave. Again the linear behavior persists in the non-linear regime and the oblique waves have a higher energy content in the developed structure than the two-dimensional waves, although at this intermediate Mach number both two-dimensional and oblique waves are important. At the highest Mach number, $M_1 = 1.05$, the oblique waves have a much larger growth rate than the two-dimensional waves and by the end of the simulation the energy content of the $(1,1)$ and $(1,-1)$ modes is one and a half orders of magnitude higher than the $(1,0)$ mode.

In each of the simulations the linear theory correctly predicts the initial growth rate of the instability waves. The most amplified wave is also the most important wave in the developed structure. The dominance of oblique waves at high Mach

numbers, predicted by the linear stability theory, extends to the non-linear regime in the simulations studied here.

To illustrate the resolution of these simulations the energy content of all the modes is shown in carpet plots of $E(k_x, k_z)$ at the $y = 0$ plane (the mixing layer centerline) on figures 5.22 through 5.24 for Mach numbers 0.4, 0.8 and 1.05. The drop off in energy from the most energetic wave to the highest wavenumbers was kept to about 8 orders of magnitude by increasing the resolution during the simulations. When the highest wavenumbers became important the simulations had to be stopped. The plots are shown for the last time step in the simulation, when the resolution was considered to be adequate.

The high frequency part of these spectra should not be mistaken for small eddies in the flow. These high wavenumbers arise from the Fourier representation of the large structures in the flow; a steep gradient at some point in the structure requires many Fourier modes to resolve it. For example, a purely two-dimensional flow would have energy only along the $k_x = 0$ line. At low Mach number the carpet plot (figure 5.22) shows oblique ridges, due to oblique steep gradients that need to be resolved. The plots at higher Mach numbers (figures 5.23 and 5.24) show the development of ridges in the k_z direction, along the $k_x = 0$ line. These indicate the presence of steep spanwise gradients in the flow.

Low pressure regions are associated with strong rotation. Perspective views of a pressure surface, that encloses a minima of pressure, are shown on figure 5.25 for $M_1 = 0.4$ and on figures 5.27 and 5.28 for Mach numbers 0.8 and 1.05, and show the change in large-scale structure in the flow as Mach number is increased. At $M_1 = 0.4$ we have the translative mode discussed in the previous section, with the vortex tube oscillating in the spanwise direction. Again we have pre-collapse streamwise and vertical vorticity in the saddle region between adjacent rollers, shown by the surface of streamwise vorticity on figure 5.26.

At $M_1 = 0.8$ (figure 5.27) we find a weakening of the spanwise structure, and the development of oblique vortices in the saddle point region where at lower Mach numbers the streamwise braid vortices would form. By $M_1 = 1.05$ (figure 5.28) we find that the two-dimensional mode has all but vanished, and we are left with a pattern of four regions of rotating fluid. There is one pair of equal and opposite oblique vortices in the region where the spanwise vortex was located at lower Mach

number ($x = 0$), and another pair of counter-rotating vortices, with opposite sense to the first two, in the region of the low Mach number saddle point ($x = L_x/2$).

The essential change in structure is shown on figures 5.29 through 5.31, where two vortex lines (lines tangent to the local vorticity vector) per structure are plotted. At low Mach number one of these lines is the spanwise structure, while the other weaves back and forth and appears as the streamwise vortices in the saddle point region. At higher Mach number both vortex lines have a zig-zag structure, or a 'double hairpin with peak-valley splitting' structure, using boundary-layer terminology. The pressure minima in figures 5.27 and 5.28 show the positions along the vortex lines where there is strong rotation taking place. At other regions, for example near the heads of the hairpins, there is very little rotation of fluid taking place. The presence of a vortex line in this region should not be mistaken for the presence of a vortex.

The sense of rotation of the vortices is always clockwise if a cut through the $x-y$ plane is considered, which can be clearly seen in the mixture fraction field. Cuts through the pressure and mixture fraction fields at the plane $y = 0$ are shown on figure 5.32 for $M_1 = 0.4$ and on figures 5.33 and 5.34 for $M_1 = 0.8$ and $M_1 = 1.05$ respectively. Fluid from below the mixing layer being moved upward appears as a local minima in the mixture fraction, and vice versa for fluid from above being moved down. To enhance the effect contour plots are made with 0.5 subtracted from the mixture fraction, which lies between 0 and 1. Negative values are shown with dashed contours, labeling fluid from below the mixing layer which has been moved upwards. Positive values are shown with solid contours and show fluid from above that has been moved downwards.

The effect of Mach number on the bulging mode is now considered. At low Mach numbers this mode was not important, while at high Mach numbers the structure is expected to develop from oblique instability waves alone, with no effect from the relative phase of any two-dimensional mode. At the intermediate Mach number $M_1 = 0.8$ a simulation was run with phase $\phi = 0$ (equation (5.1)). The growth in vorticity thickness and mode energies for this simulation are shown on figures 5.35 and 5.36, and the developed structure on figure 5.37. As with the other simulation at this Mach number the oblique waves are the most amplified instability waves through both the linear and non-linear stages of roll-up. The final structure, though different in detail, is just as three-dimensional as that which developed with phase $\phi = \pi/4$. It also contains oblique inclined vortical regions. It is concluded that at

intermediate Mach numbers the phase of the two-dimensional wave relative to the oblique waves has an effect on the final structure. However the trend towards more three-dimensionality at higher Mach numbers is not affected.

5.4 Simulations with Random Initial Conditions

The purpose of these simulations is to check that the linear stability theory is correctly predicting the most amplified waves in the flow, and to check for the presence of modes other than those found in the linear analysis. The box length was chosen to be 40 initial vorticity thicknesses in both the x and z directions, which is long enough to allow approximately 5 of the most amplified waves to grow at Mach number $M_1 = 0.4$, or 3 waves at $M_1 = 0.8$, or about 2 waves at the highest Mach number $M_1 = 1.05$. The initial condition was specified by adding a small random number to each of the computational variables $Q = (\rho, \rho u, \rho v, \rho w, e)$ at each mesh point. For example

$$\rho(x, y, z) = \rho(x, y, z) + Are^{-y^2} \tag{5.3}$$

where r is a random number uniformly distributed between -0.5 and 0.5, and the amplitude A was set to 0.0001. The exponential term is used to ensure that the disturbances decay to zero in the free-stream. The random numbers were initially applied to a $16 \times 33 \times 16$ grid, which was then extended to $32 \times 33 \times 32$ so that random numbers in the highest frequency modes could not alias back and affect the growth rates of low wavenumber modes.

The simulations were run for the same conditions as in the previous section *i.e.* at $M_1 = 0.4$ ($Re = 400$), $M_1 = 0.8$ ($Re = 600$) and $M_1 = 1.05$ ($Re = 800$). The simulations were run through the linear regime of small disturbance growth. During this time the mean flow changes by viscous diffusion. This is illustrated by the variation in vorticity thickness during these simulations, shown on figure 5.38. The mean flow sets the length scale for the growth of small disturbances, so the variation in the mean flow means that different wavelength disturbances are more rapidly amplified at different times during the simulations. Specifically, longer wavelengths will become more rapidly amplified as the simulations proceed, which needs to be kept in mind when analyzing the results.

The growth in energy $E(k_x, k_z)$ for selected modes is shown on figures 5.39 though 5.41 for the Mach numbers $M_1 = 0.4$, 0.8 and 1.05 respectively. At $M_1 = 0.4$ the growth of the two-dimensional modes is plotted. Initially the $(5,0)$ mode is the most amplified of those shown, in agreement with linear stability theory. However, by the end of the simulation, when the layer has grown by viscous diffusion, the $(3,0)$ mode is the most amplified. Modes with wavelengths longer than the initially most amplified wavelength have growth rates that increase with time, whereas modes with shorter wavelengths have growth rates that diminish with time. At $M_1 = 0.8$ the $(3,4)$ mode is more amplified than the $(3,0)$, $(3,2)$ for $(3,6)$ modes. At $M_1 = 1.05$ the $(2,4)$ mode is the most amplified wave, growing more strongly than the $(2,0)$, $(2,2)$ or $(2,6)$ modes. Both these results are in general agreement with the linear stability result that the most amplified waves satisfy $M_c \cos\theta = 0.6$.

The final flowfield at $M_1 = 0.4$ is shown on figure 5.42 by plotting a single contour of zero vertical velocity in the $x - z$ plane at $y = 0$. This contour divides fluid moving upwards from fluid moving downwards and gives an idea of the dominant structures in the flow. Clearly there is a preference for structures oriented in the spanwise direction, though there is no strong coherence.

The lack of the strong coherence exhibited here at $M_1 = 0.4$, compared to incompressible experiments, may have many causes. In the simulations all waves $(0,0)$ through $(7,7)$ and $(7,-7)$ were seeded, so there are many waves with approximately the correct orientation to grow nearly as strongly as the most amplified wave. The actual amplitude at the end of the simulations depends upon how well the particular instability mode was initialized. Other possible causes are compressibility effects, non-linear effects, or the variation in the mean flow during the simulation. It may also be due to effects peculiar to the experiments. For example, the flow is especially receptive to disturbances at the splitter plate edge, which is two-dimensional. Also, the experiments which show strong spanwise coherence are 'clean' experiments with laminar boundary-layers coming off the splitter plate. These boundary-layers will contain instability waves which, though not of high amplitude, may have been growing for a long enough time to have sorted out the two-dimensional Tollmien-Schlichting waves. These would then be a forcing on the mixing layer, tending to make it more two-dimensional.

The changing nature of the most unstable waves due to compressibility is clearly illustrated in the sequence of figures 5.42 through 5.44. These show the $v = 0$

contour in a cut through the $x - z$ plane at $y = 0$ for Mach numbers 0.4, 0.8 and 1.05 respectively. At $M_1 = 0.8$ there is no longer any tendency towards a spanwise coherence, and waves at about 45° are most common. The situation is clearer at $M_1 = 1.05$ where the linear theory predicts a fairly narrow band of waves around 60° to be most amplified. The contours of $v = 0$ on figure 5.44 show strong evidence for waves at this angle. There are regions where the + and − oblique waves are amplified separately, and regions where both are amplified at the same region in space.

The simulations with random initial conditions confirmed the linear stability finding that oblique waves become the most amplified waves as the Mach number of the mixing layer is increased. No evidence was found for the existence of modes other than those already considered in the linear stability analysis.

5.5 Structure at High Mach Number

Using results from the previous sections we can make some predictions about the kind of large-scale structures which may grow from the inflectional instability in the mixing layer at high Mach number, especially above $M_c = 1$ where the oblique waves are much more strongly amplified than the two-dimensional waves. From figure 5.44, which showed the structure growing from low amplitude random noise, we see that there are regions in the flow where one of the oblique waves seems to dominate over the other, and regions where both oblique waves seem to be about equally important. Therefore two simulations were run, one with a single oblique wave and the other with a pair of equal and opposite oblique waves. The Mach number for these simulations was chosen to be 0.8, so that a lower Reynolds number of 400 could be used, to simulate further into the non-linear development. The two-dimensional wave was not included in the initial field, so these structures are expected to be more typical of flows at higher Mach numbers, except that those structures are expected to become more oblique. A wave angle of 45° was selected, since this is the most amplified wave at $M_1 = 0.8$. The growth in vorticity thickness is shown on figure 5.45.

The developed structure arising from a single oblique wave is, not surprisingly, an oblique vortex. The structure developing from two equal and opposite oblique

waves is more complex. Pressure surfaces are shown on figures 5.46 and 5.47 for the two cases. In the structure developing from the pair of oblique waves there are four main regions of rotating fluid. At $x = 0$ there are two counter rotating vortices, inclined in y relative to the x axis, and oblique in z relative to the x axis. There are two more vortices at $x = L_x/2$ similar to the first two, but with the opposite sense of ω_x rotation. The region where two of the vortices come close may be considered similar to the hairpin structures found in transitional boundary-layer flows. The induced motion of the head of the hairpin due to the legs is alternately up or down, explaining the inclined nature of the vortices. In fact, the vortices become more inclined as the simulation proceeds. The actual rotation at the heads of the hairpins is weak, and there is no suggestion of rotation of the head of one hairpin around the tail of the hairpin beneath it. The structure can be thought of as two vortex lines, passing through the peaks in vorticity. One line passes through the vortices at $x = 0$, $z = L_z/4, 3L_z/4$ and the other passes through the vortices at $x = L_x/2$, $z = L_z/4, 3L_z/4$. Perspective and top views of the vortex lines are shown on figure 5.48. These vortex lines are staggered in the streamwise direction, similar to the peak valley splitting of boundary-layer transition. However, the boundary layer case is a subharmonic secondary instability, whereas the case described here is a fundamental primary instability.

The mixture fraction field for the structure resulting from two equal and opposite oblique waves is especially rich in detail. The mixture fraction, f, was initially specified by a hyperbolic tangent profile (4.3), and tags fluid from the free-streams with a value between 0 (lower stream) and 1 (upper stream). Contours are plotted of $f - 0.5$, with negative contours dashed, so that solid contours mark fluid that originated on the upper side, and dashed contours mark fluid that originated on the lower side. A cut through the $x - z$ plane at $y = 0$ is shown on figure 5.49. The four main vortices show clearly. The regions of strong mixture fraction gradient at $x = L_x/4, 3L_x/4$, $z = L_z/4, 3L_z/4$ are complex three-dimensional saddle points, where fluid is being brought to rest, and high pressure ensues. Cuts of mixture fraction through the $y - z$ plane at $x = L_x/4$ and $x = L_x/2$ are shown on figure 5.50. Mushroom structures are found at $x = 0, L_x/2$ due to the counter-rotating vortices. Examples of cuts in the $x - y$ plane are shown on figure 5.51 for $z = L_z/4$ and $z = L_z/2$. This illustrates that care is needed when interpreting experimental cuts in the $x - y$ plane or span averaged photographs such as Schlieren. The cuts

at $z = L_z/4, 3L_z/4$ are at first glance reminiscent of the two-dimensional low Mach number structure, even though the complete structure is highly three-dimensional. We note that there are two of the hairpin structures per period, which may explain the reduction in structure spacing to thickness ratio observed by Papamoschou [1986] above a convective Mach number of 0.8.

5.6 Sensitivity to Initial Conditions

In this section we present simulations in which random noise was added to the initial condition. The objective of these simulations was to see whether the structures presented in the previous sections are strongly affected by background noise, and in particular whether non-linear interactions act to disrupt the organized structure.

A simulation at $M_1 = 0.8$ showed that the growth of the linear eigenfunctions was not significantly affected by the presence of random noise. This simulation was run with the same Reynolds number, box size and configuration of instability waves as in section 5.3 ($Re = 600$, $L_x = L_z = 13.37$, forcing with a two-dimensional wave and a pair of equal and opposite oblique waves). The amplitude of each wave was 0.025. Random noise was added to this initial condition in the same way as in section 5.4, with amplitude $A = 0.025$ (equation (5.3)). All modes from (0,0) through (7,7) and (7,-7) were seeded. The growth in mode energies of the unstable waves are shown on figure 5.52, and are nearly indistinguishable from the growth rates shown on figure 5.20, where there was no random noise. The final structure was very similar to that of the simulation described in section 5.4 and is not presented again here.

A more stringent test was run in which the initial eigenfunctions were not put into the simulations, and the flow had to sort out the most amplified waves from an initial field consisting only of random noise. The same Mach number, Reynolds number and box size were used as in section 5.3 and in the preceding paragraph. The random noise was added with amplitude $A = 0.025$, seeding modes (0,0) through (7,7) and (7,-7) in the usual way. A carpet plot of the initial mode energies is shown on figure 5.53*a*, and a cut through the pressure field at the $y = 0$ plane is shown on figure 5.53*b*. The simulation was run forward in time and a carpet plot and pressure field at time $t = 29.6$ are shown on figures 5.54*a* and 5.54*b* respectively. From the carpet plot it can be seen that the energy that was initially put into modes with

high k_x has decayed very rapidly. The peaks that have appeared in the carpet plot are the unstable waves. From linear stability theory waves (1,0), (1,1), (1,-1), (1,2) and (1,-2) are all unstable. Other parts of the carpet plot are associated either with the Fourier representation of the non-linear structure that is developing from the linear instabilities, or with the decaying initial random number field.

The amplitude of each wave is dependent not only on the growth rate, but also on the initial random field. From the carpet plot (figure 5.54*a*) it appears that the (1,1) mode was most strongly seeded, followed by the (1,-2) and (1,-1) modes. As time advances in the simulation we see more of the effect of amplification rate, and less of the effect of the initial conditions. The pressure field shown on figure 5.54*b* shows that one of the oblique waves is stronger than the others for this initial random field.

The simulation with purely random initial conditions was run long enough for the instability waves to grow to near-saturation conditions. Organized structure was found. At time $t = 52.0$ the carpet plot of mode energies, and the pressure field at $y = 0$ are shown on figures 5.55*a* and 5.55*b* respectively. The energy spectra has now filled out. This is attributed to the Fourier modes needed to resolve the large-scale structure in the flowfield. An oblique view of a surface of constant pressure is shown on figure 5.56. This can be compared with figure 5.27 (structure developing from a two-dimensional wave and a pair of oblique waves with relative phase $\phi = \pi/2$), figure 5.37 (same but with $\phi = 0$), and figure 5.47 (structure developing from a pair of oblique waves alone). The developed structure is similar to the case of figure 5.47, where the structure was allowed to develop from a pair of equal and opposite oblique instability waves.

Figure 5.57 shows how the linearly unstable waves grow from out of the random initial condition. There is an adjustment period, extending up to about $t = 10$, during which the unstable waves emerge from the background noise. Depending on the initial field different waves may emerge first. It is apparent that the (1,1) mode was most strongly seeded in this case. This wave grows at the same rate as the (1,-1) wave but appears to start from an earlier time (approximately 5 time units). The two-dimensional wave was not strongly seeded in this simulation, and does not play a significant role in the evolution of this flow.

A plot of the growth in vorticity thickness (equation (2.20)) is shown on figure 5.58*a*, and a plot of the growth in vorticity thickness based on a mass-weighted

velocity profile is shown on figure 5.58*b*. As was noted in section 4.3 the vorticity thickness is very sensitive to features of the large-scale structure. Figure 5.58*a* shows a dip in the vorticity thickness for times between 40 and 50, while figure 5.58*b* shows a strong increase at these times. These effects are probably specific to this simulation, and may be associated with the 'collapse' of vorticity into vortices, which occurs at about these times.

The conclusions of these simulations are (1) that the linear instability processes are not very sensitive to the presence of background noise, and (2) that an organized structure develops from simulations started with random initial conditions. This organized structure is similar to that which was presented in earlier sections, where the structures developed from combinations of the instability waves with the highest linear amplification rates.

The apparent 'cleanliness' of these simulations is not due to the choice of initial conditions, but to the dominance of the primary (inviscid inflectional) instability in this prototypical free shear layer. Even with random initial conditions the unstable modes eventually dominate the flow. For reasons of computational expense the simulations have not been run to later times, when secondary instabilities will presumably develop, or through to the 'mixing transition' which (by analogy with the incompressible flow) is when small eddies develop in the mixing layer. However, even beyond these stages the strong instability mechanism will certainly persist, and it is felt that the large-scale organized structure in the compressible mixing layer will result from the saturation of the various combinations of instability waves, as simulated in this thesis.

5.7 Chapter Summary

The three-dimensional simulations presented in this chapter confirm the earlier linear stability finding that oblique waves are more amplified than two-dimensional waves at high Mach numbers. Simulations with random initial conditions showed that the structures developing from linear instabilities become more oblique as Mach number is increased. No evidence was found for any modes of instability other than those already found in the linear stability analysis.

At convective Mach number $M_c = 0.8$ it was found that the oblique wave was more amplified than the two-dimensional wave during the entire simulation, and

oblique modes contained more energy than two-dimensional modes. With the convective Mach number above 1 ($M_c = 1.05$) it was found that the two-dimensional instability played only a small role in the development of large-scale structure.

The expected structures at high Mach number were examined in more detail in two more simulations – one of a single oblique wave and the other of a pair of equal and opposite oblique waves. The oblique wave developed into an oblique vortex, while the pair of waves developed into a complex structure consisting of four regions of strong rotation, placed along two vortex lines with hairpin shapes in the spanwise direction, and with peak-valley splitting in the streamwise direction.

Simulations with random initial conditions were run to check the sensitivity of the organized structure to initial conditions. A very similar structure was found to develop. The growth rate of the linear instabilities was found to be insensitive to the presence of finite amplitude random noise.

No shock waves were found in any of the three-dimensional simulations, even with the free-stream Mach number above 1. Whilst this does not prove that there will never be shock waves in mixing layers at high Mach number, it does appear that the flow can adjust in a three-dimensional manner so that shock waves are not required at high Mach numbers.

The expected structure of the compressible mixing layer can be summarized as follows. Below $M_c = 0.4$ we expect the usual two-dimensional rollers that have been found in incompressible experiments and simulations. Above $M_c = 1$ we expect to find the double hairpin structure, which develops from pairs of oblique waves. In between the situation is more complex, since a broad range of instability waves are strongly amplified. Between $M_c = 0.4$ and $M_c = 0.6$ we expect that the roller structure will disappear. Above $M_c = 0.6$ we expect to see more and more evidence of structures with strong streamwise vorticity, such as might develop from combinations of two-dimensional and oblique instability waves.

CHAPTER 6

Conclusions and Recommendations

This work has been concerned with a numerical study of the compressible mixing layer. The methods used were linear stability analysis and direct numerical simulation of the compressible Navier-Stokes equations. The stability equations were solved by a shooting method. The full equations were solved by an explicit code, with derivatives evaluated spectrally or with high order finite differences. The conclusions are divided into the three main areas of study: linear stability, two-dimensional simulations and three-dimensional simulations.

Linear Stability Theory:

- Linear stability theory can be used to predict mixing layer growth rates. The relation $\delta' \sim |\alpha_i|_{\max}$ gives the correct trends in growth rate due to velocity ratio, density ratio and Mach number. The amplification rate of the most amplified wave has to be computed using spatial stability theory, with a solution to the boundary-layer equations as the base state.
- The experimental finding of Papamoschou [1989] that convective velocities do not match the prediction of the U_c formula (1.2) was reproduced in the linear theory, using the phase speed of the neutral modes as a prediction of convective velocities of large-scale structures.
- Oblique waves were found to be more amplified above a convective Mach number of 0.6. A simple relation, $M_c \cos\theta = 0.6$ was proposed to give an approximate orientation of the most amplified waves in the flow.
- Several different methods of achieving high convective Mach numbers were compared. There was no overall collapse of growth rates at high Mach numbers, indicating that the convective Mach number $M_c = (U_1^* - U_2^*)/(c_1^* + c_2^*)$ may be only a first order measure of compressibility effects.

Two-Dimensional Simulations:

- The growth rate of the two-dimensional mixing layer was observed to drop rapidly as the Mach number was increased, nonlinearly as well as linearly.
- The reduction in growth rate was associated with a change in shape of the developed vortices. These became more elongated in the streamwise direction as Mach number was increased.
- Shock waves were observed in two-dimensional simulations above a convective Mach number of 0.7.
- Peak strain rate in the simulations was found to be always the same order as the global strain rate, indicating that the global strain rate can be used to predict the magnitude of local strain rate in the mixing layer.
- Simulations with a density ratio of 0.2 were performed for a case where the U_c formula (1.2) would predict zero convection speed. It was found that the structures did indeed move, in agreement with the phase speed of the neutrally stable mode.
- The supersonic modes of instability, which are the only unstable modes in two-dimensions at high Mach number, were simulated. The modes were confirmed to be radiating, with a pattern of shock and expansion waves forming on the side of the mixing layer relative to which the instability was supersonic. These modes were found to be vortical, and did lead to roll-up. However, the growth rate was very small.

Three-Dimensional Simulations:

- At low Mach numbers it was found that the phase of a two-dimensional wave relative to a pair of equal and opposite oblique waves could be chosen to give the 'bulging' or 'translative' secondary stability modes of Pierrehumbert and Widnall [1982]. Simulations of these cases confirmed their finding that there was significant instability only for the translative mode.
- Raising the Mach number, with the phasing chosen to give the translative mode, was found to lead to a change in structure. The linear stability result that oblique waves are more amplified than two-dimensional waves was found

to carry over into the nonlinear regime. Above a convective Mach number of 0.6 the oblique modes of the developed structure were found to contain more energy than the two-dimensional mode.

- Above a convective Mach number of 1 there was found to be very little influence of the two-dimensional wave on the developed structure.
- No shock waves were found in the three-dimensional simulations, even above a convective Mach number of 1.
- Simulations with random initial conditions confirmed the linear stability finding of oblique waves being more amplified at high Mach numbers. The linear theory was found to predict well the angle of the most unstable modes as Mach number was increased. No evidence was found for any modes of instability other than those already found in the linear stability analysis.
- The addition of random noise did not significantly change the growth rate of linear instability waves.
- Typical structures which may be found in the mixing layer at high Mach numbers were computed, based on the nonlinear evolution of oblique instability waves. A single oblique wave led to an oblique vortex. A pair of equal and opposite oblique waves led to a structure with four regions of strong rotation, arranged along two kinked spanwise vortex tubes, staggered in the streamwise direction. The structure resembles a peak-valley splitting arrangement of the hairpin structures found in boundary-layer transition.
- A simulation starting with random initial conditions developed a large-scale structure very similar to that computed from the non-linear development of combinations of instability waves.
- The mixing layer below a convective Mach number $M_c = 0.4$ is expected to have a 'roller' structure similar to the incompressible flow. Between $M_c = 0.4$ and $M_c = 1.0$ we expect to find a complex structure, due to many instability waves being equally amplified, but with a tendency to stronger streamwise and oblique vortices as the Mach number is raised. Above $M_c = 1$ we expect to find a cleaner structure of pairs of hairpins, which develop from pairs of oblique instability waves.

Open Questions for Future Research

Numerical simulation of compressible turbulent flows is a relatively new area of research and many questions remain to be answered. Future work could be directed towards some of the following questions, which arose from this work.

Linear Instability Model:

- What are the limitations of the model discussed in section 2.3?

  The immediate need is for more experimental measurements of growth rates and convective velocities as a function of density ratio and Mach number. Stability analysis of actual self-similar experimental velocity and density profiles may help to isolate some of the limitations of the simple model.

Subharmonic Growth Mechanism:

- What is the high Mach number analog of the vortex pairing process?

  There is presumed to be some mechanism by which the largest structures in flow merge so that the mixing layer cross-stream length scale can grow and the mixing layer can be self-similar. At high Mach numbers this probably involves oblique subharmonic waves. It is not clear what kind of 'oblique pairing' of vortices, or 'merging of hairpin structures', will take place. Simulation of this process will be expensive, since twice the resolution in each direction will be required, compared to the current work.

Mixing Transition:

- How do small eddies form in a free-shear layer?

  The mechanism is not understood even in incompressible flow, but the experimental observation is of a large increase in formation of products of a chemical reaction at some point in the mixing layer development (Breidenthal [1981]). The resolution required for the Reynolds numbers at which mixing transition occurs is probably near current supercomputer capability.

Statistics:

- How do we make engineering computations of compressible turbulent flows?

  Traditional models require a knowledge of the time-averaged character of the flow. Statistical information from compressible turbulence simulations could be used to point to the relevant terms in the equations which need to be

modelled differently at higher Mach numbers. However it is felt that no simulation has yet produced a statistically self-similar mixing layer, even in two-dimensional incompressible flow. A large enough sample of the largest structures (*e.g.* 60-100) would have to be accumulated to get reliable statistics (Sandham and Reynolds [1989]). A logical sequence for progress on statistics seems to be: two-dimensional incompressible, three-dimensional incompressible, and finally three-dimensional compressible. Compressible simulations typically require twice the storage and three times the CPU time of incompressible simulations.

Mixing:

- Does the scalar pdf change at the higher Mach numbers?

  The change in large-scale structure suggests that the scalar probability density function (pdf) will be different at higher Mach numbers. A change in the pdf also means that fast chemical reactions will behave differently to the low Mach number flow. Scalar pdf's can be accumulated from the simulations presented here. However, they are of limited value since we are not simulating through the mixing transition, and have no small-scales doing the mixing. Also we do not have a self-similar mixing layer, so the pdf varies with time in the simulations.

Chemical Reactions:

- How to make supersonic combustion more efficient?

  We need to understand how heat release affects the compressible mixing layer flow. One possible avenue for research is to follow the procedure of this thesis. First of all, the stability problem could be solved for the compressible mixing layer, with an artificial temperature profile to reflect the effects of heat release. Then direct numerical simulations could be performed with two species, including reaction rate terms. The effect of changes in the instability of the flow could be studied, as well as the effect of finite-rate chemistry.

APPENDIX A

A Direct Method for Linear Stability Analysis

In Chapter 2 the linearized equations were reduced to a single equation which was then solved by shooting. In this appendix an alternative procedure is described, which makes use of a spectral representation of the mean and perturbed flow to formulate the linear stability problem as a matrix eigenvalue problem. This method was developed in collaboration with J. H. Chen; results for compressible wake instability can be found in Chen *et al.* [1989].

We begin with the linearized equations which were derived in section 2.1.2. As before the notation D is used for the d/dy operator. The linearized continuity equation is:

$$\hat{\rho}i(\alpha\overline{u}-\omega)+\hat{v}D\overline{\rho}+\overline{\rho}[i(\alpha\hat{u}+\beta\hat{w})+D\hat{v}]=0 \qquad (A.1)$$

After substituting for the linearized perfect gas law, equation (2.39), the linearized momentum equations in the x, y and z directions become:

$$\overline{\rho}[i(\alpha\overline{u}-\omega)\hat{u}+\hat{v}D\overline{u}]=\frac{-i\alpha(\overline{\rho}\hat{T}+\hat{\rho}\overline{T})}{\gamma M_1^2} \qquad (A.2)$$

$$\overline{\rho}i(\alpha\overline{u}-\omega)\hat{v}=\frac{-(\overline{\rho}D\hat{T}+\hat{T}D\overline{\rho}+\hat{\rho}D\overline{T}+\overline{T}D\hat{\rho})}{\gamma M_1^2} \qquad (A.3)$$

$$\overline{\rho}i(\alpha\overline{u}-\omega)\hat{w}=\frac{-i\beta(\overline{\rho}\hat{T}+\hat{\rho}\overline{T})}{\gamma M_1^2} \qquad (A.4)$$

and the linearized energy equation is:

$$\overline{\rho}[i(\alpha\overline{u}-\omega)\hat{T}+\hat{v}D\overline{T}]=-(\gamma-1)[i(\alpha\hat{u}+\beta\hat{w})+D\hat{v}] \qquad (A.5)$$

The first step is to rearrange these equations into the form of a matrix multiplied by a vector, with the desired eigenvalue isolated. For temporal stability calculations we wish to isolate ω, so we write the above equations as:

$$A_t\vec{x}=\omega\vec{x} \qquad (A.6)$$

where $\vec{x}$ is a column vector of the eigenfunctions $\vec{x} = (\hat{\rho}, \hat{u}, \hat{v}, \hat{w}, \hat{T})^T$ and the matrix A_t is given by

$$A_t = \begin{pmatrix} \alpha\overline{u} & \alpha\overline{\rho} & -i(D\overline{\rho} + \overline{\rho}D) & \beta\overline{\rho} & 0 \\ \frac{\alpha\overline{T}}{\overline{\rho}\gamma M_1^2} & \alpha\overline{u} & -iD\overline{u} & 0 & \frac{\alpha}{\gamma M_1^2} \\ \frac{-i(D\overline{T}+\overline{T}D)}{\overline{\rho}\gamma M_1^2} & 0 & \alpha\overline{u} & 0 & \frac{-i(D\overline{\rho}+\overline{\rho}D)}{\overline{\rho}\gamma M_1^2} \\ \frac{\beta\overline{T}}{\overline{\rho}\gamma M_1^2} & 0 & 0 & \alpha\overline{u} & \frac{\beta}{\gamma M_1^2} \\ 0 & \frac{(\gamma-1)\alpha}{\overline{\rho}} & -i(D\overline{T} + \frac{(\gamma-1)D}{\overline{\rho}}) & \frac{(\gamma-1)\beta}{\overline{\rho}} & \alpha\overline{u} \end{pmatrix} \tag{A.7}$$

For spatial stability we isolate α, and write:

$$A_s\vec{x} = \alpha B_s\vec{x} \tag{A.8}$$

where the matrix A_s is given by:

$$A_s = \begin{pmatrix} \omega & 0 & i(D\overline{\rho} + \overline{\rho}D) & -\beta\overline{\rho} & 0 \\ 0 & \omega & iD\overline{u} & 0 & 0 \\ \frac{i(D\overline{T}+\overline{T}D)}{\overline{\rho}\gamma M_1^2} & 0 & \omega & 0 & \frac{i(D\overline{\rho}+\overline{\rho}D)}{\overline{\rho}\gamma M_1^2} \\ \frac{-i\beta\overline{T}}{\overline{\rho}\gamma M_1^2} & 0 & 0 & \omega & \frac{-\beta}{\gamma M_1^2} \\ 0 & 0 & i(D\overline{T} + \frac{(\gamma-1)D}{\overline{\rho}}) & \frac{-(\gamma-1)\beta}{\overline{\rho}} & \omega \end{pmatrix} \tag{A.9}$$

and the matrix B_s is given by:

$$B_s = \begin{pmatrix} \overline{u} & \overline{\rho} & 0 & 0 & 0 \\ \frac{\overline{T}}{\overline{\rho}\gamma M_1^2} & \overline{u} & 0 & 0 & \frac{1}{\gamma M_1^2} \\ 0 & 0 & \overline{u} & 0 & 0 \\ 0 & 0 & 0 & \overline{u} & 0 \\ 0 & \frac{(\gamma-1)}{\overline{\rho}} & 0 & 0 & \overline{u} \end{pmatrix} \tag{A.10}$$

The next step is to derive a matrix form of the operator D. The mapped Fourier method of Cain *et al.* [1984] was selected since it allows solution over an infinite physical domain. We start with the definition of a Fourier transform pair:

$$\tilde{\phi}_k = \frac{1}{N}\sum_{j=0}^{N-1} \phi(\eta_j)e^{-ik2\pi\eta_j} \tag{A.11}$$

$$\phi(\eta_j) = \sum_{k=-N/2}^{N/2-1} \tilde{\phi}_k e^{ik2\pi\eta_j} \qquad (A.12)$$

where N is the number of points, η_j are the grid points, ϕ is the function and $\tilde{\phi}$ is the transformed function. Cain *et al.* [1984] defined a cotangent mapping:

$$y = -a_c \text{cotan}(2\pi\eta) \qquad (A.13)$$

where a_c is a constant that determines the amount of stretching in the mapping. Under this mapping the mixing layer physical domain $-\infty < y < \infty$ maps onto $0 < \eta < 1/2$. The computational domain $0 < \eta < 1$ is periodic, allowing the use of Fourier methods.

Derivatives are calculated as:

$$\frac{d\phi}{dy} = \frac{1}{h'}\frac{d\phi}{d\eta} \qquad (A.14)$$

where $h' = dy/d\eta$ is the metric. For Cain's mapping this is given by:

$$\frac{1}{h'} = \frac{1}{2\pi a_c}\sin^2(2\pi\eta) = \frac{1}{4\pi a_c}\left[1 - \frac{e^{i2(2\pi\eta)} + e^{-i2(2\pi\eta)}}{2}\right] \qquad (A.15)$$

Substituting this into (A.14), using (A.12) and combining terms, gives an expression for the derivative at grid point j:

$$\left.\frac{d\phi}{dy}\right|_j = \frac{1}{2a_c}\sum_{k=-N/2+1}^{N/2-1}\left[ik\tilde{\phi}_k - \frac{i(k-2)}{2}\tilde{\phi}_{k-2} - \frac{i(k+2)}{2}\tilde{\phi}_{k+2}\right]e^{ik2\pi\eta_j} \qquad (A.16)$$

where all terms with wavenumbers outside the summation limits are discarded.

The next step is to substitute in for $\tilde{\phi}$ from equation (A.11), and compare with a matrix formulation:

$$\left.\frac{d\phi}{dy}\right|_l = d_{lj}\phi(\eta_j) \qquad (A.17)$$

The d_{lj} are terms of a matrix, given by:

$$d_{lj} = \frac{1}{2a_c N} \sum_{k=-N/2+1}^{N/2-1} \left[ik - \frac{i(k-2)}{2} e^{i4\pi\eta_j} - \frac{i(k+2)}{2} e^{-i4\pi\eta_j} \right] e^{i2\pi k(\eta_l - \eta_j)} \quad (A.18)$$

This expression can be simplified using trigonometry and geometric series.
For $l = j$ we obtain:

$$d_{lj} = -\frac{(N-1)}{a_c N} \sin(4\pi\eta_j) \quad (A.19a)$$

and for $l \neq j$:

$$d_{lj} = \frac{1 - \cos(4\pi\eta_j)}{4a_c} (-1)^{l-j} \cot\left(\frac{\pi(l-j)}{N}\right) - \frac{\sin(4\pi\eta_j)}{a_c N} \frac{\sin[\pi(l-j)\frac{N-1}{N}]}{\sin[\frac{\pi(l-j)}{N}]} \quad (A.19b)$$

As a last step we use the symmetry of the Cain mapping to reduce the size of the matrix from $N \times N$ to $N^* \times N^*$, where $N^* = N/2 + 1$. A new matrix e_{lj} is defined as follows.
For $j = 1$ and $j = N^*$:

$$e_{lj} = d_{lj} \quad (A.20a)$$

and for $j = 2$ to $N^* - 1$:

$$e_{lj} = d_{lj} + d_{l(N+2-j)} \quad (A.20b)$$

This matrix is used to represent derivative terms in matrices A_t (equation (A.7)) and A_s (equation (A.9)). The result is a $5N^* \times 5N^*$ matrix (5×5 matrices at each grid point). The eigenvalues and eigenvectors of this matrix were found using standard (IMSL) subroutines.

The performance of the method was checked by running the test case of table 2.2. Curves of amplification rate against wavenumber are shown on figure A.1 for several values of N^*, and compared with the result from the shooting method of Chapter 2. It can be seen that convergence of the direct method is good for the most amplified wave, but very poor near the neutral mode and at very low ω. In general, it was found that weakly amplified waves were difficult to resolve with the direct method. At high Mach numbers it was difficult to capture the weakly amplified instability modes, even using N^* as high as 60.

References

ANDERSON, D. A., TANNEHILL, J. C. & PLETCHER, R. H. 1984 *Computational Fluid Mechanics and Heat Transfer*, McGraw-Hill, New York.

ASHURST, W. T. & MEIBURG, E. 1988 Three-dimensional shear layers via vortex dynamics. *J. Fluid Mech.* **189**, 87-116.

BERNAL, L. P. & ROSHKO, A. 1986 Streamwise vortex structure in plane mixing layers. *J. Fluid Mech.* **170**, 499-525.

BETCHOV, R. & SZEWCZYK, A. 1963 Stability of a Shear Layer between Parallel Streams. *Phys. Fluids* Vol. 6 No. 10, 1391-1396.

BIRCH, S. F. & EGGERS, J. M. 1973 A Critical Review of the Experimental Data for Developed Free Turbulent Shear Layers. *NASA SP-321*, 11-40.

BLUMEN, W. 1970 Shear layer instability of an inviscid compressible fluid. *J. Fluid Mech.* **40**, 769-781.

BLUMEN, W., DRAZIN, P. G. & BILLINGS, D. F. 1975 Shear layer instability of an inviscid compressible fluid. Part 2. *J. Fluid Mech.* **71**, 305-316.

BOGDANOFF, D. W. 1983 Compressibility Effects in Turbulent Shear Layers. *AIAA Journal* Vol. 21, June 1983, 926-927.

BOGDANOFF, D. W. 1984 Interferometric Measurement of Heterogeneous Shear-Layer Spreading Rates. *AIAA Journal* Vol. 22, Nov. 1984, 1550-1555.

BRADSHAW, P. 1966 The effect of initial conditions on the development of a free shear layer. *J. Fluid Mech.* **26**, 225-236.

BREIDENTHAL, R. 1981 Structure in turbulent mixing layers and wakes using a chemical reaction. *J. Fluid Mech.* **109**, 1-24.

BROADWELL, J. E. & BREIDENTHAL, R. E. 1982 A simple model of mixing and chemical reaction in a turbulent shear layer. *J. Fluid Mech* **125**, 397-410.

BROADWELL, J. E. & MUNGAL, M. G. 1988 Molecular Mixing and Chemical Reactions in Turbulent Shear Layers. *Twenty-Second International Symposium on Combustion*, University of Washington, Seattle, Washington, Aug. 14-18, 1988.

BROWAND, F. K. & WEIDMAN, P. D. 1976 Large scales in the developing mixing layer. *J. Fluid Mech.* **76**, 127-144.

BROWAND, F. K. & LATIGO, B. O. 1979 Growth of the two-dimensional mixing layer from a turbulent and nonturbulent boundary layer. *Phys. Fluids* **22**, 1011-1019.

BROWN, G. L. & ROSHKO, A. 1974 On density effects and large structure in turbulent mixing layers. *J. Fluid Mech.* **64**, 775-816.

BROWN, G. L. 1974 The entrainment and large structure in turbulent mixing layers. *Fifth Australasian Conference on Hydraulics and Fluid Mechanics*, Christchurch, New Zealand.

CAIN, A. B., REYNOLDS, W. C. & FERZIGER, J. H. 1981 A three-dimensional simulation of transition and early turbulence in a time-developing mixing layer. *Report No. TF-14.* Department of Mechanical Engineering, Stanford University, Stanford, California.

CAIN, A. B., FERZIGER, J. H. & REYNOLDS, W. C. 1984 Discrete Orthogonal Function Expansions for Non-uniform Grids Using the Fast Fourier Transform. *J. Comp. Phys.* **56**, 272-286.

CHANDRSUDA, C., MEHTA, R. D., WEIR, A. D. & BRADSHAW, P. 1978 Effect of free-stream turbulence on large structure in turbulent mixing layers. *J. Fluid Mech.* **85**, 693-704.

CHEN, J. H., CANTWELL, B. J. & MANSOUR, N. N. 1989 The Effect of Mach Number on the Stability of a Plane Supersonic Wake. *AIAA Paper*, no. 89-0285.

CLEMENS, N. T., MUNGAL, M. G., BERGER, T. E. & VANDSBURGER, U. 1989 Visualizations of a compressible turbulent mixing layer. *Open Forum Abstract, Seventh Symposium on Turbulent Shear Flows*, Stanford, CA, August 21-23, 1989.

CORCOS, G. M. & SHERMAN, F. S. 1984 The mixing layer: deterministic models of a turbulent flow. Part 1. Introduction and the two-dimensional flow. *J. Fluid Mech.* **139**, 29-65.

CORCOS, G. M. & LIN, S. J. 1984 The mixing layer: deterministic models of a turbulent flow. Part 2. The origin of the three-dimensional motion. *J. Fluid Mech.* **139**, 67-95.

DAVEY, R. F. & ROSHKO, A. 1972 The effect of a density difference on shear-layer instability. *J. Fluid Mech.* **53**, 523-543.

DIMOTAKIS, P. E. & BROWN, G. L. 1976 The mixing layer at high Reynolds number: large-structure dynamics and entrainment. *J. Fluid Mech.* **78**, 535-560.

DIMOTAKIS, P. E. 1986 Two-Dimensional Shear-Layer Entrainment. *AIAA Journal* Vol. 24, Nov. 1986, 1791-1796.

DIMOTAKIS, P. E. 1989 Turbulent Free Shear Layer Mixing. *AIAA Paper*, no. 89-0262.

DRAZIN, P. G. & DAVEY, A. 1977 Shear layer instability of an inviscid compressible fluid. Part 3. *J. Fluid Mech.* **82**, 255-260.

EBERHARDT, S, RILEY, J. J., SOESTRISNO, M. & GREENOUGH, J. A. 1988 A Numerical Study of Inviscid, Supersonic Mixing Layers. *Workshop on the Physics of Compressible Turbulent Mixing*, Princeton, Oct. 1988.

FIEDLER, H. E. 1974 Transport of Heat Across a Plane Turbulent Mixing Layer. *Advances in Geophysics* Vol. 18A, 93-109.

GREENOUGH, J., RILEY, J., SOESTRISNO, M, & EBERHARDT, D. 1989 The Effects of Walls on a Compressible Mixing Layer. *AIAA Paper*, no. 89-0372.

GROPENGIESSER, H. 1970 Study on the stability of boundary layers and compressible fluids. *NASA TT F-12,786.*

HERBERT, T. 1983 Secondary instability of plane channel flow to subharmonic three-dimensional disturbances. *Phys. Fluids* **26**, 871-874.

HERBERT, T. & BODONYI, R. J. 1989 Studies of Transition in Boundary Layers. *AIAA Paper*, no. 89-0034.

HO, C.-M. & HUERRE, P. 1984 Perturbed Free Shear Layers. *Ann. Rev. Fluid Mech.* **16**, 365-424.

HO, C.-M., ZOHAR, Y, MOSER, R. D., ROGERS, M. M., LELE, S. K. & BUELL, J. C. 1988 Phase decorrelation, streamwise vortices and acoustic radiation in mixing layers. *Proceedings of the 1988 Summer Program, Report CTR-S88*, Center for Turbulence Research, Stanford/NASA-Ames, 29-39.

HUERRE, P. & MONKEWITZ, P. A. 1985 Absolute and convective instabilities in free shear layers. *J. Fluid Mech.* **159**, 151-168.

JACKSON, T. L. & GROSCH, C. E. 1988 Spatial stability of a compressible mixing layer. *ICASE Report* No. 88-33.

KAYS, W. M. & CRAWFORD, M. E. 1980 *Convective Heat and Mass Transfer*, 2d ed., McGraw-Hill, New York.

KOOCHESFAHANI, M. M. & DIMOTAKIS, P. E. 1986 Mixing and chemical reactions in a turbulent liquid mixing layer. *J. Fluid Mech.* **170**, 83-112.

LELE, S. 1988 Vortex Evolution in Compressible Free Shear Layers. *Workshop on the Physics of Compressible Turbulent Mixing*, Princeton, Oct. 1988.

LELE, S. 1989 Direct Numerical Simulation of Compressible Free Shear Flows. *AIAA Paper*, no. 89-0374.

LESSEN, M., FOX, J. A. & ZIEN, H. M. 1965 On the inviscid stability of the laminar mixing of two parallel streams of a compressible fluid. *J. Fluid Mech.* **23**, 355-367.

LESSEN, M., FOX, J. A. & ZIEN, H. M. 1966 Stability of the laminar mixing of two parallel streams with respect to supersonic disturbances. *J. Fluid Mech.* **25**, 737-742.

LIEPMANN, H. W. & LAUFER, J. 1947 Investigations of free turbulent mixing. *NACA TN 1257.*

LIEPMANN, H. W. & ROSHKO, A. 1957 *Elements of Gasdynamics*, John Wiley and Sons, New York.

LIN, S. J. & CORCOS, G. M. 1984 The mixing layer: deterministic models of a turbulent flow. Part 3. The effect of plane strain on the dynamics of streamwise vortices. *J. Fluid Mech.* **141**, 139-178.

LOWERY, P. S. & REYNOLDS, W. C. 1986 Numerical simulation of a Spatially-Developing, Forced, Plane Mixing Layer. *Report No. TF-26*, Department of Mechanical Engineering, Stanford University, Stanford, California.

MACK, L. M. 1984 Boundary-Layer Linear Stability Theory. *Special Course on Stability and Transition of Laminar Flow*, AGARD Report No. 709., 3-1 to 3-81.

MACK, L. M. 1989 On the inviscid acoustic-mode instability of supersonic shear flows. *Fourth Symp. on Numerical and Physical Aspects of Aerodynamic Flows*, California State University, Long Beach, CA.

MANSOUR, N. N., FERZIGER, J. H. & REYNOLDS, W. C. 1978 Large-Eddy Simulation of a Turbulent Mixing Layer. *Report No. TF-11*, Department of Mechanical Engineering, Stanford University, Stanford, California.

MASLOWE, S. A. & KELLY, R. E. 1971 Inviscid instability of an unbounded heterogeneous shear layer. *J. Fluid Mech.* **48**, 405-415.

METCALFE, R. W., ORSZAG, S. A., BRACHET, M. E., MENON, S. & RILEY, J. J. 1987 Secondary instability of a temporally growing mixing layer. *J. Fluid Mech.* **184**, 207-243.

MICHALKE, A. 1965a On the inviscid instability of the hyperbolic-tangent velocity profile. *J. Fluid Mech.* **19**, 543-556.

MICHALKE, A. 1965b Vortex formation in a free boundary layer according to stability theory. *J. Fluid Mech.* **22**, 371-383.

MICHALKE, A. 1965c On spatially growing disturbances in an inviscid shear layer. *J. Fluid Mech.* **23**, 521-544.

MONKEWITZ, P. A. & HUERRE, P. 1982 Influence of the velocity ratio on the spatial instability of mixing layers. *Phys. Fluids* **25**, 1137-1143.

MORKOVIN, M. V. 1988 Guide to Experiments on Instability and Laminar-Turbulent Transition in Shear Layers. *NASA-Ames short course.*

MUNGAL, M. G. & DIMOTAKIS, P. E. 1984 Mixing and combustion with low heat release in a turbulent shear layer. *J. Fluid Mech.* **148**, 349-382.

MUNGAL, M. G., HERMANSON, J. C. & DIMOTAKIS, P. E. 1985 Reynolds Number Effects on Mixing and Combustion in a Reacting Shear Layer. *AIAA Journal* Vol. 23 No. 9, 1418-1423.

MUNGAL, M. G. & FRIELER, C. E. 1988 The Effects of Damköhler Number in a Turbulent Shear Layer. *Combustion and Flame* **71**, 23-34.

ORSZAG, S. A. & PAO, Y 1974 Numerical computation of turbulent shear flows. *Advances in Geophysics* Vol. 18A, 225-236.

OSTER, D. & WYGNANSKI, I. 1982 The forced mixing layer between parallel streams. *J. Fluid Mech.*, **123**, 91-130.

PAPAMOSCHOU, D. & ROSHKO, A. 1986 Observations of Supersonic Free Shear Layers. *AIAA Paper*, no. 86-0162.

PAPAMOSCHOU, D. 1986 Experimental investigation of heterogeneous compressible shear layers. *Ph.D. Thesis.* Graduate Aeronautical Laboratories, California Institute of Technology, Pasadena, California.

PAPAMOSCHOU, D. & ROSHKO, A. 1988 The compressible turbulent shear layer: an experimental study. *J. Fluid Mech.* **197**, 453-477.

PAPAMOSCHOU, D. 1989 Structure of the Compressible Turbulent Shear Layer. *AIAA Paper*, no. 89-0126.

PIERREHUMBERT, R. T. & WIDNALL, S. E. 1982 The two- and three-dimensional instabilities of a spatially periodic shear layer. *J. Fluid Mech.* **114**, 59-82.

PRESS, W. H., FLANNERY, B. P., TEUKOLSKY, S. A. & VETTERLING, W. T. 1986 *Numerical Recipes*, Cambridge University Press, Cambridge.

RAGAB, S. A. & WU, J. L. 1988 Instabilities in the Free Shear Layer Formed by Two Supersonic Streams. *AIAA Paper*, no. 88-0038.

RAGAB, S. A. & WU, J. L. 1989 Linear Subharmonic Instabilities of Periodic Compressible Mixing Layers. *AIAA Paper*, no. 89-0039.

RAYLEIGH, LORD. 1880 On the stability, or instability, of certain fluid motions. *Scientific Papers*, Vol. 1, 474-487.

REYNOLDS, W. C. 1988 Fundamentals of Turbulence for Turbulence Modeling and Simulation. *Class Notes*, Department of Mechanical Engineering, Stanford University.

RILEY, J. J. & METCALFE, R. W. 1980 Direct numerical simulation of a perturbed, turbulent mixing layer. *AIAA Paper* 80-0274.

ROGERS, M. M. & MOSER, R. D. 1989 The Development of Three-dimensional Temporally-evolving Mixing Layers. *Seventh Symposium on Turbulent Shear Flows*, Stanford University, Stanford, California, August 21-23 1989.

SAMIMY, M., ERWIN, D. E. & ELLIOT, G. S. 1989 Compressibility and Shock Wave Interaction Effects on Free Shear Layers. AIAA Paper No. 89-2460, AIAA 25th Joint Propulsion Conference, July 10-12, 1989.

SANDHAM, N. D. & REYNOLDS, W. C. 1989 Some inlet-plane effects on the numerically simulated spatially-developing mixing layer. *Turbulent Shear Flows 6*, Springer-Verlag Berlin Heidelberg, 441-454.

SANDHAM, N. D., MUNGAL, M. G., BROADWELL, J. E. & REYNOLDS, W. C. 1988 Scalar entrainment in the mixing layer. *Proceedings of the 1988 Summer Program, Report CTR-S88*, Center for Turbulence Research, Stanford/NASA-Ames, 69-76.

SANDHAM, N. D. & YEE, H. C. 1989 A Numerical Study of a Class of TVD Schemes for Compressible Mixing Layers. *NASA TM* 102194.

SCHLICHTING, H. 1979 *Boundary-Layer Theory*, 7th edition, McGraw-Hill, New York.

SINGER, B., FERZIGER, J. H. & REED, H. 1987 Numerical Simulation Studies of Laminar-Turbulent Transition in the Plane Channel. *Report No. TF-31* Department of Mechanical Engineering, Stanford University, Stanford, California.

SOESTRISNO, M., EBERHARDT, S., RILEY, J. & McMURTRY, P. 1988 A Study of Inviscid, Supersonic Mixing Layers Using a Second-Order TVD Scheme. *AIAA Paper*, no. 88-3676.

SQUIRE, H. B. 1933 On the Stability for Three-Dimensional Disturbances of Viscous Fluid Flow between Parallel Walls. *Proc. Royal Soc. of London, Series A*, Vol. 142, 621-628.

STUART, J. T. 1967 On finite amplitude oscillations in laminar mixing layers. *J. Fluid Mech.* **29**, 417-440.

SWITHENBANK, J., EAMES, I., CHIN, S., EWAN, B., YANG, Z., CAO, J. & ZHAO, X. 1989 Turbulent Mixing in Supersonic Combustion Systems. *AIAA Paper*, no. 89-0260.

TAYLOR, G. I. 1923 On the decay of vortices in a viscous fluid. *The Scientific Papers of G. I. Taylor*, G. K. Batchelor, ed., Vol. IV, 90-92.

THOMPSON, K. W. 1987 Time Dependent Boundary Conditions for Hyperbolic Systems. *J. Comp. Phys.* **68**, 1-24.

WHITE, F. M. 1974 *Viscous fluid flow*, McGraw-Hill, New York.

WINANT, C. D. & BROWAND, F. K. 1974 Vortex pairing: the mechanism of turbulent mixing-layer growth at moderate Reynolds number. *J. Fluid Mech.* **63**, 237-255.

WRAY, A. A. 1986 Very low storage time-advancement schemes. *Internal Report*, NASA-Ames Research Center, Moffett Field, California.

WRAY, A. A. 1988 Vectoral Manual. *Internal Report*, NASA-Ames Research Center, Moffett Field, California.

YEE, H. C. 1989 A Class of High-Resolution Explicit and Implicit Shock-Capturing Methods. *NASA TM* 101088.

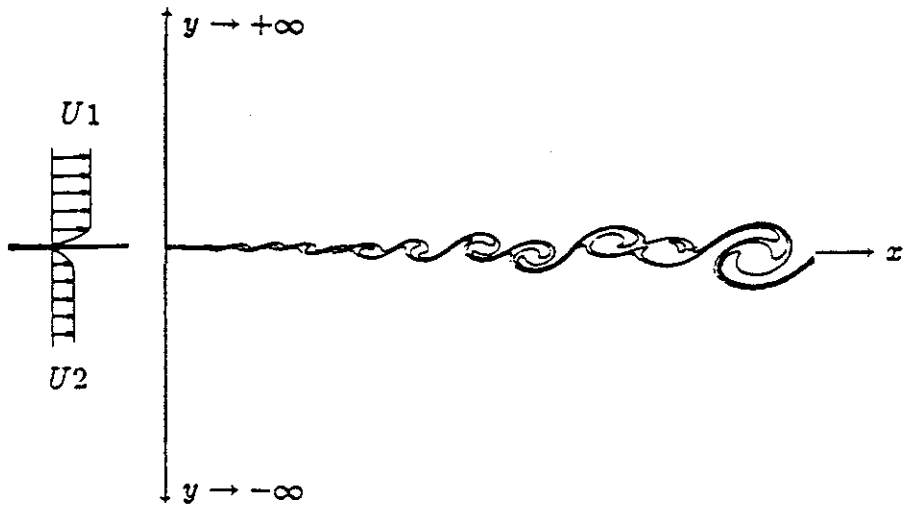

Figure 1.1 Spatially-developing mixing layer.

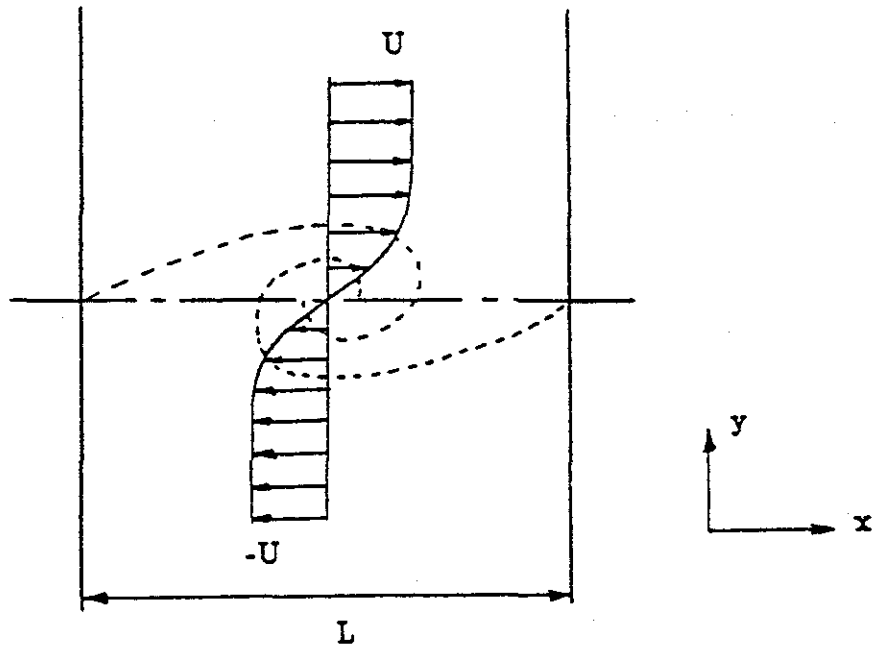

Figure 1.2 Time-developing mixing layer.

(a)

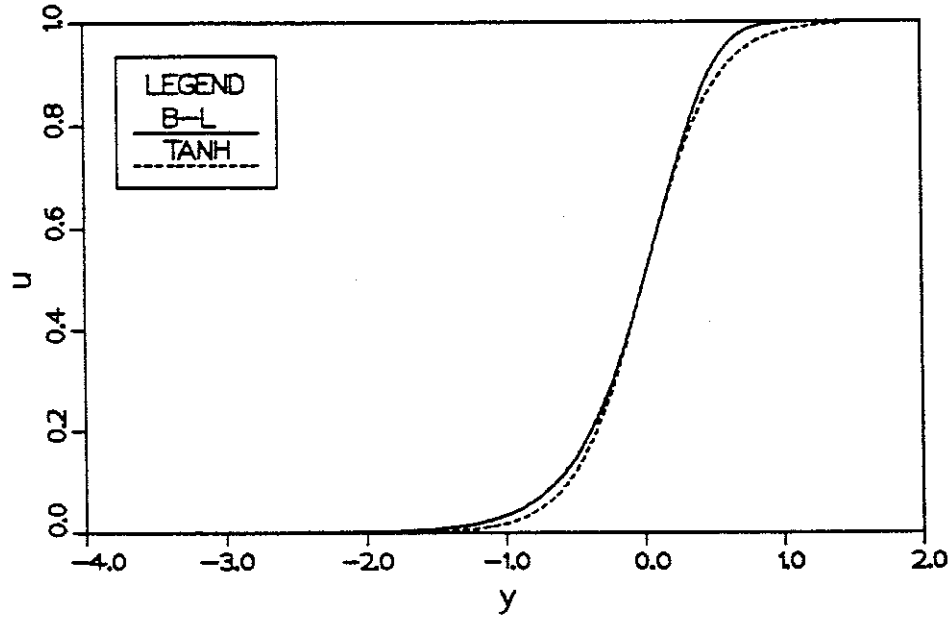

(b)

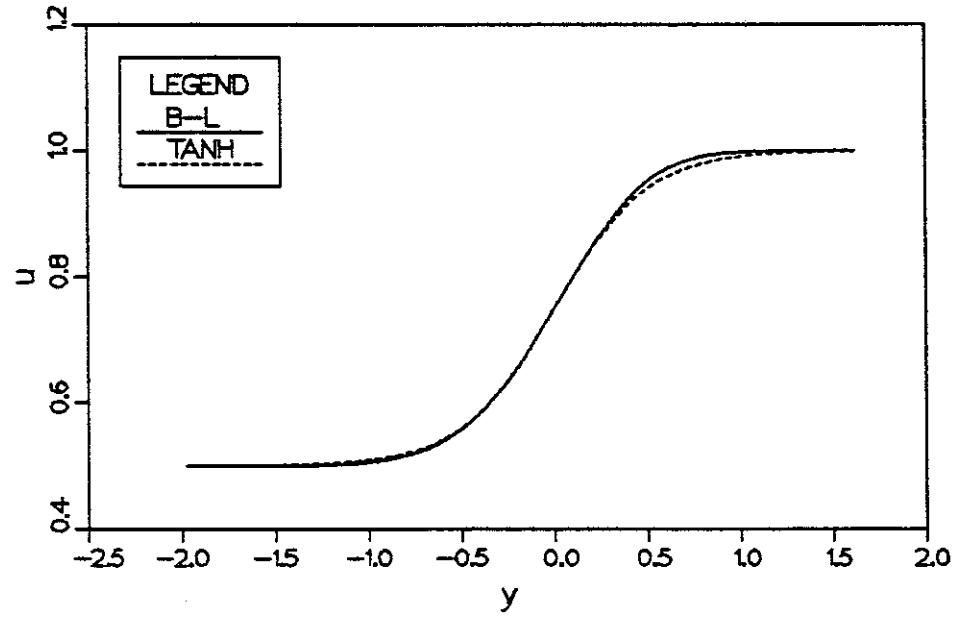

Figure 2.1 Comparison of velocity profile from solution of the boundary-layer equations with a hyperbolic tangent (a) $U_2 = 0$, (b) $U_2 = 0.5$.

(a)

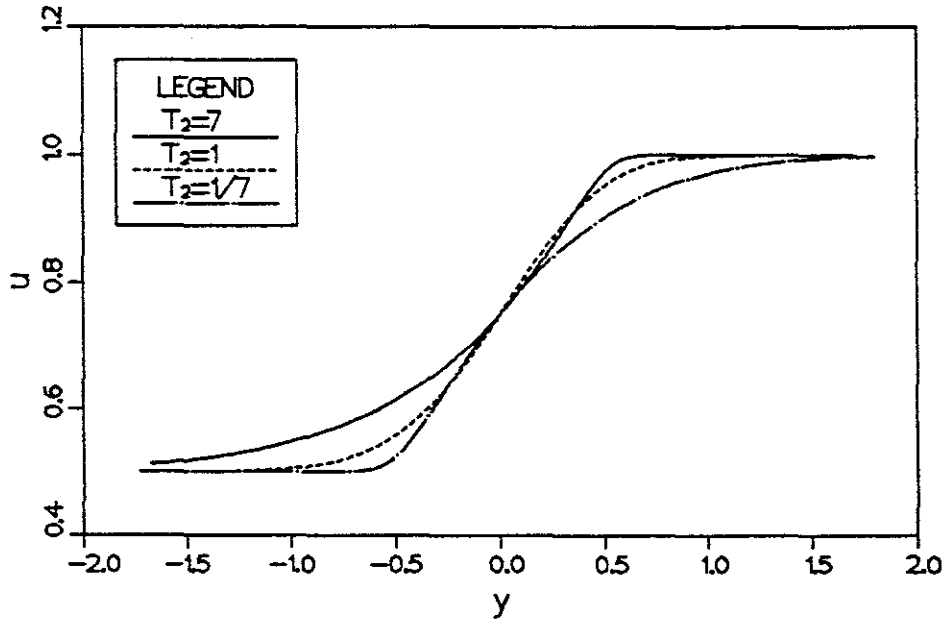

(b)

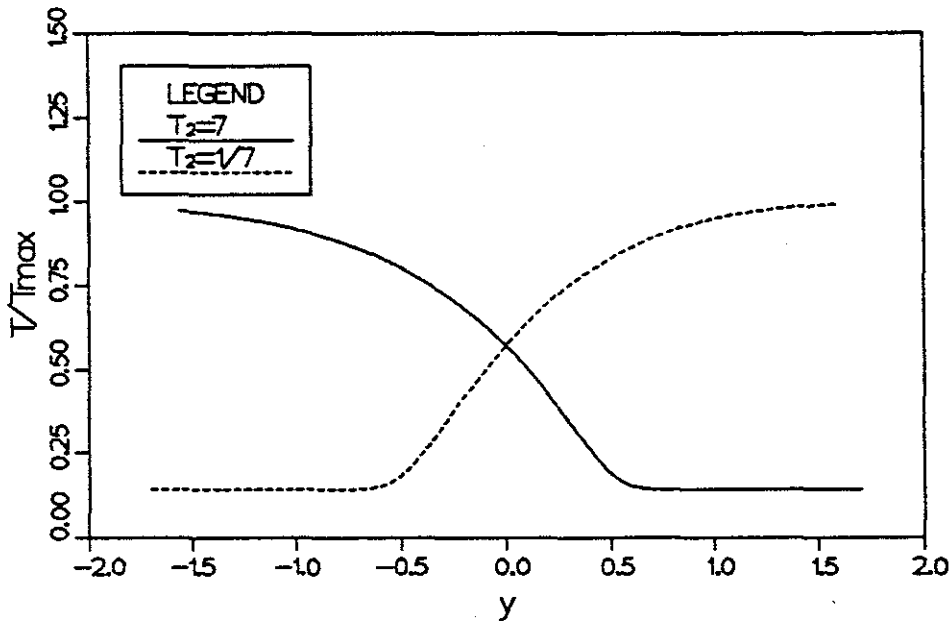

Figure 2.2 Velocity and density profiles computed from the boundary-layer equations, showing the effect of density ratio: (a) velocity profiles, (b) density profiles.

(a)

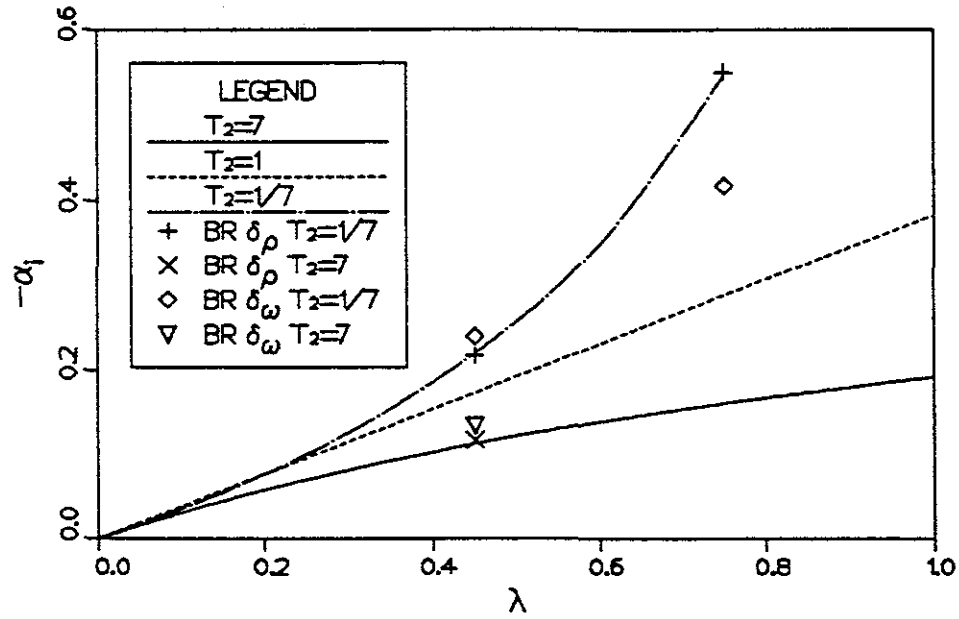

(b)

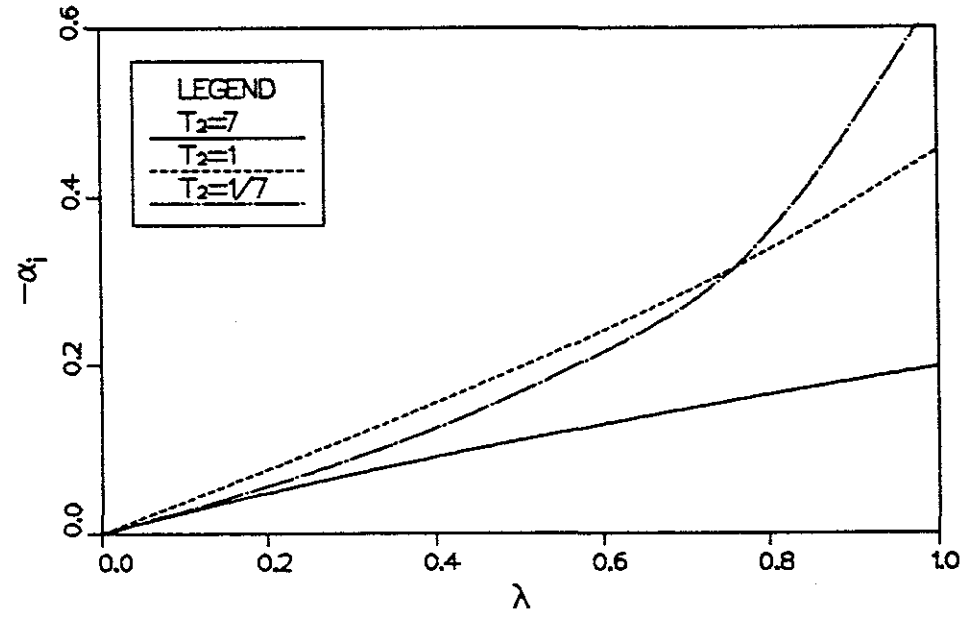

Figure 2.3 Spatial amplification rate plotted against $\lambda = (U_1^* - U_2^*)/(U_1^* + U_2^*)$, showing the combined effects of velocity and density ratio: (a) profiles from boundary-layer equations, (b) hyperbolic tangent.

(a)

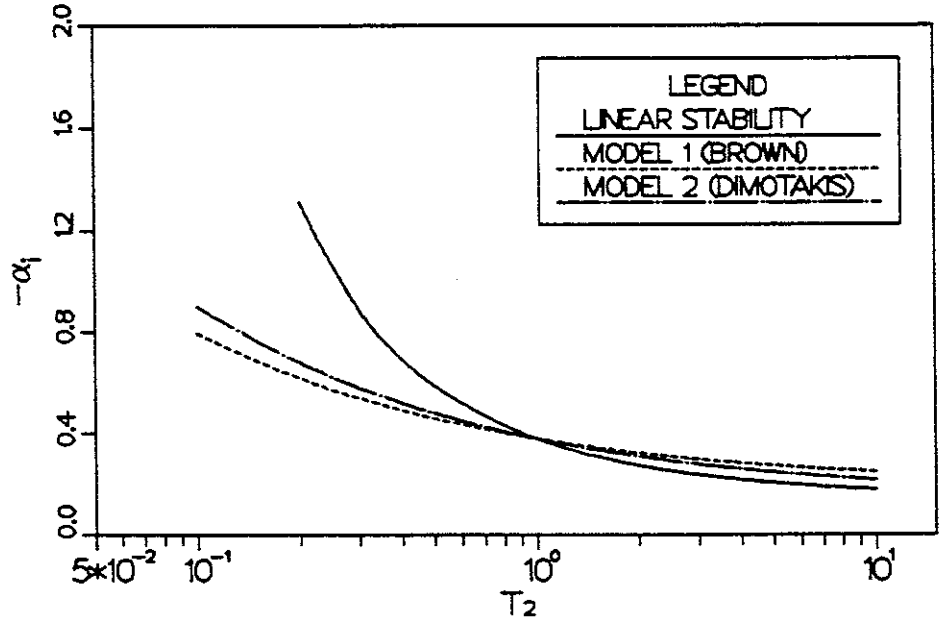

(b)

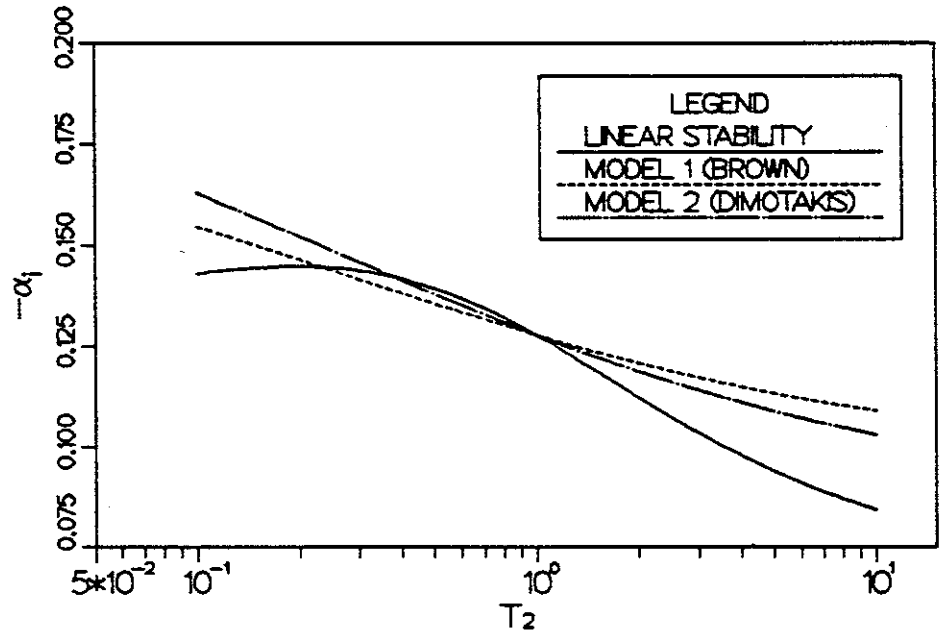

Figure 2.4 Variation in maximum spatial amplification rate with density ratio compared with models for growth rate from Brown [1974] and Dimotakis [1986], for velocity ratios: (a) $U_2 = 0$, (b) $U_2 = 0.5$.

(a)

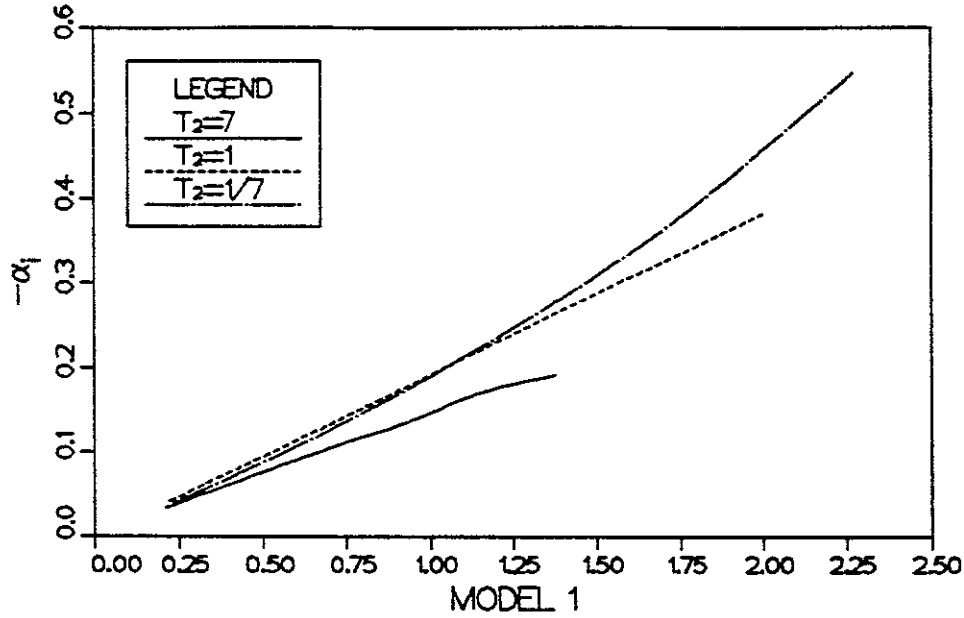

(b)

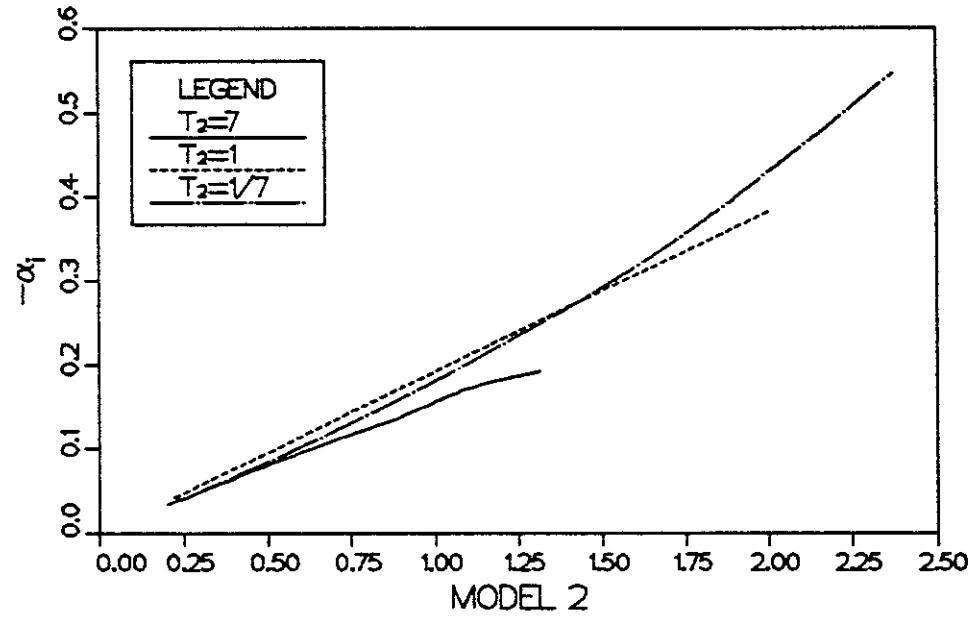

Figure 2.5 Plot of amplification rate against the functional form of the models of (a) Brown [1974] (model 1) and (b) Dimotakis [1986] (model 2).

(a)

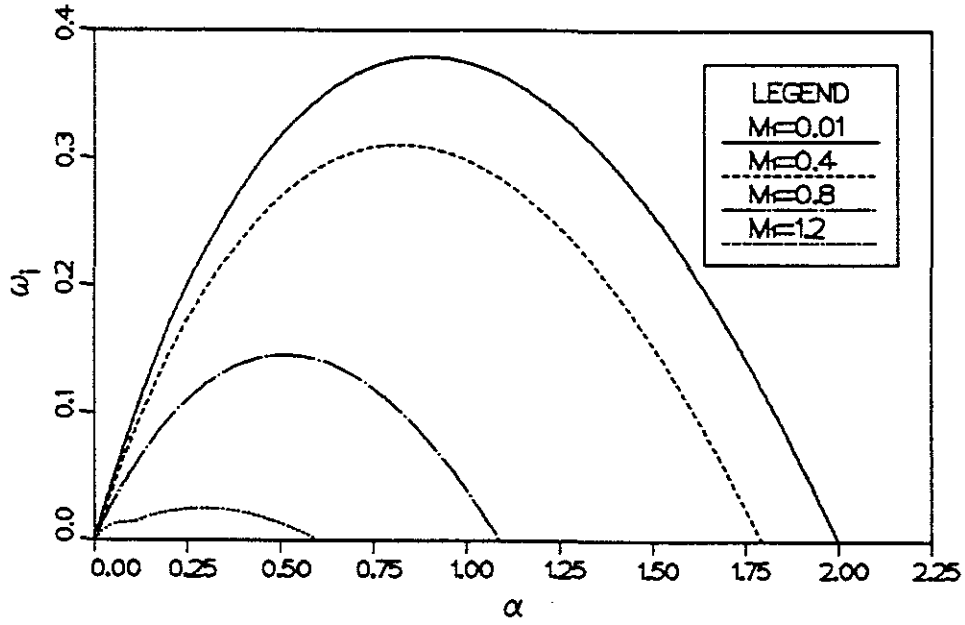

(b)

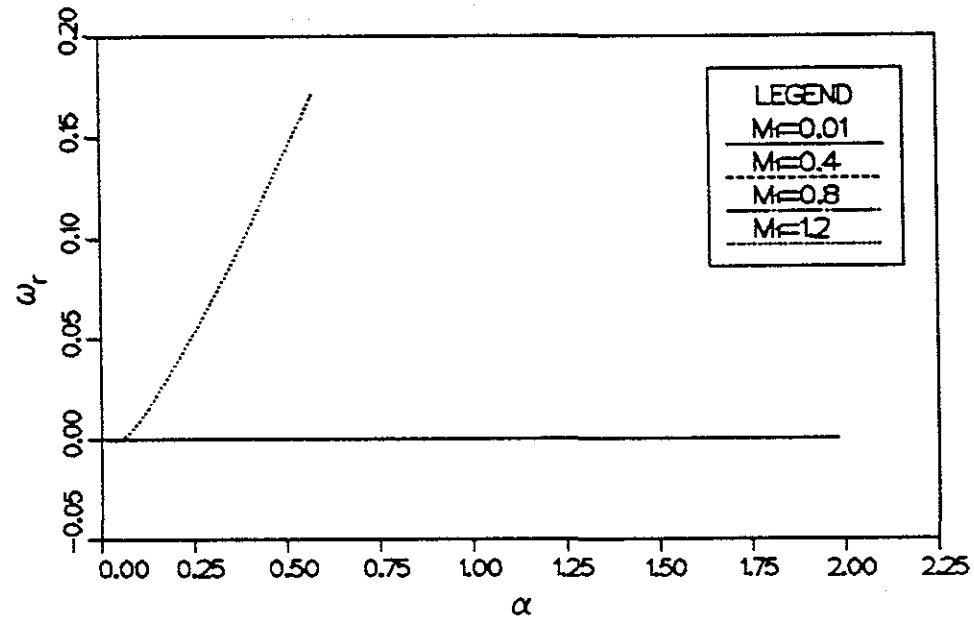

Figure 2.6 Effect of Mach number M_1 on the temporal eigenvalue (a) ω_i, (b) ω_r.

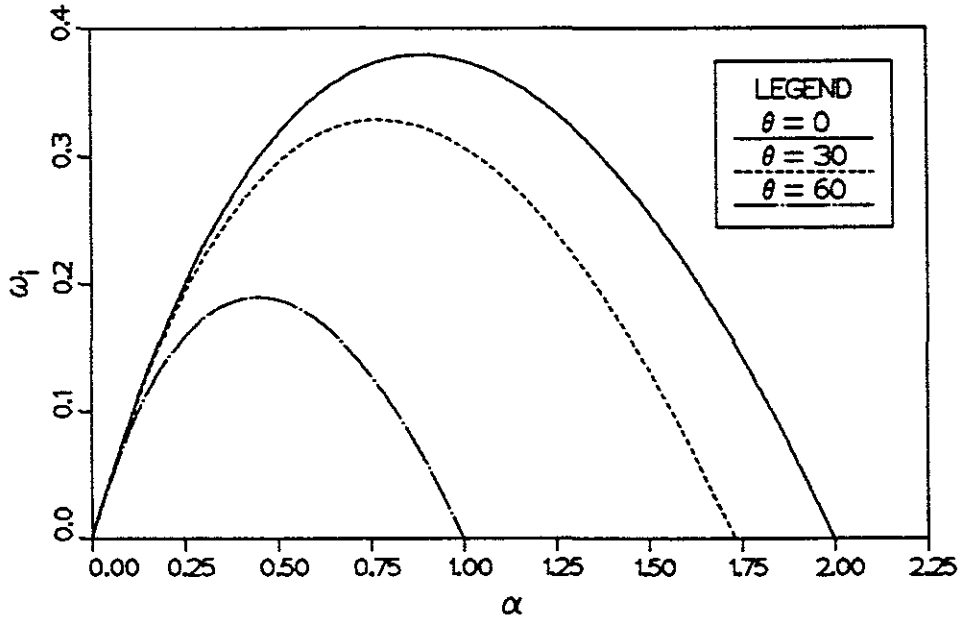

Figure 2.7 Temporal amplification rate of oblique waves at $M_1 = 0.01$

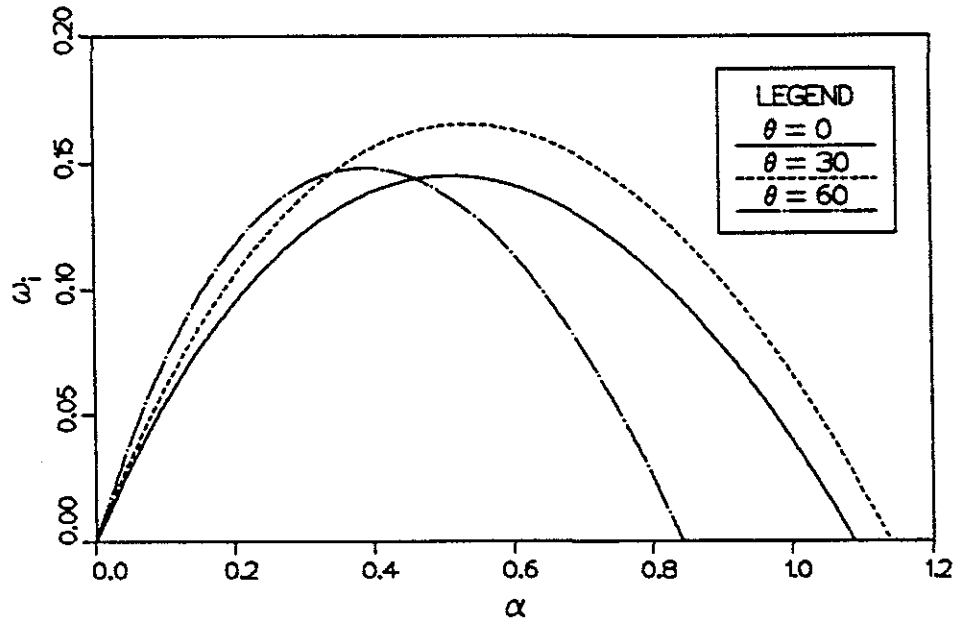

Figure 2.8 Temporal amplification rate of oblique waves at $M_1 = 0.8$

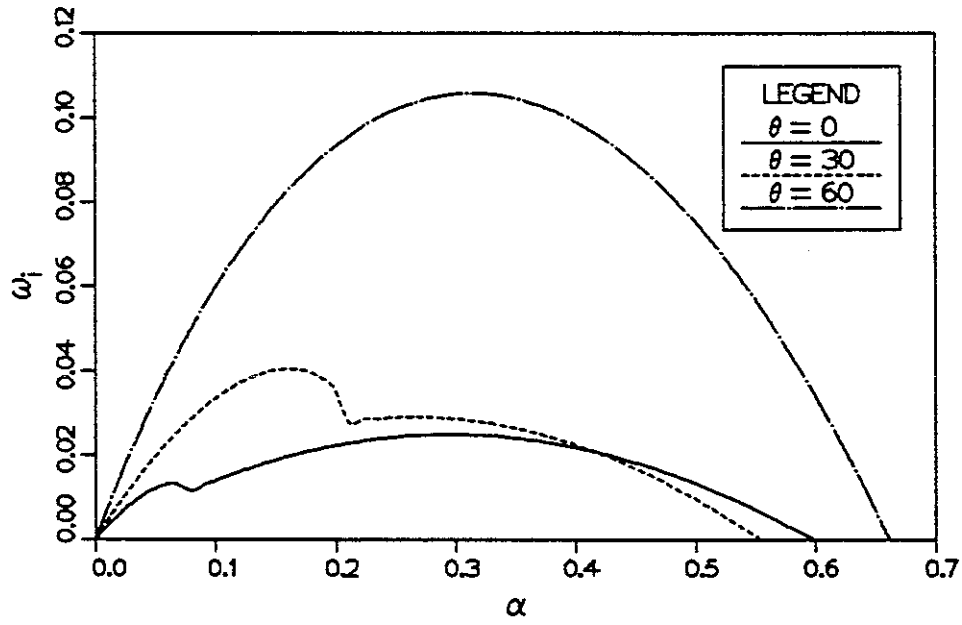

Figure 2.9 Temporal amplification rate of oblique waves at $M_1 = 1.2$

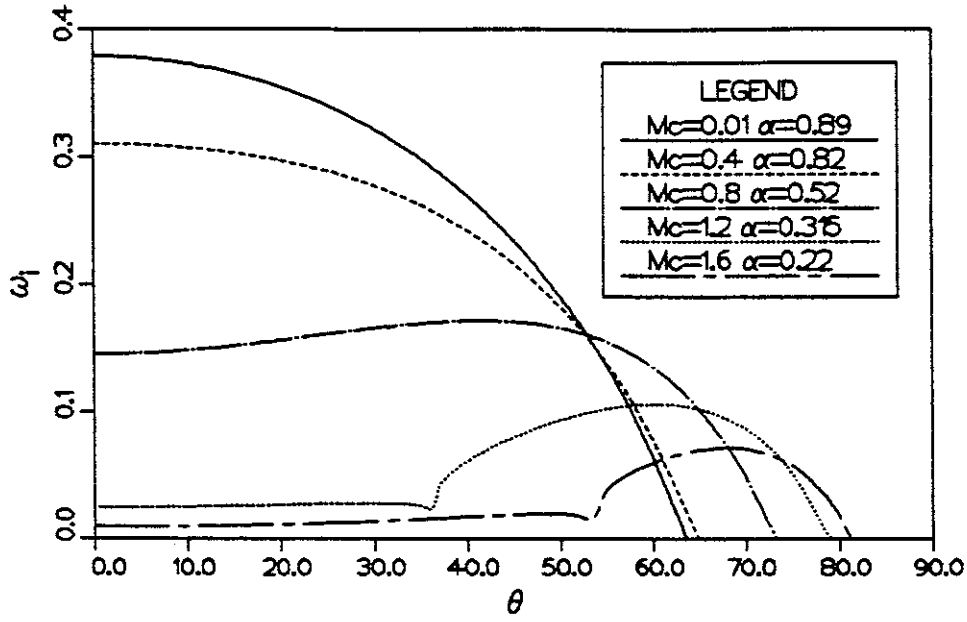

Figure 2.10 Variation of temporal amplification rate with angle of disturbance for the hyperbolic tangent velocity profile.

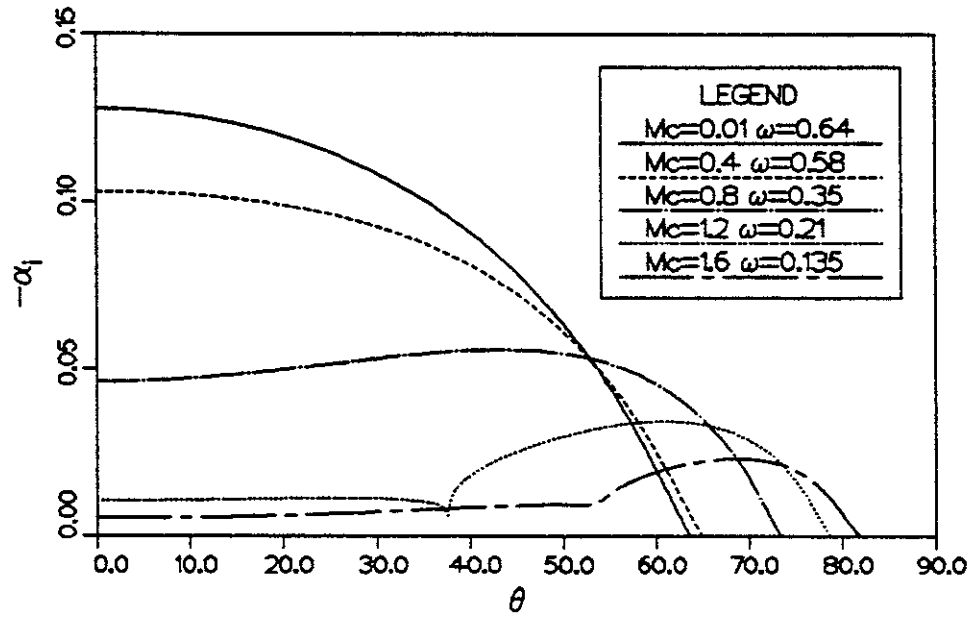

Figure 2.11 Variation of spatial amplification rate with angle of disturbance for the mixing layer with $T_2 = 1.0$ and $U_2 = 0.5$, with velocity profile from solution of the boundary-layer equations.

(a)

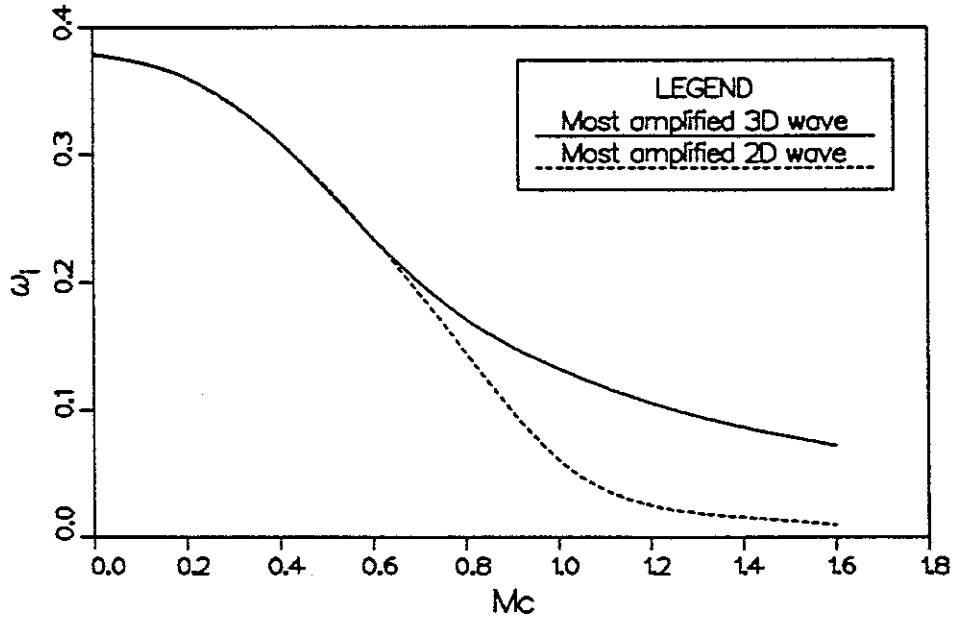

(b)

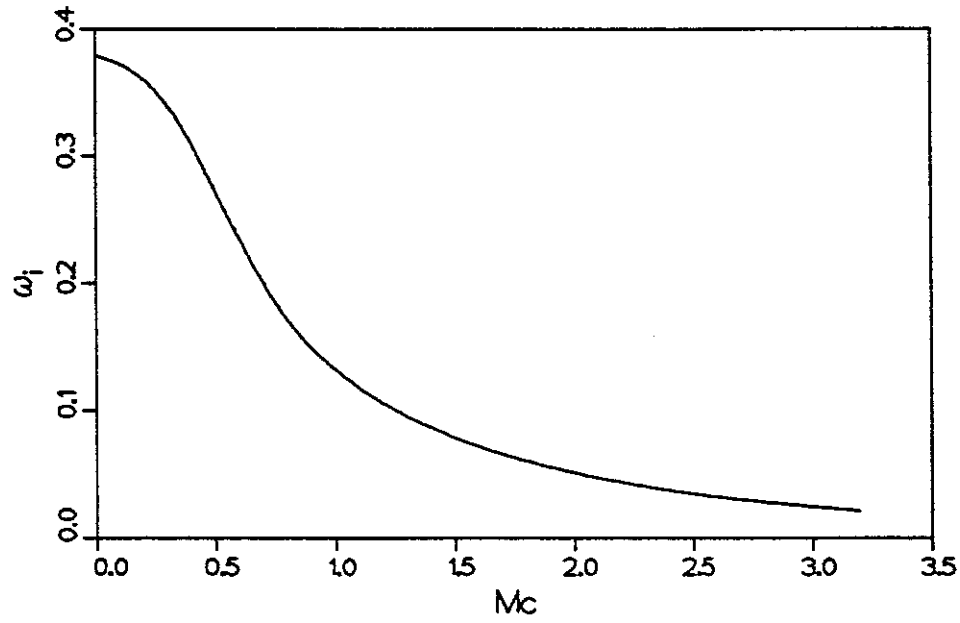

Figure 2.12 Variation of the amplification rate of the most unstable wave with Mach number, (a) comparing the most amplified wave with the most amplified two-dimensional wave, (b) extension to $M_c = 3.2$ for the most unstable wave.

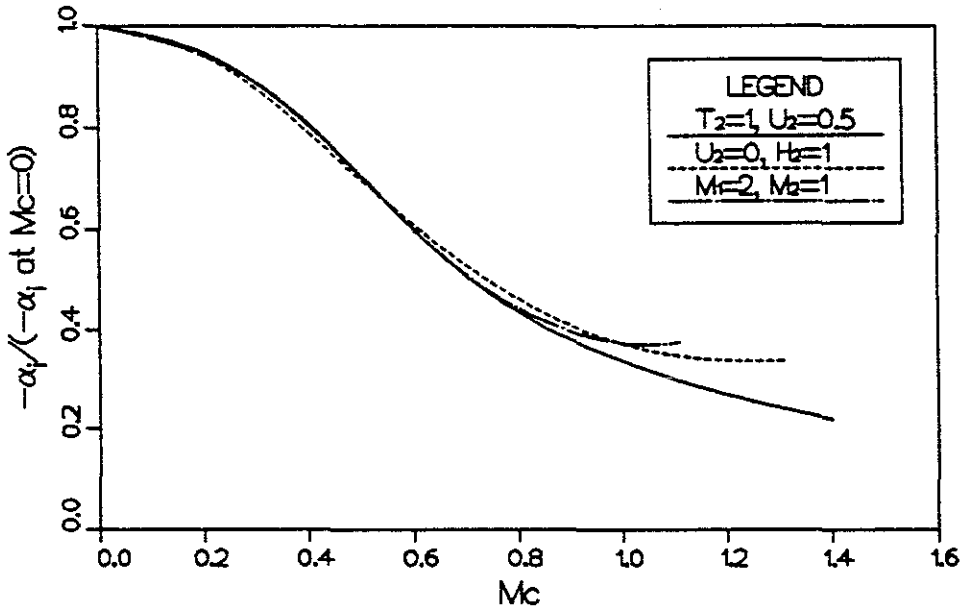

Figure 2.13 Variation of spatial amplification rate of the most unstable wave with convective Mach number for three different methods of varying convective Mach number.

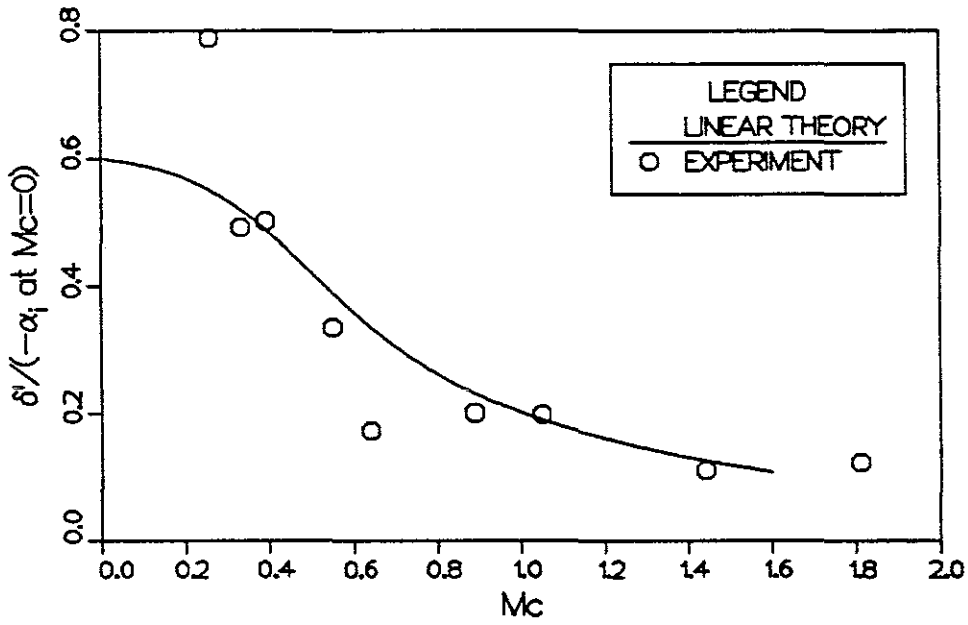

Figure 2.14 Growth rate data from Papamoschou [1986] normalized by the amplification rate of the most unstable wave, for the given velocity and density ratio, at zero Mach number

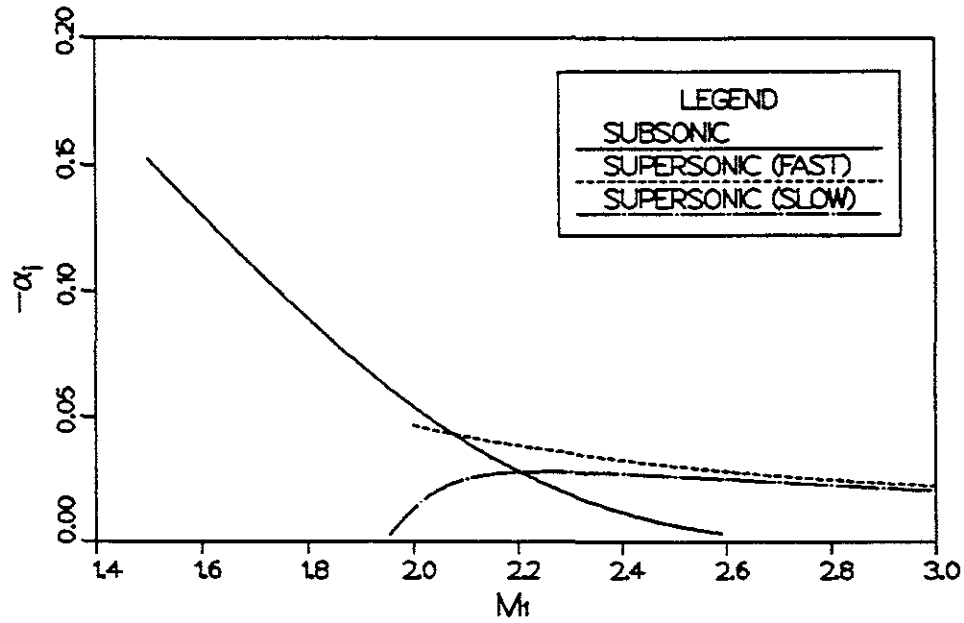

Figure 2.15 Variation in amplification rate with Mach number M_1 for the subsonic mode, the 'fast' supersonic mode, and the 'slow' supersonic mode.

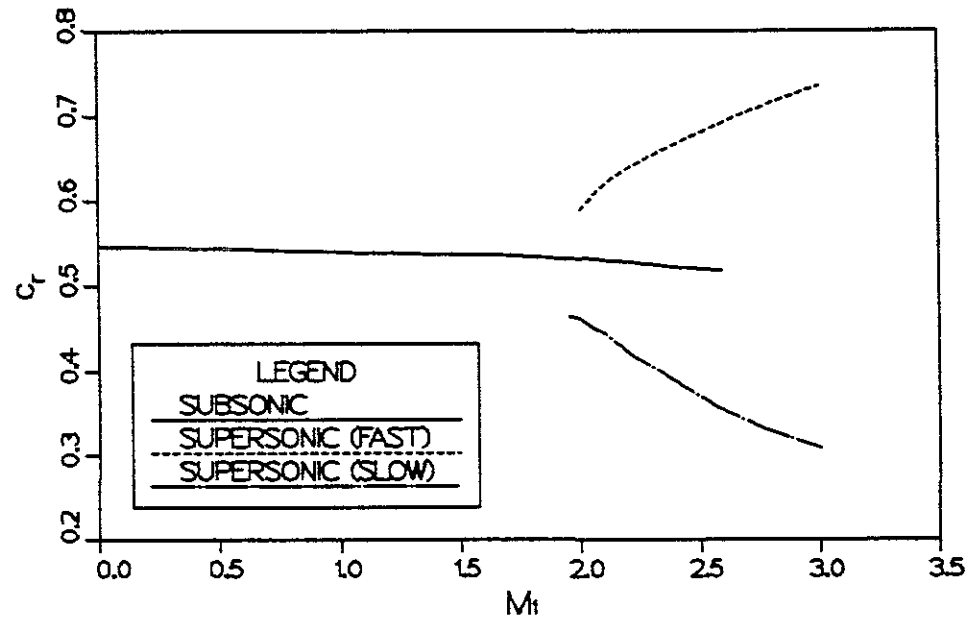

Figure 2.16 Phase speeds of subsonic and supersonic modes.

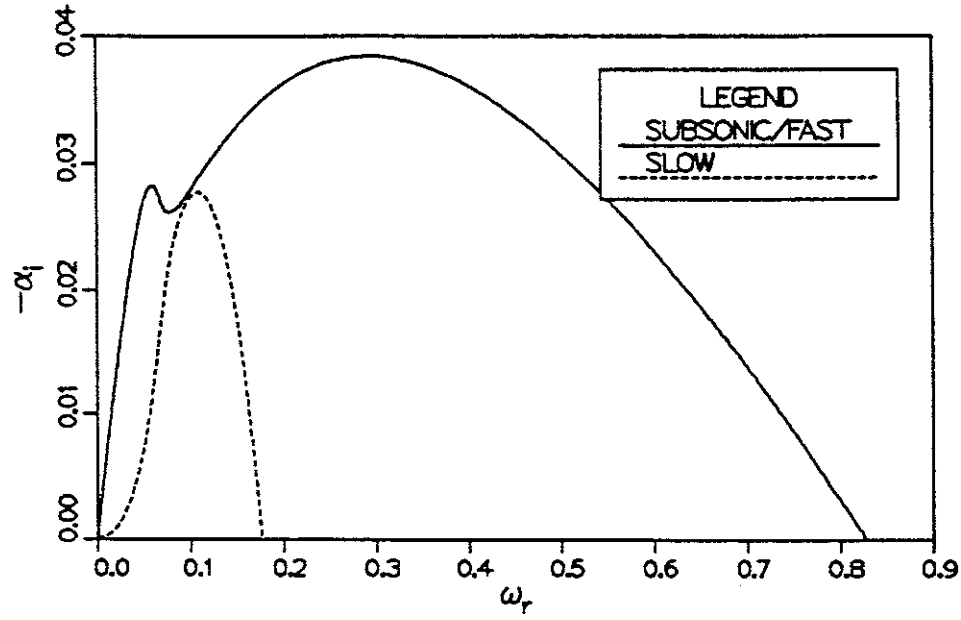

Figure 2.17 Amplification rate of supersonic modes against frequency.

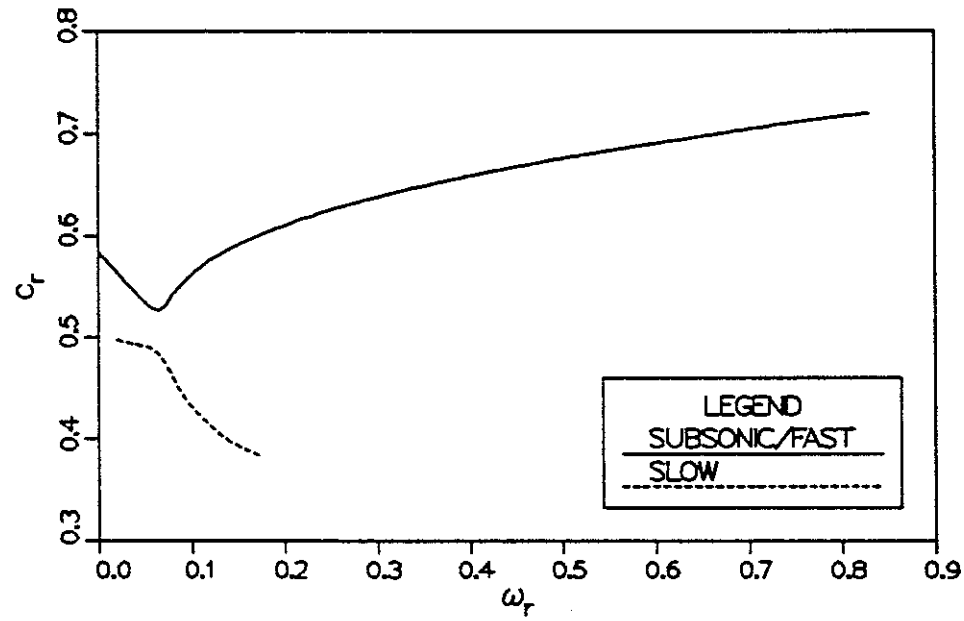

Figure 2.18 Phase speeds of supersonic modes against frequency.

(a)

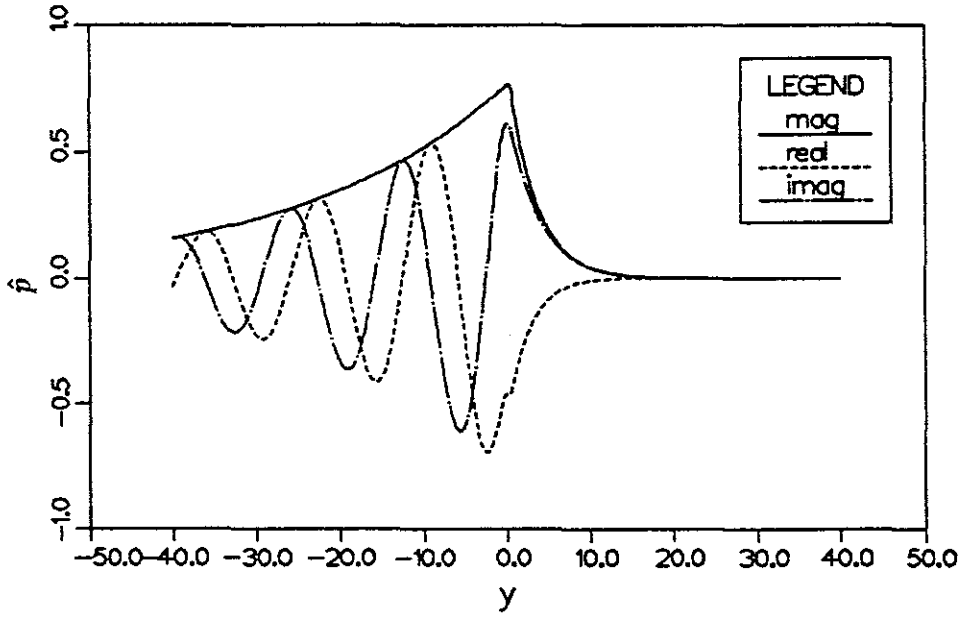
LEGEND
mag
real
imag
1.0
0.5
0.0
−0.5
−1.0
$\hat{p}$
−50.0 −40.0 −30.0 −20.0 −10.0 0.0 10.0 20.0 30.0 40.0 50.0
y

(b)

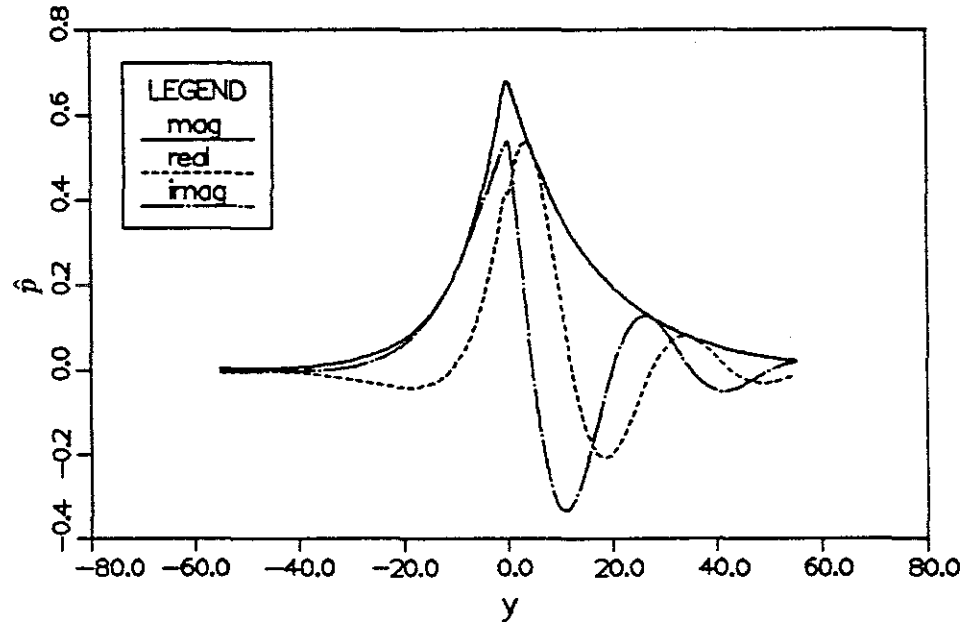
LEGEND
mag
real
imag
0.8
0.6
0.4
0.2
0.0
−0.2
−0.4
$\hat{p}$
−80.0 −60.0 −40.0 −20.0 0.0 20.0 40.0 60.0 80.0
y

(c)

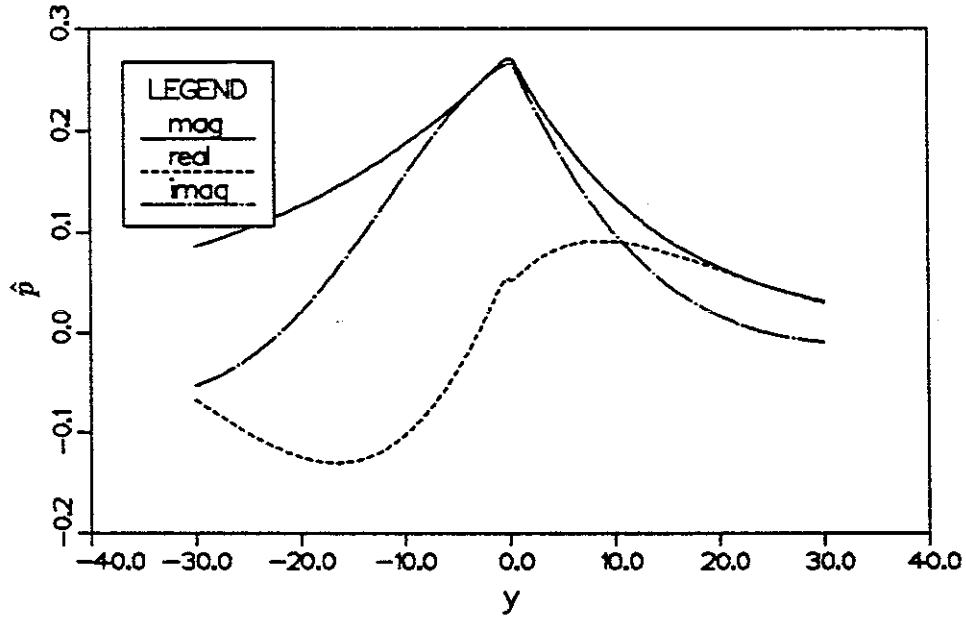

Figure 2.19 Eigenfunctions of pressure at $M_1 = 2.2$ for (a) the fast supersonic mode, (b) the slow supersonic modes and (c) the subsonic mode.

(a)

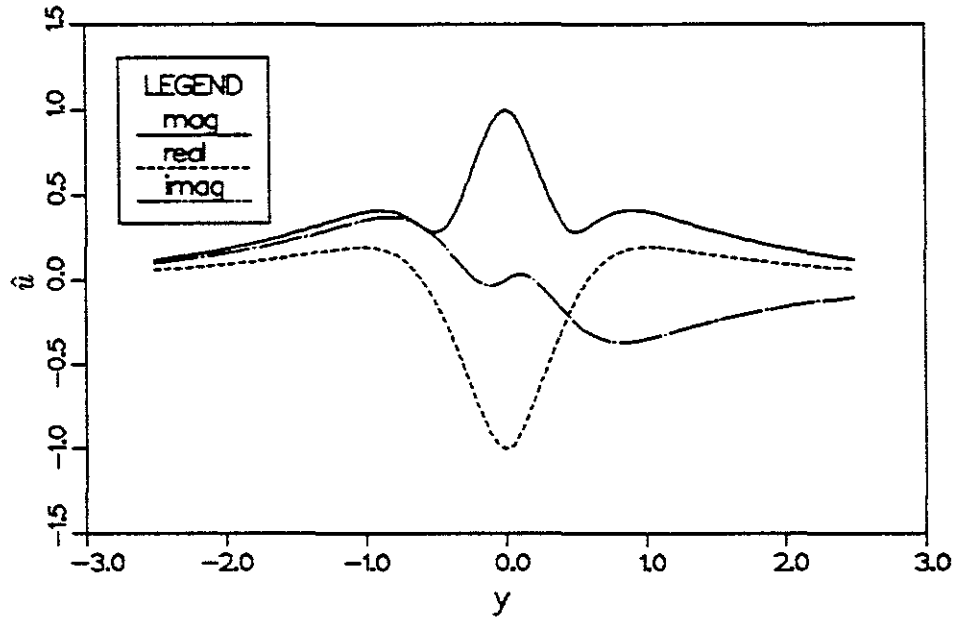
LEGEND
mag
real
imag
$\hat{u}$
y
1.5
1.0
0.5
0.0
−0.5
−1.0
−1.5
−3.0
−2.0
−1.0
0.0
1.0
2.0
3.0

(b)

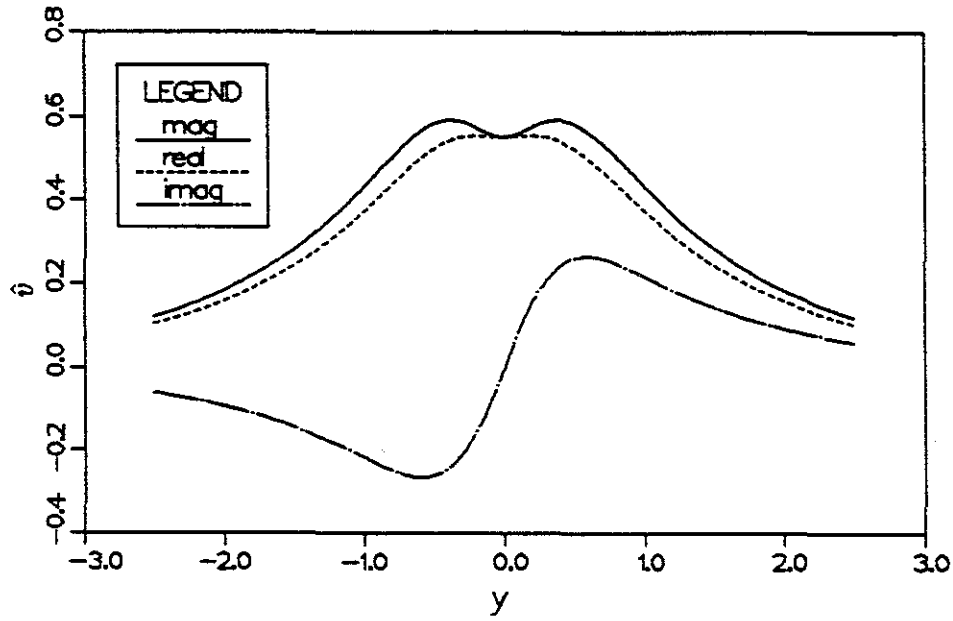
LEGEND
mag
real
imag
$\hat{v}$
y
0.8
0.6
0.4
0.2
0.0
−0.2
−0.4
−3.0
−2.0
−1.0
0.0
1.0
2.0
3.0

(c)

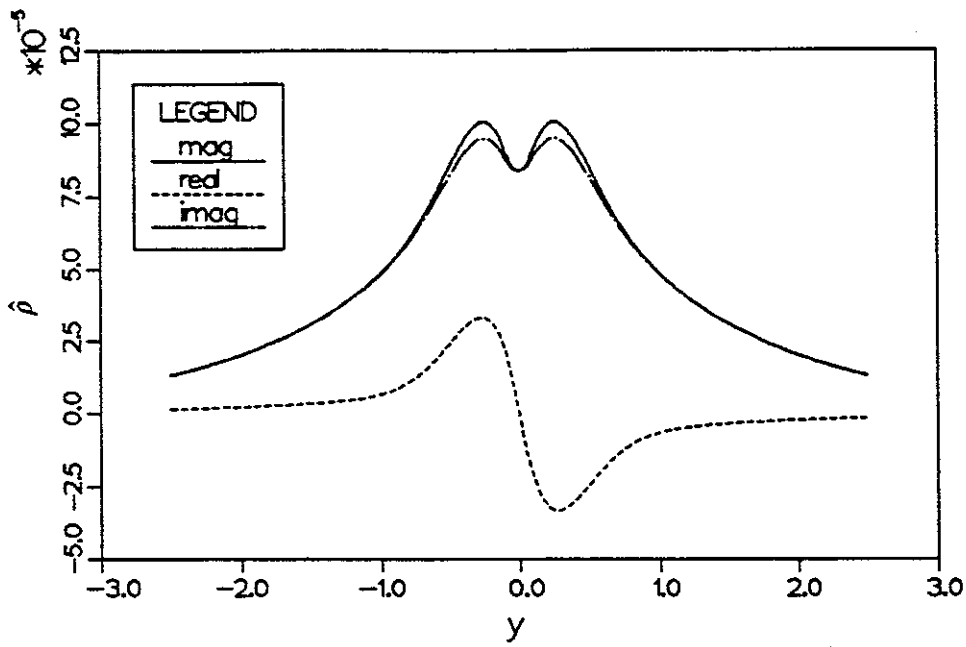

(d)

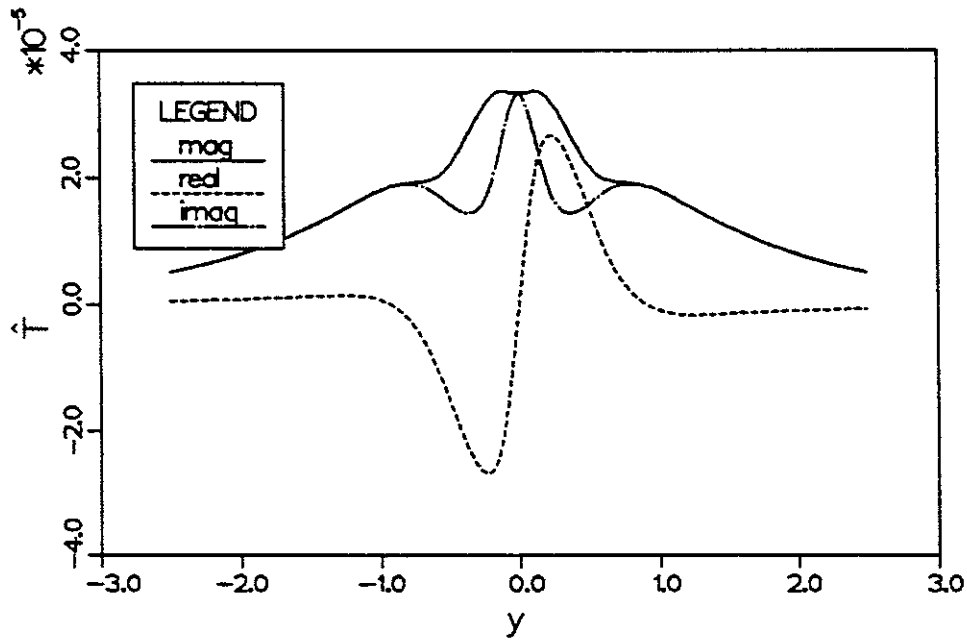

Figure 2.20 Eigenfunctions from temporal stability analysis at $M_1 = 0.01$ (a) $\hat{u}$, (b)$\hat{v}$, (c)$\hat{\rho}$, (d)$\hat{T}$.

(a)

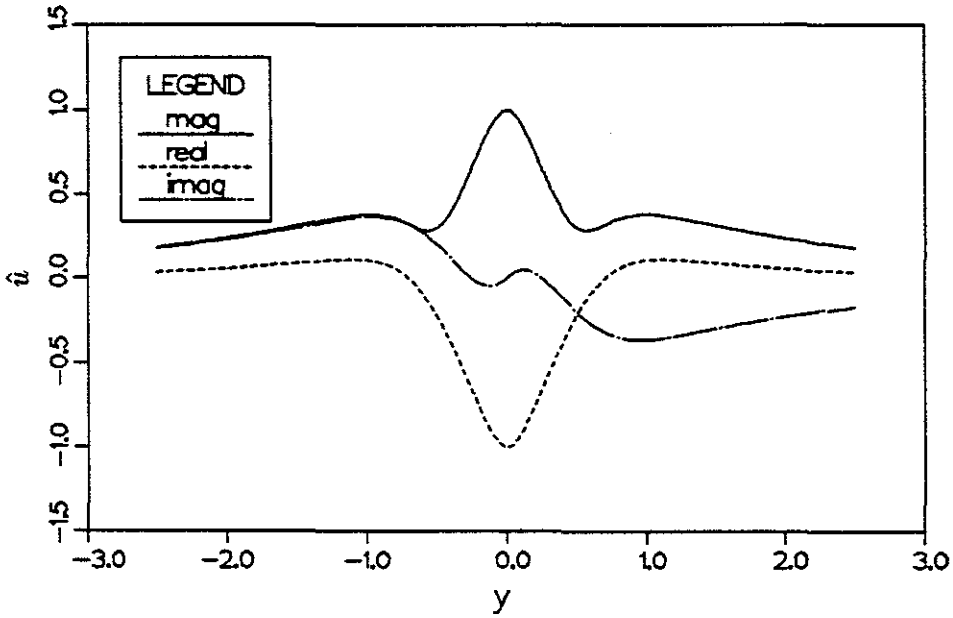
LEGEND
mag
real
imag
1.5
1.0
0.5
0.0
−0.5
−1.0
−1.5
û
−3.0
−2.0
−1.0
0.0
1.0
2.0
3.0
y

(b)

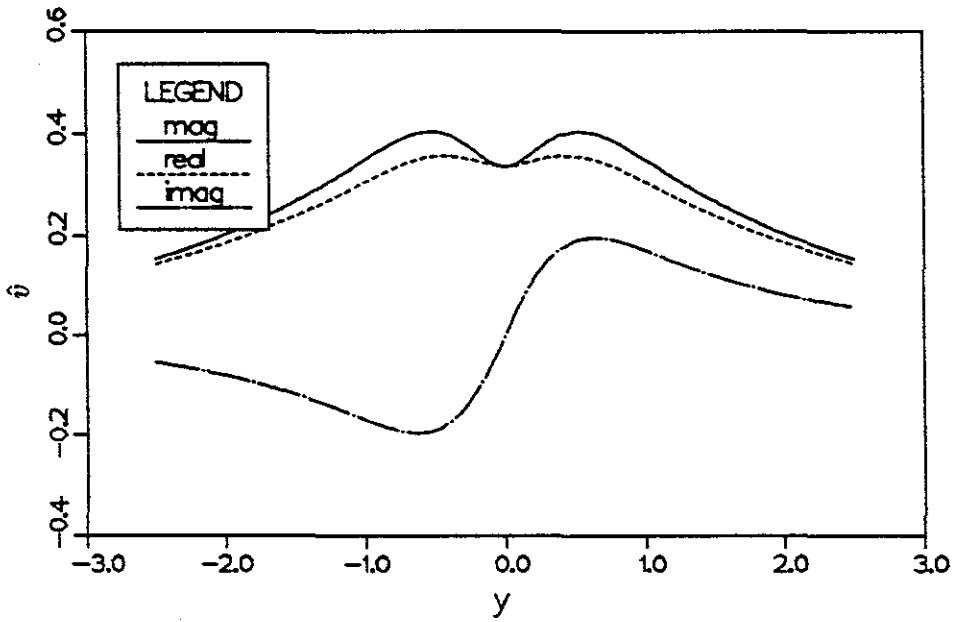
LEGEND
mag
real
imag
0.6
0.4
0.2
0.0
−0.2
−0.4
v̂
−3.0
−2.0
−1.0
0.0
1.0
2.0
3.0
y

(c)

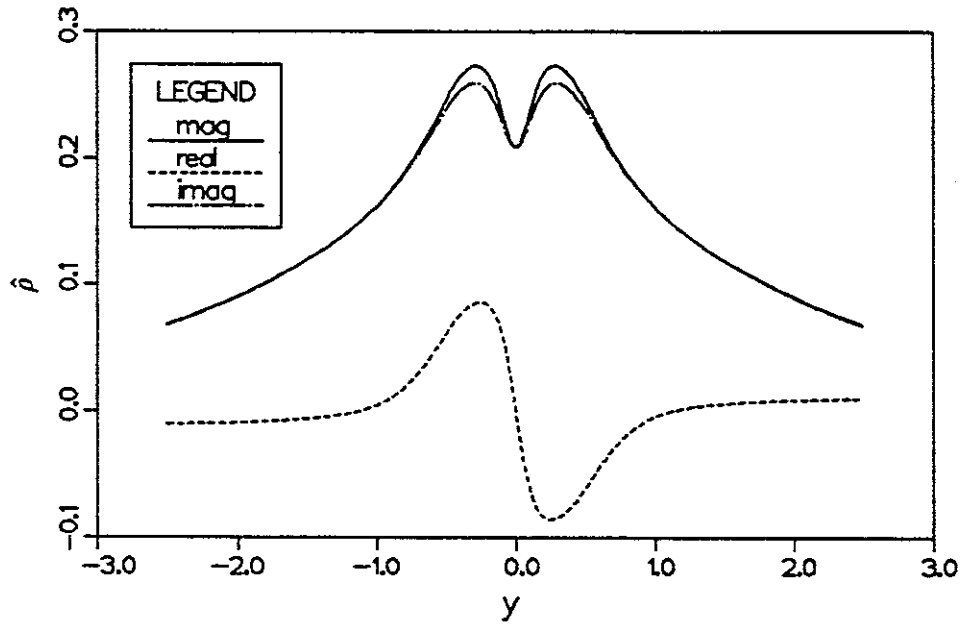

(d)

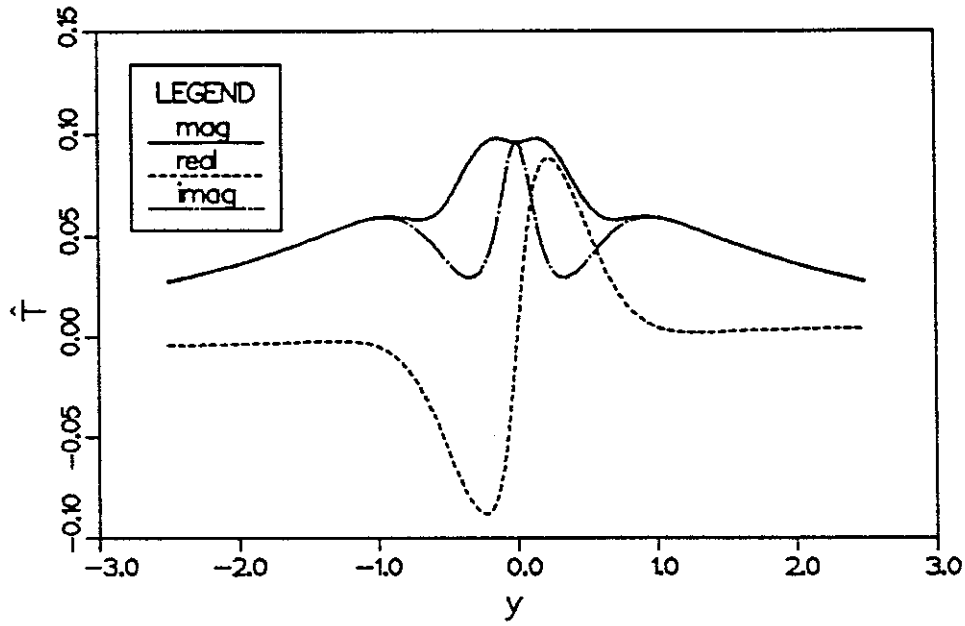

Figure 2.21 Eigenfunctions from temporal stability analysis at $M_1 = 0.6$ (a) $\hat{u}$, (b)$\hat{v}$, (c)$\hat{\rho}$, (d)$\hat{T}$.

(a) max=2.79 min=-0.105

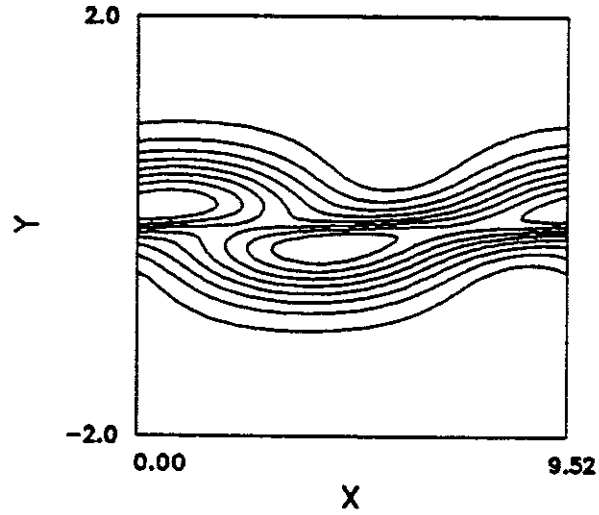

(b) max=3.30 min=-9.93e-2

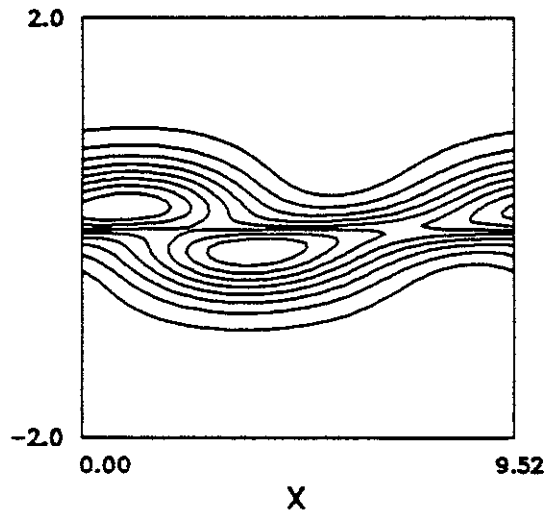

(c) max=1.10 min=0.809

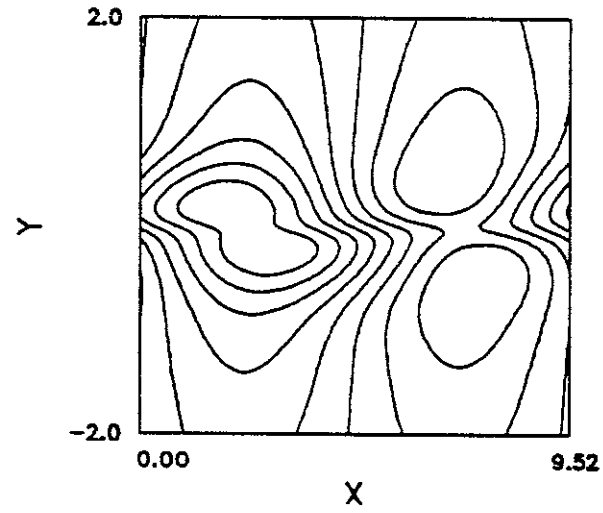

(d) max=1.99 min=1.98

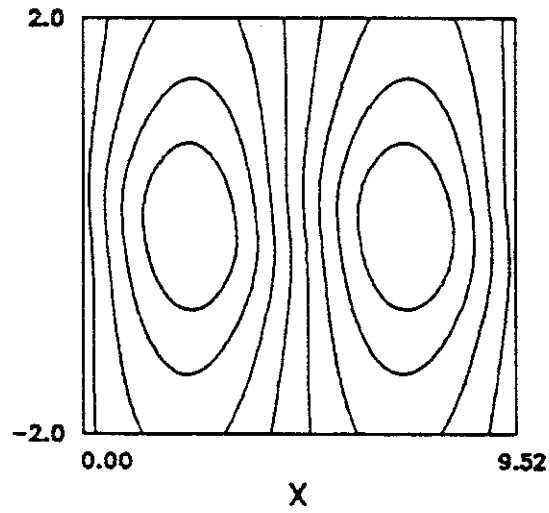

(e) max=1.20e–3 min=–1.20e–3

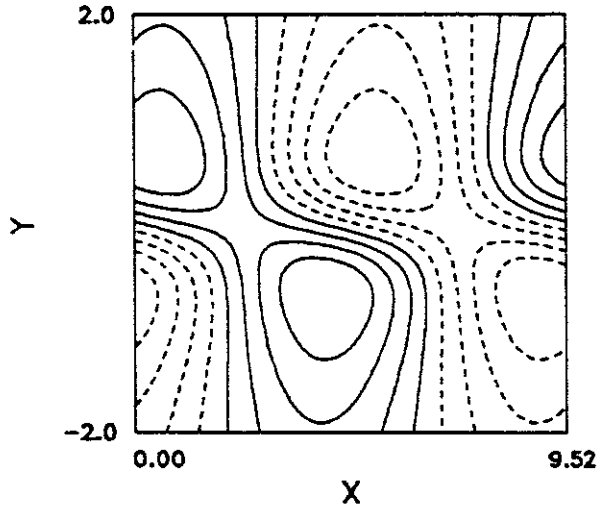

(f) max=1.37e–3 min=–1.41e–3

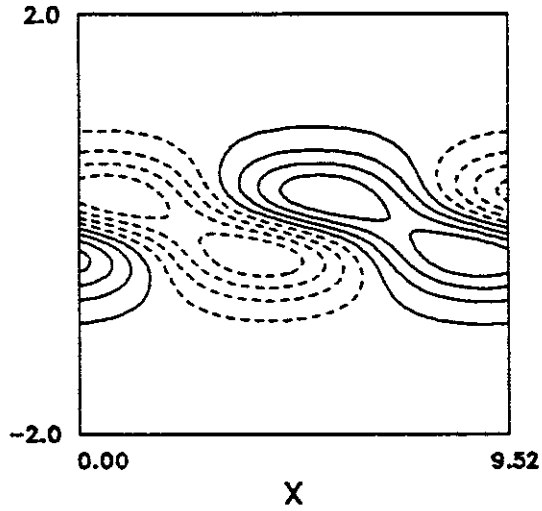

(g) max=4.68e–4 min=–4.78e–4

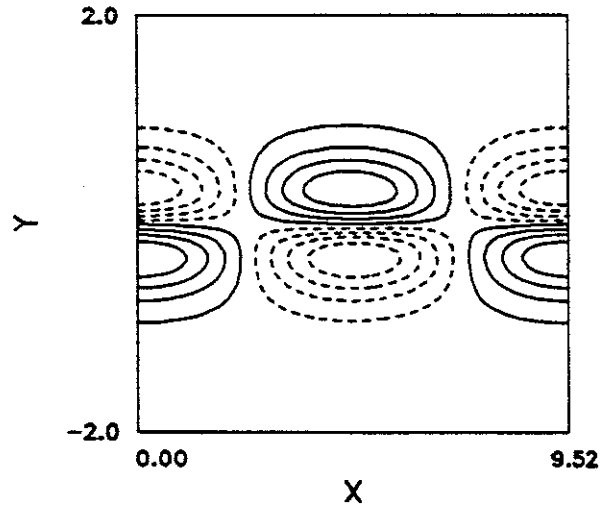

Figure 2.22 Contour plots from linear eigenfunctions at $M_1 = 0.6$ (a) ω_z, (b) ω_z/ρ, (c) density, (d) pressure, (e) dilatation, (f) dilatation term, (g) baroclinic term.

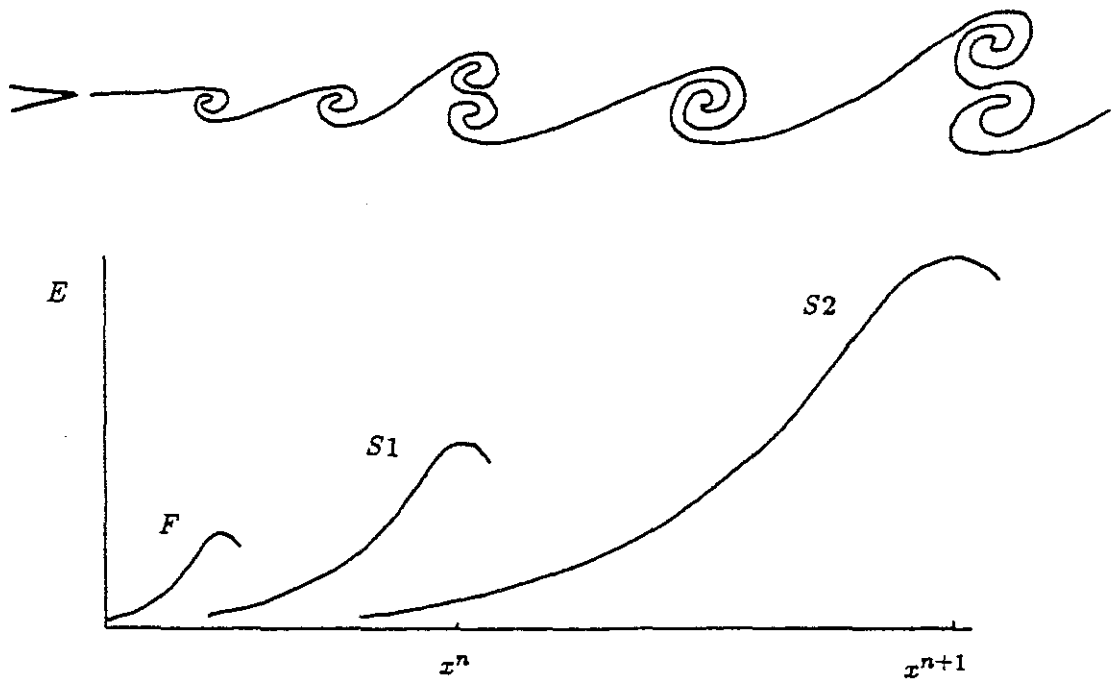

Figure 2.23 Schematic of the successive growth of linear waves in the spatially-developing mixing layer.

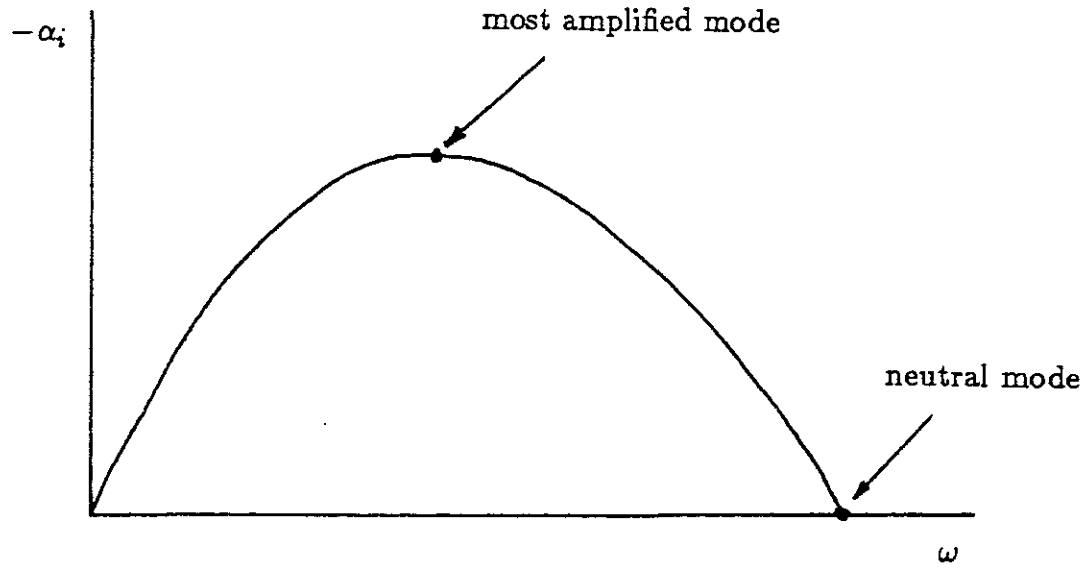

Figure 2.24 Amplification rate versus frequency, defining the most amplified wave, and the neutral wave.

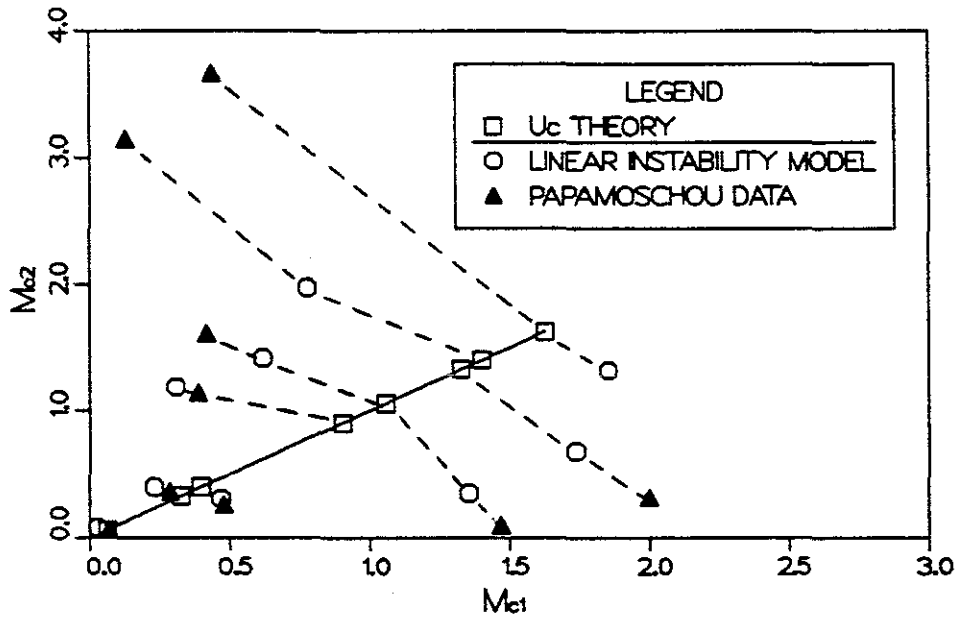

Figure 2.25 Plot of M_{c1} versus M_{c2} showing a comparison between the theoretical U_c from equation (1.2), the linear stability prediction (the phase speed of the neutral mode), and the experimental data from Papamoschou [1989].

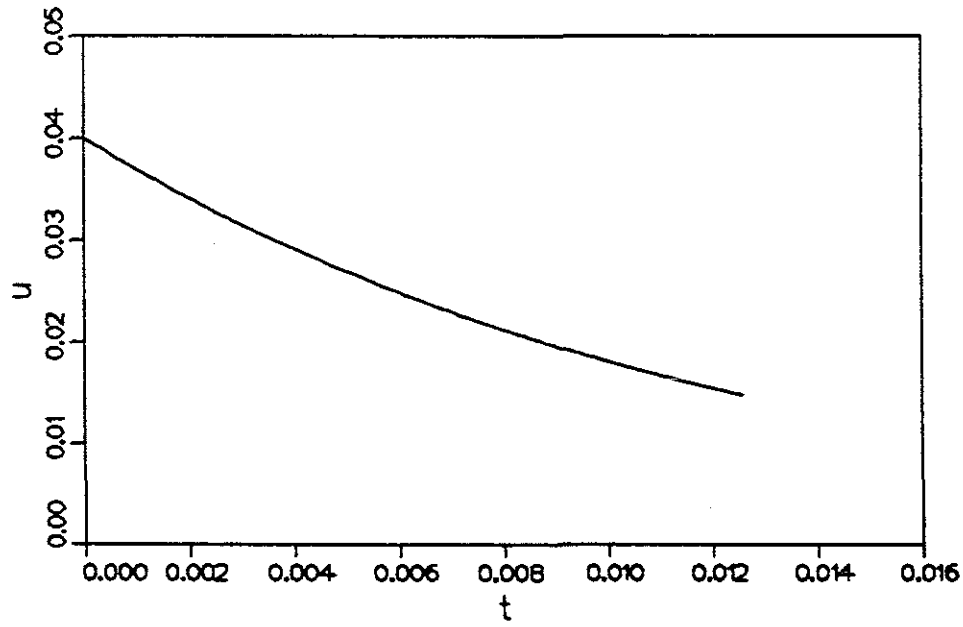

Figure 3.1 Decay of u velocity at $x = 0.5$ $z = 0.25$, for Taylor-Green problem.

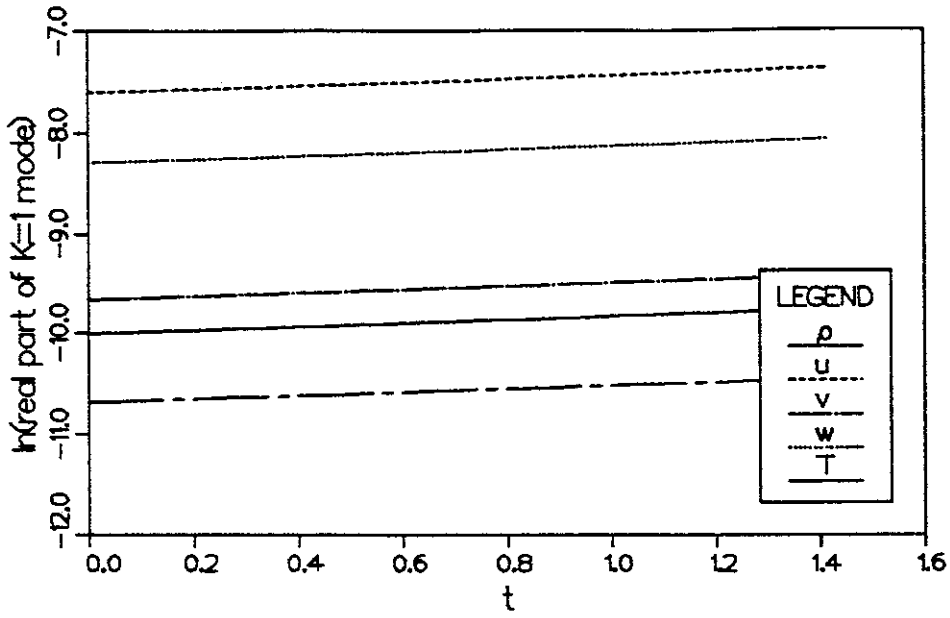

Figure 3.2 Check on linear growth rates for the inviscid eigenfunctions in the three-dimensional code.

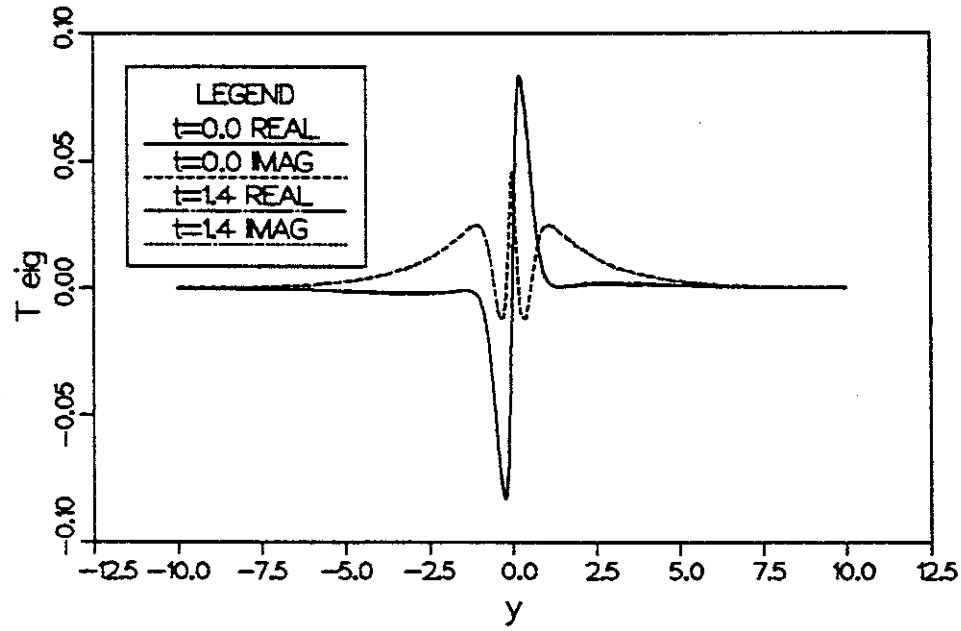

Figure 3.3 Temperature eigenfunction from direct simulation, compared to initial eigenfunction.

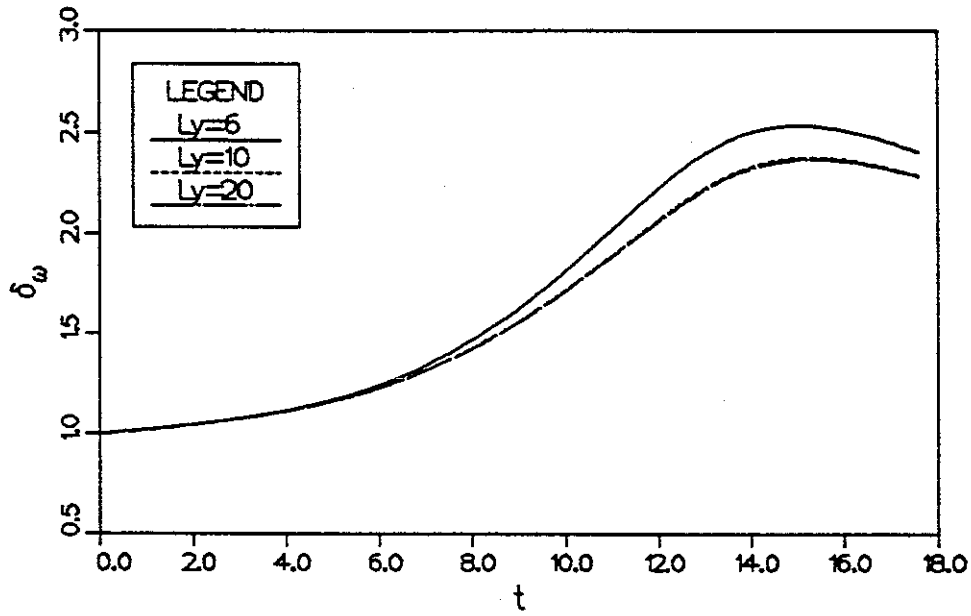

Figure 3.4 Growth of vorticity thickness with time, showing the effect of changing the position of the free-stream boundary condition.

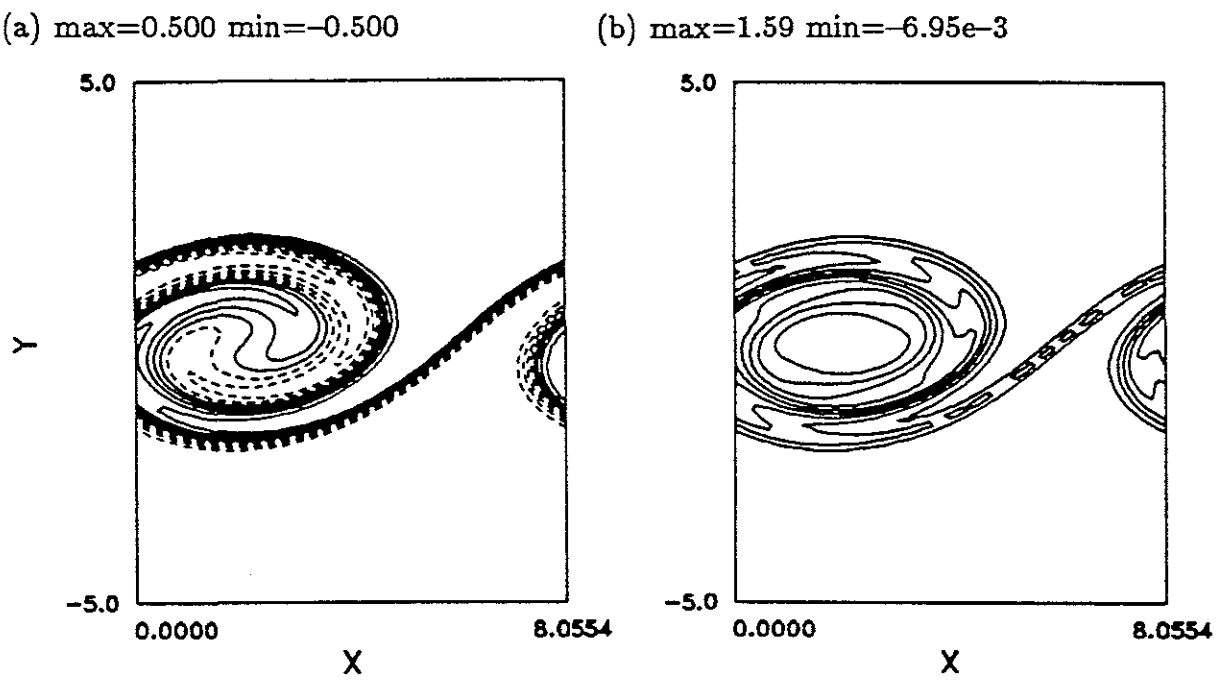

Figure 3.5 Developed structure for $L_y = 10$ (a) mixture fraction (b) vorticity.

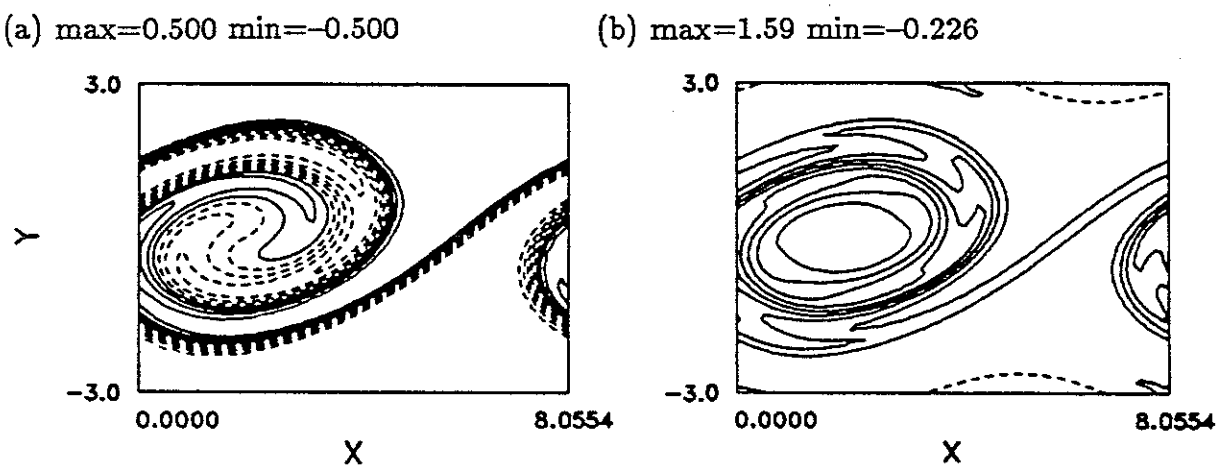

Figure 3.6 Developed structure for $L_y = 6$ (a) mixture fraction (b) vorticity.

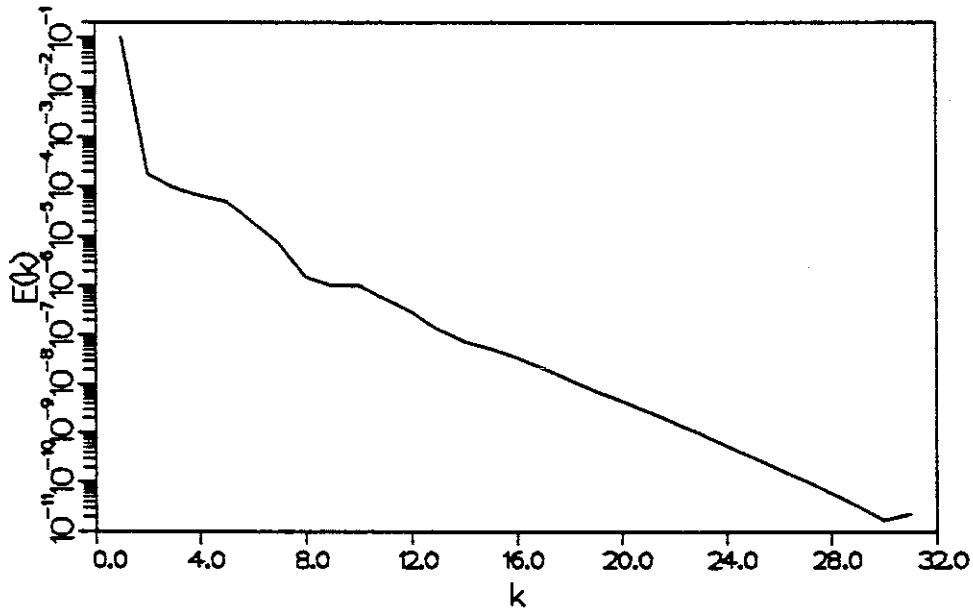

Figure 3.7 Energy spectrum for the case $L_y = 10$, $M_1 = 0.4$.

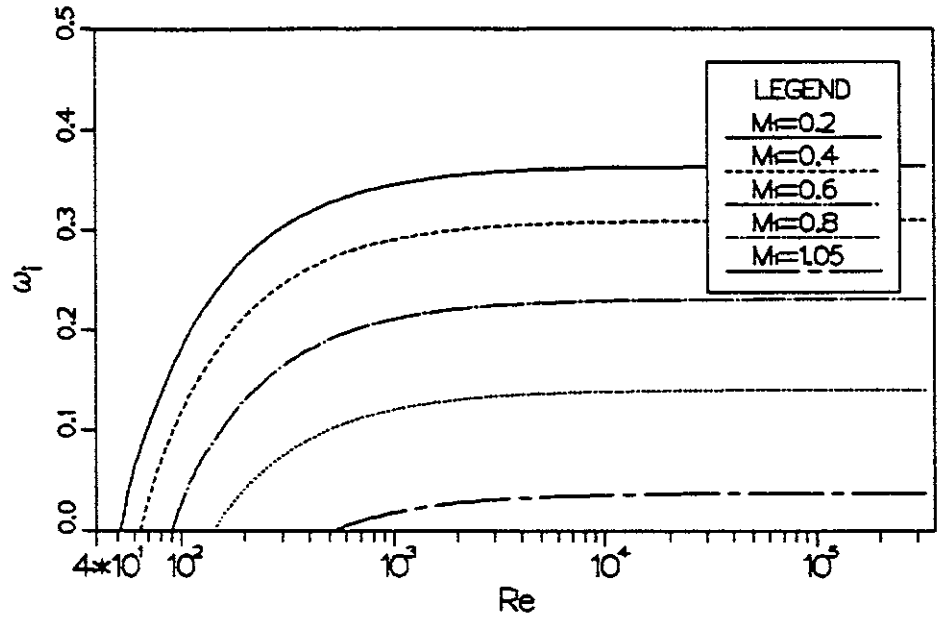

Figure 4.1 Linear amplification rate of the inviscid eigenfunction, as a function of Reynolds number.

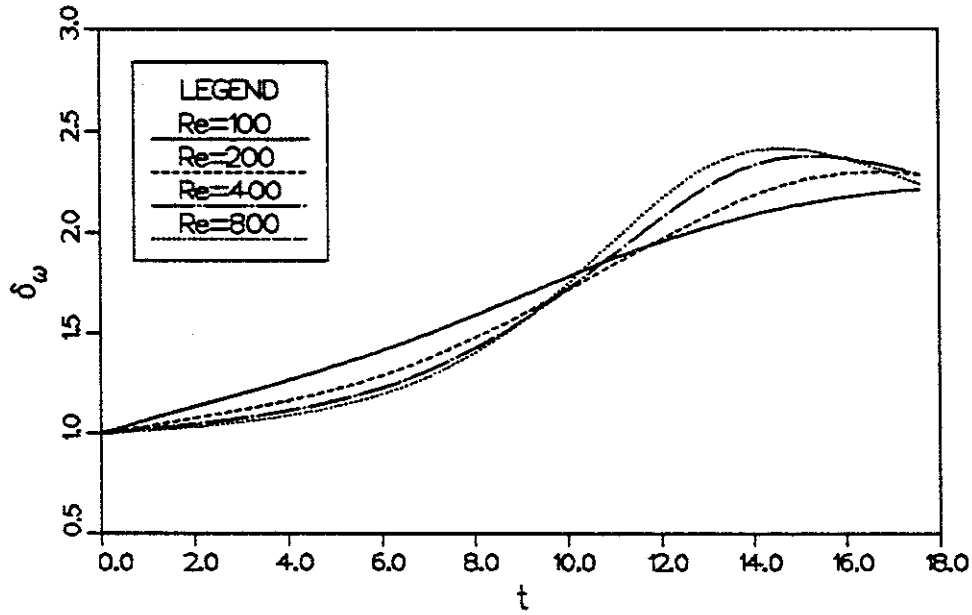

Figure 4.2 Effect of Reynolds number on the growth history of vorticity thickness at $M_1 = 0.4$.

(a) max=0.500 min=–0.500 (b) max=1.29 min=–3.06e–3

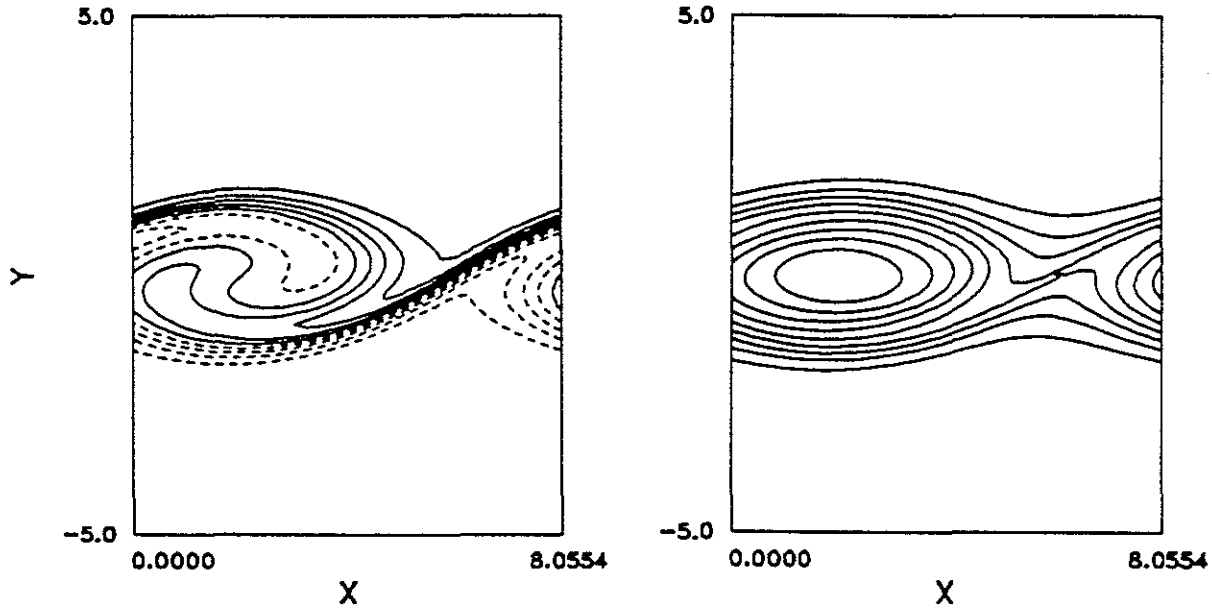

Figure 4.3 Developed structure at $M_1 = 0.4$, $Re = 100$ (a) mixture fraction (b) vorticity.

(a) max=0.509 min=–0.509 (b) max=1.65 min=–8.61e–3

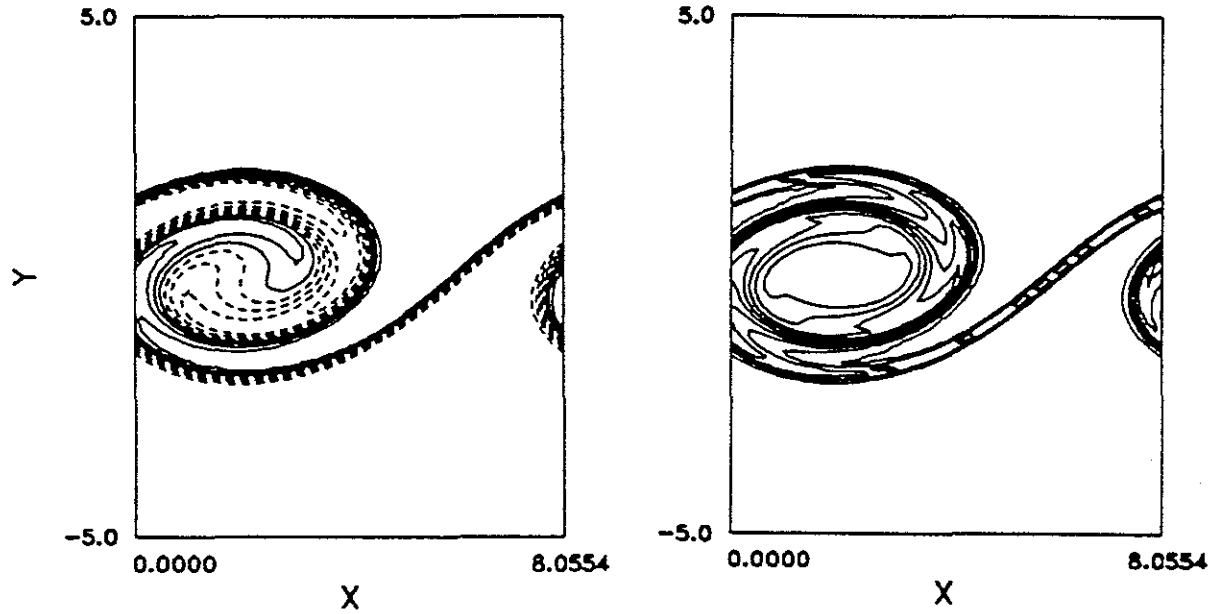

Figure 4.4 Developed structure at $M_1 = 0.4$, $Re = 800$ (a) mixture fraction (b) vorticity.

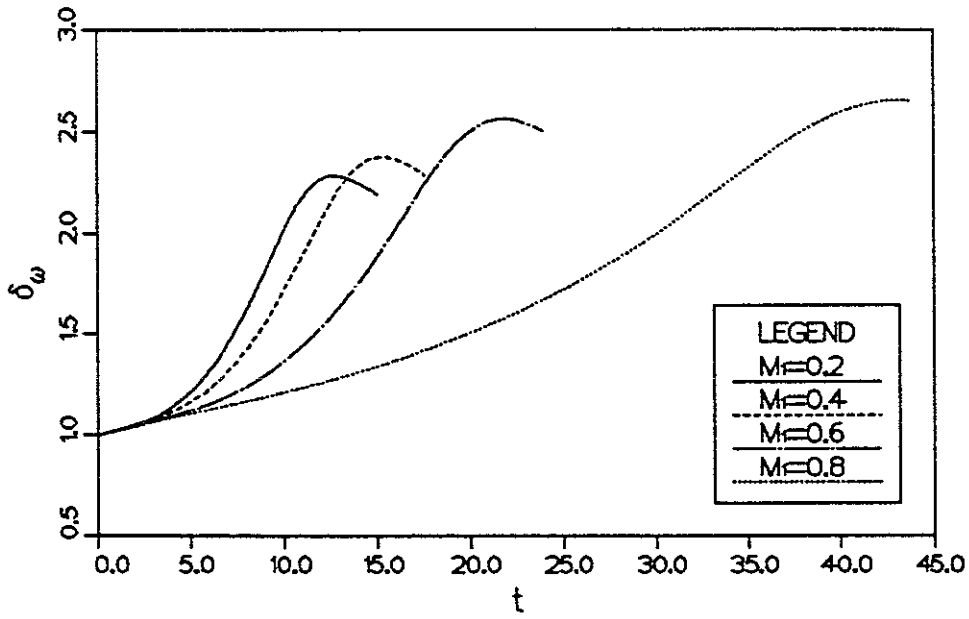

Figure 4.5 Effect of Mach number M_1 on the growth of the fundamental, most amplified disturbance.

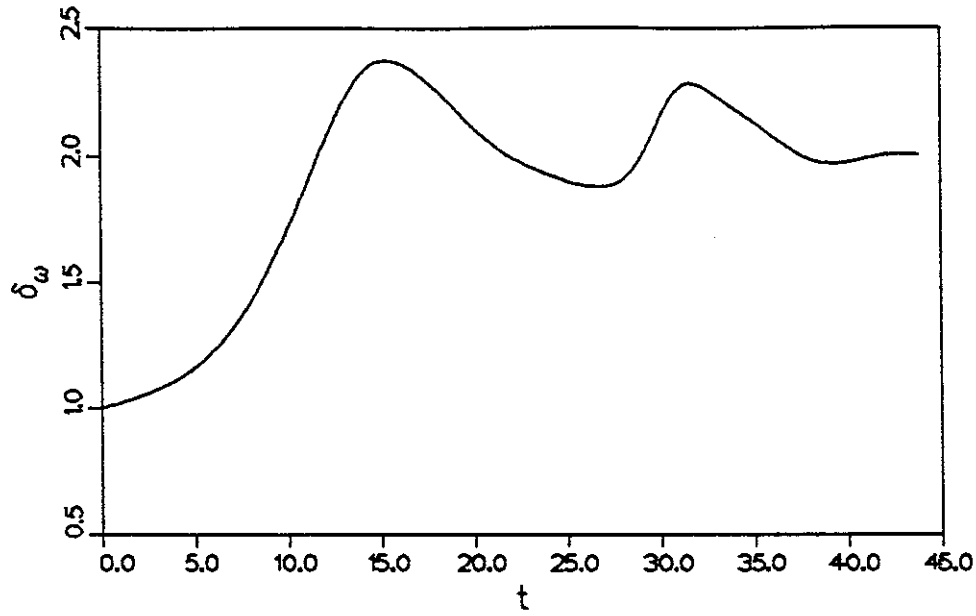

Figure 4.6 Long-time behavior of vorticity thickness at $M_1 = 0.4$.

(a) max=0.500 min=–0.500 (b) max=1.57 min=–5.28e–3

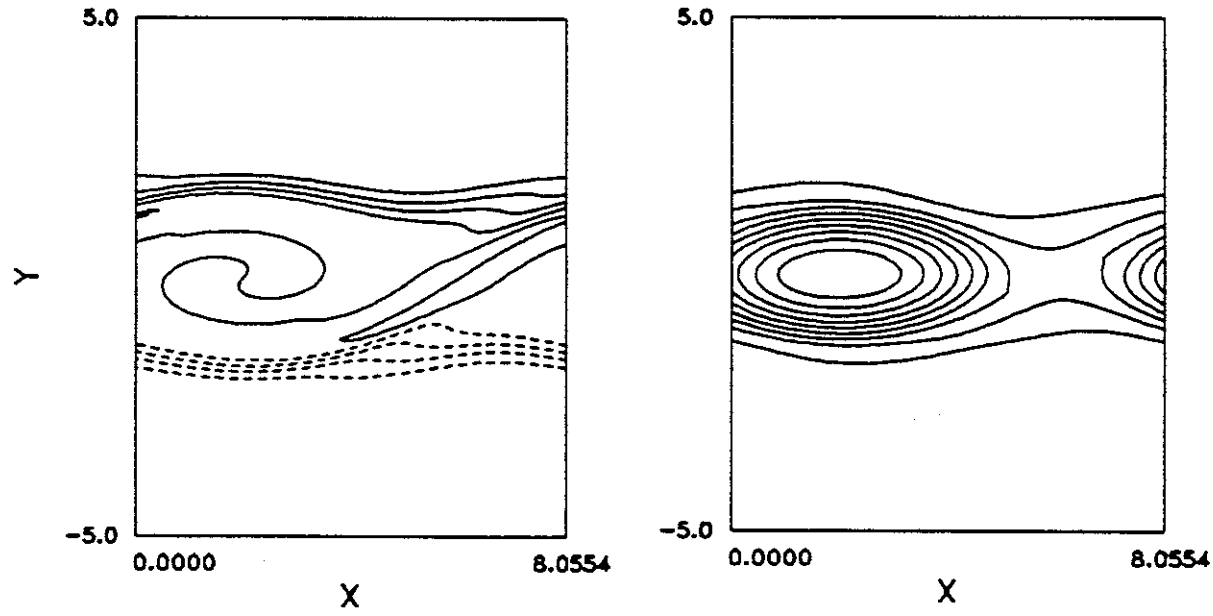

Figure 4.7 Structure at long time (a) mixture fraction, (b) vorticity.

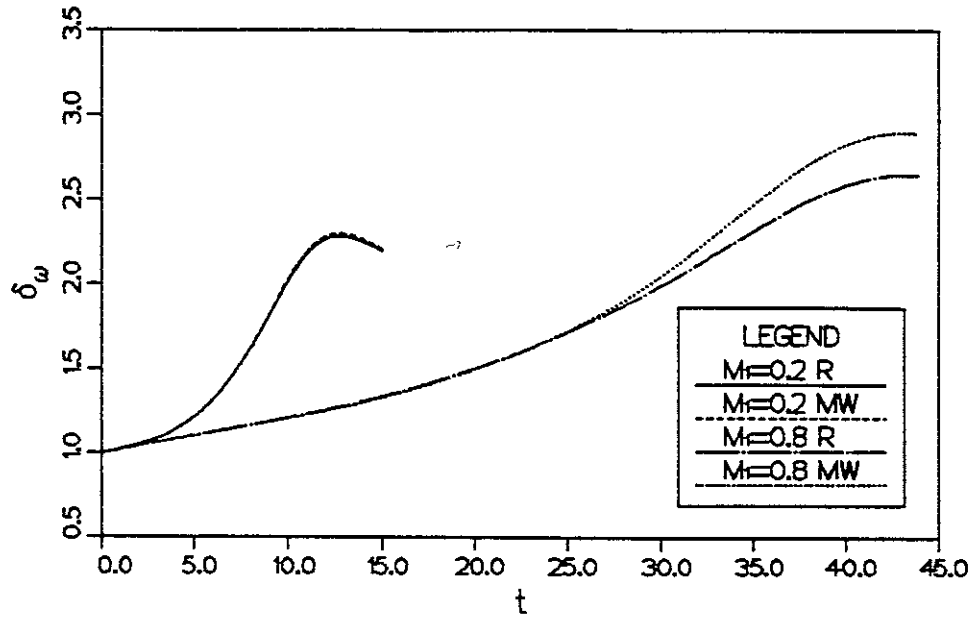

Figure 4.8 Comparison of vorticity thickness measures, based on mean velocity profile (R), or mass-weighted mean velocity profile (MW).

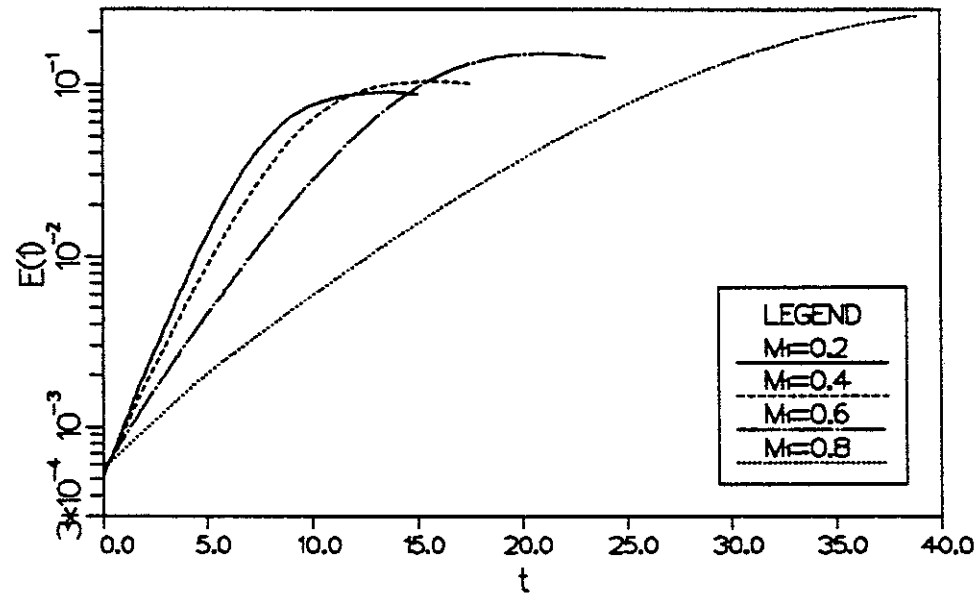

Figure 4.9 Effect of Mach number on the growth in mode energy E of the most amplified disturbance.

(a) max=0.500 min=–0.500

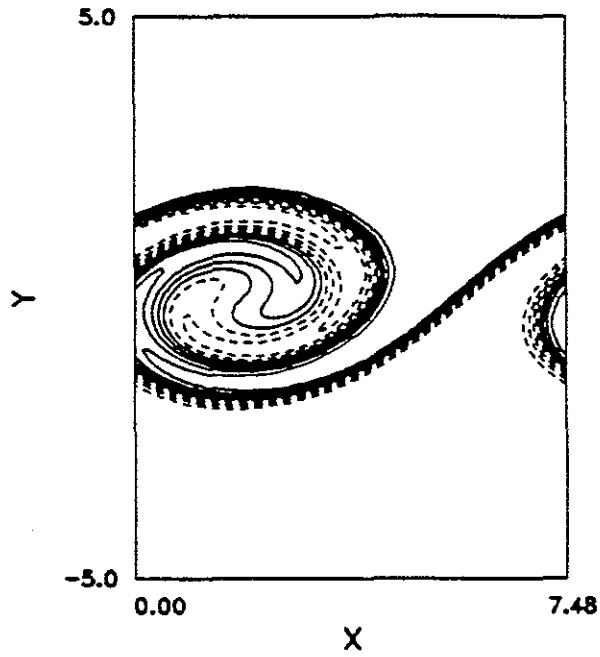

(b) max=18.3 min=16.8

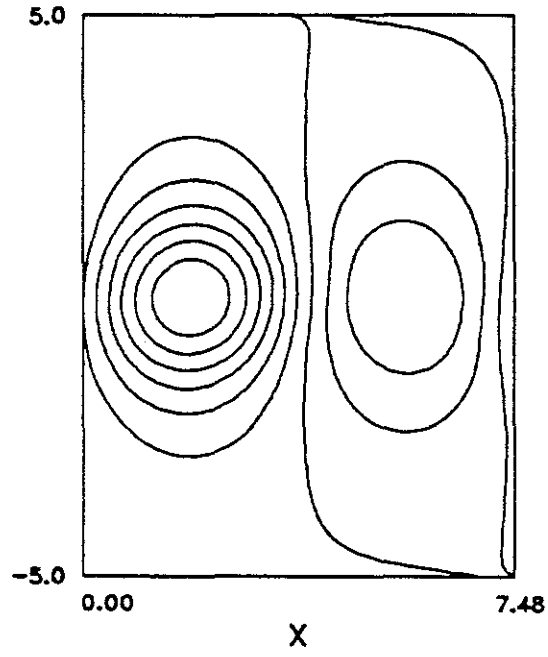

(c) max=1.81 min=–4.44e–3

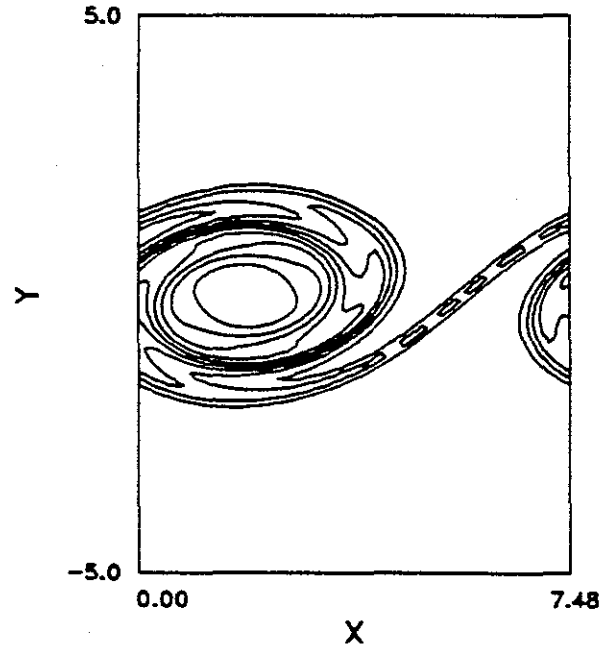

(d) max=1.91 min=–4.44e–3

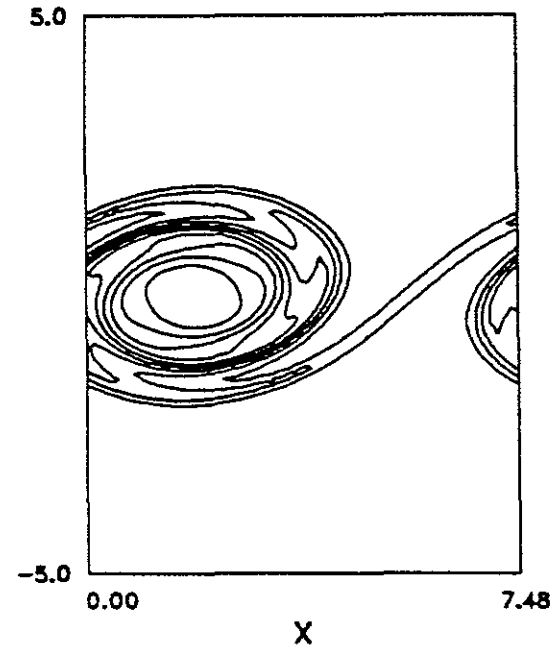

Figure 4.10 Developed structure at $M_1 = 0.2$ (a) mixture fraction, (b) pressure, (c) ω_z, (d) ω_z/ρ.

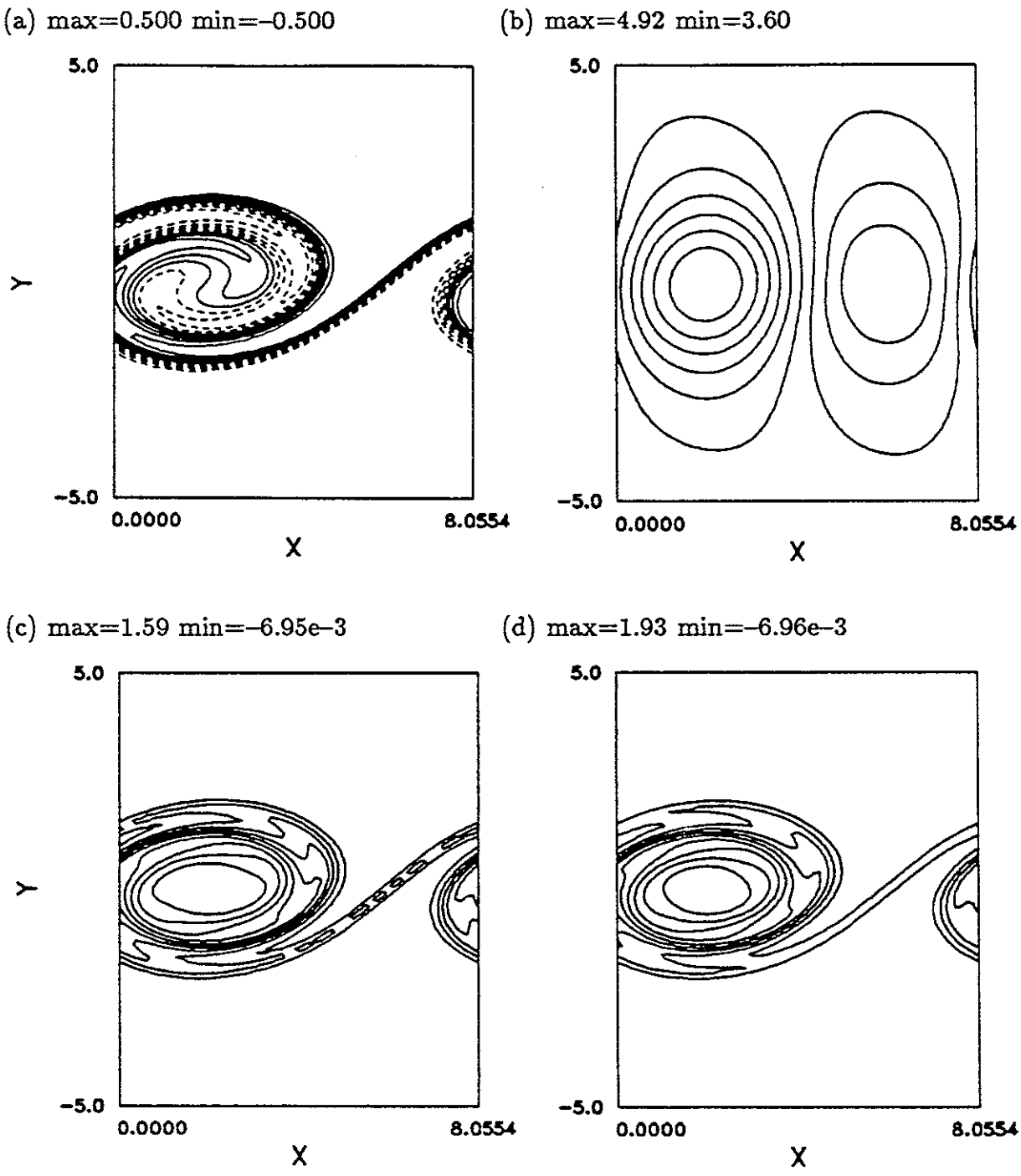

Figure 4.11 Developed structure at $M_1 = 0.4$ (a) mixture fraction, (b) pressure, (c) ω_z, (d) ω_z/ρ.

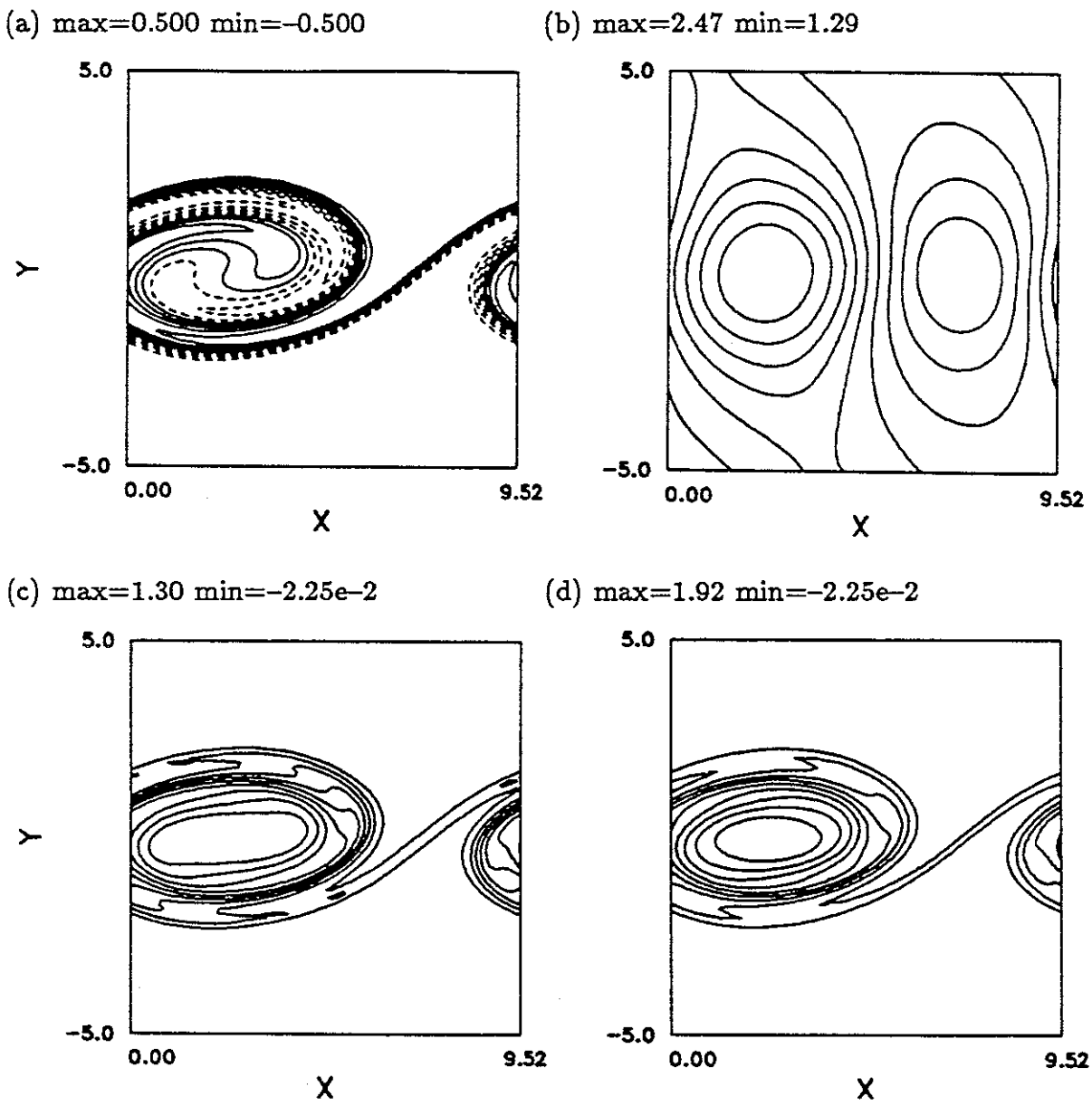

Figure 4.12 Developed structure at $M_1 = 0.6$ (a) mixture fraction, (b) pressure, (c) ω_z, (d) ω_z/ρ.

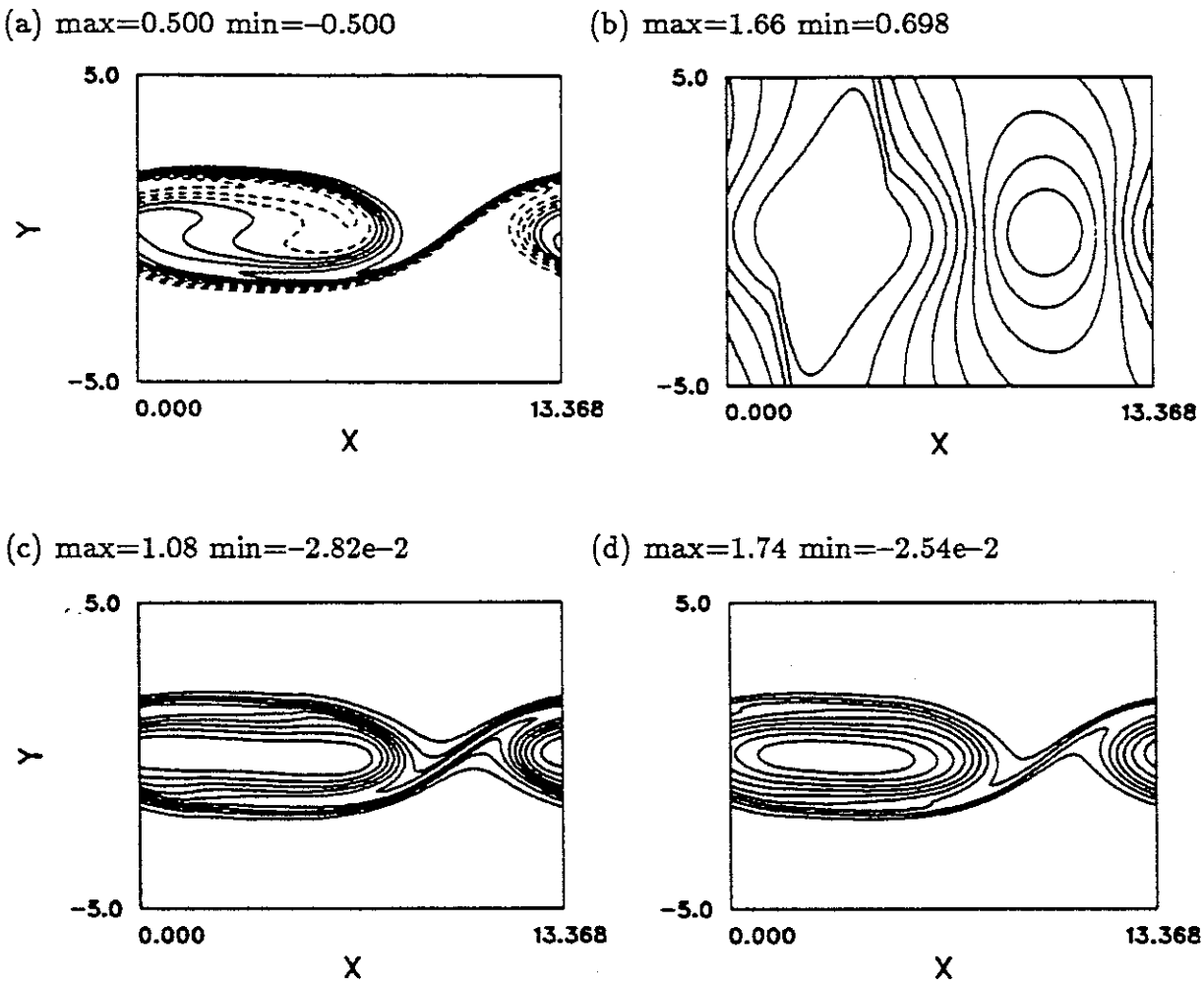

Figure 4.13 Developed structure at $M_1 = 0.8$ (a) mixture fraction, (b) pressure, (c) ω_z, (d) ω_z/ρ.

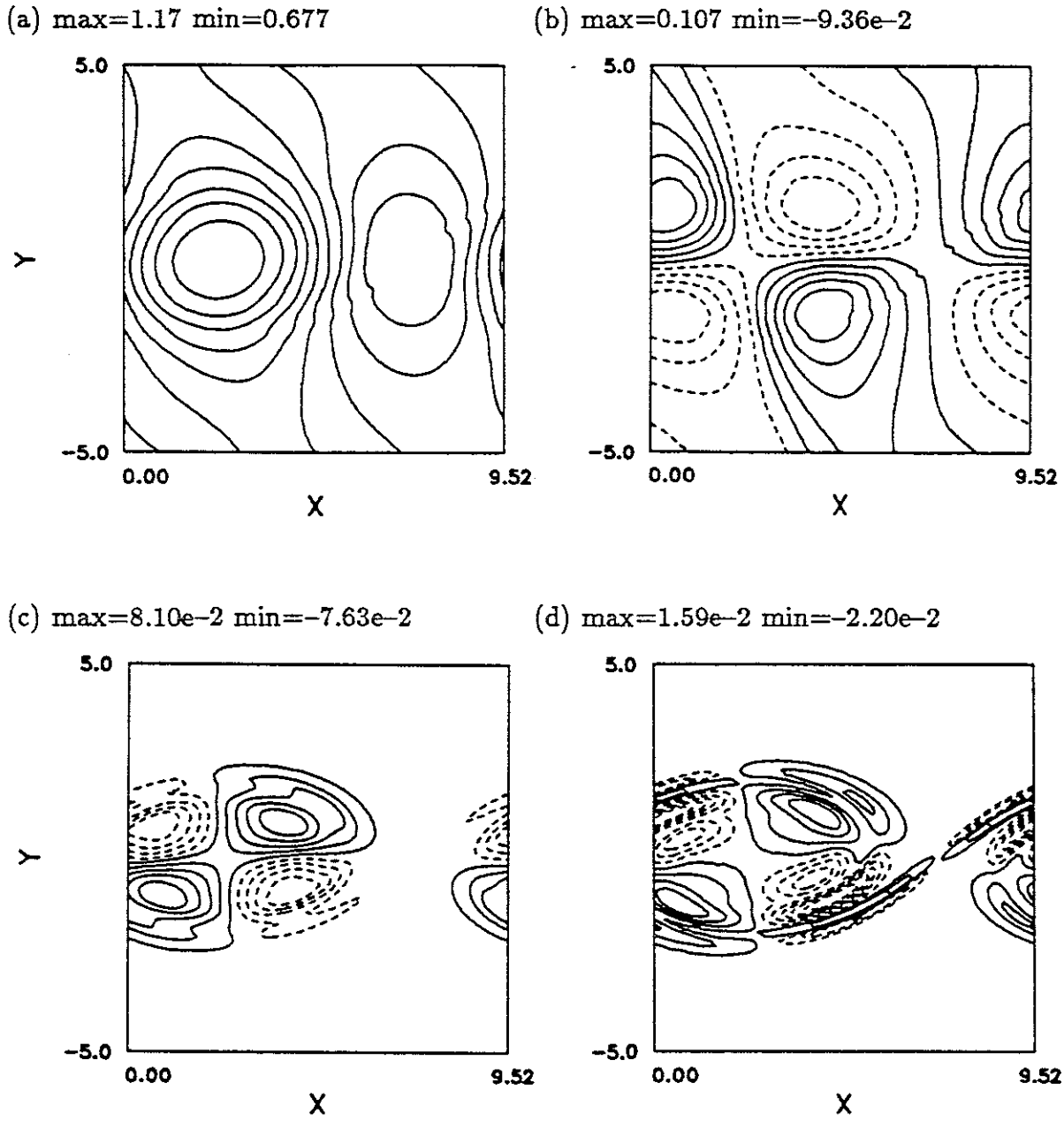

Figure 4.14 Developed structure at $M_1 = 0.6$ (a) density, (b) dilatation, (c) dilatational term in vorticity equation, (d) baroclinic term.

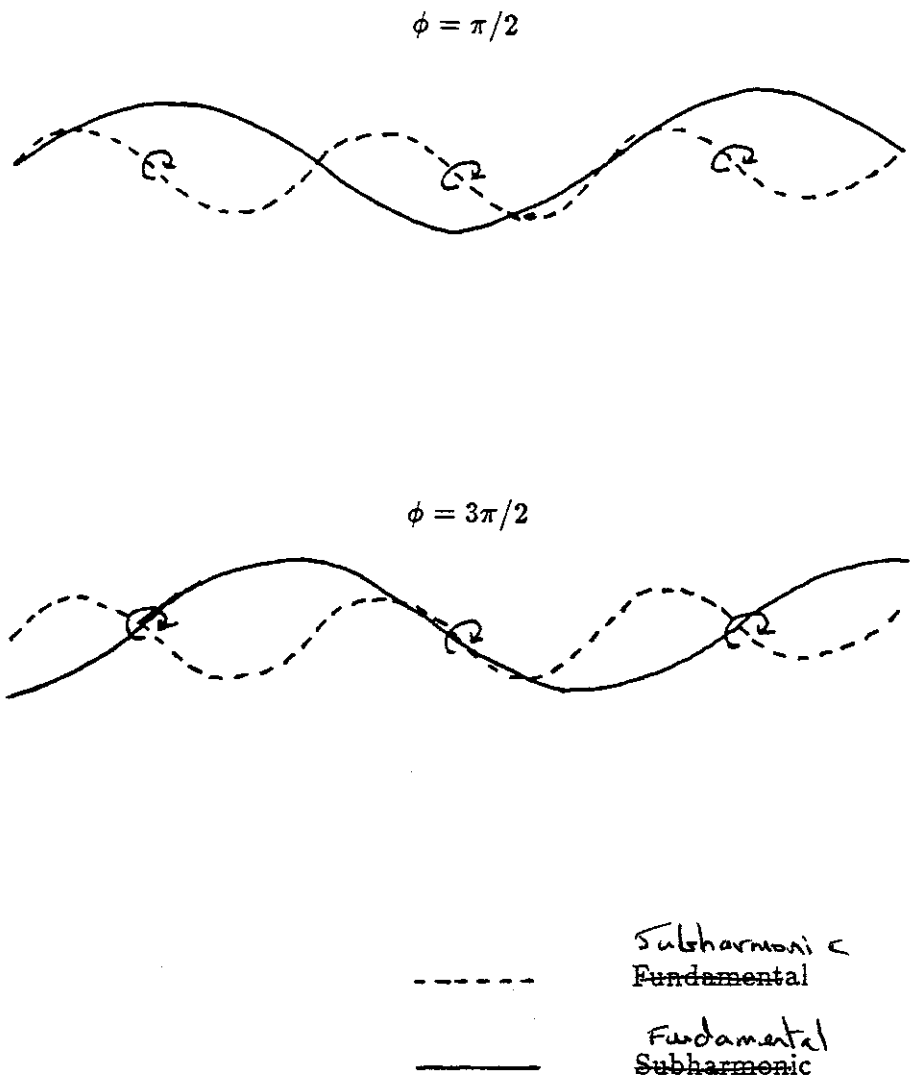

Figure 4.15 Choice of phase between subharmonic and fundamental modes.

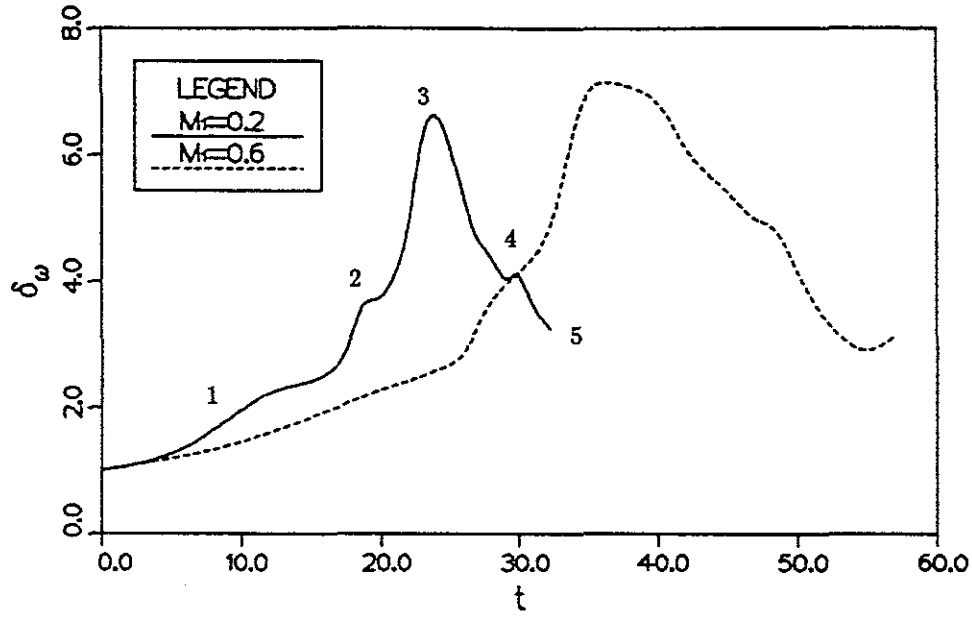

Figure 4.16 Growth in vorticity thickness, comparing $M_1 = 0.2$ with $M_1 = 0.6$.

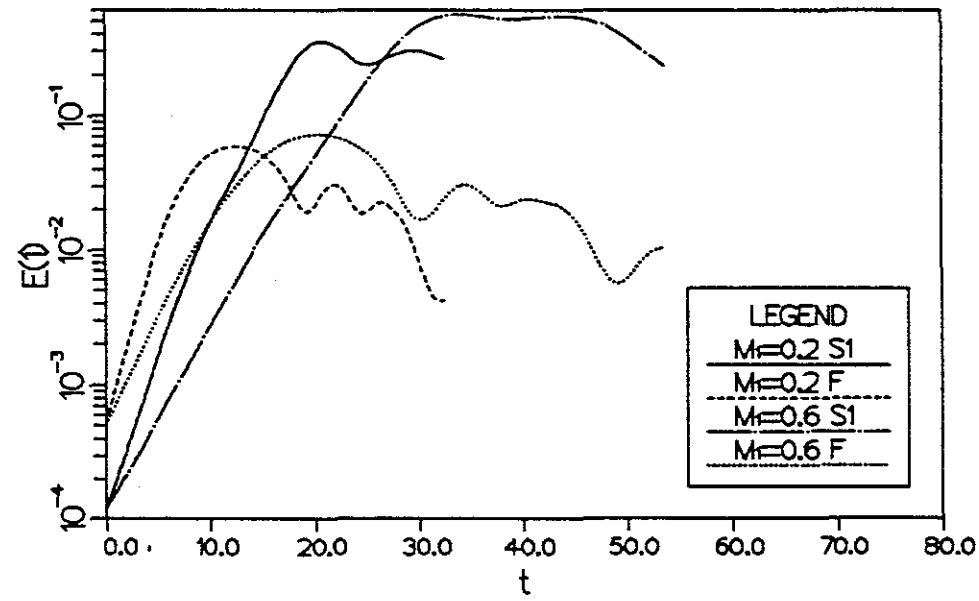

Figure 4.17 Growth in mode energy E, comparing $M_1 = 0.2$ with $M_1 = 0.6$.

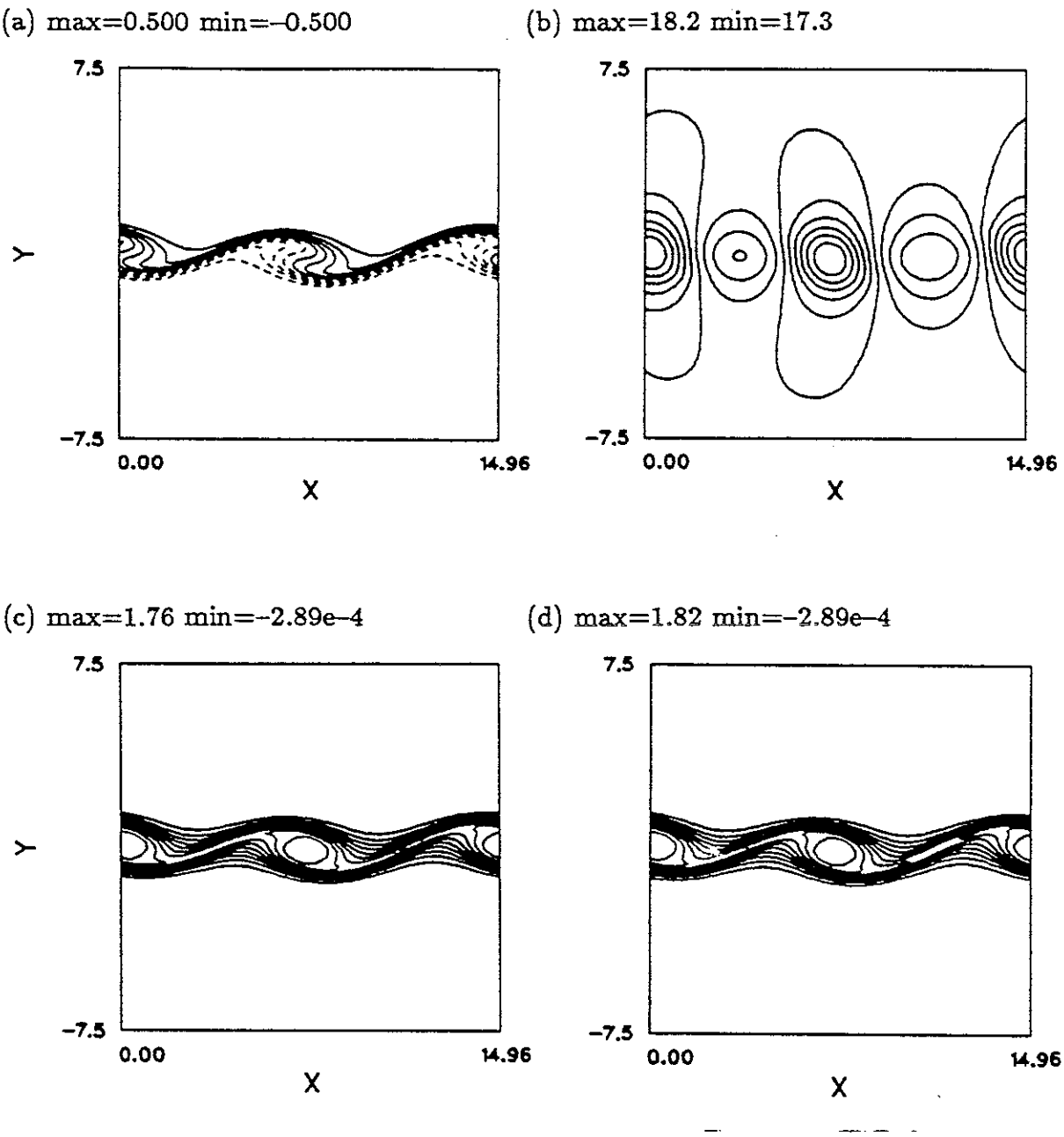

Figure 4.18 Step 1 in pairing process at $M_1 = 0.2$ (a) mixture fraction, (b) pressure, (c) ω_z, (d) ω_z/ρ.

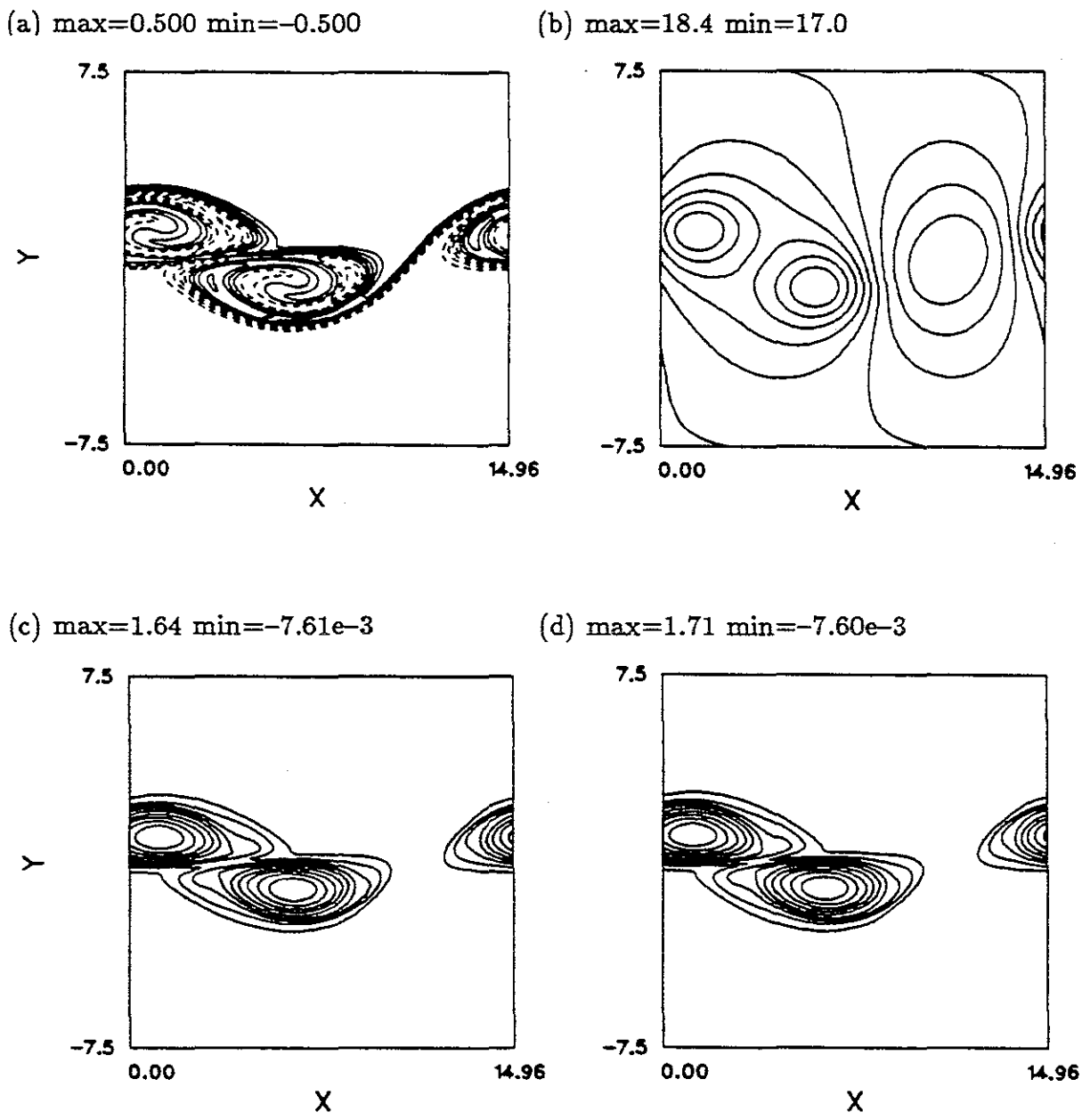

Figure 4.19 Step 2 in pairing process at $M_1 = 0.2$ (a) mixture fraction, (b) pressure, (c) ω_z, (d) ω_z/ρ.

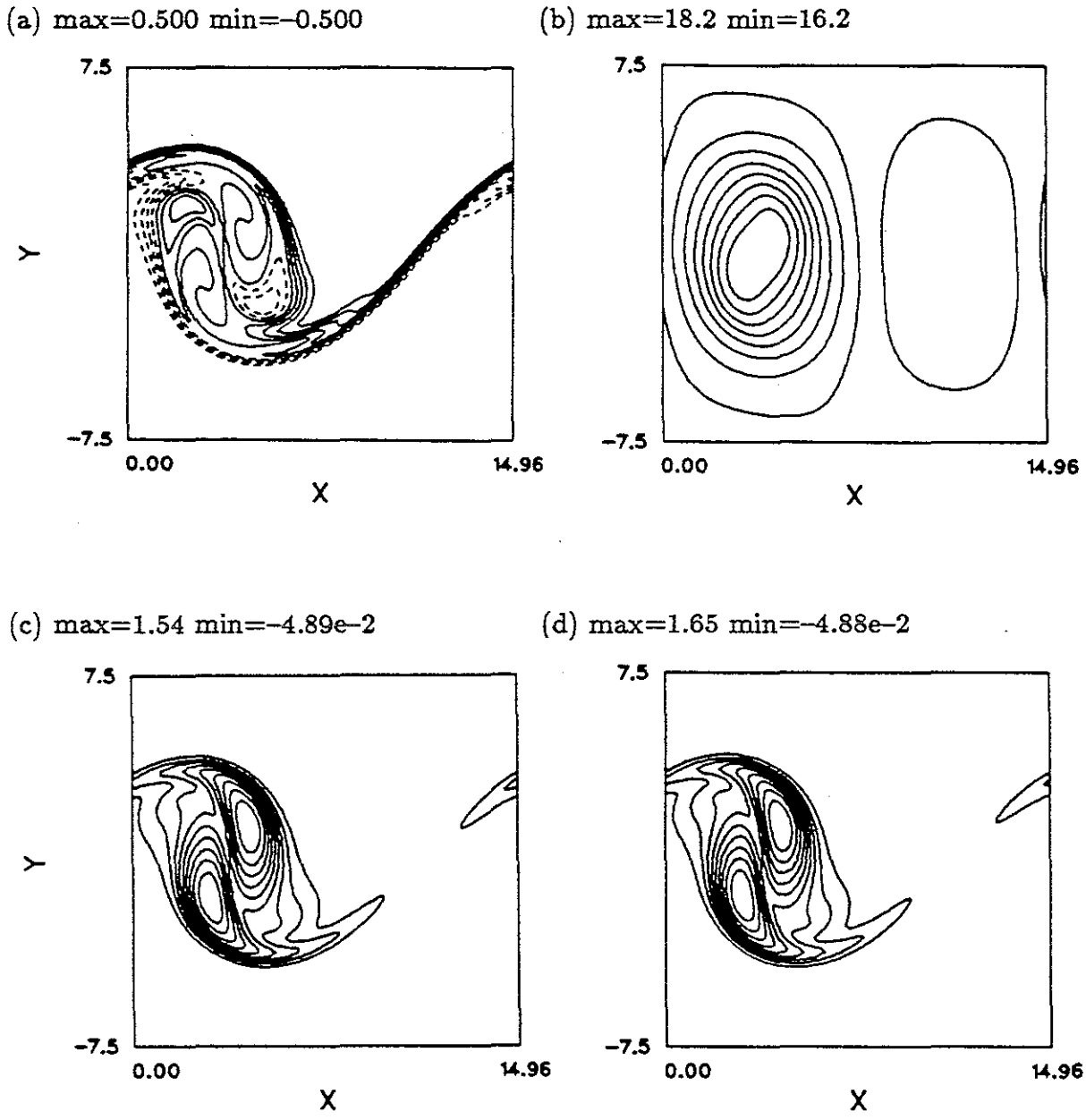

Figure 4.20 Step 3 in pairing process at $M_1 = 0.2$ (a) mixture fraction, (b) pressure, (c) ω_z, (d) ω_z/ρ.

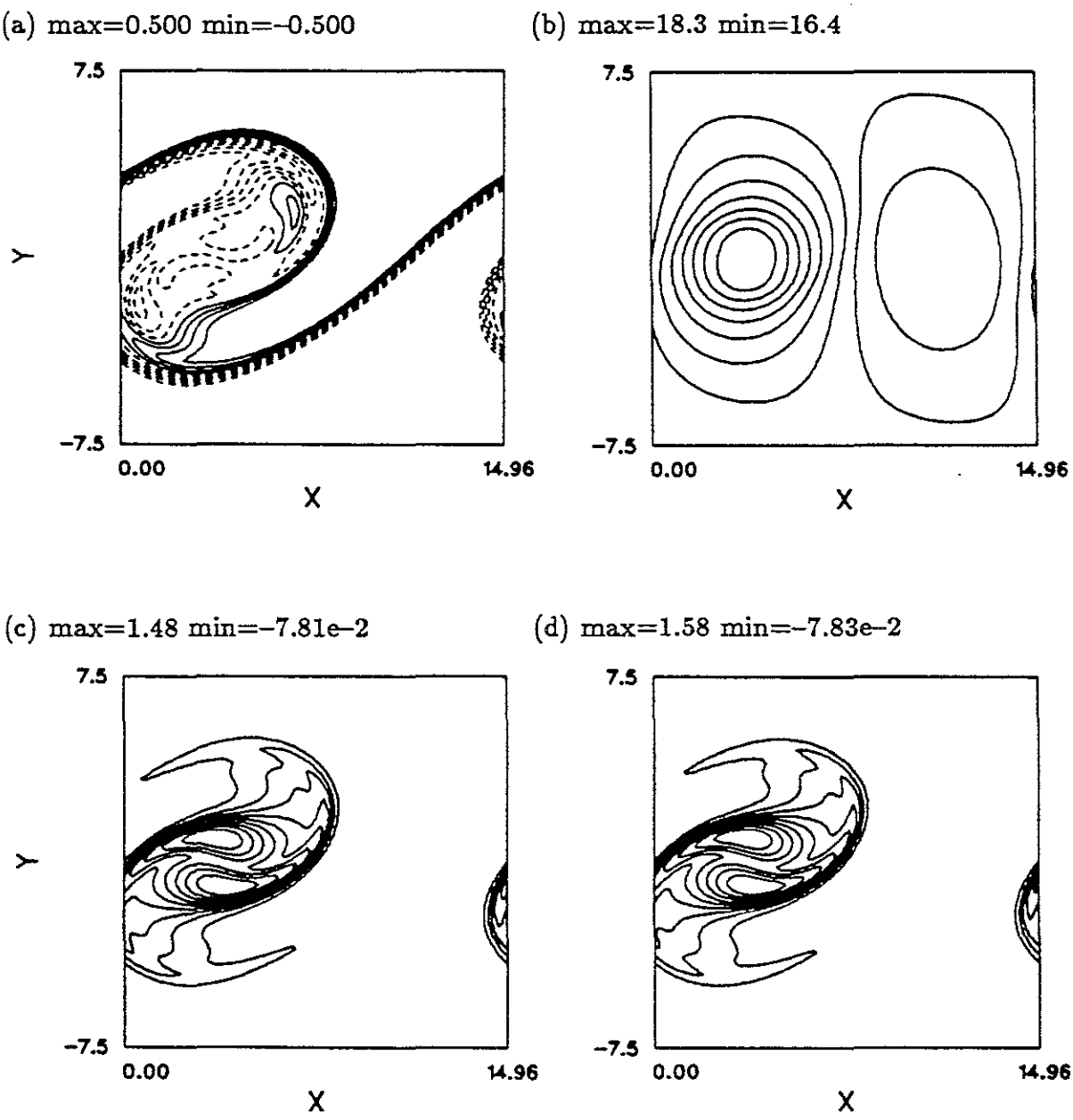

Figure 4.21 Step 4 in pairing process at $M_1 = 0.2$ (a) mixture fraction, (b) pressure, (c) ω_z, (d) ω_z/ρ.

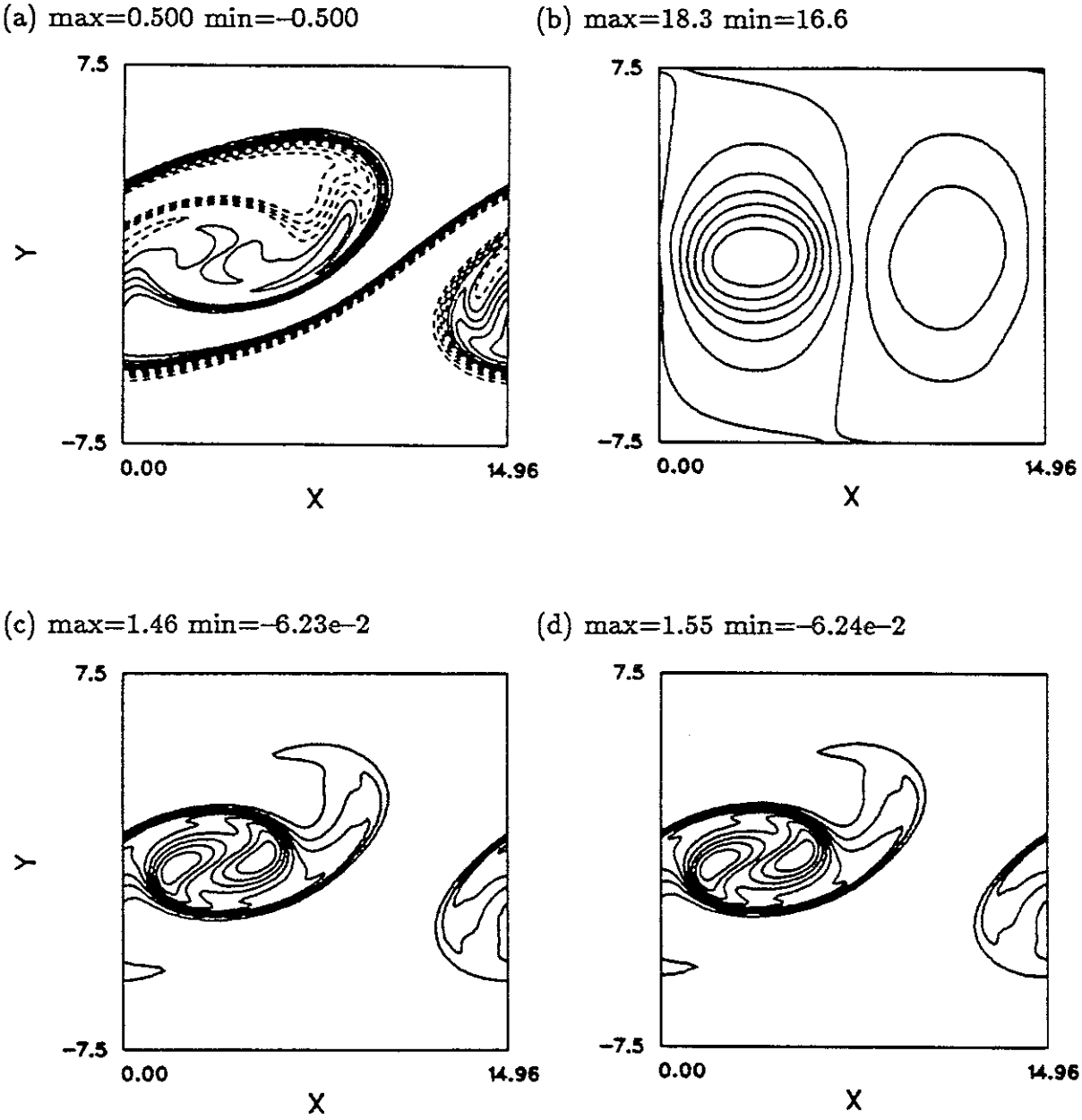

Figure 4.22 Step 5 in pairing process at $M_1 = 0.2$ (a) mixture fraction, (b) pressure, (c) ω_z, (d) ω_z/ρ.

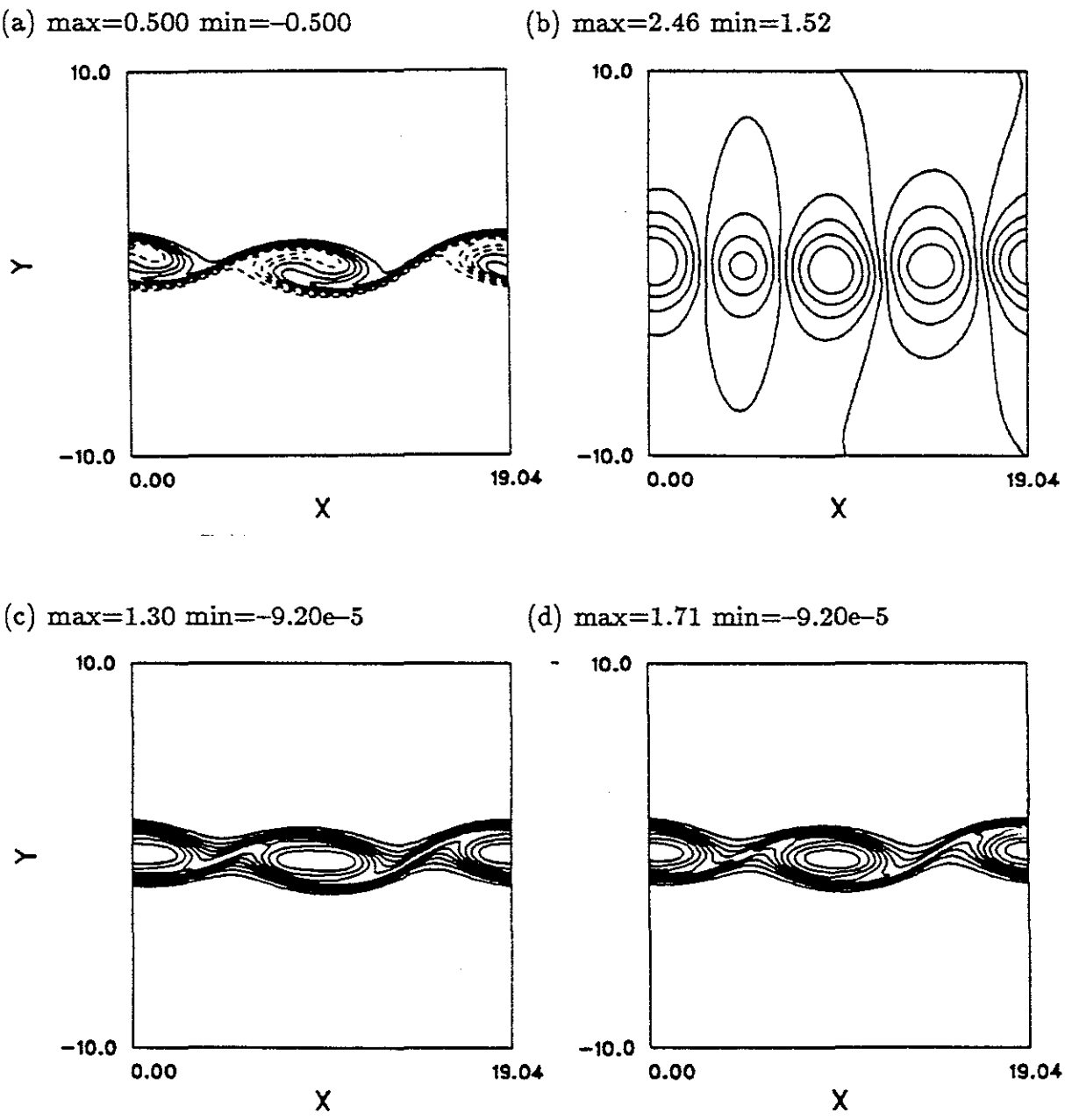

Figure 4.23 Step 1 in pairing process at $M_1 = 0.6$ (a) mixture fraction, (b) pressure, (c) ω_z, (d) ω_z/ρ.

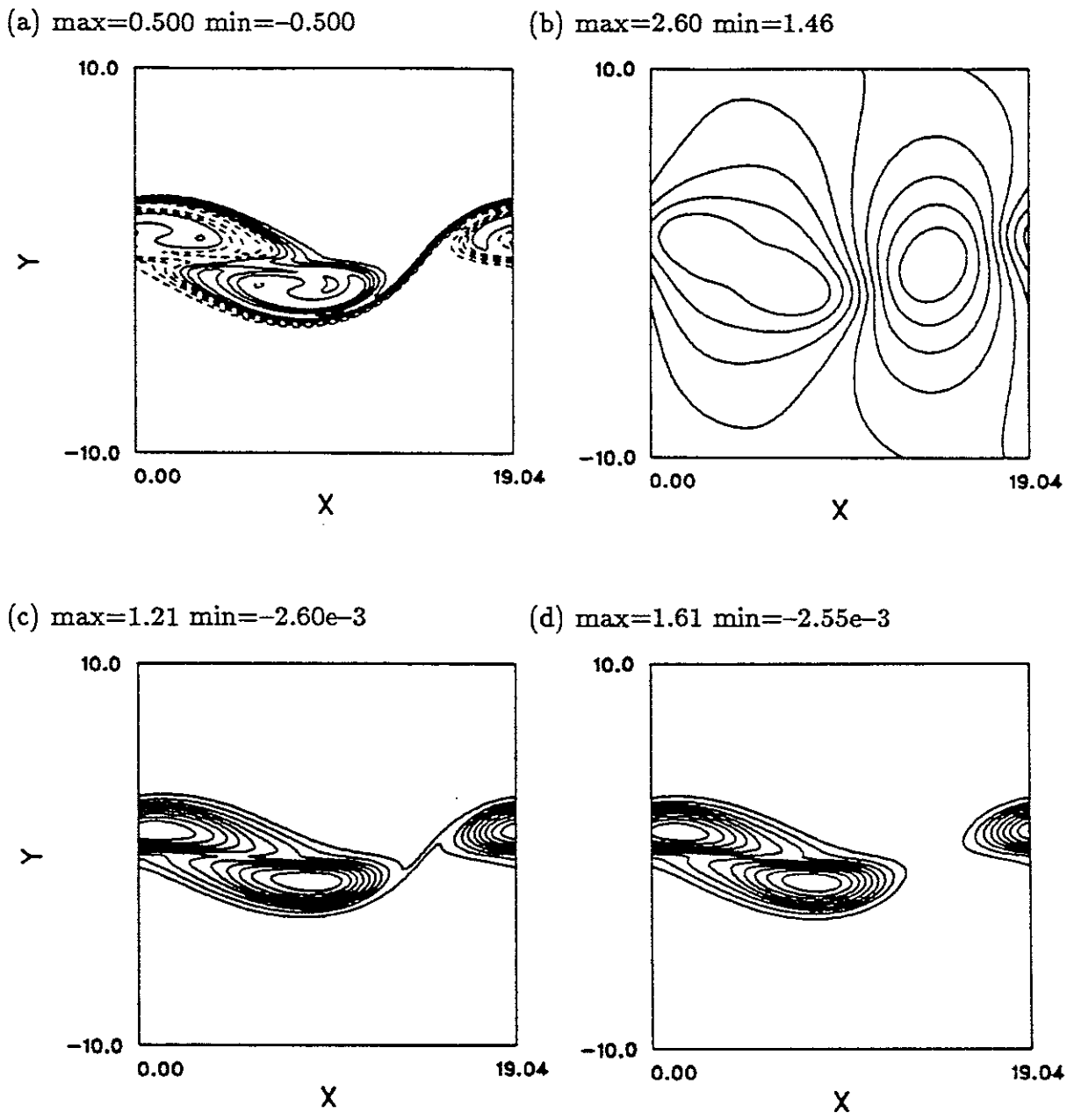

Figure 4.24 Step 2 in pairing process at $M_1 = 0.6$ (a) mixture fraction, (b) pressure, (c) ω_z, (d) ω_z/ρ.

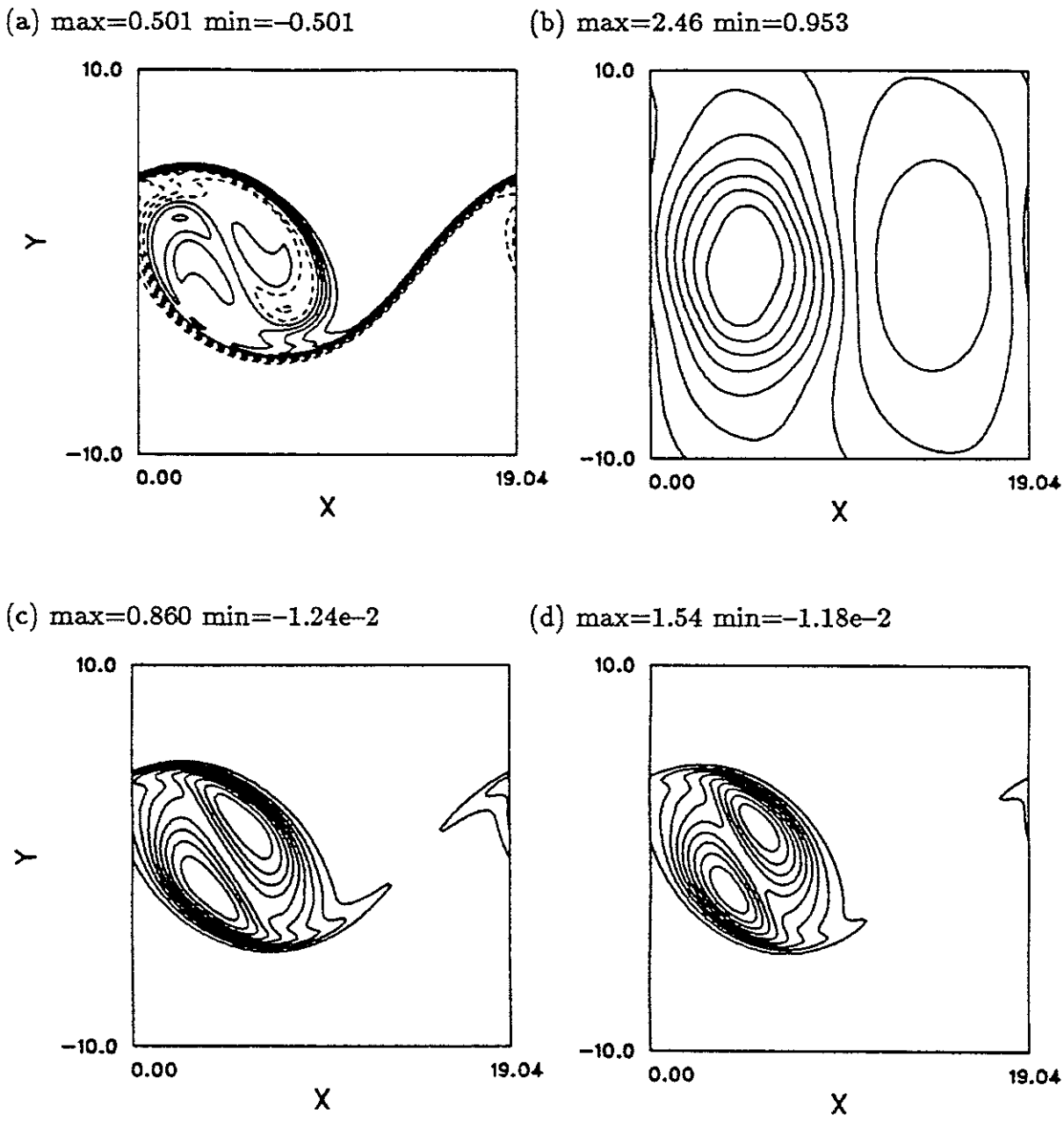

Figure 4.25 Step 3 in pairing process at $M_1 = 0.6$ (a) mixture fraction, (b) pressure, (c) ω_z, (d) ω_z/ρ.

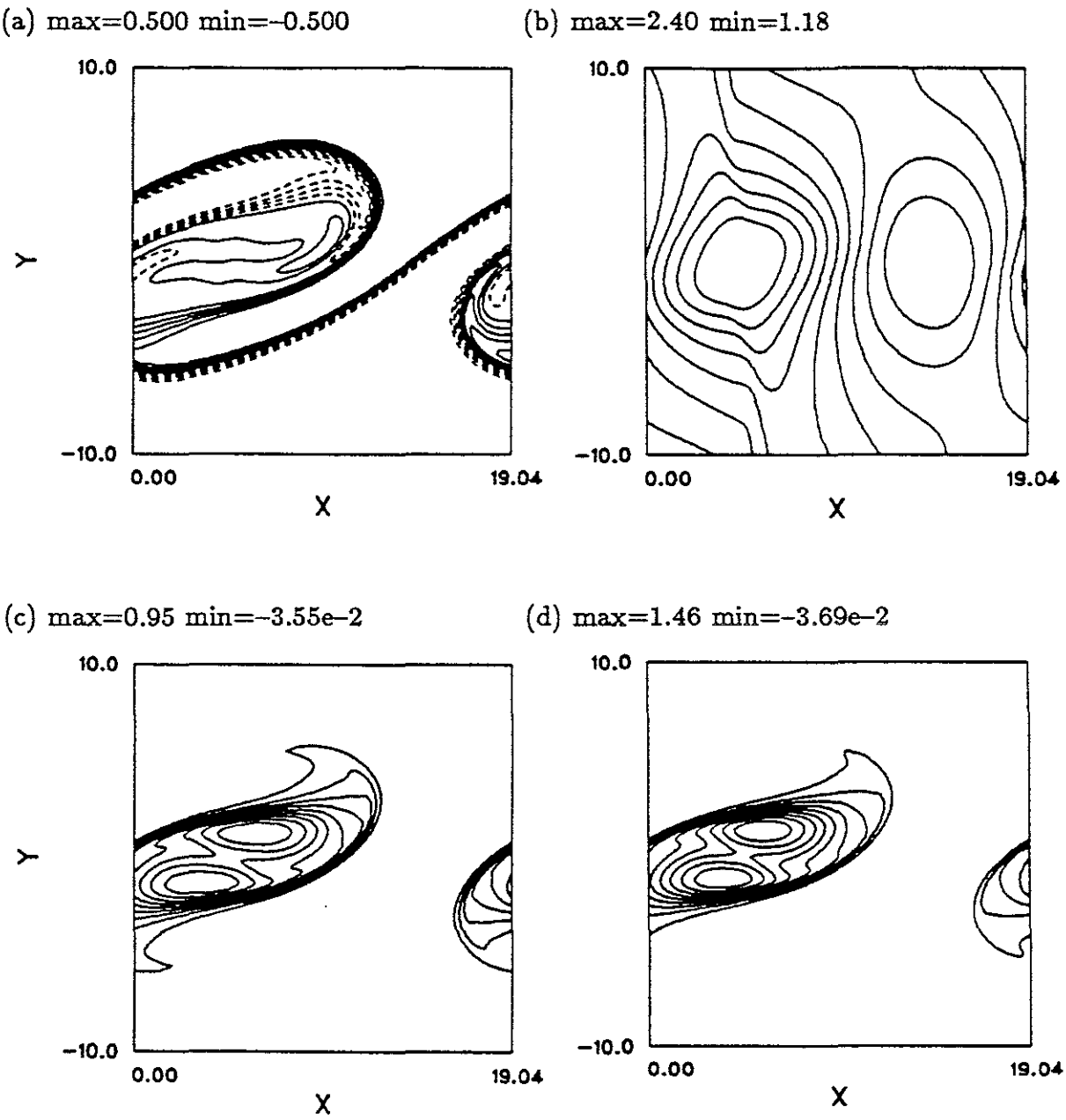

Figure 4.26 Step 4 in pairing process at $M_1 = 0.6$ (a) mixture fraction, (b) pressure, (c) ω_z, (d) ω_z/ρ.

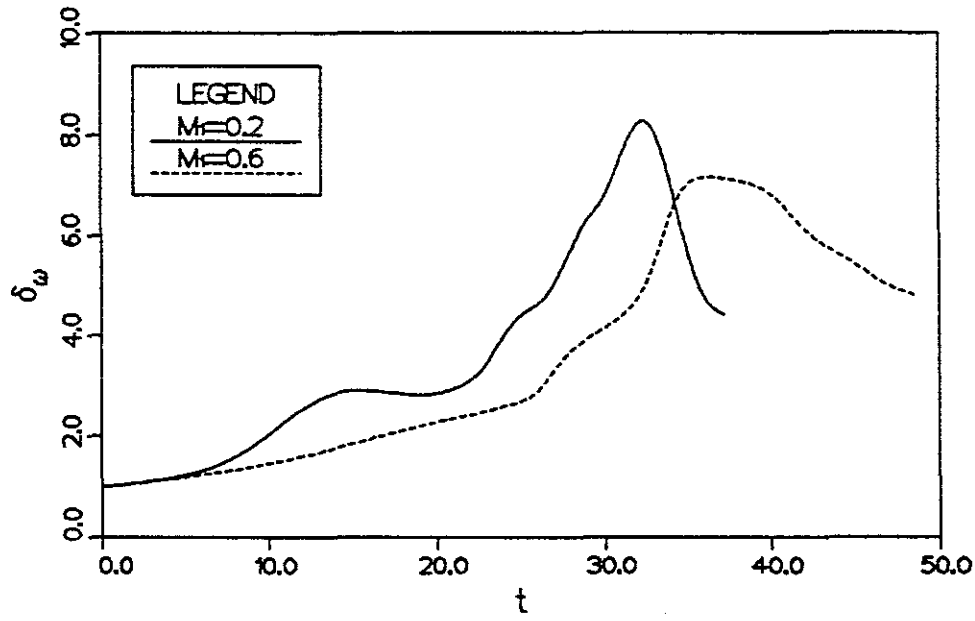

Figure 4.27 Comparison of vorticity thickness growth at two Mach numbers where the initial wavelengths are the same.

(a) max=1.07 min=0.938

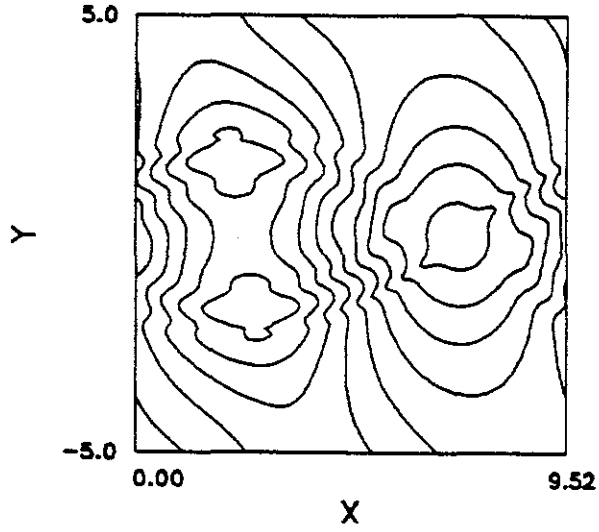

(b) max=7.51 min=6.67

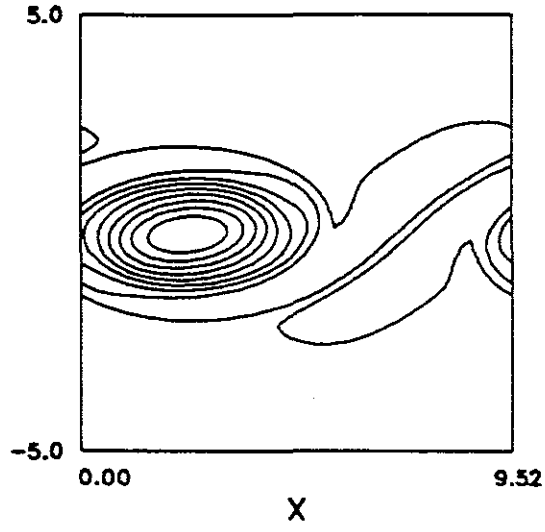

(c) max=0.573 min=5.41e-5

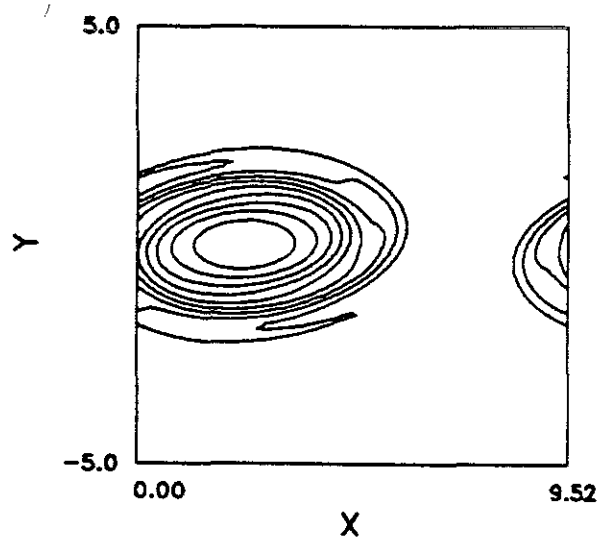

Figure 4.28 Developed structure at $M_1 = 0.6$ (a) temperature, (b) stagnation enthalpy, (c) entropy.

(a) max=0.500 min=–0.500

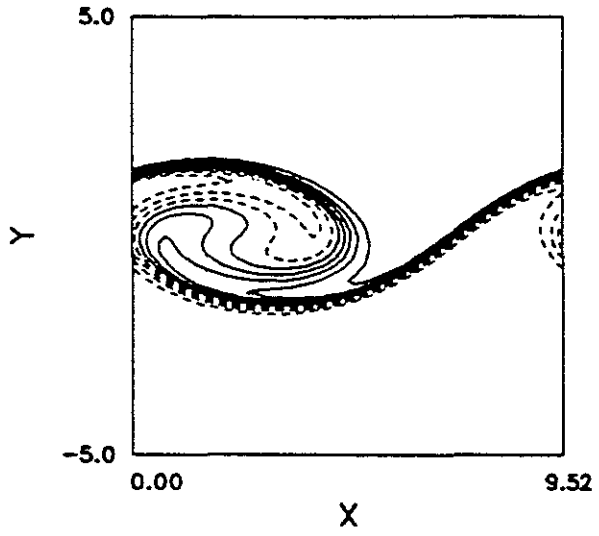

(b) max=0.877 min=1.67e–2

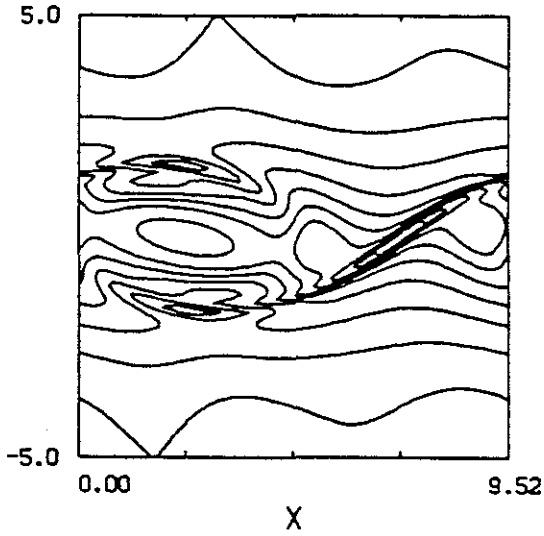

Figure 4.29 Plot of strain rate and mixture fraction at $M_1 = 0.6$, $t = 18.2$ (a) mixture fraction, (b) strain rate S.

(a) max=0.500 min=–0.500

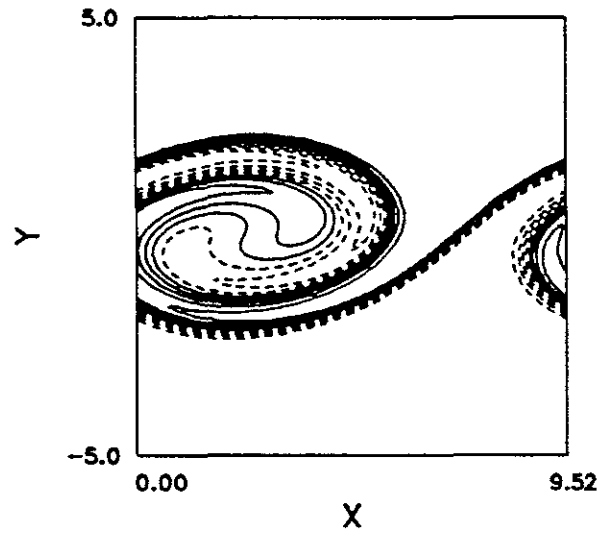

(b) max=0.659 min=3.97e–3

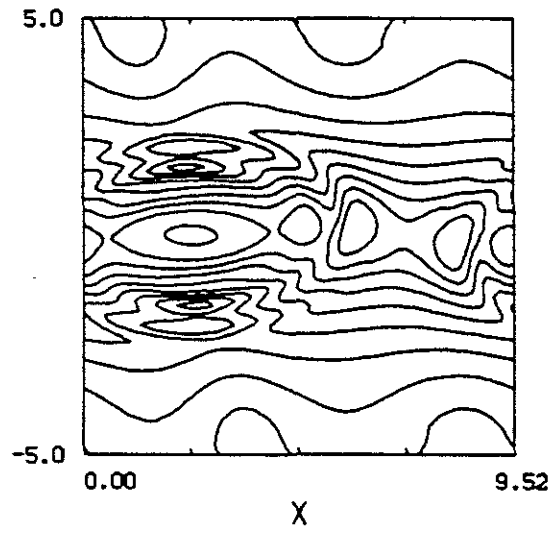

Figure 4.30 Plot of strain rate and mixture fraction at $M_1 = 0.6$, $t = 24.0$ (a) mixture fraction, (b) strain rate S.

(a)

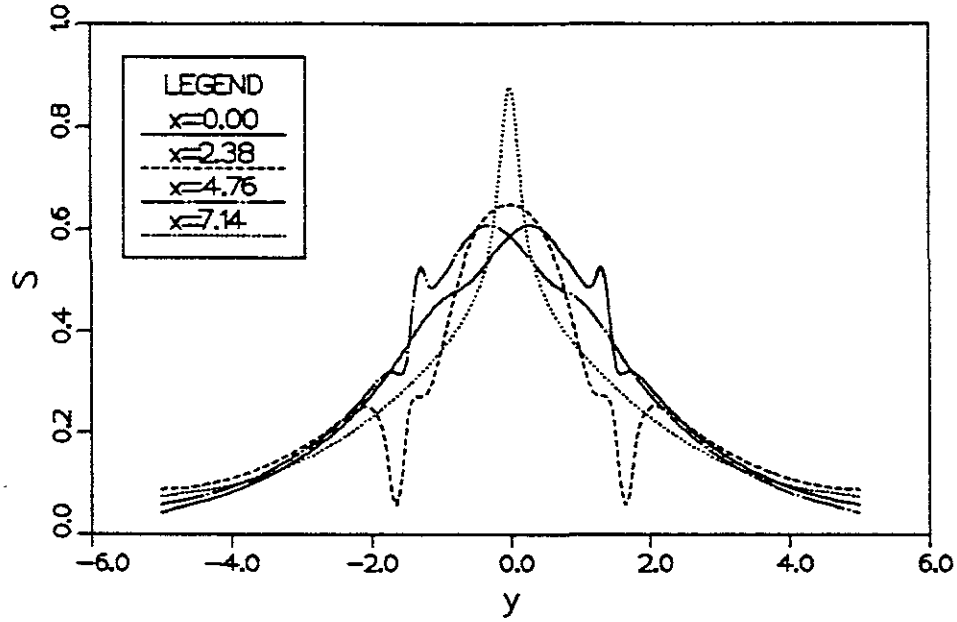

(b)

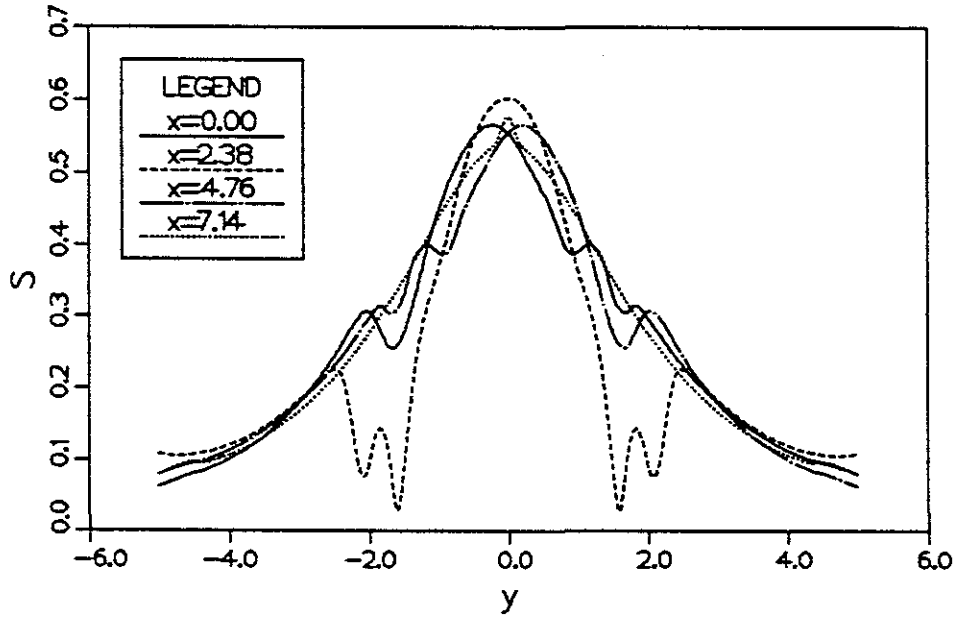

Figure 4.31 Slices through the strain rate field (a) $t = 18.2$, (b) $t = 24.0$.

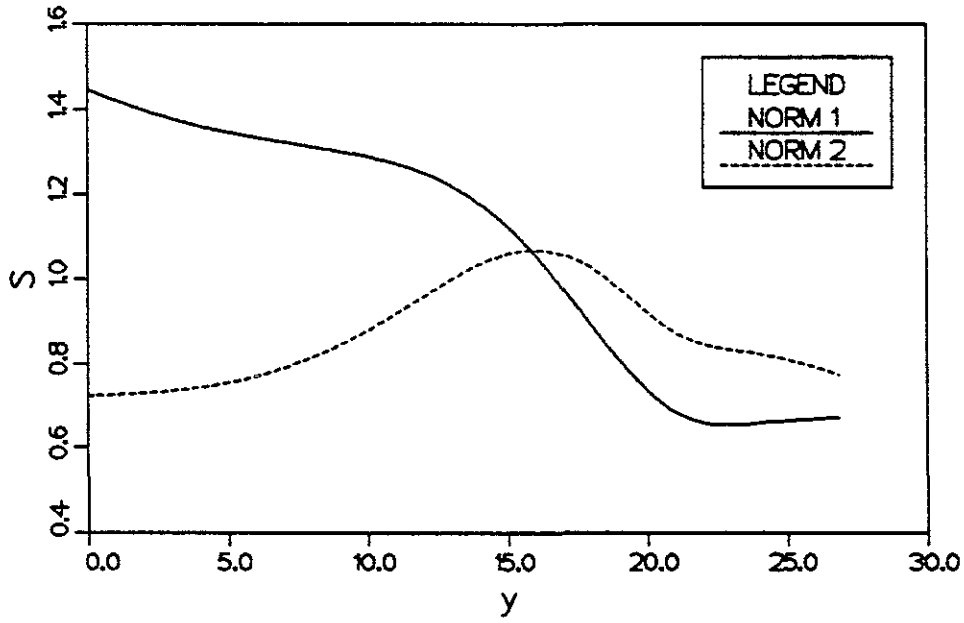

Figure 4.32 Time history of the peak strain rate. Non-dimensionalized as $S = S^*\delta_0^*/U_1^*$ (norm 1), or as $S = S^*\delta^*/U_1^*$ (norm 2).

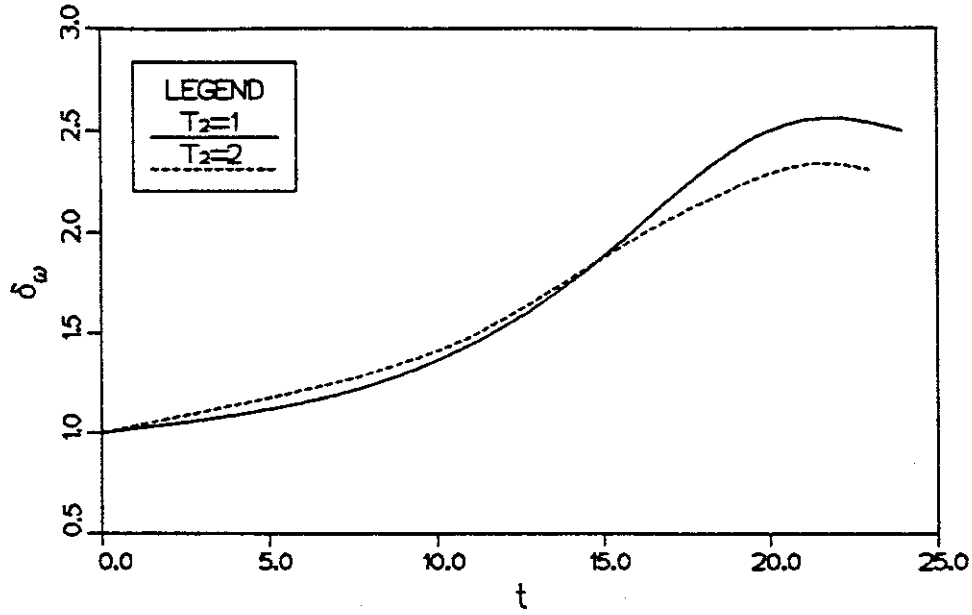

Figure 4.33 Growth in vorticity thickness for temperature ratios 1 and 2.

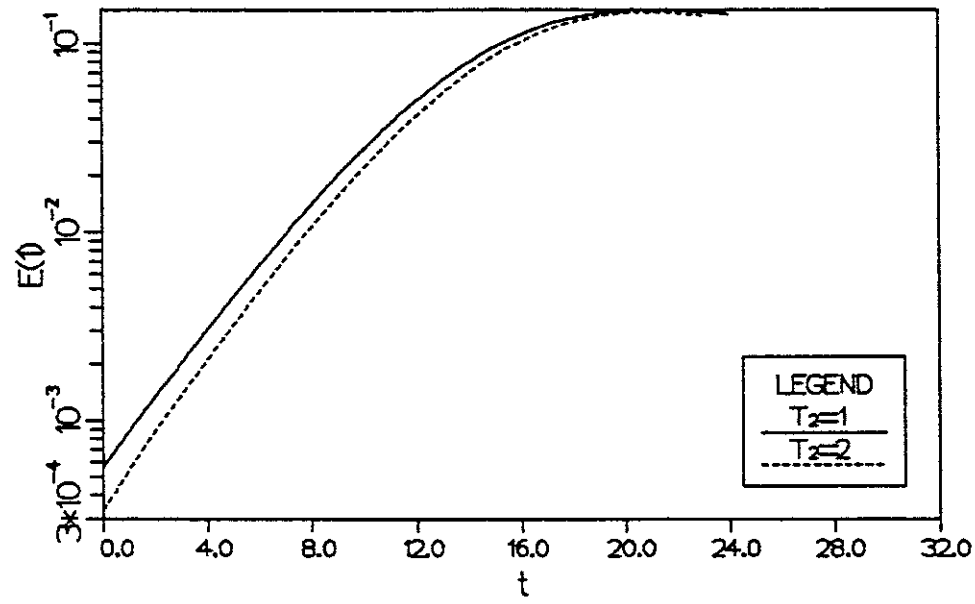

Figure 4.34 Growth in mode energy E, for temperature ratios 1 and 2.

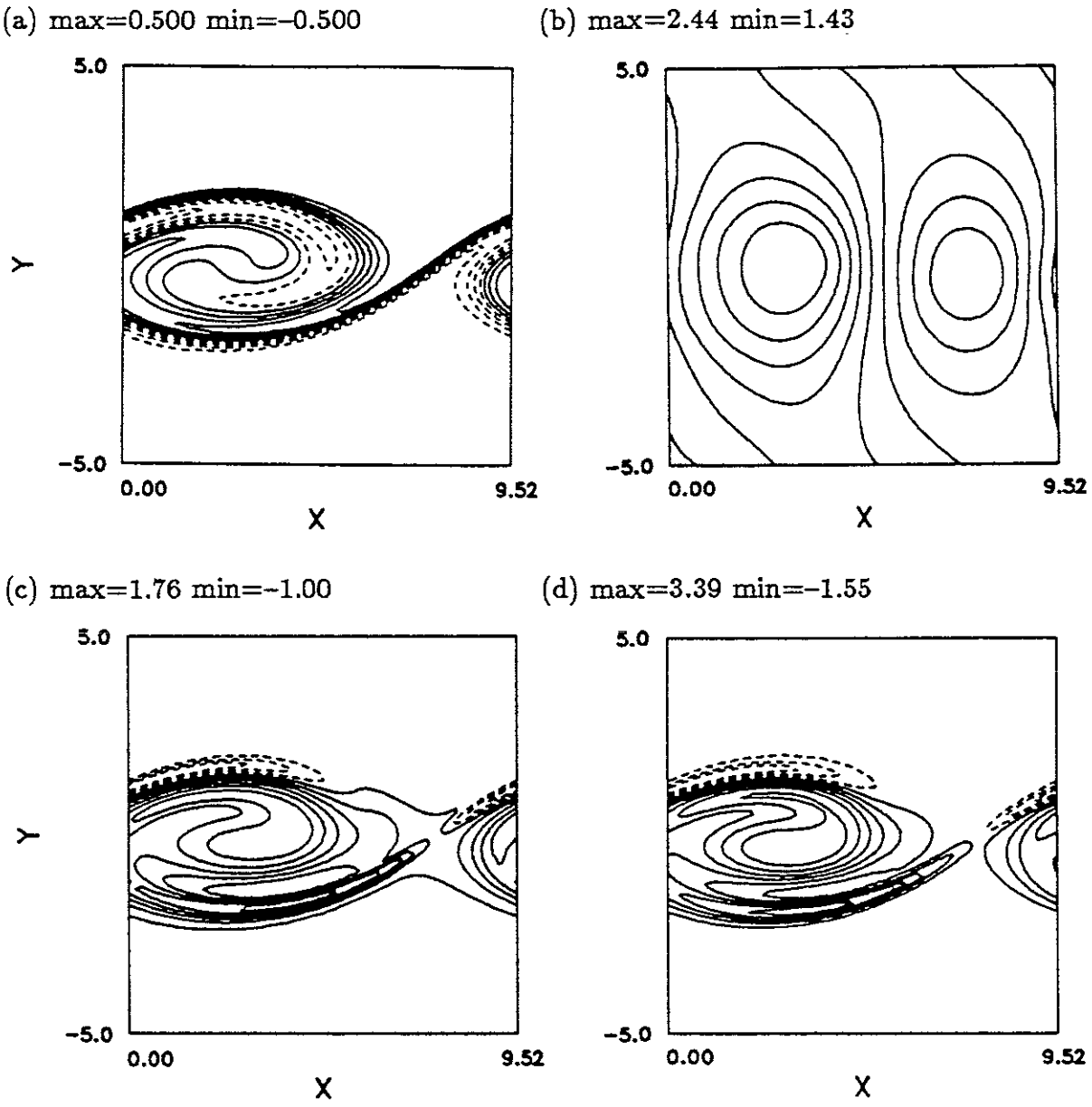

Figure 4.35 Developed structure at $M_1 = 0.6$, $T_2 = 2$ (a) mixture fraction, (b) pressure, (c) ω_z, (d) ω_z/ρ.

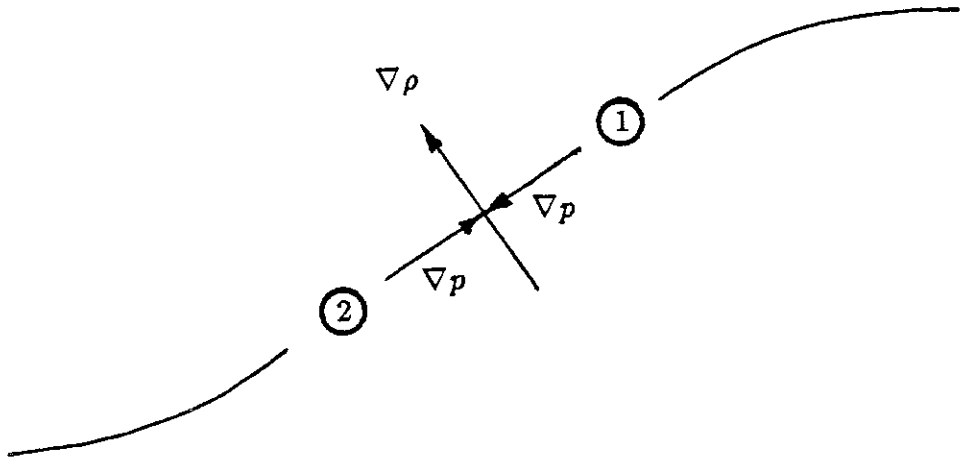

(1) Generation of clockwise vorticity

(2) Generation of counter-clockwise vorticity

Figure 4.36 Generation of baroclinic torques in the saddle region.

(a) max=0.500 min=–0.499

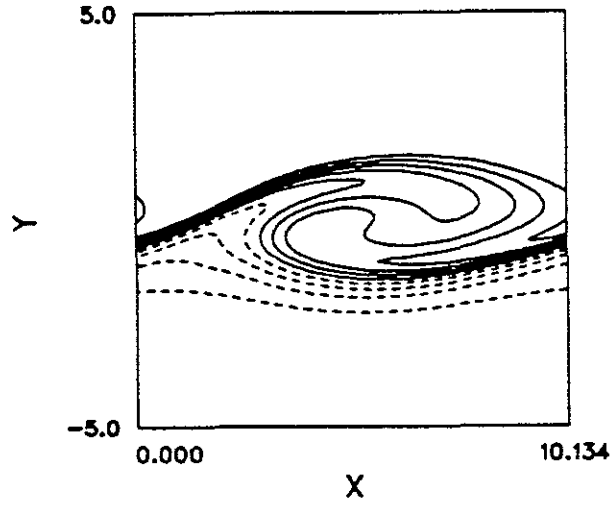

(b) max=2.23 min=1.71

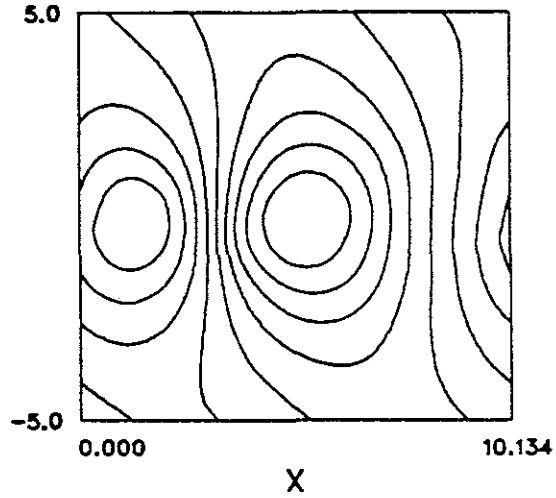

(c) max=2.16 min=–1.04

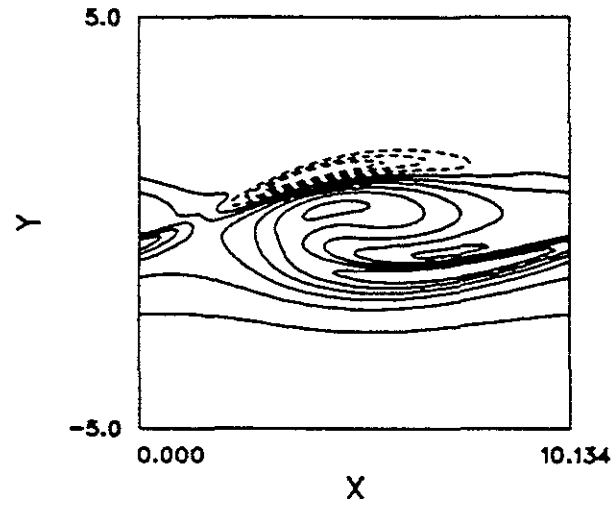

(d) max=6.28 min=–2.15

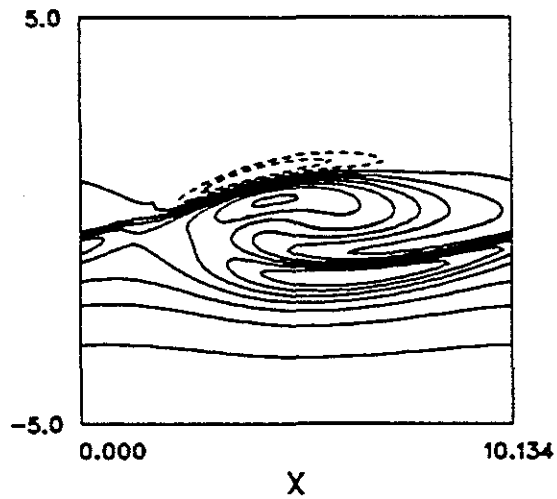

Figure 4.37 Developed structure at $M_1 = 0.6$, $T_2 = 5$ (a) mixture fraction, (b) pressure, (c) ω_z, (d) ω_z/ρ.

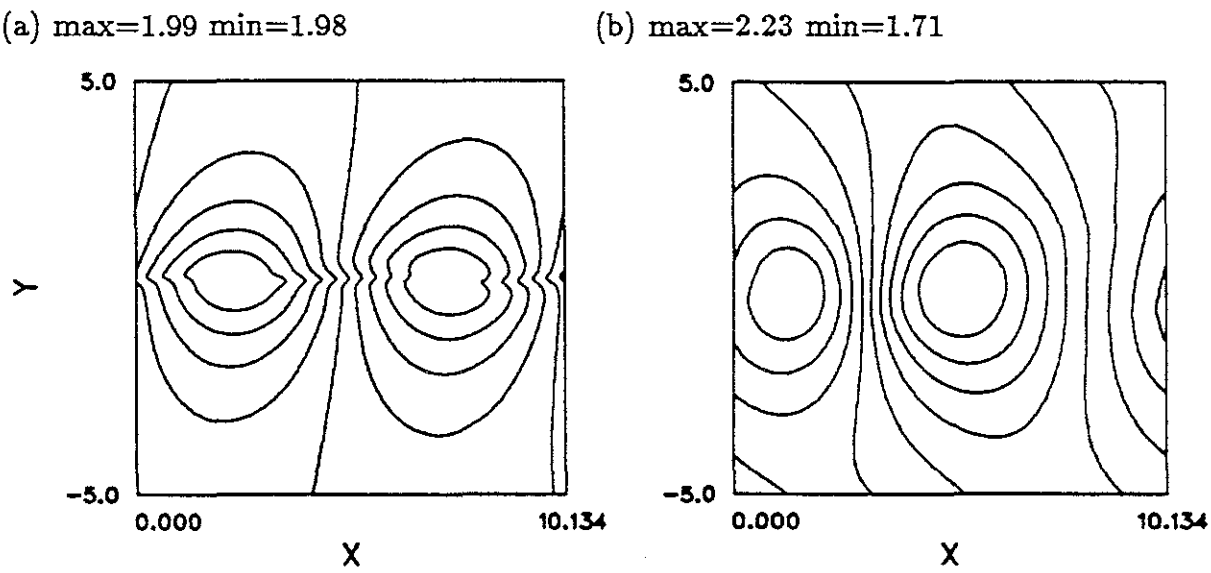

Figure 4.38 Convection of structure at $T_2 = 5$ shown by pressure contours (a) $t = 0.0$, (b) $t = 26.4$.

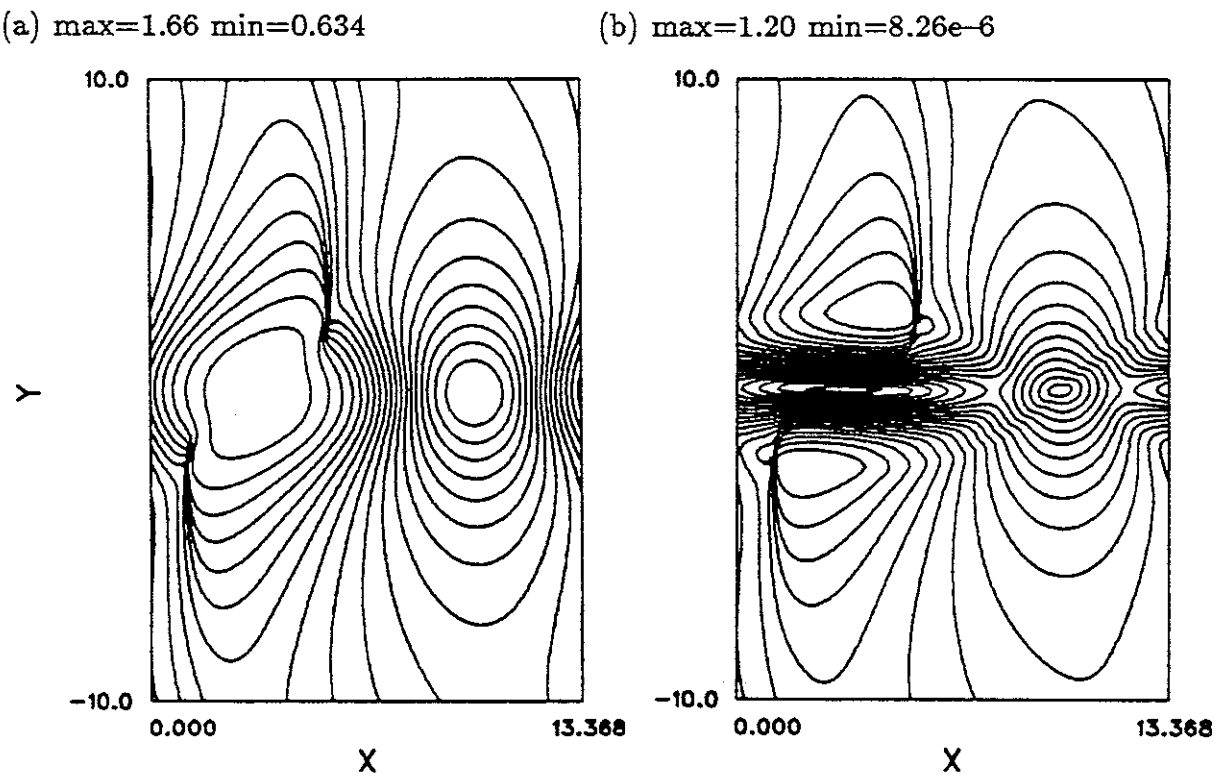

Figure 4.39 Embedded shock waves (a) pressure contours, (b) Mach contours $M = \sqrt{u^2 + v^2}/c$.

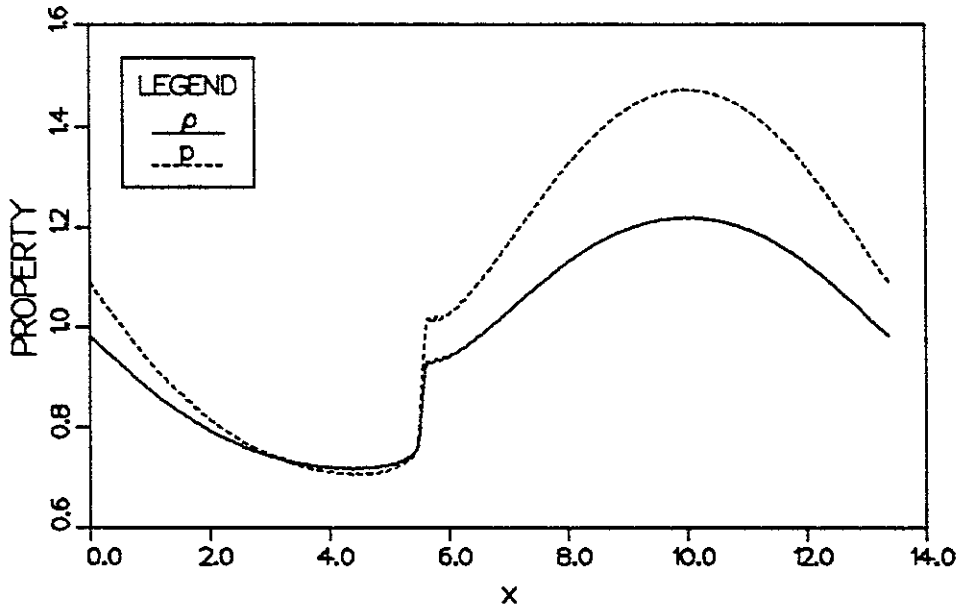

Figure 4.40 Profiles through the shock wave (a) density, (b) pressure.

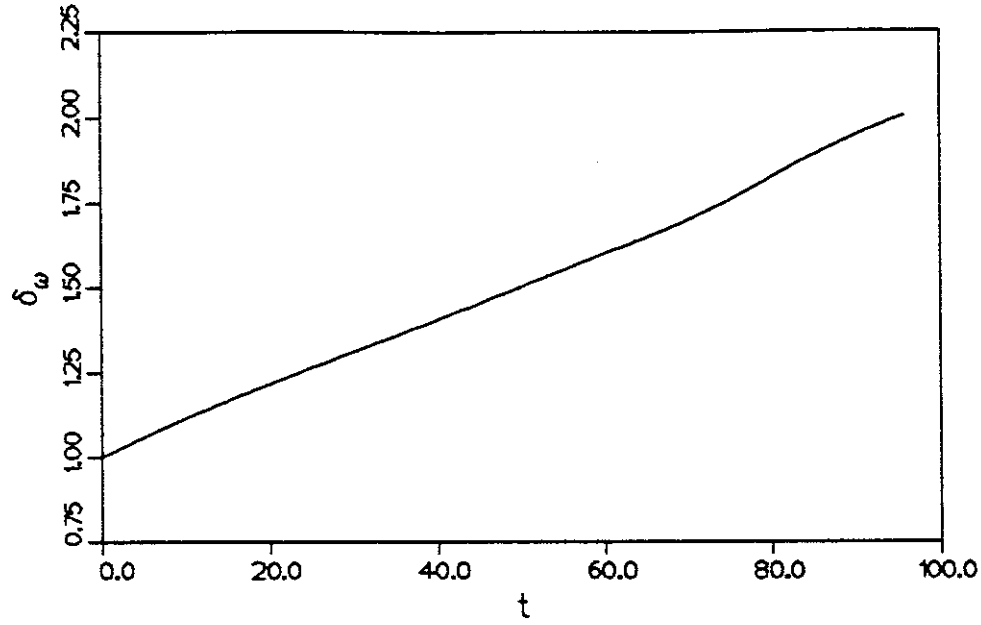

Figure 4.41 Growth of vorticity thickness for supersonic instability mode.

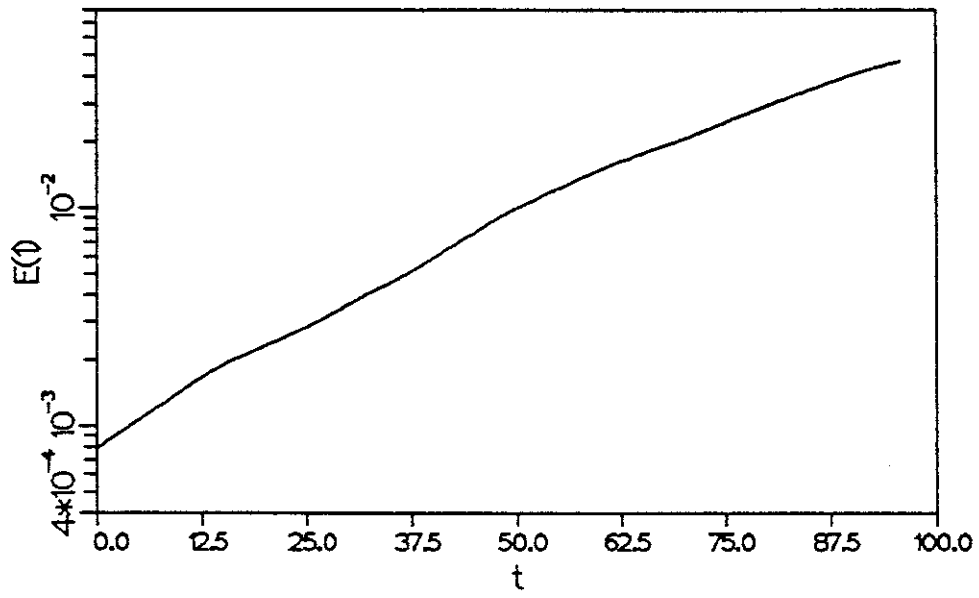

Figure 4.42 Growth of mode energy for supersonic instability mode.

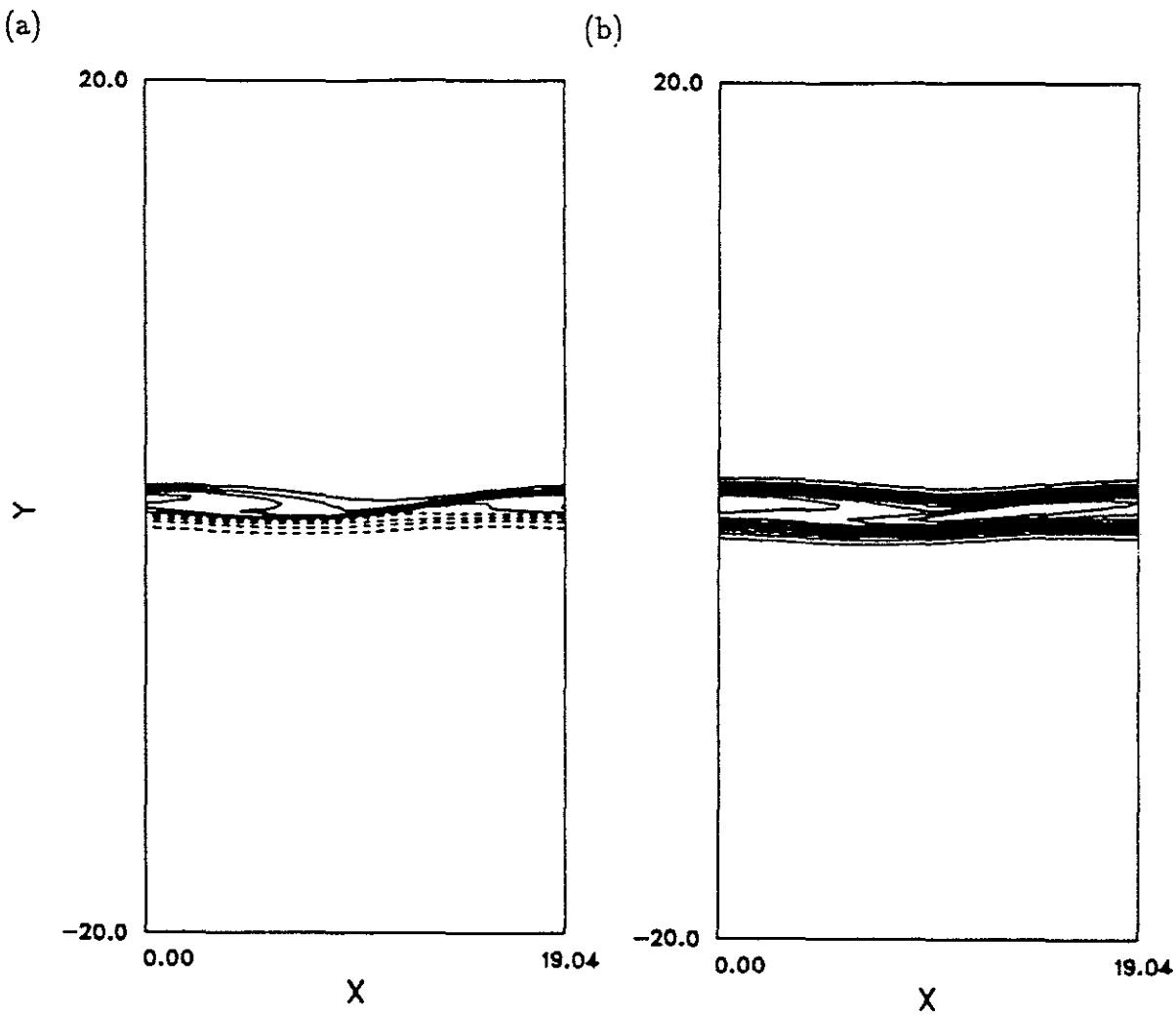
(a)
(b)
20.0
-20.0
0.00
19.04
Y
X
20.0
-20.0
0.00
19.04
X

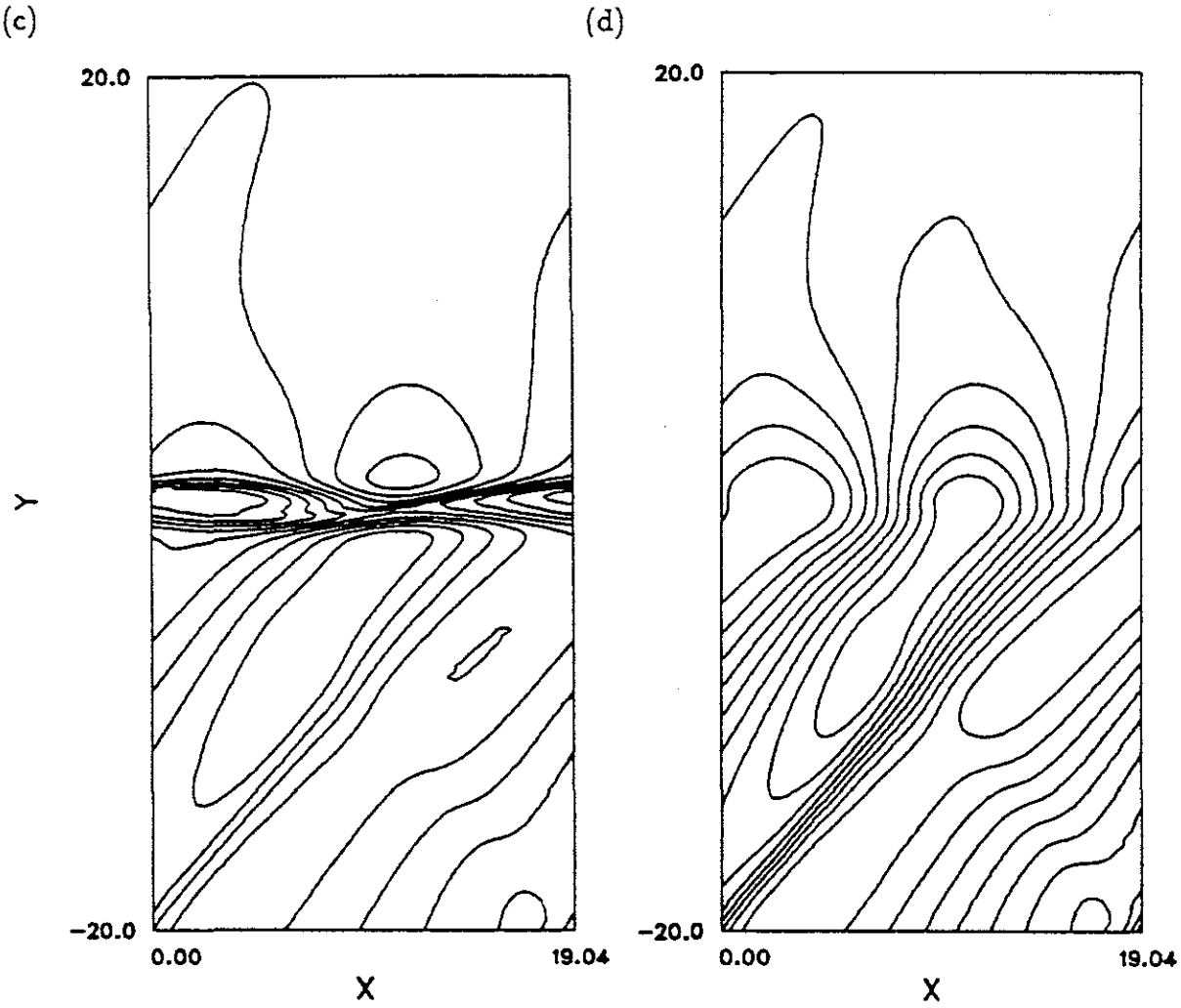

Figure 4.43 Non-linear structure developing from supersonic mode instability: (a) mixture fraction, (b) vorticity, (c) density, (d) pressure.

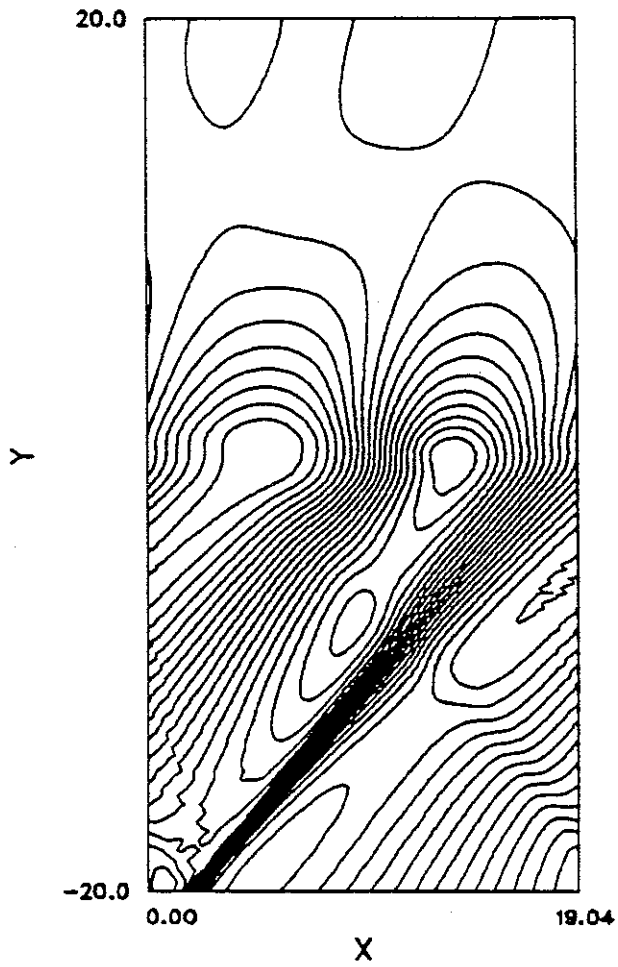

Figure 4.44 Pressure contours showing development of shock waves from supersonic mode instability.

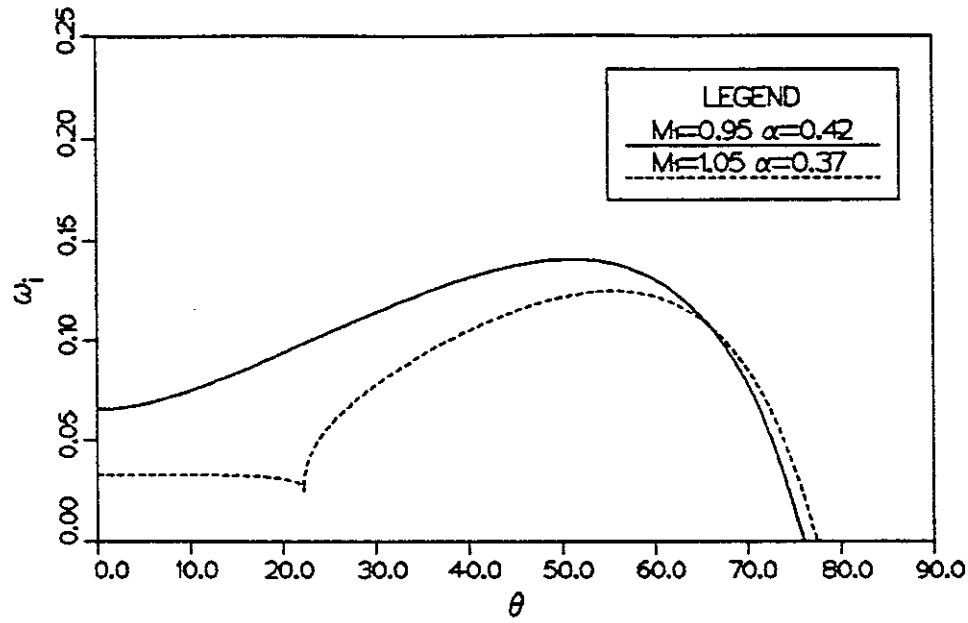

Figure 5.1 Linear temporal amplification rate versus wave angle at Mach numbers 0.95 and 1.05.

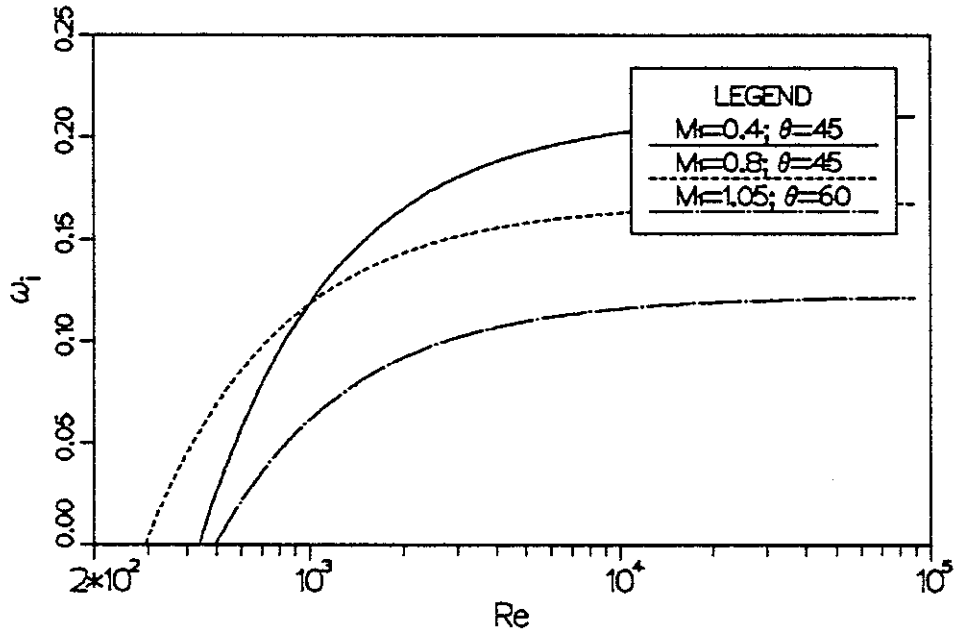

Figure 5.2 Effect of Reynolds number on the temporal amplification rate of oblique disturbances in the compressible mixing layer.

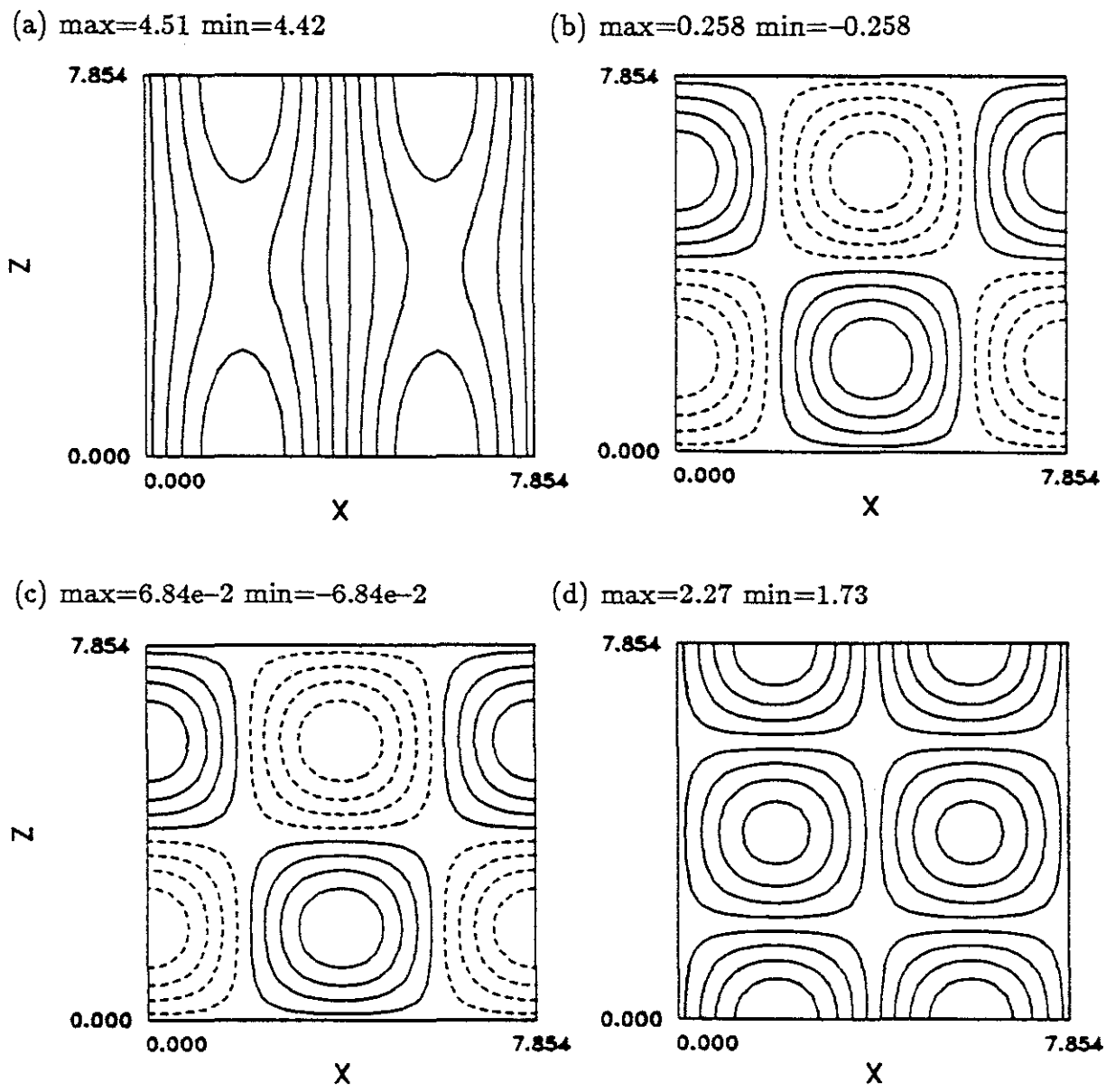

Figure 5.3 Initial condition for the bulging mode of instability (a) pressure - minimum at $L_x/4$, maximum at $3L_x/4$ (b) ω_x (c) ω_y (d) ω_z.

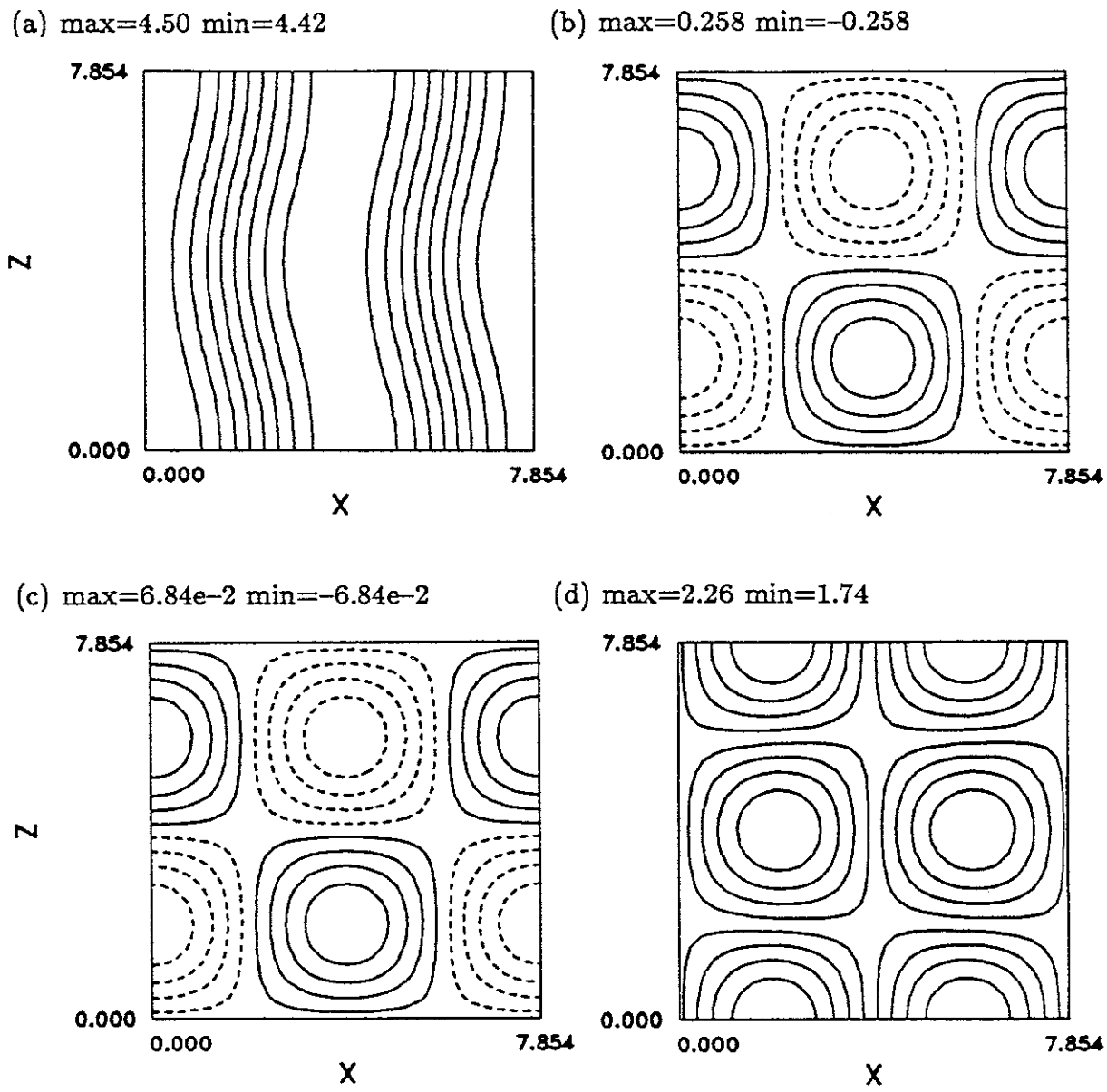

Figure 5.4 Initial condition for the translative mode of instability (a) pressure - minimum at $x = 0$, maximum at $L_x/2$ (b) ω_x (c) ω_y (d) ω_z.

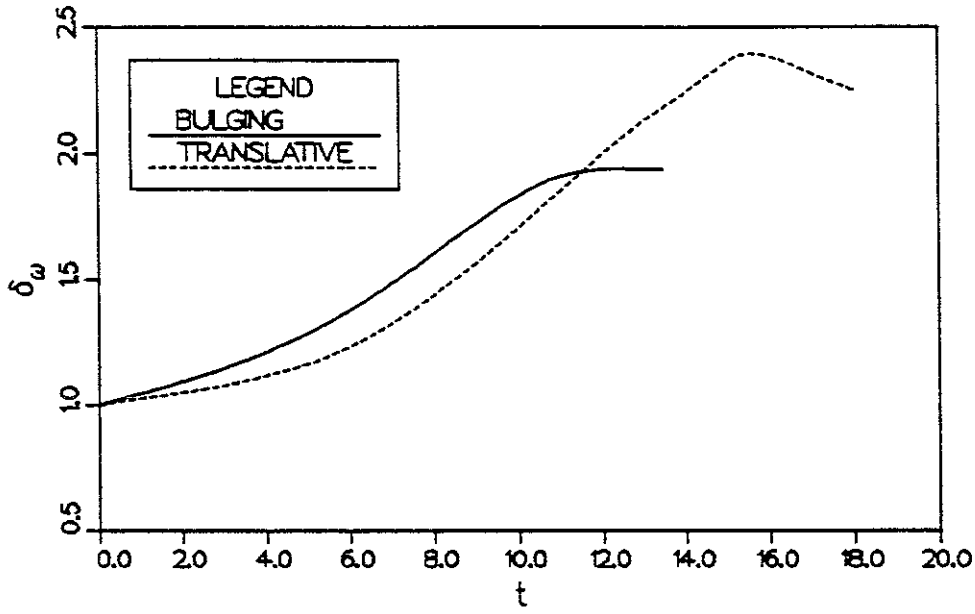

Figure 5.5 Vorticity thickness growth for the bulging and translative modes at $M_1 = 0.4$.

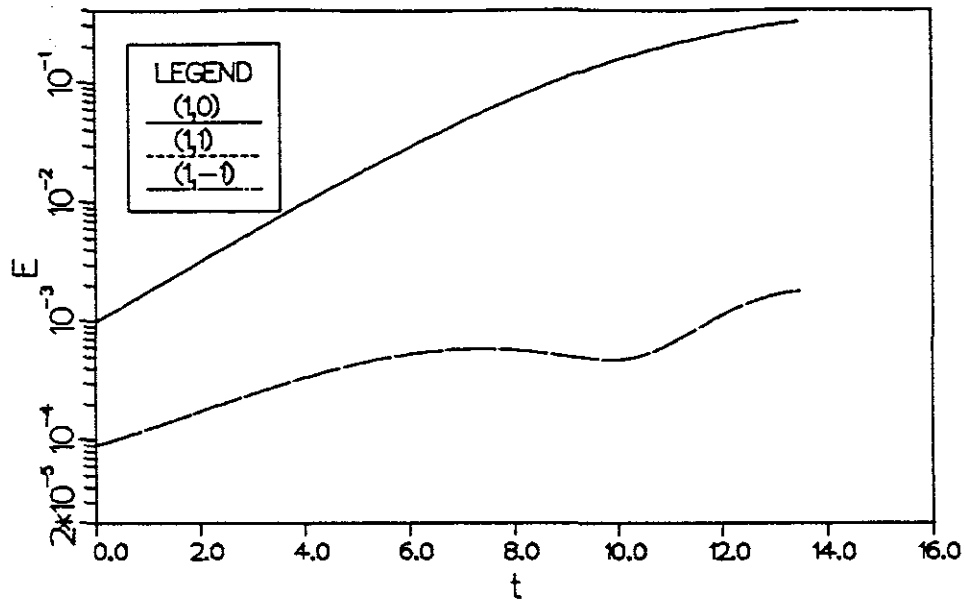

Figure 5.6 Growth in energy for the bulging instability at $M_1 = 0.4$. $(1,0)$ is the two-dimensional wave. $(1,1)$ and $(1,-1)$ are the oblique waves.

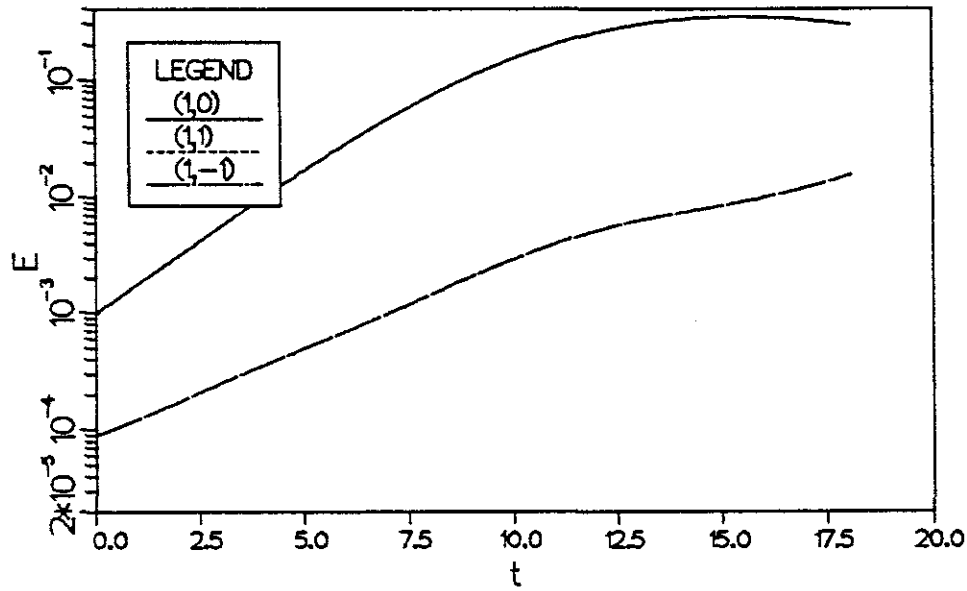

Figure 5.7 Growth in energy for the translative instability at $M_1 = 0.4$. $(1,0)$ is the two-dimensional wave. $(1,1)$ and $(1,-1)$ are the oblique waves.

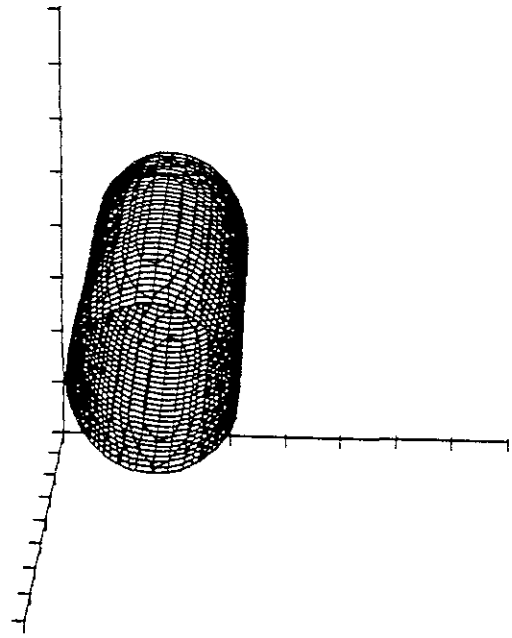

Figure 5.8 Surface of constant pressure showing the rotational region in the structure developing from the bulging instability at $M_1 = 0.4$.

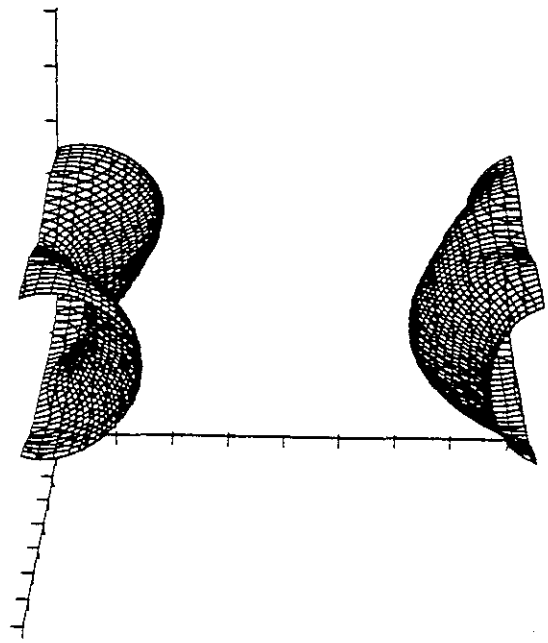

Figure 5.9 Surface of constant pressure showing the rotational region in the structure developing from the translative instability at $M_1 = 0.4$.

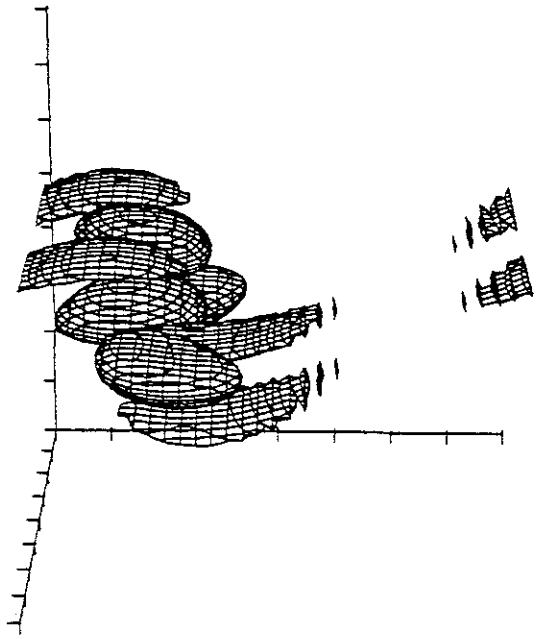

Figure 5.10 Perspective view of streamwise vorticity in the structure that developed from the bulging mode of instability at $M_1 = 0.4$

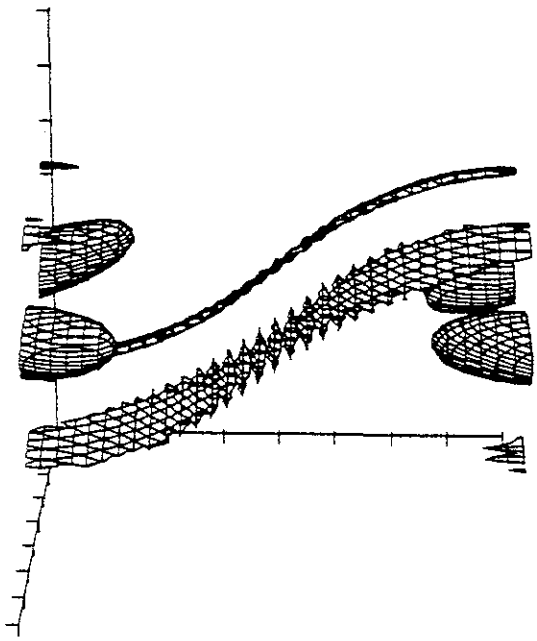

Figure 5.11 Perspective view of streamwise vorticity in the structure that developed from the translative mode of instability at $M_1 = 0.4$

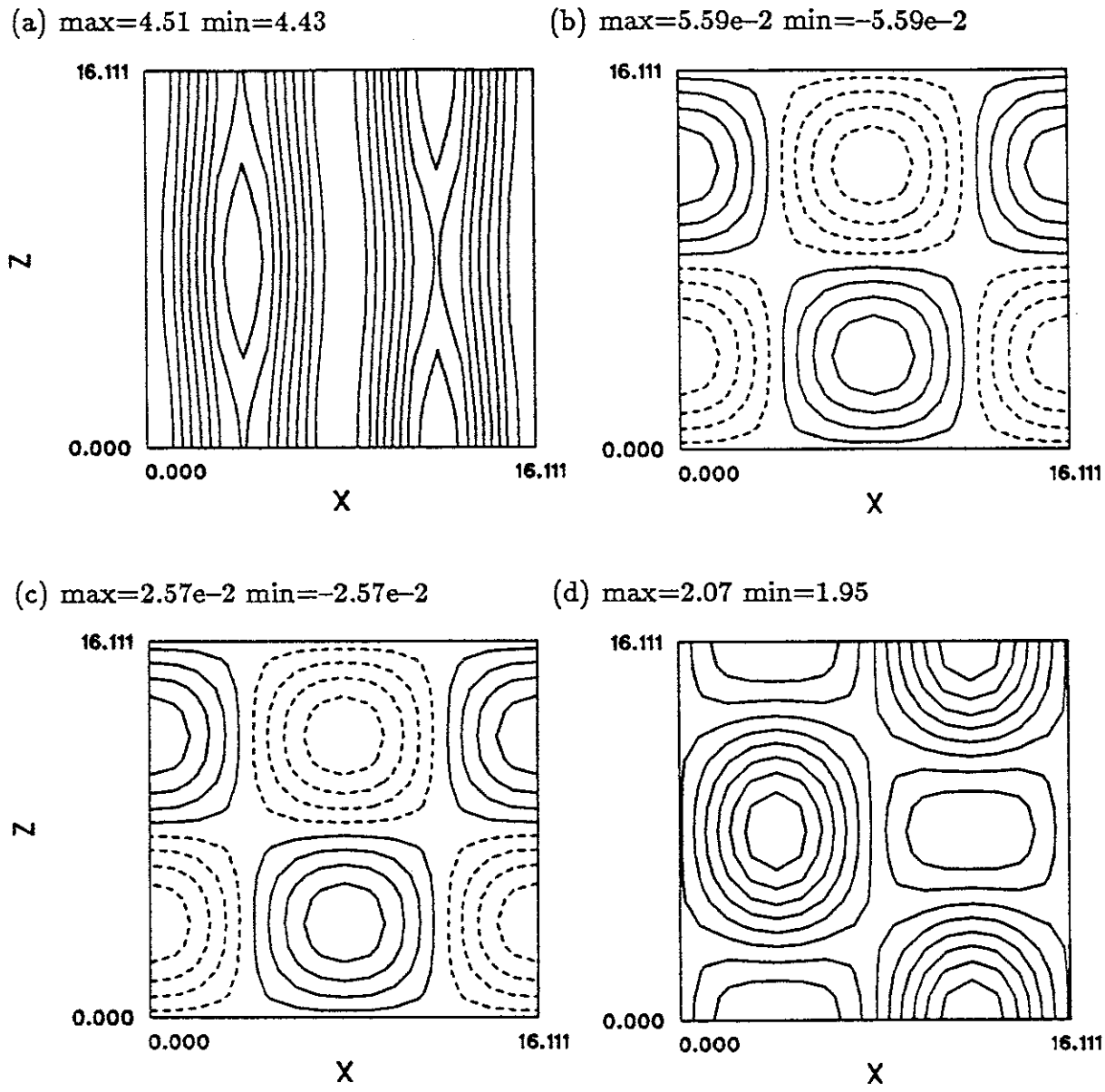

Figure 5.12 Initial condition for the 'helical' subharmonic mode of instability at $M_1 = 0.4$ (a) pressure - minimum at $x = 0$, $Lx/2$, maximum at $L_x/4$, $3L_x/4$ (b) ω_x (c) ω_y (d) ω_z.

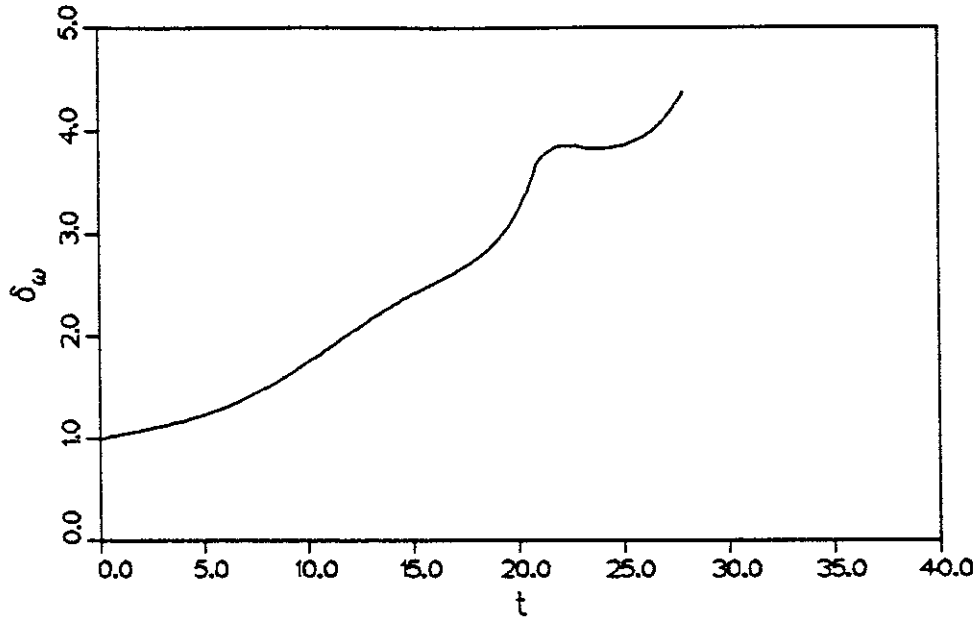

Figure 5.13 Vorticity thickness growth for the helical subharmonic mode at $M_1 = 0.4$.

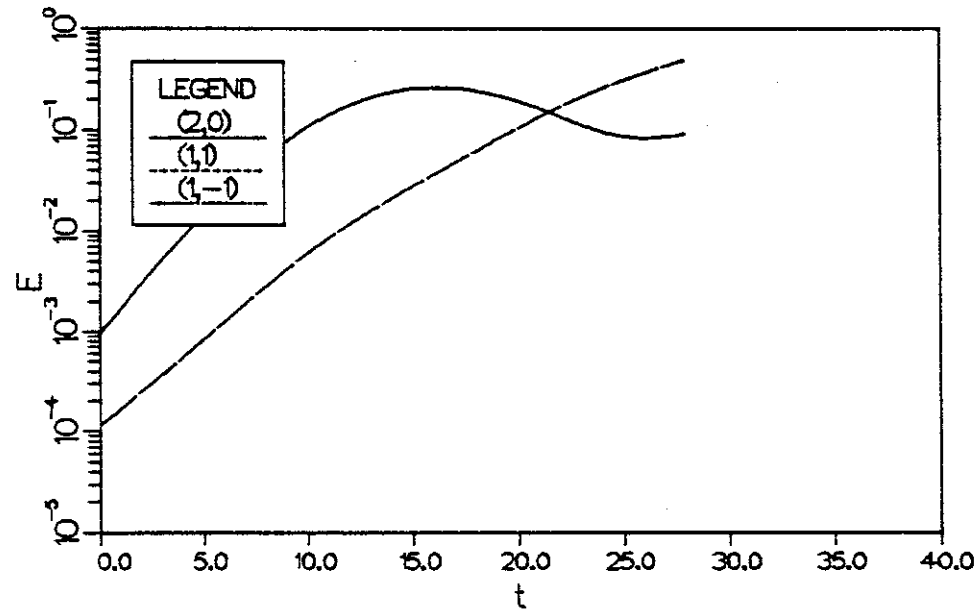

Figure 5.14 Growth in energy for the bulging instability at $M_1 = 0.4$. $(2,0)$ is the two-dimensional wave. $(1,1)$ and $(1,-1)$ are the oblique waves.

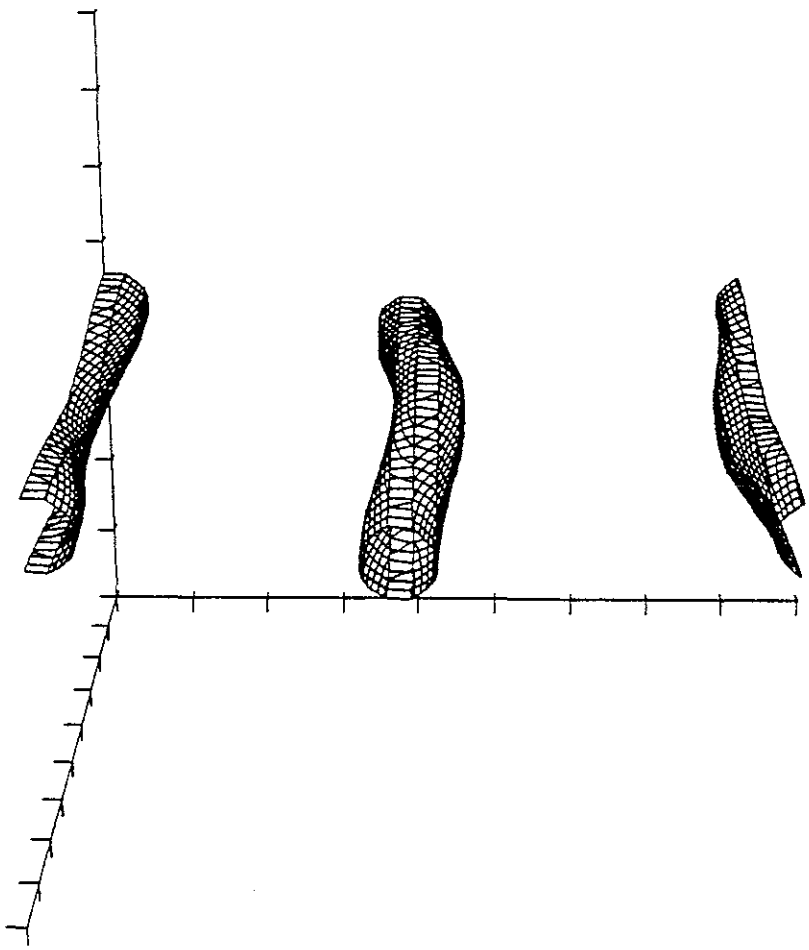

Figure 5.15 Perspective view of the pressure minima at time $t = 12.63$ for the helical subharmonic mode of instability, showing vortex cores at saturation on the fundamental instability.

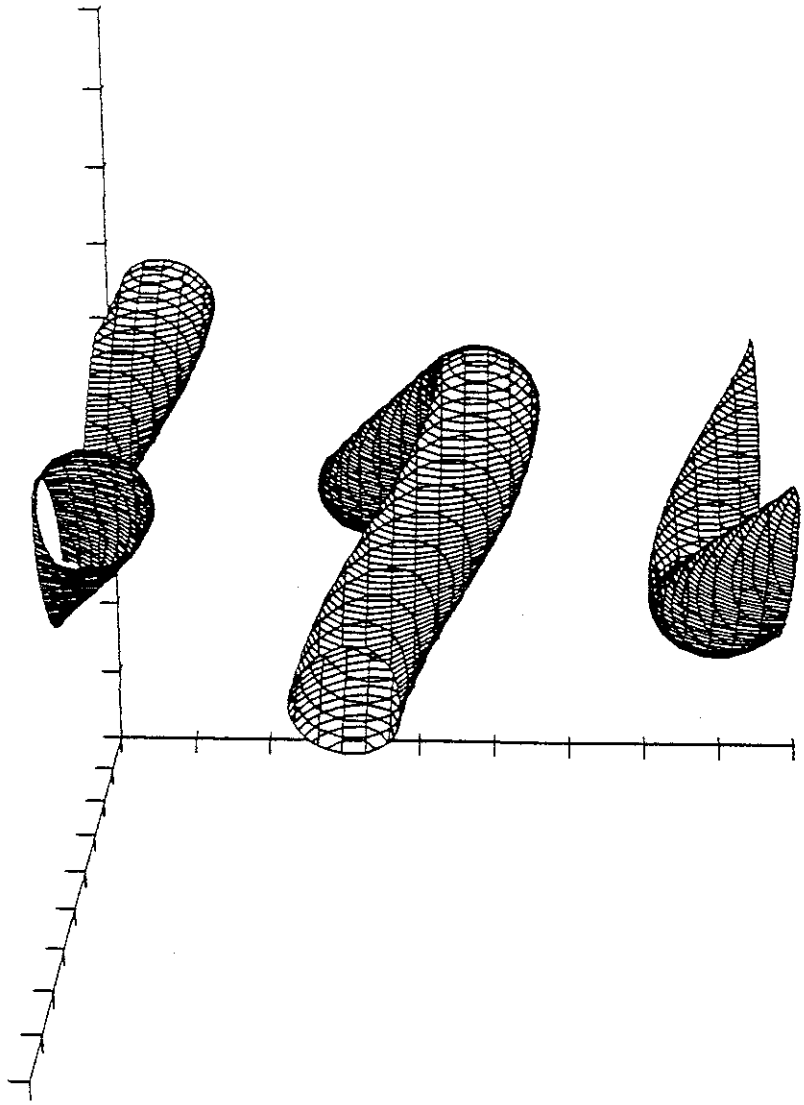

Figure 5.16 Perspective view of the pressure minima at time $t = 27.90$ for the helical subharmonic mode of instability, showing the final subharmonic structure.

(a) max=0.489 min=–0.489

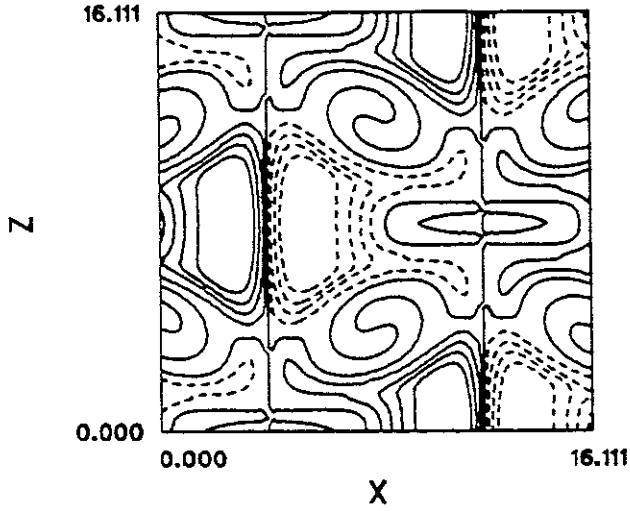

(b) max=4.98 min=3.59

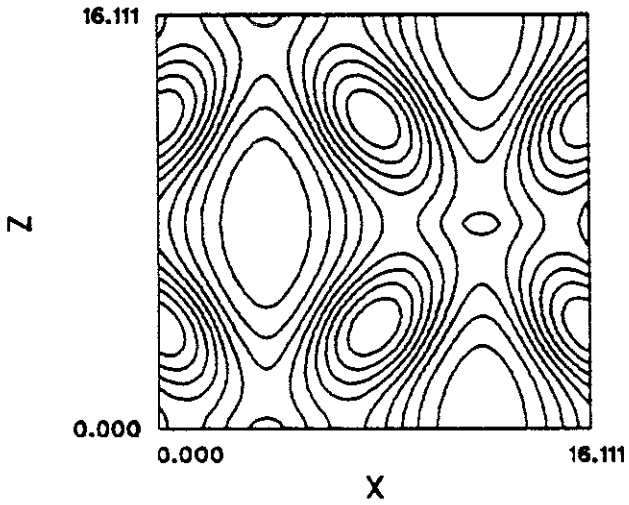

Figure 5.17 Cuts at $y = 0$ through the final structure developed from the helical subharmonic mode (a) mixture fraction (b) pressure.

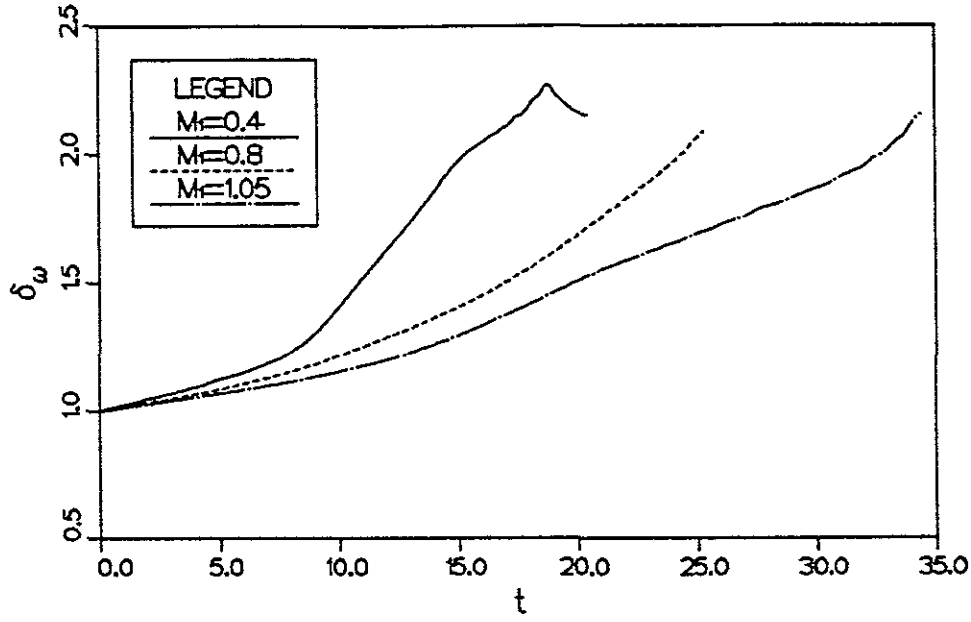

Figure 5.18 Effect of Mach number on the vorticity thickness growth, forcing with a two-dimensional wave and two equal and opposite oblique waves.

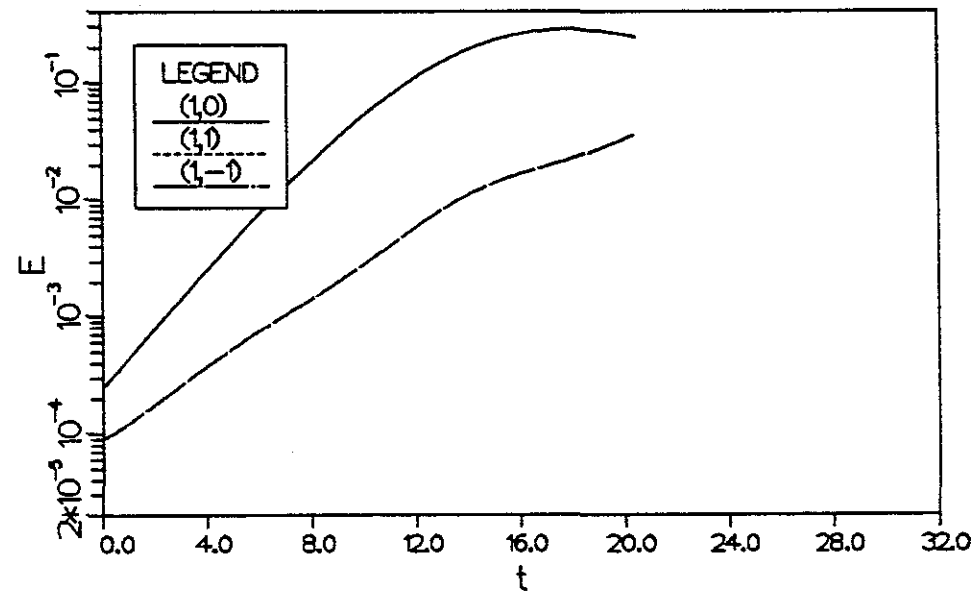

Figure 5.19 Growth in mode energies at $M_1 = 0.4$ $(1,0)$ is the two-dimensional mode. $(1,1)$ and $(1,-1)$ are the oblique waves.

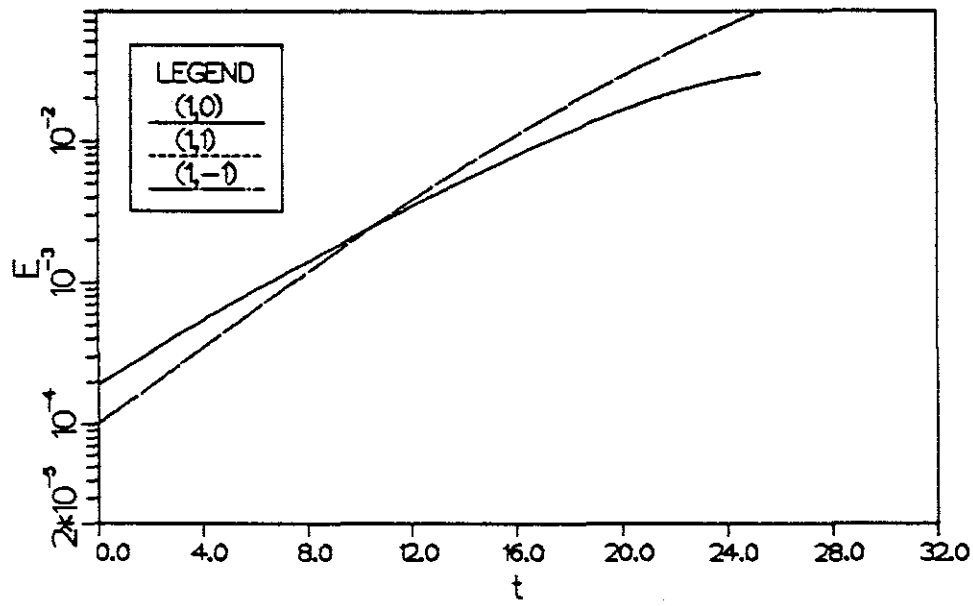

Figure 5.20 Growth in mode energies at $M_1 = 0.8$ $(1,0)$ is the two-dimensional mode. $(1,1)$ and $(1,-1)$ are the oblique waves.

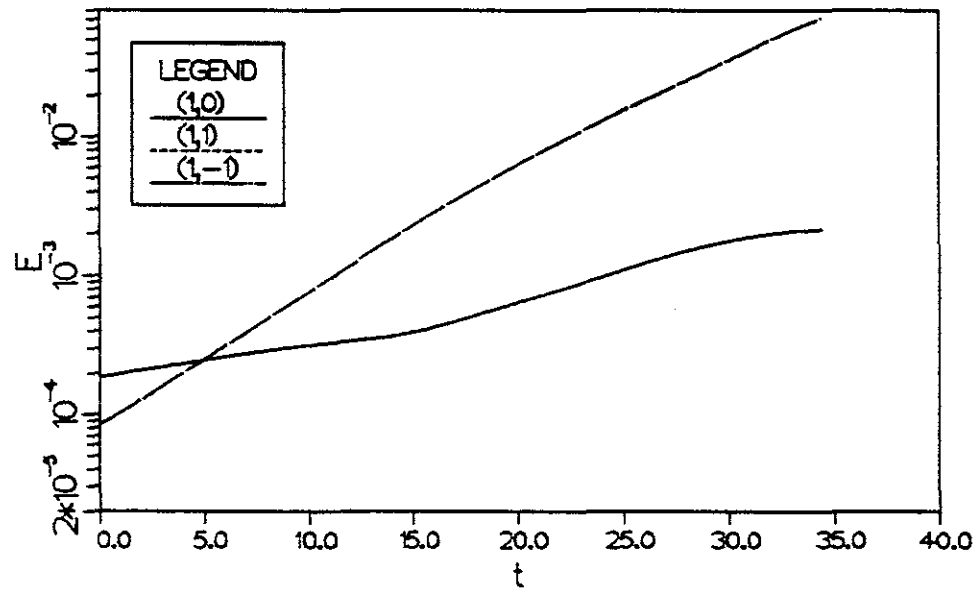

Figure 5.21 Growth in mode energies at $M_1 = 1.05$ $(1,0)$ is the two-dimensional mode. $(1,1)$ and $(1,-1)$ are the oblique waves.

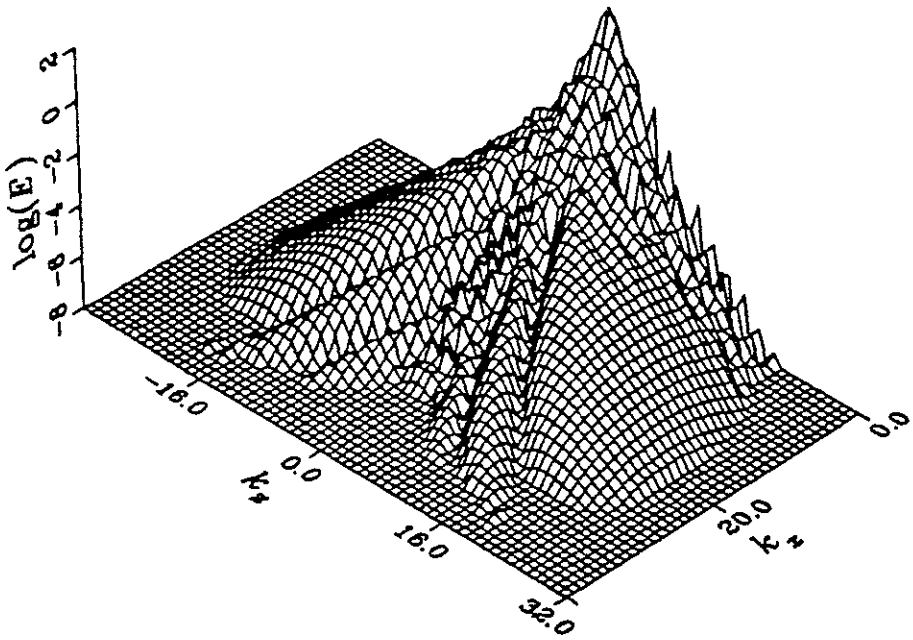

Figure 5.22 Carpet plot of the modal energy contents at the end of the three-dimensional simulation at $M_1 = 0.4$

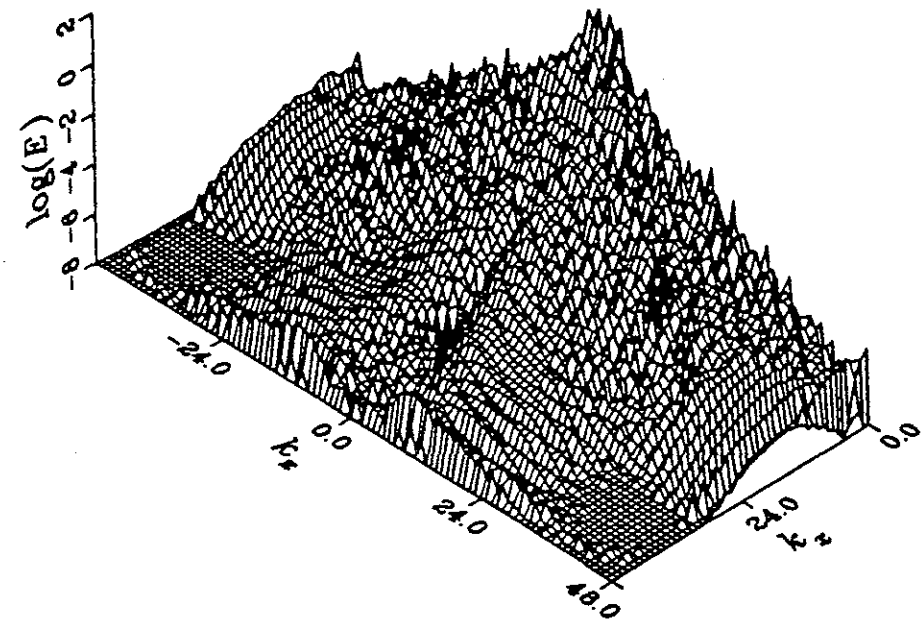

Figure 5.23 Carpet plot of the modal energy contents at the end of the three-dimensional simulation at $M_1 = 0.8$

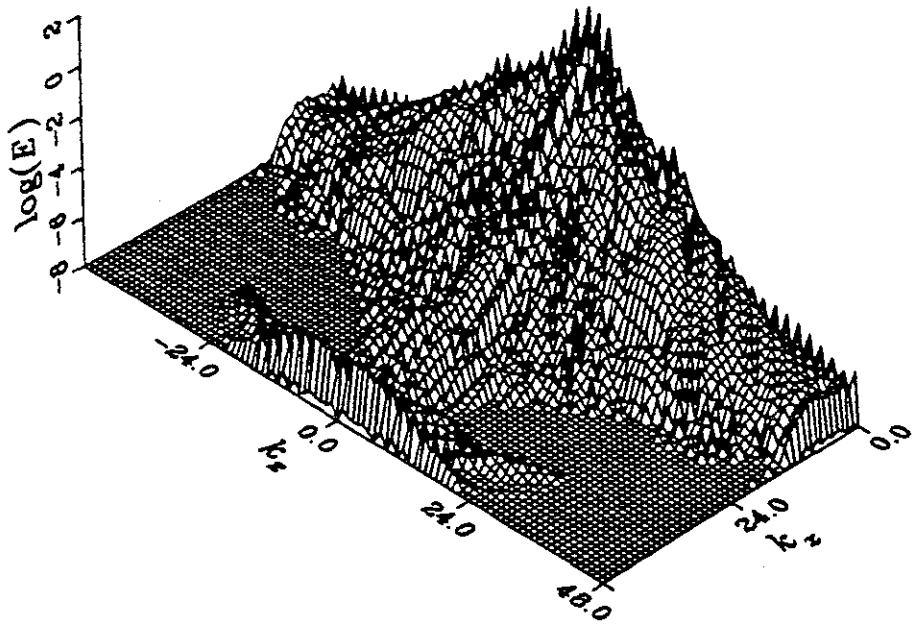

Figure 5.24 Carpet plot of the modal energy contents at the end of the three-dimensional simulation at $M_1 = 1.05$

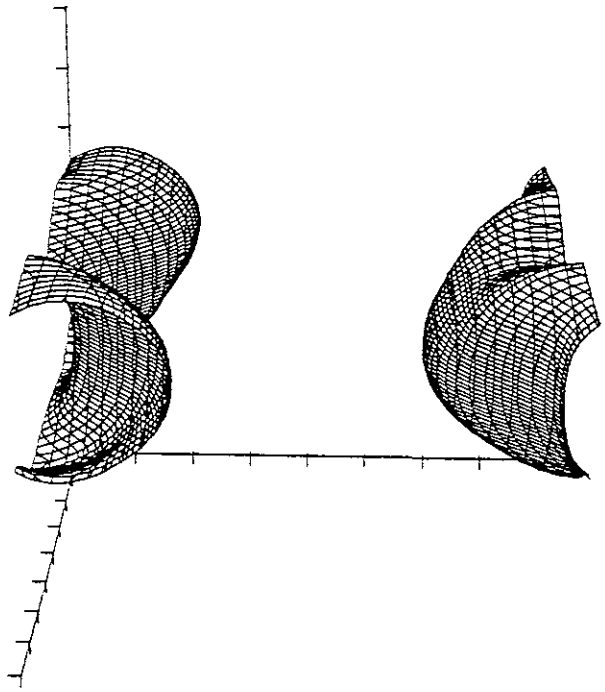

Figure 5.25 Surface of constant pressure showing the rotational region in the structure developing at $M_1 = 0.4$.

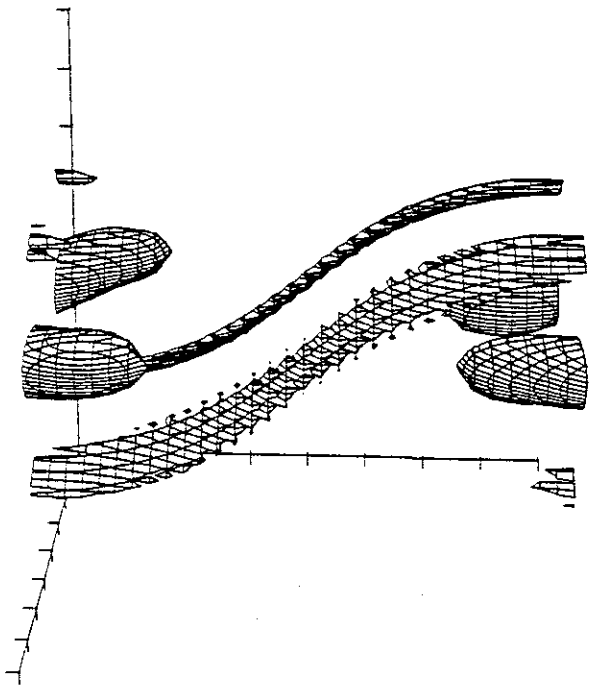

Figure 5.26 Perspective view of streamwise vorticity in the structure that developed at $M_1 = 0.4$

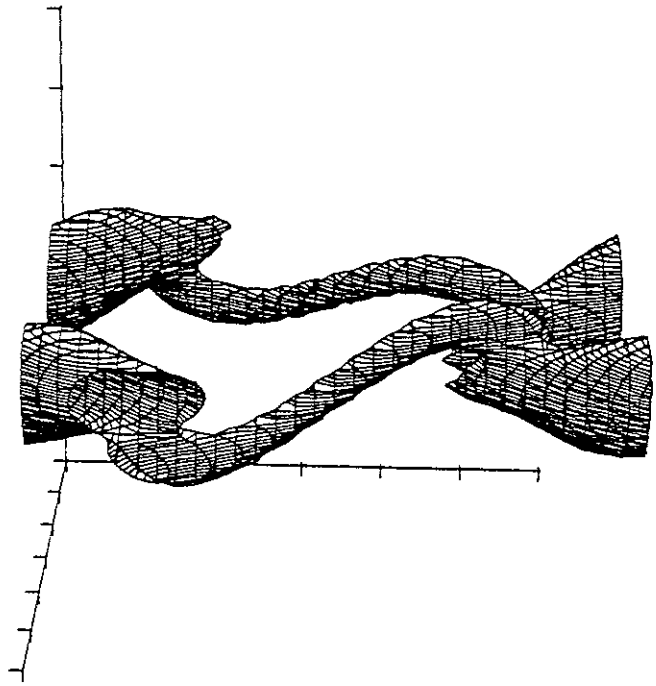

Figure 5.27 Surface of constant pressure showing the rotational region in the structure developing at $M_1 = 0.8$.

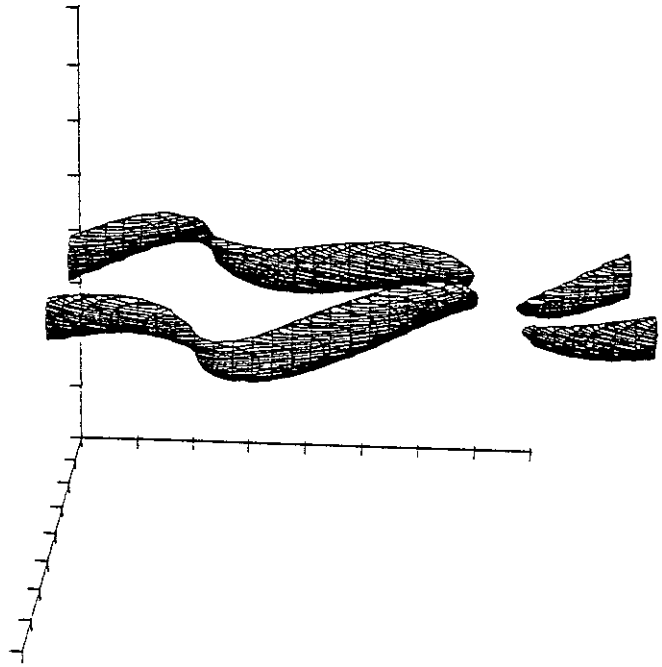

Figure 5.28 Surface of constant pressure showing the rotational region in the structure developing at $M_1 = 1.05$.

(a)

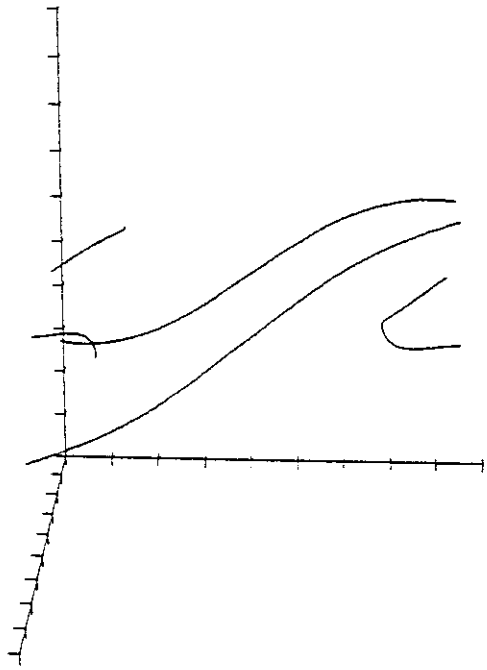

(b)

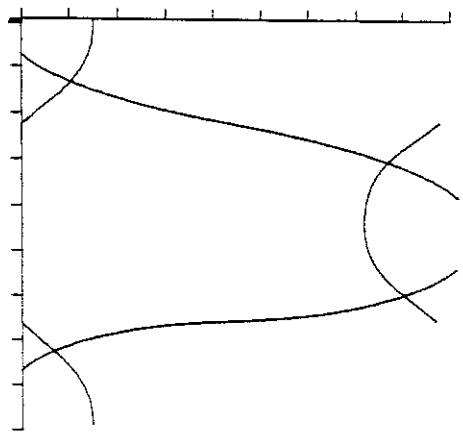

Figure 5.29 Vortex lines through the peaks of vorticity for the developed structure at $M_1 = 0.4$ (a) perspective view (b) top view.

(a)

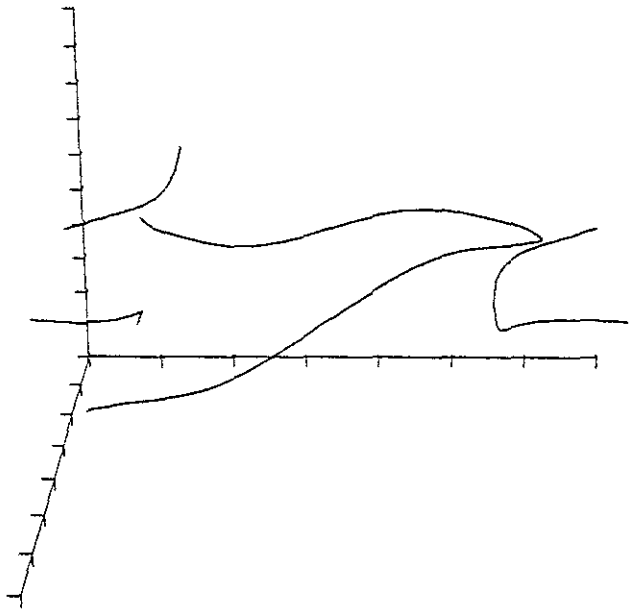

(b)

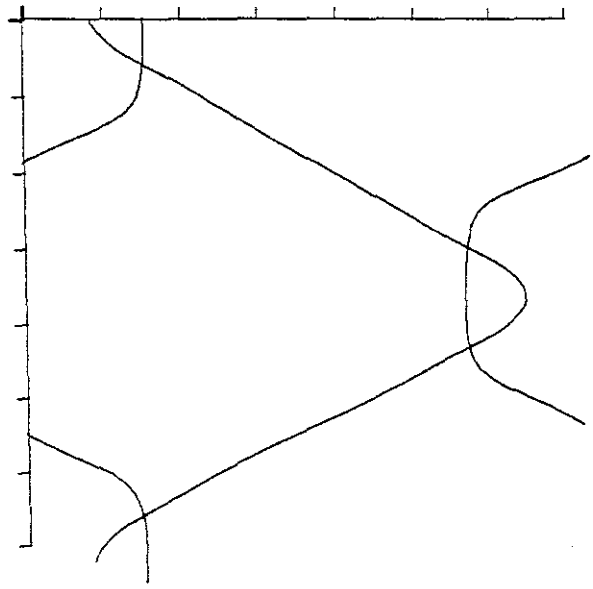

Figure 5.30 Vortex lines through the peaks of vorticity for the developed structure at $M_1 = 0.8$ (a) perspective view (b) top view.

(a)

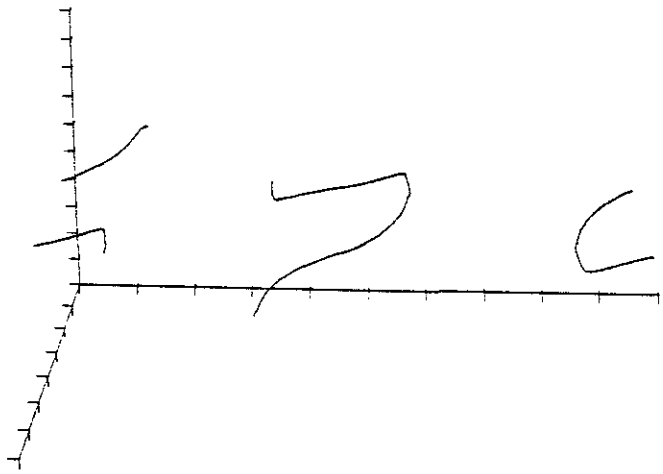

(b)

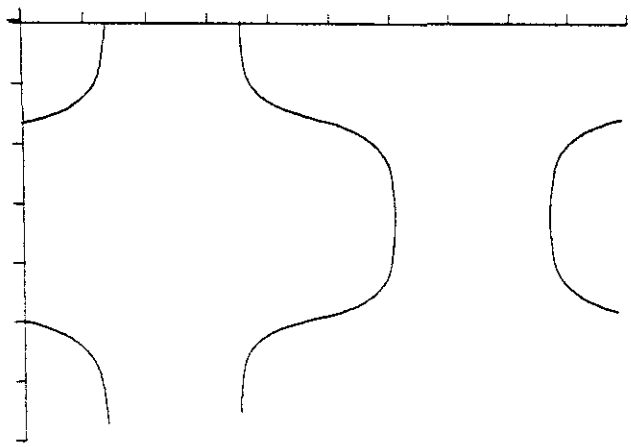

Figure 5.31 Vortex lines through the peaks of vorticity for the developed structure at $M_1 = 1.05$ (a) perspective view (b) top view.

(a) max=0.494 min=−0.494

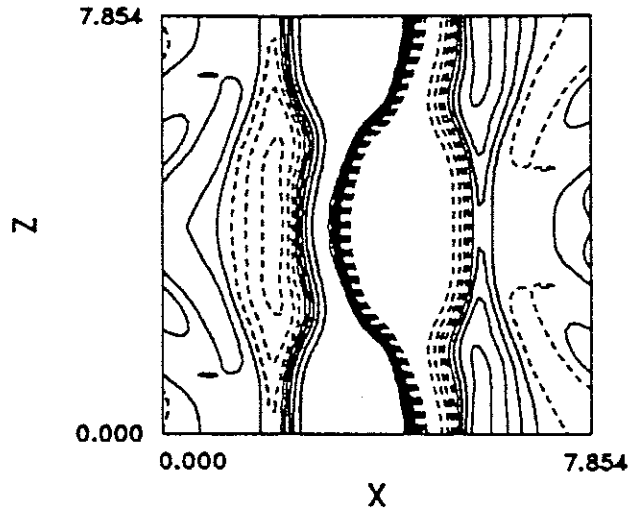

(b) max=4.86 min=3.58

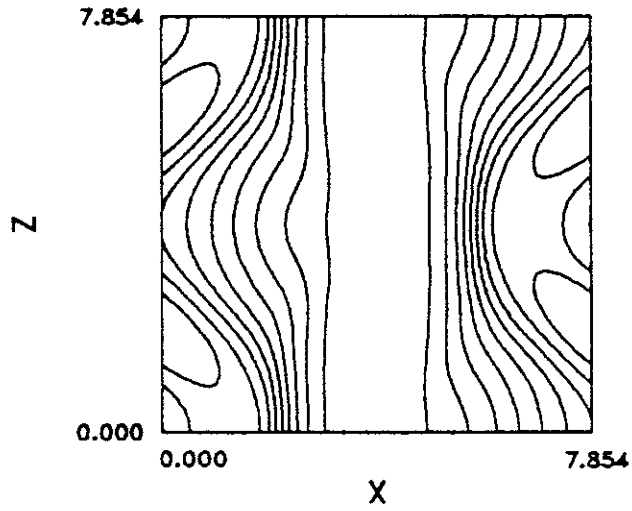

Figure 5.32 Cuts at $y = 0$ through the final structure developed at $M_1 = 0.4$ (a) mixture fraction (b) pressure.

(a) max=0.464 min=–0.464

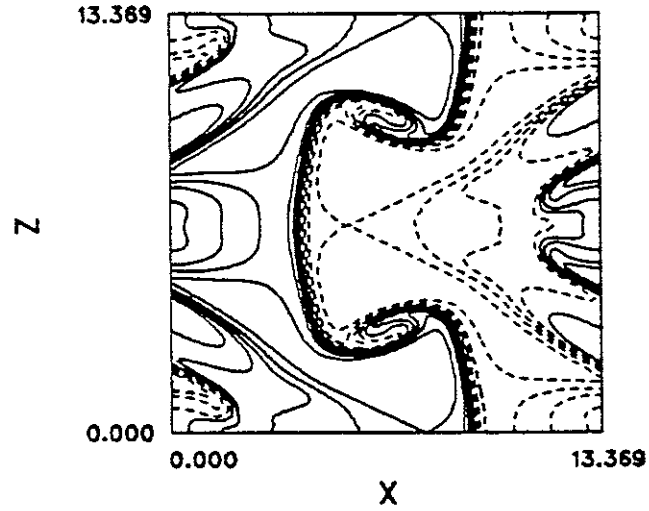

(b) max=1.43 min=0.651

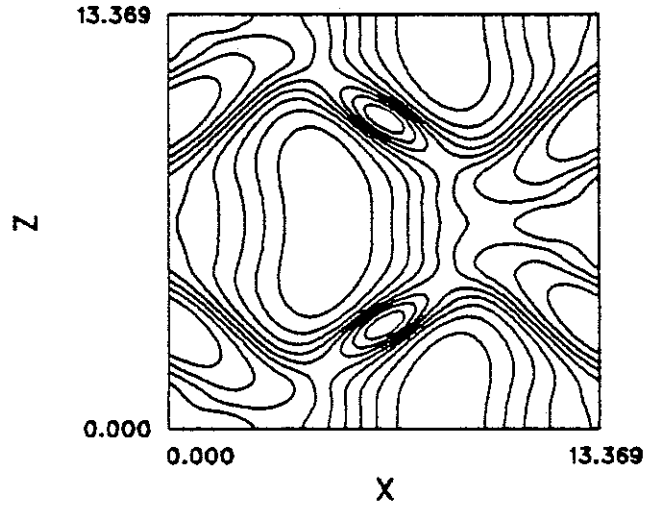

Figure 5.33 Cuts at $y = 0$ through the final structure developed at $M_1 = 0.8$ (a) mixture fraction (b) pressure.

(a) max=0.437 min=–0.437

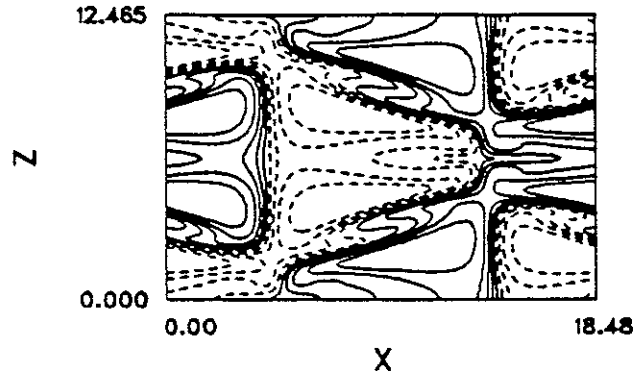

(b) max=0.812 min=0.401

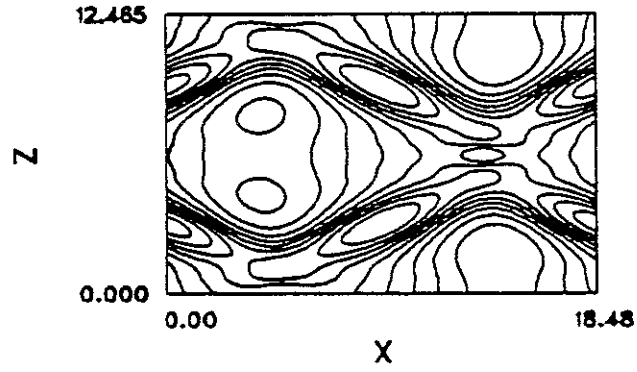

Figure 5.34 Cuts at $y = 0$ through the final structure developed at $M_1 = 1.05$ (a) mixture fraction (b) pressure.

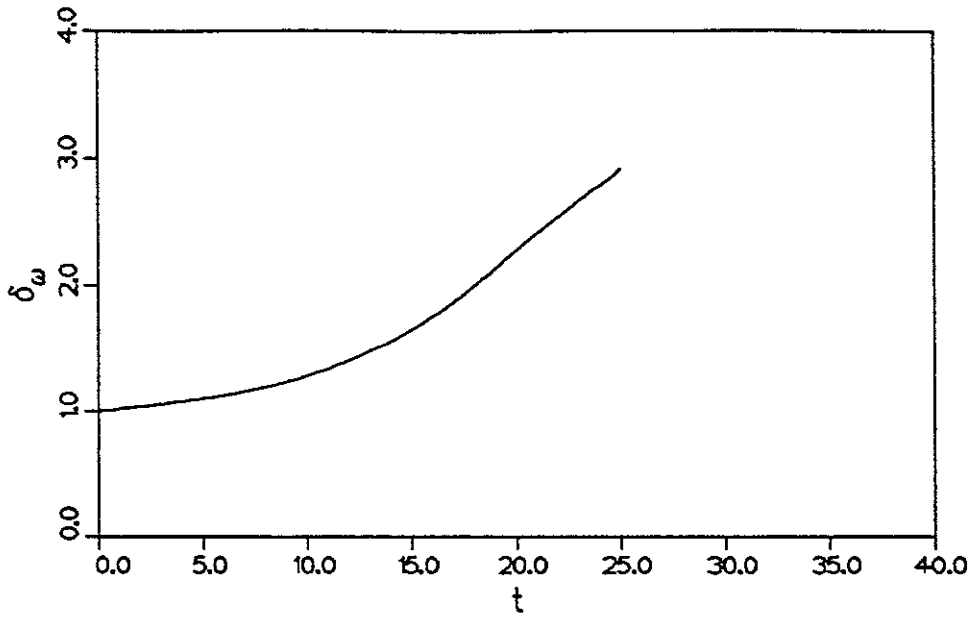

Figure 5.35 Vorticity thickness growth for simulation of the bulging mode at $M_1 = 0.8$.

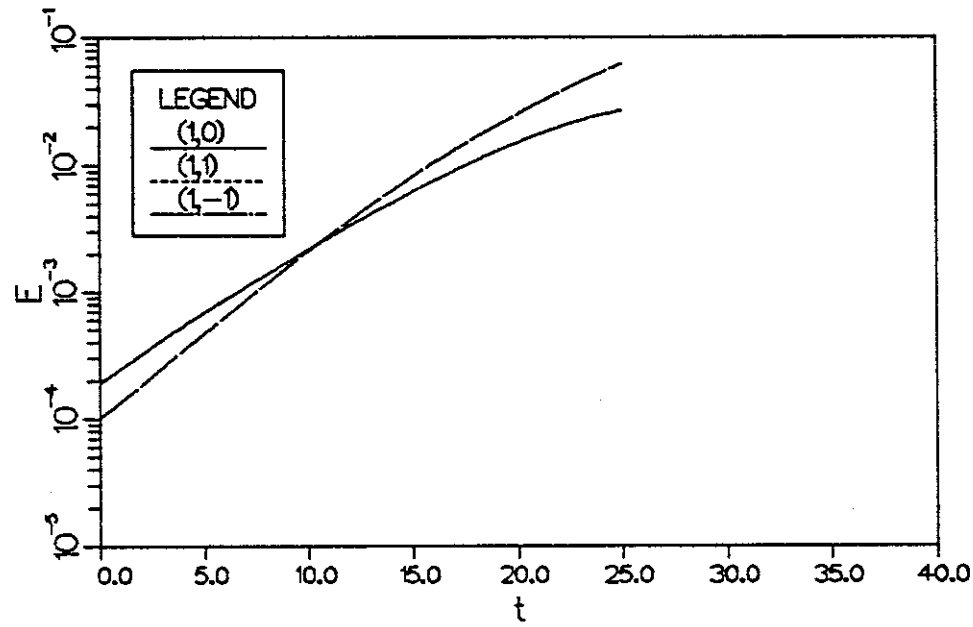

Figure 5.36 Growth in energy for the bulging instability mode at $M_1 = 0.8$.

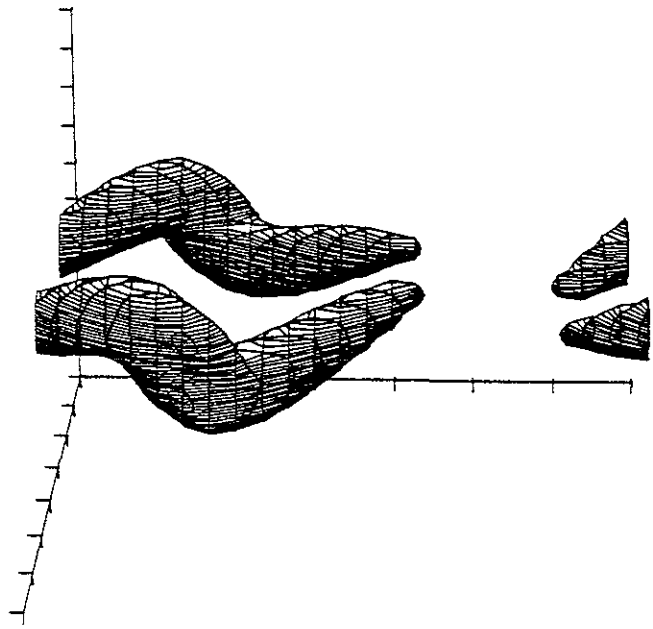

Figure 5.37 Surface of constant pressure showing the rotational region in the structure developing from the bulging mode at $M_1 = 0.8$.

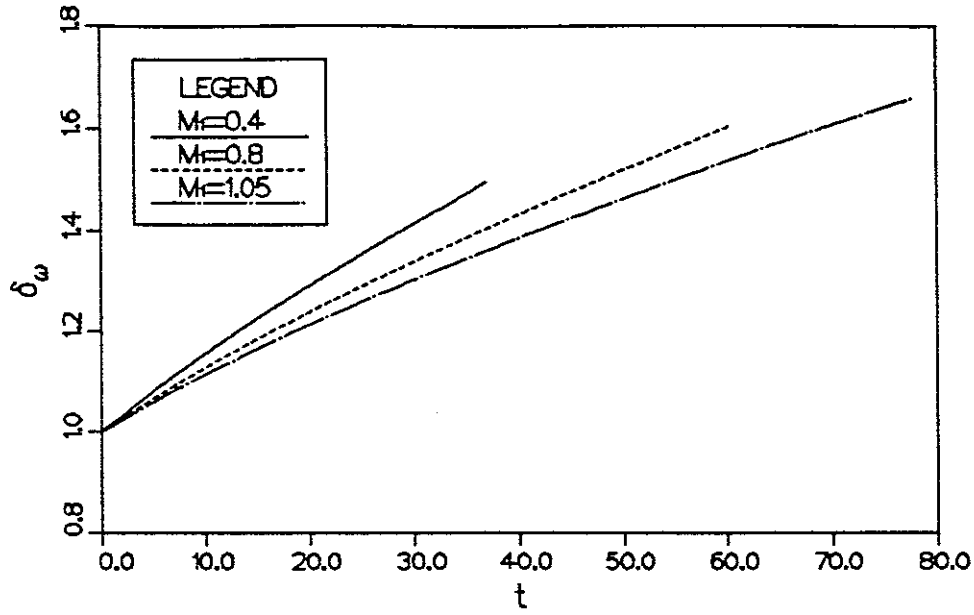

Figure 5.38 Growth in vorticity thickness for the simulations beginning with random numbers.

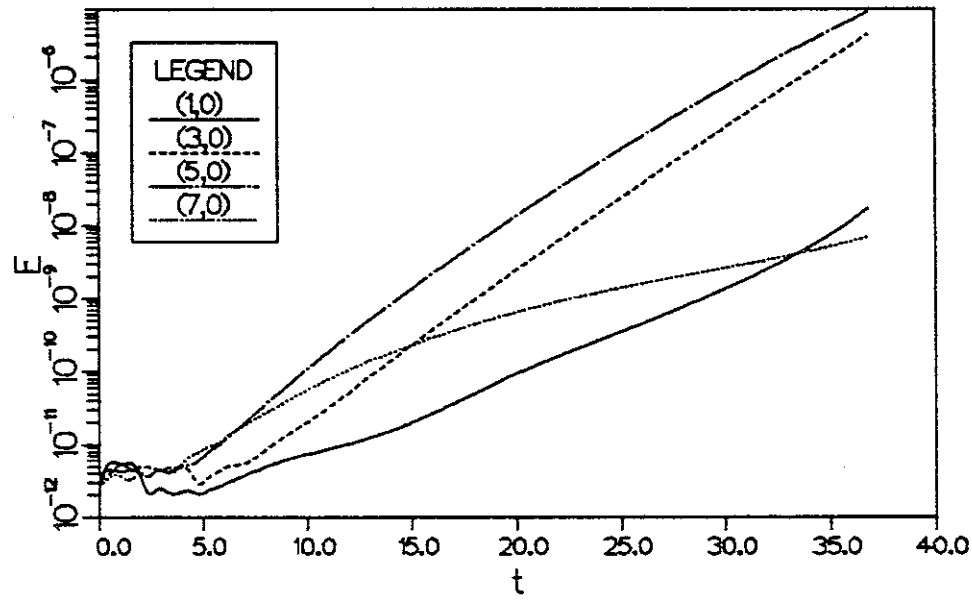

Figure 5.39 Growth in energy for selected modes from the simulation beginning with random numbers at $M_1 = 0.4$

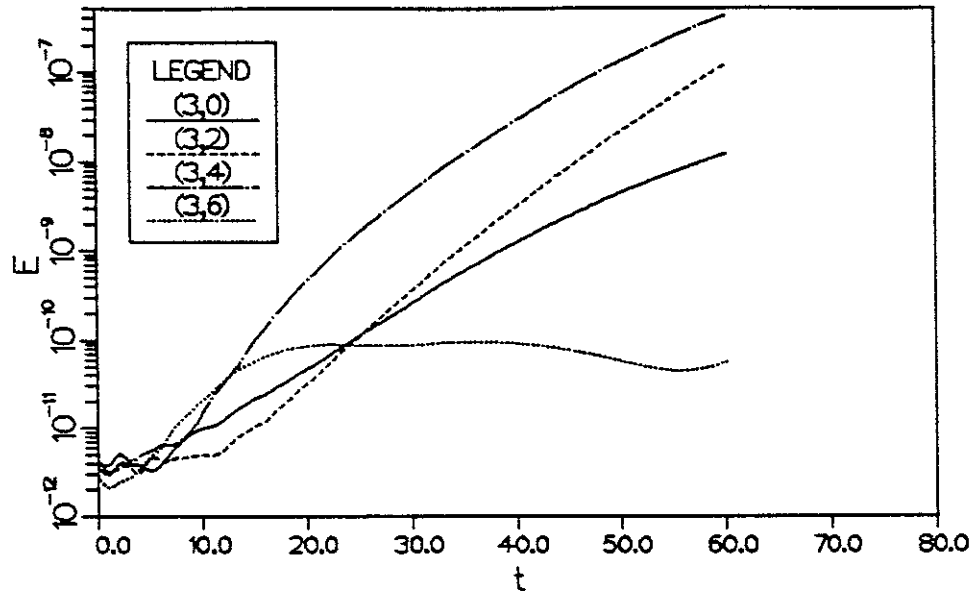

Figure 5.40 Growth in energy for selected modes from the simulation beginning with random numbers at $M_1 = 0.8$

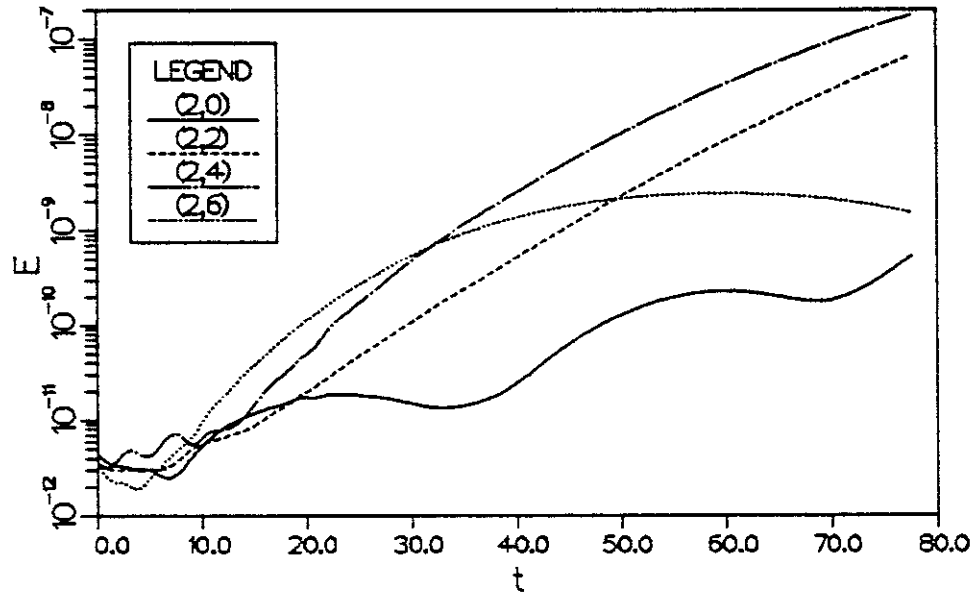

Figure 5.41 Growth in energy for selected modes from the simulation beginning with random numbers at $M_1 = 1.05$

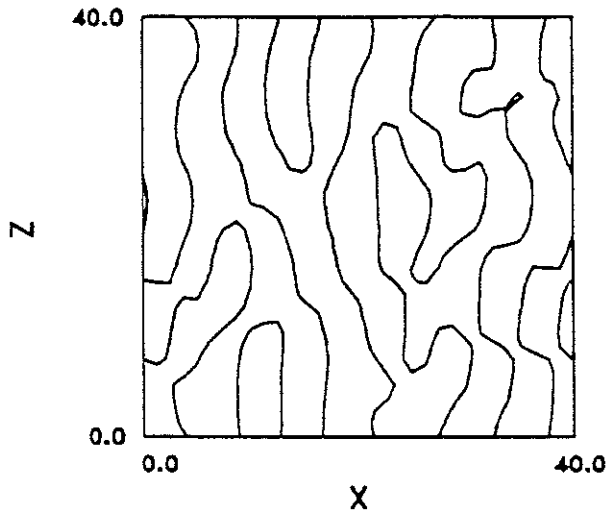

Figure 5.42 Flowfield at the end of the linear stage of instability growth at $M_1 = 0.4$, shown by the $v = 0$ contour.

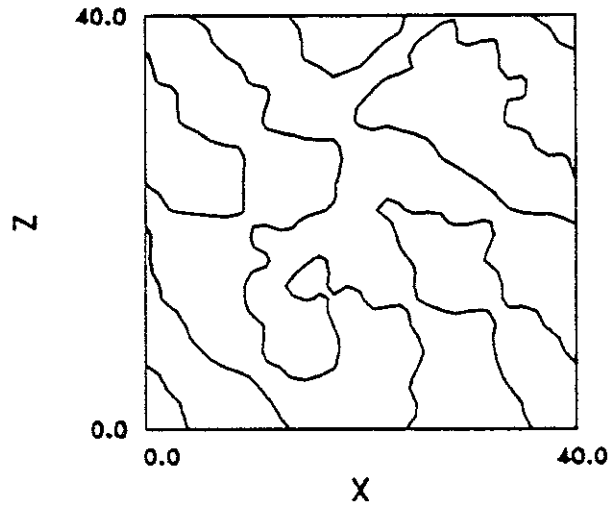

Figure 5.43 Flowfield at the end of the linear stage of instability growth at $M_1 = 0.8$, shown by the $v = 0$ contour.

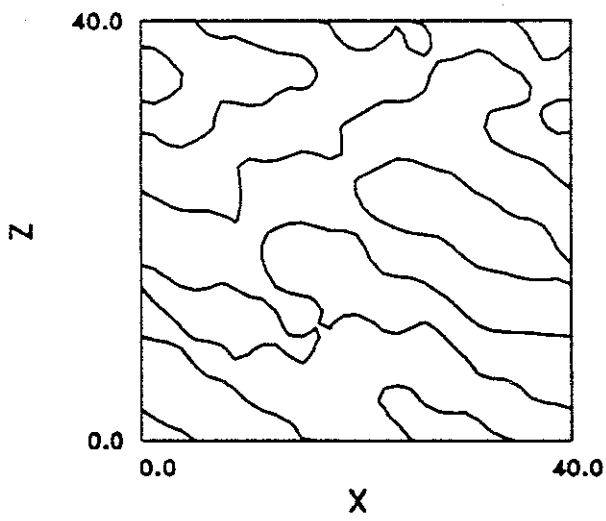

Figure 5.44 Flowfield at the end of the linear stage of instability growth at $M_1 = 1.05$, shown by the $v = 0$ contour.

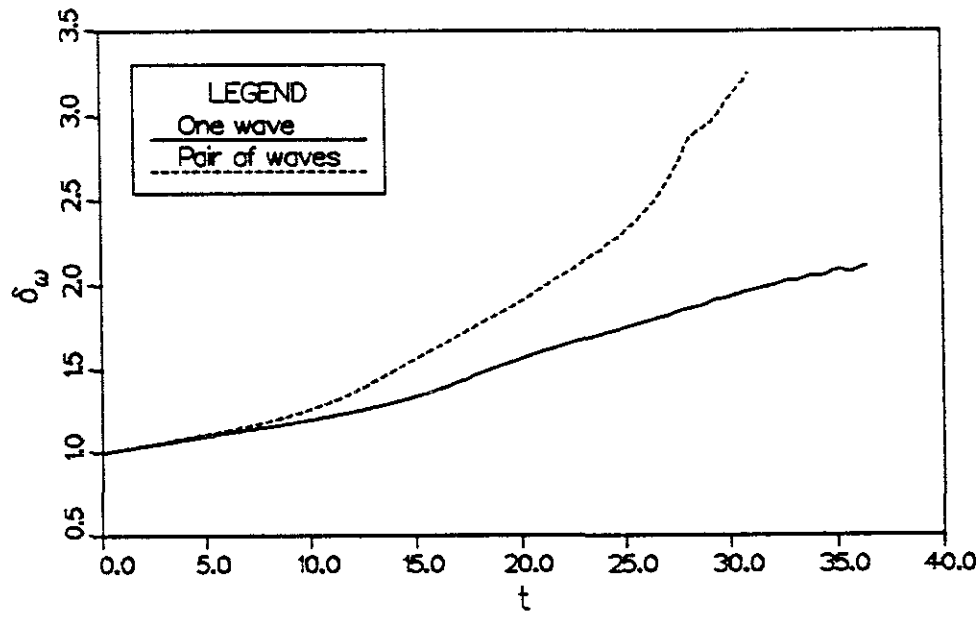

Figure 5.45 Vorticity thickness growth for a single versus a pair of oblique waves.

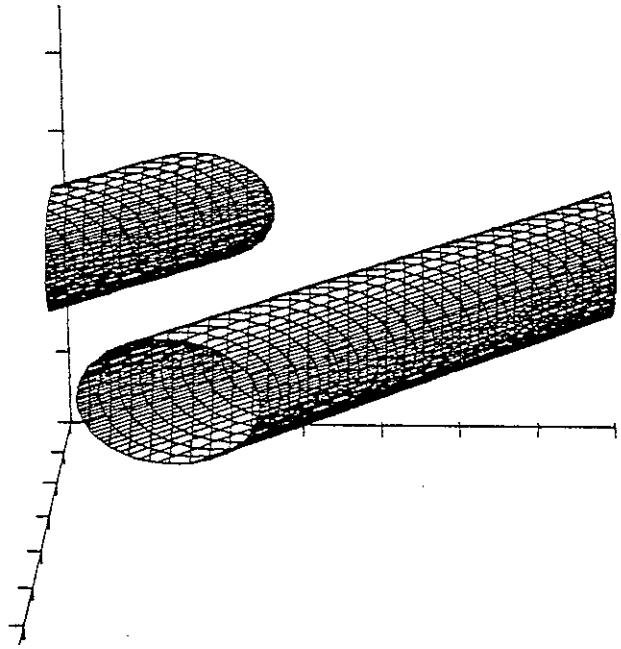

Figure 5.46 Surface of constant pressure, showing structure developed from a single oblique wave.

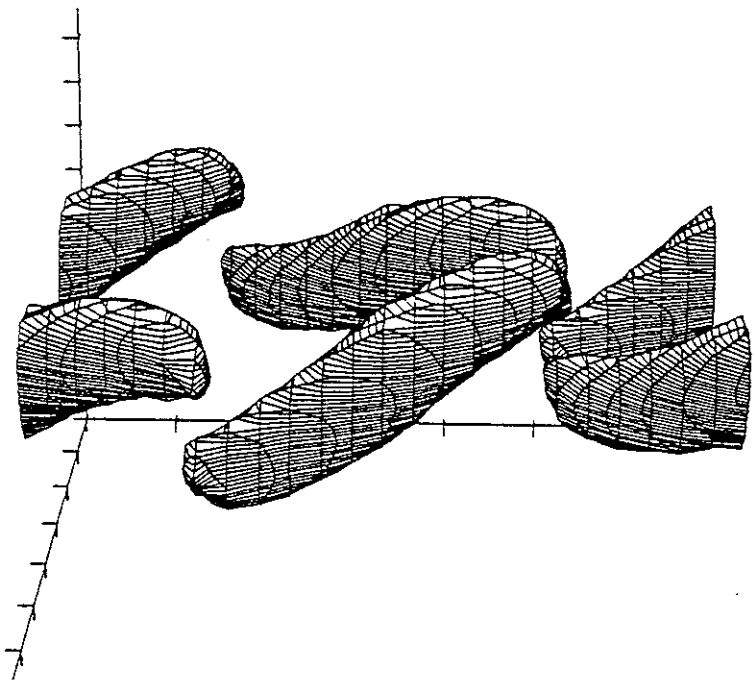

Figure 5.47 Surface of constant pressure, showing structure developed from a pair of equal and opposite oblique waves.

(a)

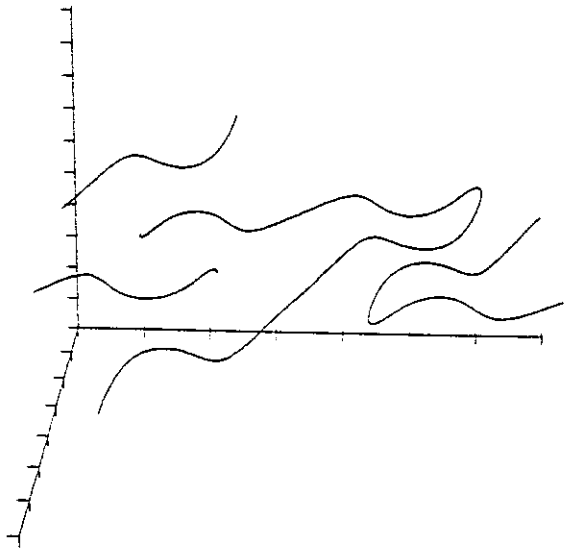

(b)

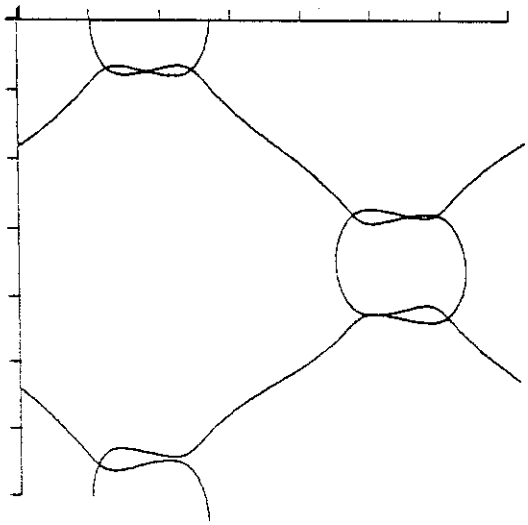

Figure 5.48 Vortex lines through structure developing from a pair of equal and opposite oblique waves.

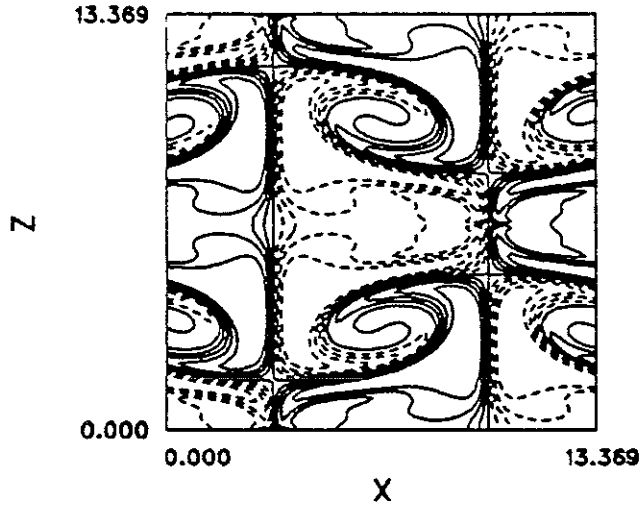

Figure 5.49 Mixture fraction cut through the $x - z$ plane at $y = 0$.

(a)

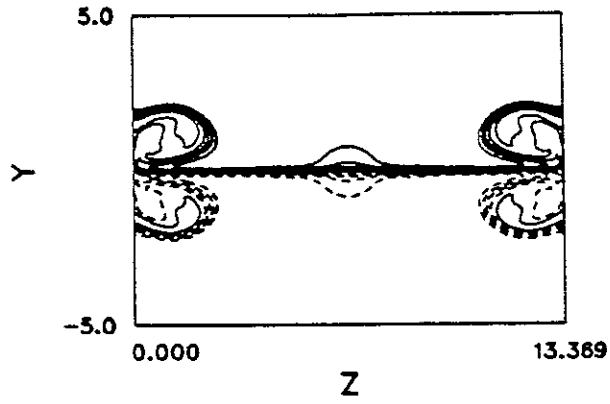

(b)

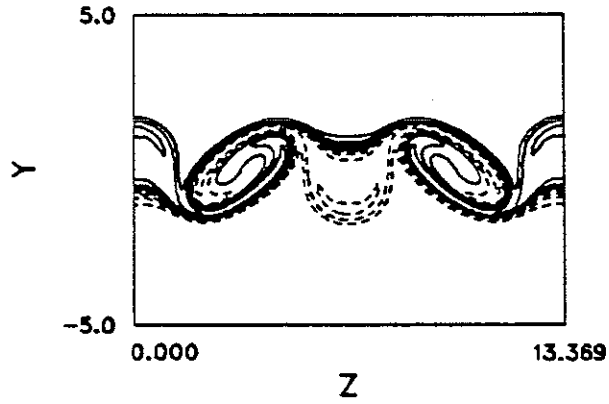

Figure 5.50 Cuts through the $y-z$ plane at (a) $x = L_x/4$ and (b) $x = L_x/2$.

(a)

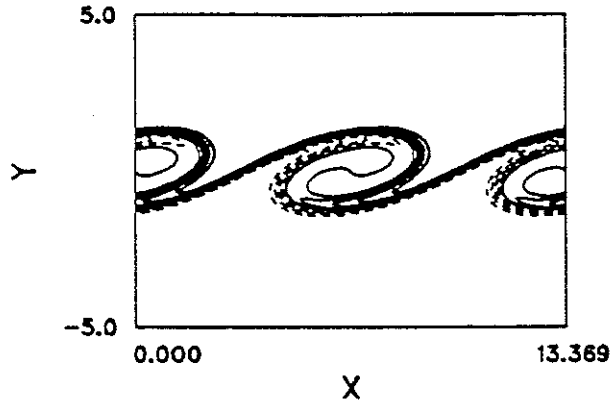

(b)

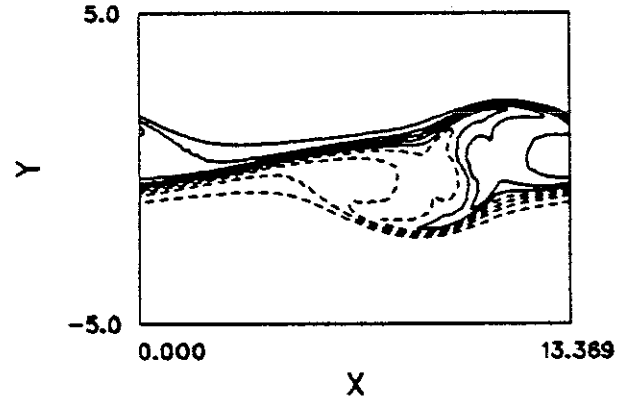

Figure 5.51 Cuts through the $x-y$ plane at (a) $z = L_z/4$ and (b) $z = L_z/2$.

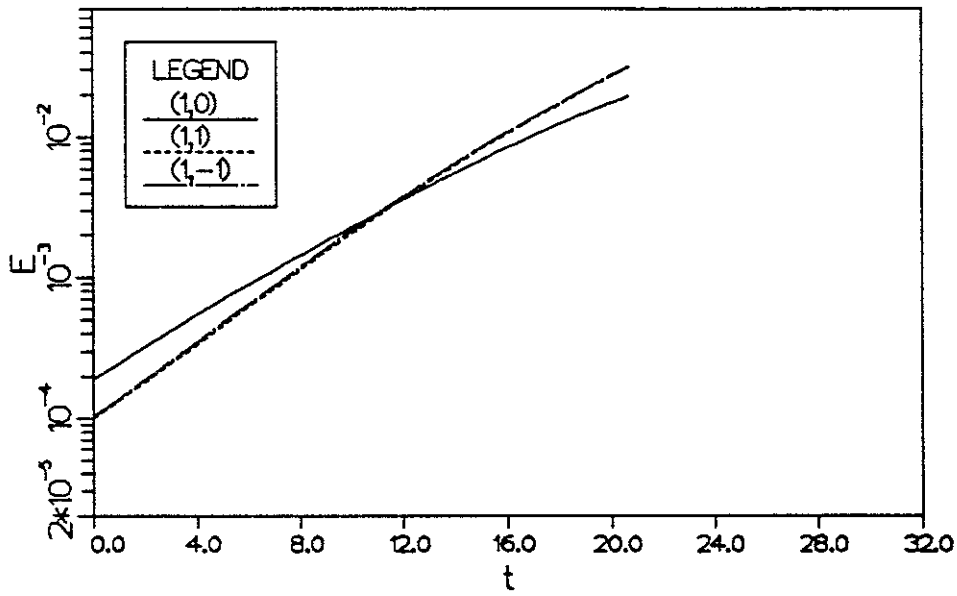

Figure 5.52 Growth in mode energies of the unstable waves in the presence of background noise.

(a)

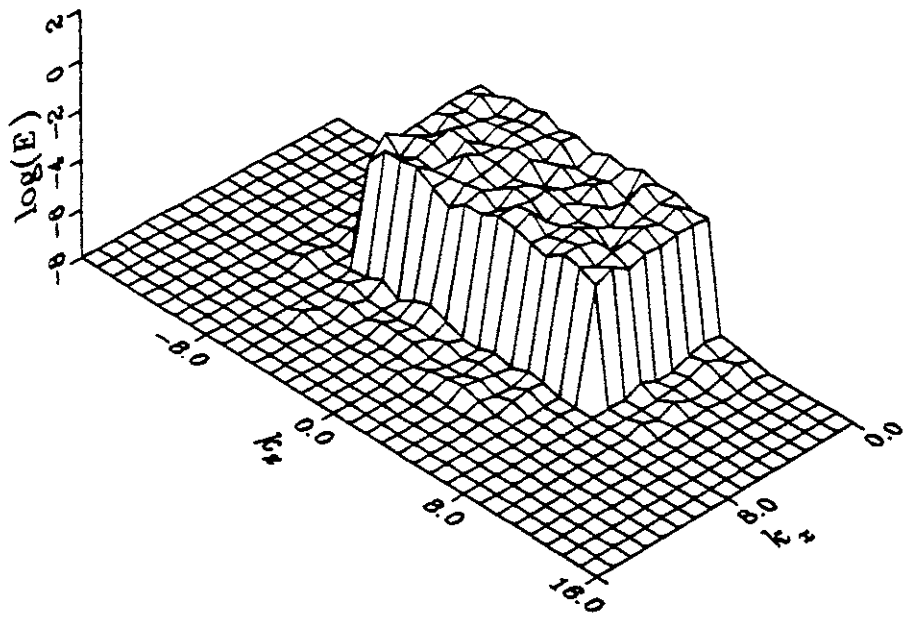

(b) max=1.14 min=1.09

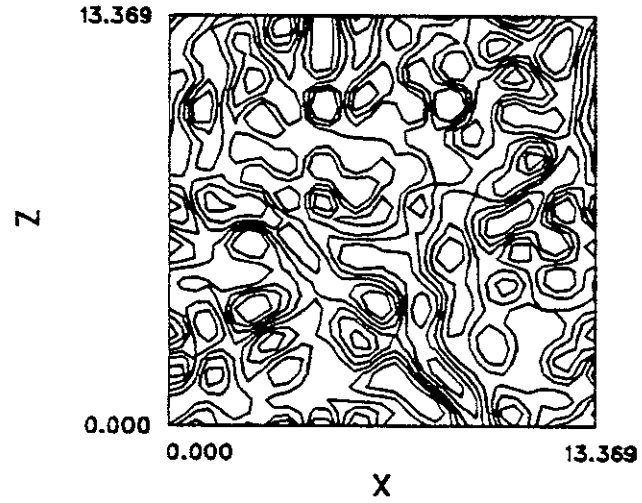

Figure 5.53 Simulation with random initial conditions at time $t = 0$ (a) carpet plot of mode energies, (b) pressure cut at $y = 0$.

(a)

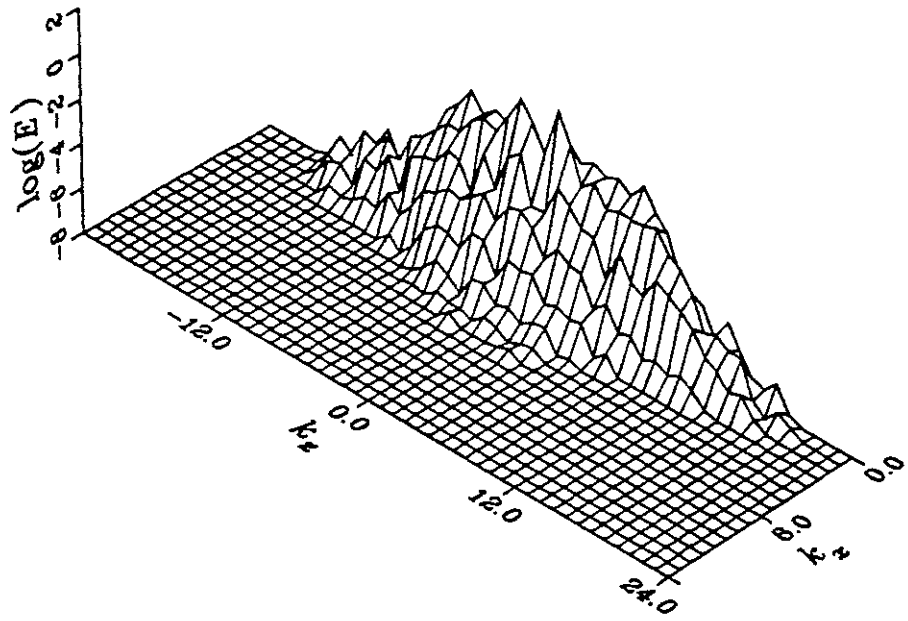

(b) max=1.14 min=1.10

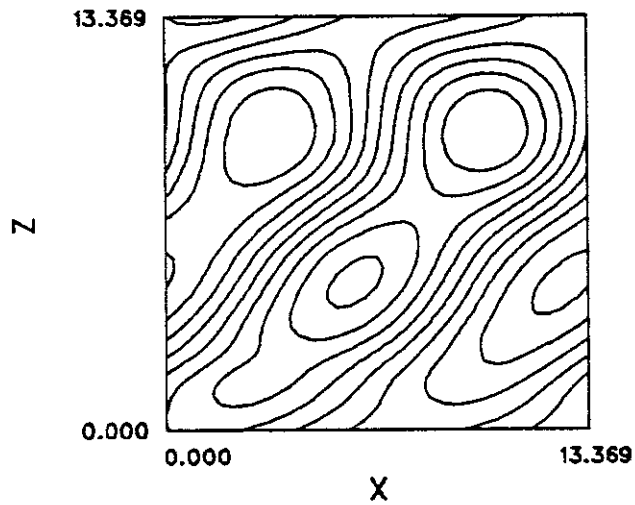

Figure 5.54 Simulation with random initial conditions at time $t = 29.6$ (a) carpet plot of mode energies, (b) pressure cut at $y = 0$.

(a)

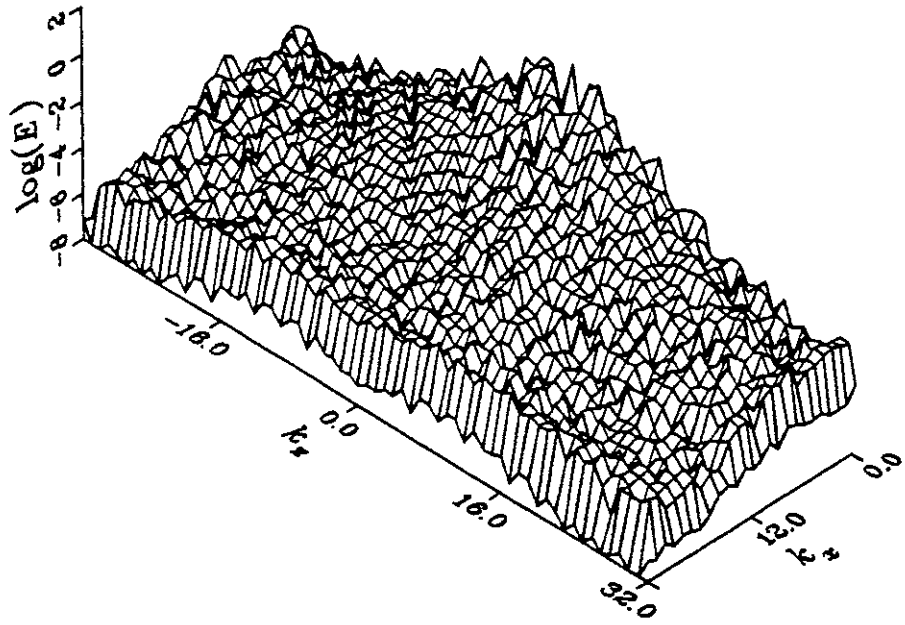

(b) max=1.28 min=0.846

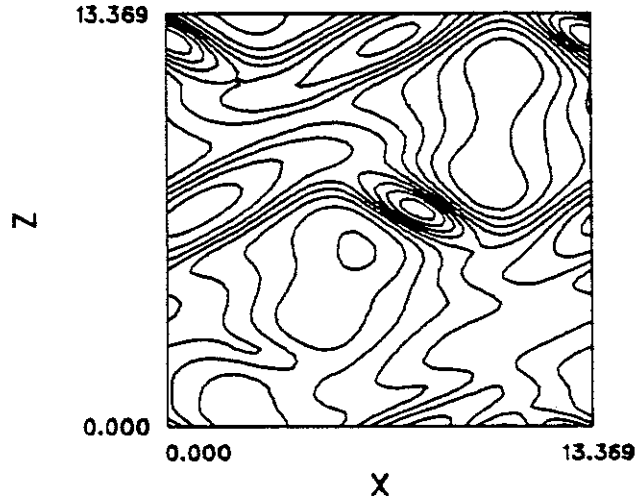

Figure 5.55 Simulation with random initial conditions at time $t = 52.0$ (a) carpet plot of mode energies, (b) pressure cut at $y = 0$.

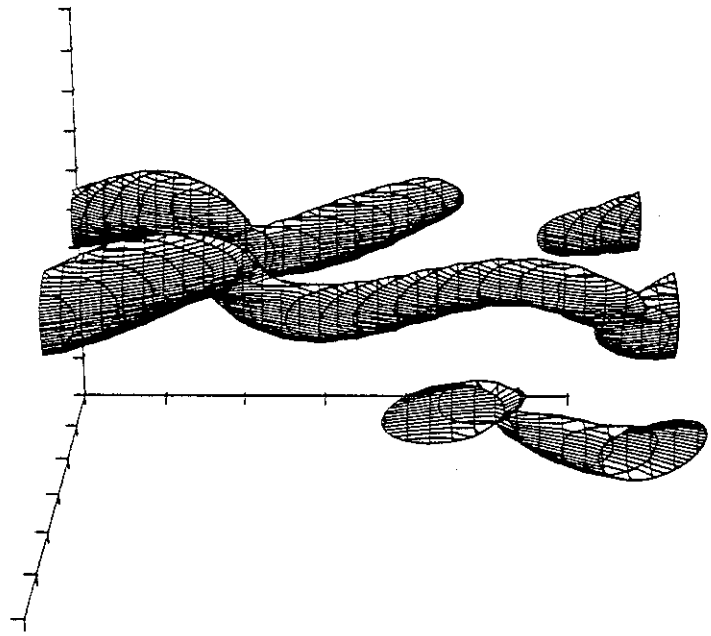

Figure 5.56 Surface of constant pressure for the simulation beginning with purely random initial conditions.

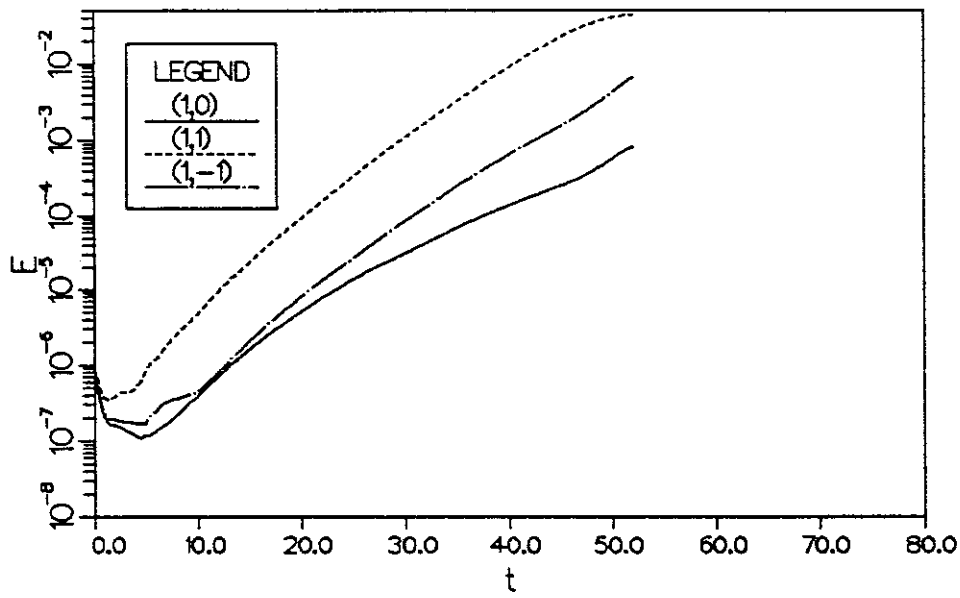

Figure 5.57 Growth in mode energies of the unstable waves in the simulation beginning with purely random initial conditions.

(a)

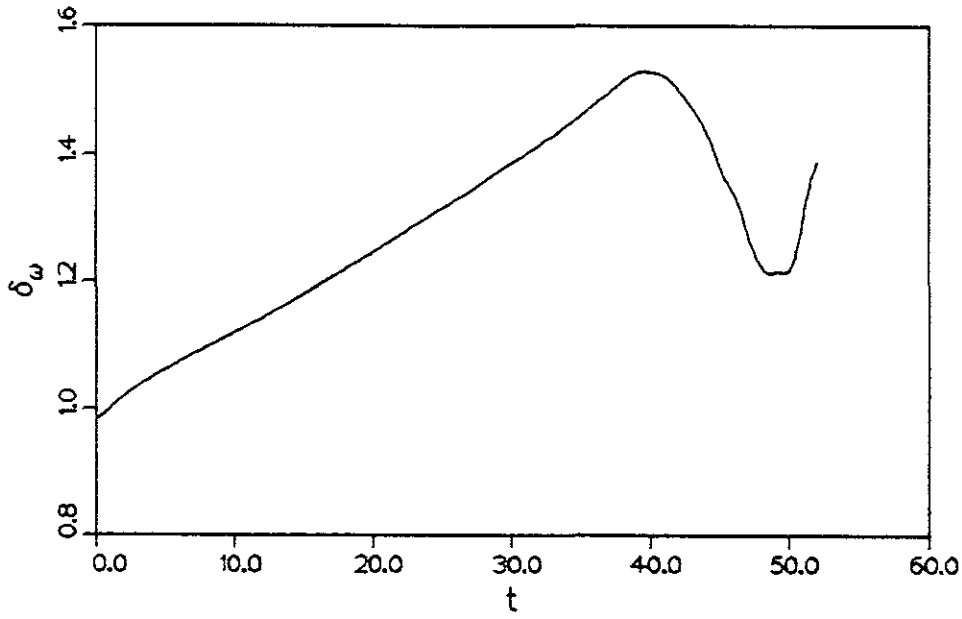

(b)

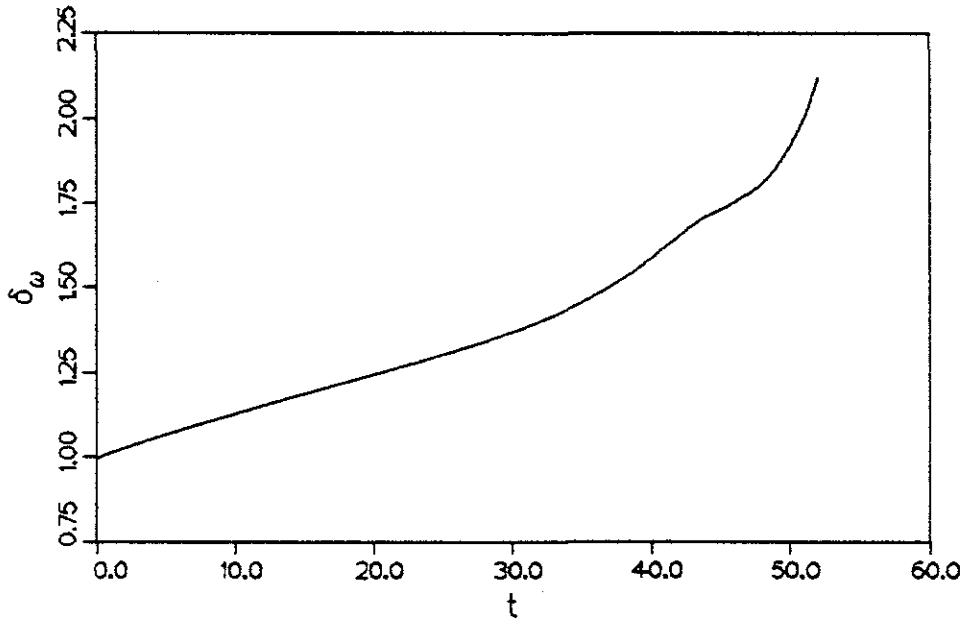

Figure 5.58 Growth in vorticity thickness for the simulation beginning with purely random initial conditions (a) regular vorticity thickness, (b) vorticity thickness based on mass-weighted velocity profile.

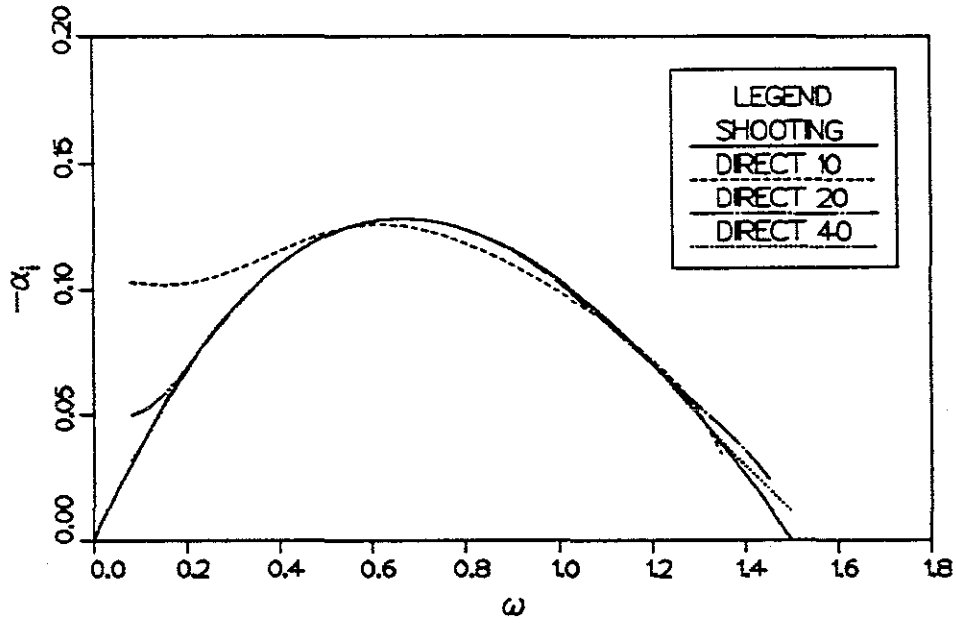

Figure A.1 Illustration of the convergence of the direct method. The number of points used (N^*) is given in the legend. The correct solution, as found by the shooting method, is also shown.